2011-08-09

The Formation and Stability of Radical-Molecule and Radical-Radical Complexes and Their Importance in Atmospheric Processes

Jared M. Clark
Brigham Young University - Provo

The Formation and Stability of Radical-Molecule and Radical-Radical Complexes and Their Importance in Atmospheric Processes

Jared Matthew Clark

A dissertation submitted to the faculty of
Brigham Young University
in partial fulfillment of the requirements for the degree of

Doctor of Philosophy

Jaron C Hansen, Chair
Milton L Lee
Daniel E Austin
Matthew C Asplund
Delbert J Eatough

Department of Chemistry and Biochemistry

Brigham Young University

December 2011

This thesis is dedicated to the patience and great goodness of my wife Ruth and my three beautiful children Katie, Nathan, and Alice

THE TEST OF A FIRST RATE INTELLIGENCE IS THE ABILITY TO HOLD TWO OPPOSED IDEAS IN THE MIND AT THE SAME TIME, AND STILL RETAIN THE ABILITY TO FUNCTION. ONE SHOULD, FOR EXAMPLE, BE ABLE TO SEE THAT THINGS ARE HOPELESS AND YET BE DETERMINED TO MAKE THEM OTHERWISE.

-- F. SCOTT FITZGERALD

ABSTRACT

The Formation and Stability of Radical-Molecule and Radical-Radical Complexes and Their Importance in Atmospheric Processes

Jared Matthew Clark
Department of Chemistry and Biochemistry, BYU
Doctor of Philosophy

This research explores the role that radical-molecule complexes play in the chemistry of Earth's atmosphere. The formation of such complexes can have direct and pronounced effects on the reaction and product outcome of atmospheric chemical reactions. Some attention is also given to the formation of radial-radical pre-reactive complexes in the HO + ClO system. Peroxy radicals (RO_2) can form stable complexes with polar compounds such as H_2O, NH_3, and CH_3OH. For the simplest RO_2 radical, HO_2, complex formation (e.g., $HO_2{-}H_2O$, $HO_2{-}NH_3$, and $HO_2{-}CH_3OH$) gives rise to a significant increase in the HO_2 self-reaction rate constant. Although this phenomenon has been observed since the mid-1970s, no satisfactory explanation has been put forward to explain this effect. Herein a rationale for the enhancement of the HO_2 self-reaction is given based on extensive geometric, mechanistic and natural bond orbital (NBO) analyses. The apparent lack of a rate enhancement for the methyl peroxy (CH_3O_2) self-reaction is also presented. The combined insights gained from these two systems are then extended to predict if a water enhancement is expected for the 2-hydroxyethyl peroxy ($HOCH_2CH_2O_2$) self-reaction kinetics. The computational results of this study are then compared to experimental work and conclusions are drawn towards a general procedure to predict the presence/absence of water initiated rate enhancements in RO_2 systems as a whole.

Original work regarding the formation of a series of organic $RO_2{-}H_2O$ complexes is presented. This work established the effects of different functional groups on the stability of organic peroxy radicals and makes estimates of the associated atmospheric lifetimes and equilibrium constants. This work is further extended to the family of peroxy radicals that form from the atmospheric oxidation of isoprene (the most abundant non-methane biologically emitted hydrocarbon). For the first time, complexes of isoprene peroxy radicals with water are presented along with atmospheric lifetime estimates. Conclusions are made as to the effect of water on the product branching ratio of the isoprene peroxy radical + NO_2. The oxidation of hexanal to form hexanal peroxy radicals is discussed within the context of the formation of hexanal peroxy water complexes.

Aerosol formation is also perturbed as a result of complexation. Aerosol formation under atmospheric conditions is hypothesized to be initiated by radical-molecule complex formation. For example, in the absence of ammonia, the nucleation of H_2SO_4 in water vapor to form sulfuric acid aerosols is slow. However, as the concentration of NH_3 rises, a marked increase in the rate of sulfuric acid aerosol formation is observed. This work explores the effects of the photolysis products of NH_3 (NH_2 and NH) on the rate of aerosol formation in systems involving H_2SO_4, HNO_3,

HC(O)OH, and $CH_3C(O)OH$. With the exception of $H_2SO_4{-}NH_3$ and $HNO_3{-}NH_3$ (geometries already published in the literature), minimum energy structures are presented here for the first time for each of the acid$-NH_x$ complexes. Thermochemical data and lifetime estimates are provided for each complex. Conclusions about the relevance of acid$-NH_2$ and acid$-$NH in the formation of atmospheric aerosols are set forth. Finally, mechanistic insights into the reaction of the hydroxyl radical (OH) and Cl_2O are obtained via analysis of the two potential energy surfaces that both involve the formation of HO$-Cl_2O$ pre-reactive complexes.

Keywords: peroxy radical, radical water complex, atmosphere, ozone, aerosol

ACKNOWLEDGEMENTS

I express my deepest appreciation and thanks to my dear wife Ruth Clark for her unfailing patience and support throughout my time as a graduate student. Her belief in me made all my efforts leading to the production of this thesis possible. I thank my adorable children for their love and for all of the times they begged me not to go into work, but to stay home and play with them.

I would like to thank my graduate advisor, Jaron Hansen, for the untold wealth of knowledge and experience he has given me and for seeing potential in me when I first arrived at BYU. I want to acknowledge my fellow graduate student Taylor Cline for all of the effort and work he put in to help make this dissertation possible. I would also like to thank Marie Chilton for her help with data modeling.

TABLE OF CONTENTS

LIST OF FIGURES

Chapter 2

Chapter 3

Chapter 4

Chapter 5

Chapter 6

Chapter 7

Chapter 8

LIST OF TABLES

Chapter 2

Chapter 3

Chapter 4

Chapter 5

Chapter 6

Chapter 7

LIST OF SUPPLEMENTARY TABLES

Chapter 2

Chapter 3

Chapter 4

Chapter 5

Chapter 7

Chapter 8

CHAPTER 1: INTRODUCTION

1.1 Radical-Molecule Complexes

The existence and significance of complexes on chemical systems relevant to atmospheric chemistry has been a topic of ongoing discussion for a number of years.[1-10] The systems of complex formation that have been traditionally studied can be classified as molecule-molecule complexes. The formation and stabilization of these molecule-molecule complexes is often characterized by the presence of hydrogen bond interactions. An example of a molecule-molecule complex is the O_3-H_2O system.[11-15] The complexation of O_3 with H_2O alters the photochemistry of the O_3 system. In the absence of H_2O, the photolysis of O_3 to form $O_2(^1\Delta_g)$ and $O(^1D)$ takes place at 310 nm:

$$O_3 + h\nu \rightarrow O_2(^1\Delta_g) + O(^1D) \qquad (1.1)$$

This reaction is primary importance for the atmosphere because it leads to the formation of hydroxyl radicals:

$$O(^1D) + H_2O \rightarrow 2\ OH \qquad (1.2)$$

Complexation of ozone has been shown to enhance the absorption of 355 nm light by two orders of magnitude.[11] This has the effect of red-shifting the photolysis of O_3 by 45 nm. In effect, the oxidative potential of the troposphere is increased as a result of an increase in the production of OH.

In addition to molecule-molecule complexes, a growing number of studies on the importance of the formation of radical-molecule complexes and the impact they have on the reaction mechanisms and photochemistry of atmospherically important reactions have been published.[16-28] Radicals are of prime importance because they are the reactive species which initiate much of the chemistry of the lower atmosphere. Understanding the chemistry of radicals is crucial to being able to describe many atmospheric processes. The present work will explore the formation of peroxy radical-water (RO_2-H_2O) complexes and will set forth the basis of the catalytic water enhancement effect of the HO_2 self-reaction. In addition, the possible role of amidogen (NH_2) and imidogen (NH) radicals in the formation of new aerosol particles will also be addressed. Finally, a potential energy surface study on the OH + OCl_2 reaction system will be addressed.

1.2 Peroxy Radicals

Peroxy radicals (HO_2 and RO_2) are important intermediates in atmospheric photo-oxidant formation. They are formed as the result of the atmospheric oxidation of carbon monoxide and volatile organic compounds (VOC) by hydroxyl radicals, nitrate radicals (NO_3), halogen atoms and ozone (O_3). For CO, oxidation by OH leads to the formation of CO_2 and H, followed by addition of O_2 to the H radical:

$$CO + OH \rightarrow CO_2 + H \quad (1.3)$$

$$H + O_2 + M \rightarrow HO_2 + M \quad (1.4)$$

VOCs undergo an initial hydrogen abstraction followed by addition of O_2:

$$RH + (OH, NO_3, \text{or } Cl) \rightarrow R + (H_2O, HNO_3, \text{or } HCl) \quad (1.5)$$

$$R + O_2 + M \rightarrow RO_2 + M \quad (1.6)$$

Depending on the prevailing NO concentration, ozone and other photo-oxidants, e.g. peroxides, peroxyacetyl nitrates (PANs) and other organic nitrates, are formed in this mechanism. If NO concentrations are low, peroxy radicals terminate via self-reaction or reaction with other RO_2 radicals that lead to a variety of products. The termination step is generalized as follows:

$$RO_2 + RO_2 \rightarrow ROOH + O_2 \quad (1.7a)$$

$$\rightarrow 2\ RO + O_2 \quad (1.7b)$$

$$\rightarrow ROH + RCHO + O_2 \quad (1.7c)$$

When a sufficient concentration of NO is present, as in urban areas, the reaction of RO_2 with NO leads to the formation of ozone, a major component of photo-oxidant smog. In general, the point at which RO_2 radicals react with NO in lieu of termination via reactions (1.7a) to (1.7c) is dependent of the prevailing RO_2 concentration. Typically, NO concentrations between ~20-55 ppt are required. The formation of O_3 is given through a series of several chemical reactions:

$$RO_2 + NO \rightarrow RHO + NO_2 \quad (1.8a)$$

$$RHO + O_2 \rightarrow RO + HO_2 \quad (1.8b)$$

$$HO_2 + NO \rightarrow HO + NO_2 \quad (1.8c)$$

$$NO_2 + h\nu \rightarrow O + NO \quad (1.8d)$$

$$O + O_2 + M \rightarrow O_3 + M \quad (1.8e)$$

A single RO_2 can be responsible for the production of two O_3 molecules. Formation of PANs and organic nitrates follows as the result of addition of NO_2 and NO, respectively, to the RO_2 radical:

$$RO_2 + NO_2 + M \rightarrow ROONO_2 + M \quad (1.9a)$$

$$RO_2 + NO \rightarrow RONO_2 \quad (1.9b)$$

While atmospheric measurements of OH are essential for establishing the accuracy of the basic theories about atmospheric photochemistry, measurements of RO_2 and HO_2 provide a deeper insight into the mechanism of photo-oxidant formation. The current work surveys the formation of RO_2-water complexes in order to understand their role in the chemistry of the atmosphere.

1.3 Aerosol Formation

Formation of new aerosol particles in the atmosphere is currently considered to be the result of the homogeneous nucleation of water and certain trace gases (e.g., H_2SO_4 and NH_3).[29] It has been understood since the early 1960s that trace amounts of H_2SO_4 are strongly correlated with the rate of new particle formation.[30,31] However, in many cases the presence of H_2SO_4 alone does not explain the high number of particles produced.[32-34] In order to explain the elevated production of aerosol particles, it is believed that the participation of a third component is required in the nucleation process. The most likely

candidate species is ammonia (NH_3) because of its abundance in the atmosphere and its ability to lower the vapor pressure of H_2SO_4 above solution, which is expected to enhance particle formation in gases containing H_2SO_4.[35,36]

The concentration of atmospheric NH_3 has doubled over the past century [37] as a result of increase nitrogen fertilization, animal husbandry, and agricultural activities. The increase in the amount of atmospheric NH_3 leads to a greater concentration of the oxidation and photolysis products of NH_3 (e.g., NH_2 and NH). Initial oxidation of NH_3 leads to the formation of NH_2:

$$NH_3 + h\nu\ (185\ nm) \rightarrow NH_2 + H \quad (1.10)$$

$$NH_3 + OH \rightarrow NH_2 + H_2O \quad (1.11)$$

Formation of NH can results from the self-reaction of NH_2 or the reaction of NH_2 with OH. The self-reaction of the NH_2 radical leads either to recombination or to disproportionation:

$$NH_2 + NH_2 + M \rightarrow N_2H_4 + M \quad (1.12a)$$

$$\rightarrow NH + NH_3 \quad (1.12b)$$

Both these channels are exothermic with reaction (1.12b) acting as the minor channel.[38-40] The reaction of NH_2 with OH follows:

$$NH_2 + OH \rightarrow NH + H_2O \quad (1.13)$$

Reaction (1.13) has been found to be a key reaction in the modeling of thermal $DeNO_x$ reaction kinetics.[41,42]

The present work surveys a number of NH_3-acid complexes and speculates on the importance of NH_2 and NH radicals in the formation of new aerosol particles.

1.4 OH + Cl_2O Chemistry

Recent concern about the depletion of stratospheric ozone by chlorine species from the decomposition of chlorofluoromethanes has emphasized the need for studies on the reaction steps involved, particularly those which control the concentration of the hydroxyl and chlorine monoxide (ClO) radicals in the stratosphere. The OH radical plays an important role in ozone destruction because it converts the inactive chlorine species (e.g. HCl, Cl_2 and Cl_2O) back into atomic chlorine.

$$OH + HCl \rightarrow H_2O + Cl \quad (1.14)$$

$$OH + Cl_2 \rightarrow HOCl + Cl \quad (1.15)$$

$$OH + Cl_2O \rightarrow HOOCl + Cl \quad (1.16)$$

Although Cl_2O is thought to be of only minor atmospheric importance, an understanding of its reaction with OH, including the overall reaction rate coefficient (as a function of temperature and pressure), and the reaction mechanism provides a benchmark for studies of other chlorine oxides (e.g., ClO, OClO, and ClOOCl) that are important to the study of atmospheric chemistry and stratospheric ozone depletion.

CHAPTER 2: AN NBO ANALYSIS OF THE CATALYTIC EFFECT OF WATER ON THE HO_2 SELF-REACTION

2.1 Abstract

The catalytic enhancement effect of H_2O on the self-reaction of HO_2 has been studied at the G2M(CC5)//B3LYP/6-311G(d,p) level of theory. The calculated potential energy surface predicts a lowering of the activation barrier by 6.4 kcal mol^{-1} for the formation of products (H_2O_2 + $^3O_2$) in the presence of an HO_2−H_2O complex. Compared with the results for the reaction without H_2O, it is noted that the H_2O molecule catalytically enhances the self-reaction rate constant of the HO_2 radical by enhancing the hydrogen bonding architecture of the HO_2−HO_2 complex allowing for a greater degree of delocalization of the electron density into the O−H anti-bond of the HO_2 radical fated to become $^3O_2$.

2.2 Introduction

The hydroperoxy (HO_2) radical is an important intermediate in both combustion and atmospheric chemistry. The self-reaction of HO_2:

$$HO_2 + HO_2 \rightarrow H_2O_2 + O_2 \quad (2.1)$$

is the primary source of H_2O_2 in the stratosphere and upper troposphere.[43] In the mid-1970's, Hamilton was the first to demonstrate that the rate of the HO_2 self-reaction increased in the presence of H_2O vapor.[16,19] He proposed that the enhancement in the rate was the result of the formation of a reactive complex between HO_2 and H_2O:

$$HO_2 + H_2O \rightarrow HO_2\text{-}H_2O \quad (2.2)$$

Numerous investigations have since substantiated the water enhancement phenomenon[19,44-51] and have also shown that other polar molecules capable of hydrogen bonding (e.g. NH_3[52,53] and CH_3OH[50,54-58]) enhance the rate as well.

In addition to the many experimental studies that have been directed at measuring the rate of the HO_2 self-reaction, *ab initio* studies have also been performed in an effort to understand the stability of the HO_2-H_2O,[18,59,60] HO_2-NH_3[19,61] and HO_2-CH_3OH[58] complexes. Both experimental and computational studies have also been conducted in an effort to understand the abundance and thermodynamic properties of the $HO_2{-}H_2O$ and $HO_2{-}CH_3OH$ complexes. In an attempt to understand the effects of H_2O on the HO_2 self-reaction, Lin[62] reported a mechanistic study of the catalytic effect of H_2O on the HO_2 self-reaction on both the singlet and triplet surfaces. Lin concluded that the HO_2 self-reaction rate is enhanced by the presence of H_2O because it catalytically reduces the barriers of formation of the products (i.e. O_2, H_2O_2, and O_3).

The purpose of the current work is to describe the role water plays in the enhancement of the HO_2 self-reaction through geometric and natural bond orbital (NBO) analysis of the HO_2-HO_2 self-reaction potential energy surfaces (PESs) in the presence and absence of water.

2.3 Methods

All calculations reported herein were performed using the Gaussian 03, Revision D.01 suite of programs.[63] The optimized geometries and vibrational frequencies were calculated using the hybrid density functional (B3LYP) method (i.e., Becke's three-parameter nonlocal exchange functional[64-66] with the correlation functional of Lee et al.[67])

using the standard 6-311G(d,p) basis set for the determination of both the geometry and frequencies. Intrinsic reaction coordinate (IRC) calculations, performed at the B3LYP/6-311G(d,p) computational level, have been performed in order to confirm the connection of each transition state with designated intermediates.

Single point energies for each species were calculated using the G2M(CC5) method.[68] This method utilizes a series of calculations based on the B3LYP/6-311G(d,p) optimized geometry in order to approximate the CCSD(T)/6-311+G(3df,2p) level of theory. These calculations include a higher-level correction (HLC) term based on the number of paired and unpaired α- and β-electrons. The total G2M energy is determined as follows:

$$E[\text{G2M(CC5)}] = E[\text{CCSD(T)/6-311G(d,p)}] + \Delta E(\text{+3df,2p}) + \Delta E(\text{HLC}) + \text{ZPE[B3LYP/6-311G(d,p)]} \quad \text{(EQ 2.1)}$$

$$\Delta E(\text{+3df,2p}) = E[\text{MP2/6-311+G(3df,2p)}] - E[\text{MP2/6-311G(d,p)}] \quad \text{(EQ 2.2)}$$

$$\Delta E(\text{HLC}) = -00530n_{\beta} - 0.00019n_{\alpha} \quad \text{(EQ 2.3)}$$

The G2M(CC5) energies were further modified through thermal corrections to 298 K. NBO analysis was performed at the MP2/6-311+G(3df,2p)//B3LYP/6-311G(d,p) level using the Gaussian 03 implementation of NBO 3.1.[69-76] Natural resonance theory (NRT) calculations were carried using NBO 5.0[77] as implemented in GAMESS.[78]

The global minimum structures for all intermediates and transition states were determined by use of an extensive random constrained sampling (RCS) methodology.[59]

The RCS method generates a large number of randomly generated radical-molecule complex geometries by packing one member of a complex around the others. The randomly placed moieties were constrained to a 3.0-Å radius sphere encompassing the stationary complex members. Each lowest energy structure was arrived at via 10,000 random starting structures performed at the B3LYP/6-311G(d,p) computational level.

All calculations were performed on a supercomputing Linux cluster consisting of 320 processing nodes equipped with two quad-core Intel Nehalem processors (2.8 GHz) and 24 GB of memory. All nodes are connected with Infiniband, a high-speed, low-latency copper interconnect.

The B3LYP/6-311G(d,p) optimized geometries and vibrational frequencies of all species considered are found in Tables S2.1-S2.12.

2.4 Results and Discussion

The HO_2 self-reaction can take place on either a singlet or triplet surface:

$$HO_2 + HO_2 \rightarrow [HO_2{-}HO_2]^{\ddagger} \rightarrow H_2O_2 + O_2(^1\Delta) \quad \text{[singlet]} \qquad (2.3a)$$

$$\rightarrow H_2O_2 + {}^3O_2 \qquad \text{[triplet]} \qquad (2.3b)$$

On either surface, the self-reaction consists of an initial step that involves the barrierless formation of a pre-reactive doubly hydrogen-bonded complex, followed by the subsequent formation of the reaction products. This pre-reactive complex can be characterized as a diradical species with an energy that lies ~9 kcal mol^{-1} below the energy of the reactants at 0 K (value calculated at the G2M(CC5) computational level and adjusted for thermal and zero point energy corrections).

The energy barrier connecting the pre-reactive complex to the transition state on the singlet and triplet surfaces have been estimated to be 17.5 and 5.7 kcal mol^{-1}, respectively.[79] The large difference in barrier height leads to the conclusion that the triplet surface formation of H_2O_2 and ground state O_2 is the predominant pathway of the HO_2 self-reaction and is the pathway under consideration in this work both in the presence and absence of H_2O.

2.4.1 HO_2—HO_2 Reaction and Hydrogen Bonding

The HO_2 self-reaction can be classified as a proton-transfer reaction. As hydrogen-bonding is essentially a proton-transfer process, the self-reaction of HO_2 can be satisfactorily explained through analysis of the hydrogen-bonding elements of each stationary point along the PES. This approach will be followed for the HO_2 reaction both in the presence and absence of water.

A hydrogen bond may be represented as a resonance hybrid of the donor and acceptor species comprised of 'partial covalent' and 'electrostatic' moieties:

$$[B: \cdots H{-}A]_{covalent} \leftrightarrow [B{-}H^{+} \cdots :A^{-}]_{electrostatic} \quad (2.4)$$

In the lexicon of NBO analyses, the resonance hybrid of (2.4) corresponds to a two-electron intermolecular donor-acceptor interaction of the form:

$$n_B \rightarrow \sigma_{AH}^{*} \quad (2.5)$$

in which electron density from a Lewis-like lone pair n_B of the donor is delocalized into an unfilled non-Lewis-like anti-bonding orbital of the acceptor. In all cases considered here in, n_B represents a lone pair of a donating oxygen atom and σ_{AH}* the anti-bonding orbital of an O−H bond. The resonance hybrid, which expresses the partial covalency of H-bonding, suggests an immediate relationship to the 'degree of completion' of a proton-transfer process:

$$A{-}H \cdots :B \rightarrow [A: \cdots H \cdots B]^{\ddagger} \rightarrow A:^{-} \cdots H{-}B^{+} \qquad (2.6)$$

The two hydrogen-bonded species in (2.6) can be visualized as points along an intrinsic reaction coordinate that connects reactant and product species through the transition state (‡). In this manner we can gain a more global perspective on how each H-bonded species is related to the overall progress along the chemical reaction pathway. In the present context, (2.6) will be represented as:

$$O_A{-}H \cdots :O_D \rightarrow [O_A: \cdots H \cdots O_D]^{\ddagger} \rightarrow O_A: \cdots H{-}O_D \qquad (2.7)$$

The significance of individual n→σ* interactions can be estimated through second-order perturbation theory. This analysis is carried out by examining all possible interactions between "filled" Lewis-type NBOs (n) and "empty" non-Lewis NBOs (σ*). Such interactions are referred to as "delocalization" corrections to the zeroth-order natural Lewis structure. For each donor NBO (i) and acceptor NBO (j), the stabilization energy *E(2)* associated with delocalization ("2e-stabilization") i ® j is estimated as:

$$E(2) = \Delta E_{j,i} = q_i \frac{F(i,j)^2}{\varepsilon_j - \varepsilon_i} \quad \text{(EQ 2.4)}$$

where q_i is the occupancy of the donor orbital, ε_i and ε_j are the orbital energies (e.g., the diagonal elements of the Fock matrix) and F(i,j) is the orbital interaction term (e.g., off-diagonal NBO Fock matrix element). The magnitude of these stabilizing interactions is directly related the extent of orbital overlap ($S_{n\sigma}$*) that exists between n and σ*. The ratio $(S_{n\sigma}*/S_{n\sigma})^2$ of the attractive donor-acceptor, $S_{n\sigma}$*, and repulsive donor-donor, $S_{n\sigma}$, overlaps terms provide an estimate of the energetic balance that exists between the attractive and repulsive terms of the equilibrium geometry. Strong H-bonds exist when both Snσ* and $(S_{n\sigma}*/S_{n\sigma})^2$ are favorable.

2.4.2 HO_2–HO_2 Potential Energy Surface

The triplet potential energy surface for the HO_2 self-reaction, as computed at the G2M(CC5) computational level, is represented in Figure 2.1. The optimized stationary-point geometries of prominent HO_2 –HO_2 PES intermediates and transition states (TS) are shown in Figure 2.2. The total and relative energies for each species are assembled in Table 2.1. The product and reactant directions followed by the transition states were verified via IRC calculations. The geometry and energy of each pre-reactive complex and TS are in good agreement with those previously published.[80]

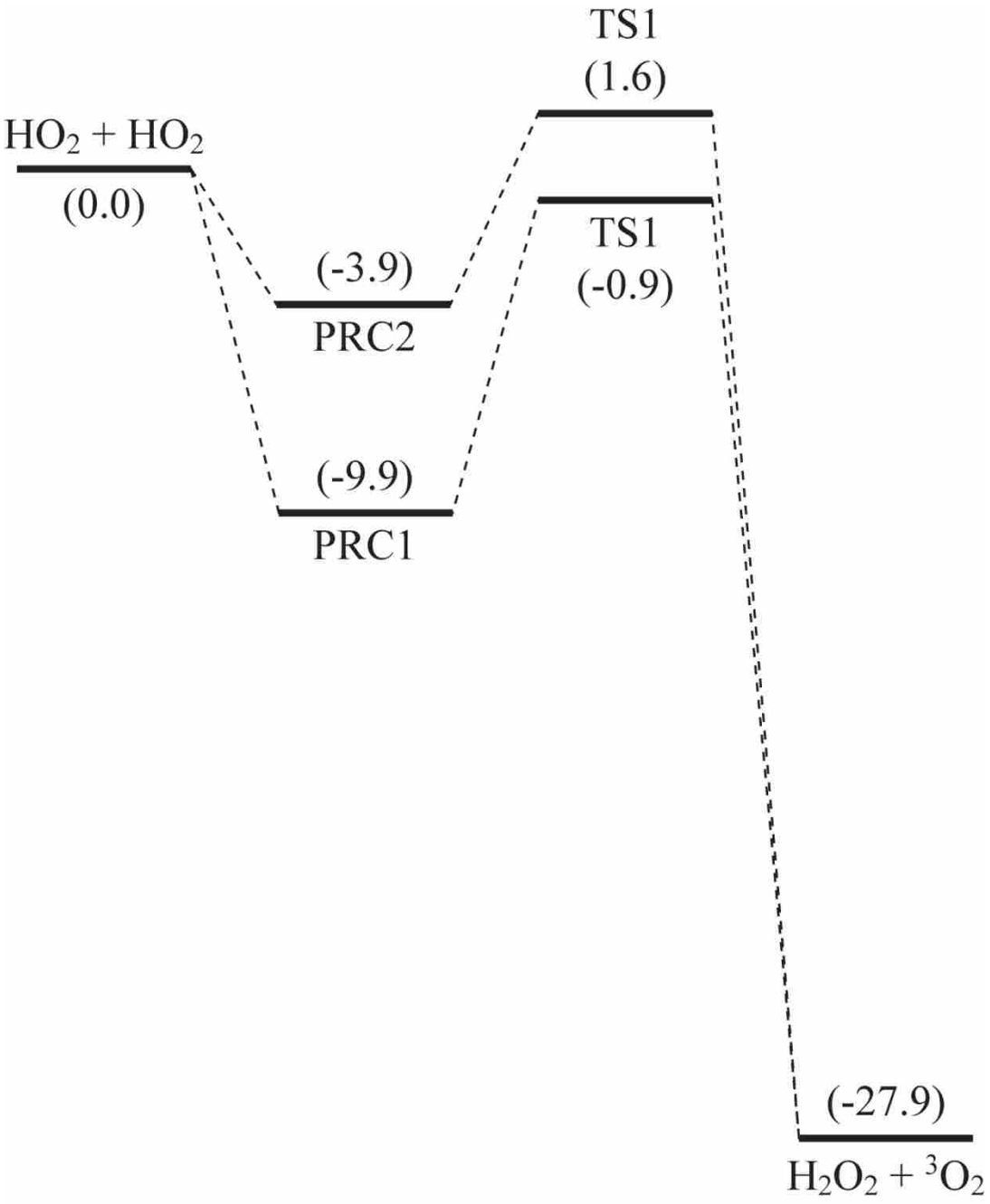

Figure 2.1. Schematic potential energy diagram of the triplet HO_2−HO_2 system computed at the G2M(CC5) level.

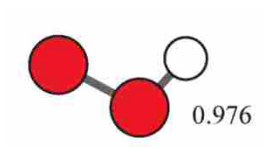

HO_2

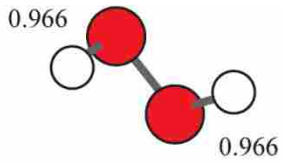

H_2O_2

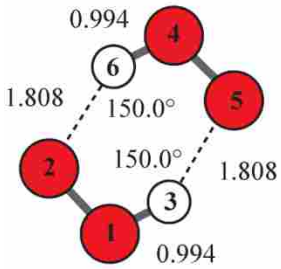

PRC1

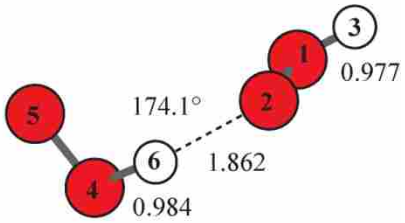

PRC2

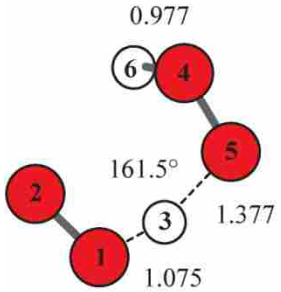

TS1

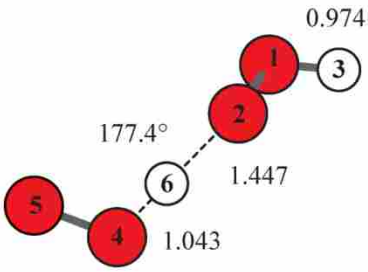

TS2

Figure 2.2. The optimized stationary-point geometries of the prominent triplet intermediates and transitions states structures of the HO_2−HO_2 reaction at the B3LYP/6-311G(d,p) level**.**

Table 2.1. Total and relative energies of all species germaine to the dry self-reaction of HO_2 calculated at different levels of theory with B3LYP/6-311G(d,p) optimized geometries.

		Energies[b]				
Species	ZPE[a]	B3LYP/6-311G(d,p)	MP2/6-311G(d,p)	MP2/6-311+G(3df,2p)	CCSD(T)/6-311G(d,p)	G2M
$HO_2 + HO_2$	17.7	-301.900816	-301.170477	-301.353189	-301.229006	-301.444018
PRC1	20.5	- 14.6	- 11.3	- 11.4	- 12.4	- 9.9
PRC2	19.5	- 7.4	- 5.9	- 6.4	- 6.7	- 3.9
TS1	17.4	- 7.8	2.2	2.3	- 0.1	- 0.9
TS2	17.7	- 5.5	2.7	2.5	1.6	1.6
$H_2O_2 + {}^3O_2$	19.0	- 35.0	- 52.6	- 52.9	- 39.7	- 27.9

[a] Values are in units of kcal mol^{-1}.

[b]The total energies of the reactants at different levels are given in au (E_h) and the relative energies (relative to the reactants) of other species at he corresponding levels are given in units of kcal mol^{-1}, ZPE corrections are included only in the G2M energies.

The formation of the products H_2O_2 + $^3O_2$ on the triplet HO_2 self-reaction PES can occur via two different pathways involving different intermediates. First, HO_2 and HO_2 can form a single linear head-to-tail, hydrogen-bonded pre-reactive complex, PRC2 (see Figure 2.2). The hydrogen bond length of PRC2 determined at the B3LYP/6-311G(d,p) level is 1.862 Å, which is ~8 % shorter than the experimentally determined value of 2.02 Å for the O···H distance of the water dimer.[81] As is usually the case for strong H-bonded systems, the OHO bond angle is nearly linear, 174.1°, and the bonding energy D_0 is predicted to be -3.9 kcal mol^{-1} at the G2M level. The two HO_2 radicals can also form a planar six-membered-ring pre-reactive complex PRC2 which consists of two equivalent hydrogen bonds. The H-bond length and OHO angle for each bond are determined to be 1.808 Å and 150.0°, respectively. The bonding energy D_0 of PRC2 is ⁻9.9 kcal mol^{-1} at the G2M level.

Both PRC1 and PRC2 are formed through the barrierless association of two HO_2 molecules. PRC2 advances toward product formation through TS2 that has a similar structure, implying that the transition state is product-like. The barrier height between PRC2 and TS2 is estimated to be 5.5 kcal mol^{-1}. In TS2, the forming H−O bond is shortened by 0.415 Å (22.3 %), the breaking O−H bond is lengthened by 0.059 Å (6.0 %) and the OHO angle is widened by 3.3° (1.9 %) to 177.4°. The relative binding energy of TS2 is estimated to be 1.6 kcal mol^{-1} above the reactants, as determined at the G2M level. PRC1 passes through TS1. Upon formation of TS1, the planar geometry of PRC1 is broken as one of the O−H bonds is rotated ~60° out of the HOO−H plane, halfway to the 120° of the HOOH dihedral of the H_2O_2 product. An important consequence of this rotation is that the hydrogen bond associated with the moving O−H bond is broken. This

fact accounts for a doubling of the barrier height (~11 kcal mol^{-1}) between PRC1 and TS1 relative to that faced by PRC2. The length of the H−O bond in TS2 is observed to increase by 0.081 Å (8.1 %) and the forming O−H bond to decrease by 0.431 Å (23.8 %). The OHO angle is TS1 increases by 11.5 Å (7.7 %).

Since the HO_2 self-reaction is essentially a proton-transfer reaction, the hydrogen bonds of each PRC and TS stationary point on the HO_2−HO_2 PES are analyzed through second-order perturbative and natural bond order analysis. The leading n→σ* interactions for the pre-reactive and transition state structures of the HO_2 self-reaction are represented in Figure 2.3. Table 2.2 represents the details of the binding-energy profile, O···H···O bond lengths (R_{OH} and R_{HO}) and the NRT bond orders (b_{OH} and b_{HO}) along the path of the PES.

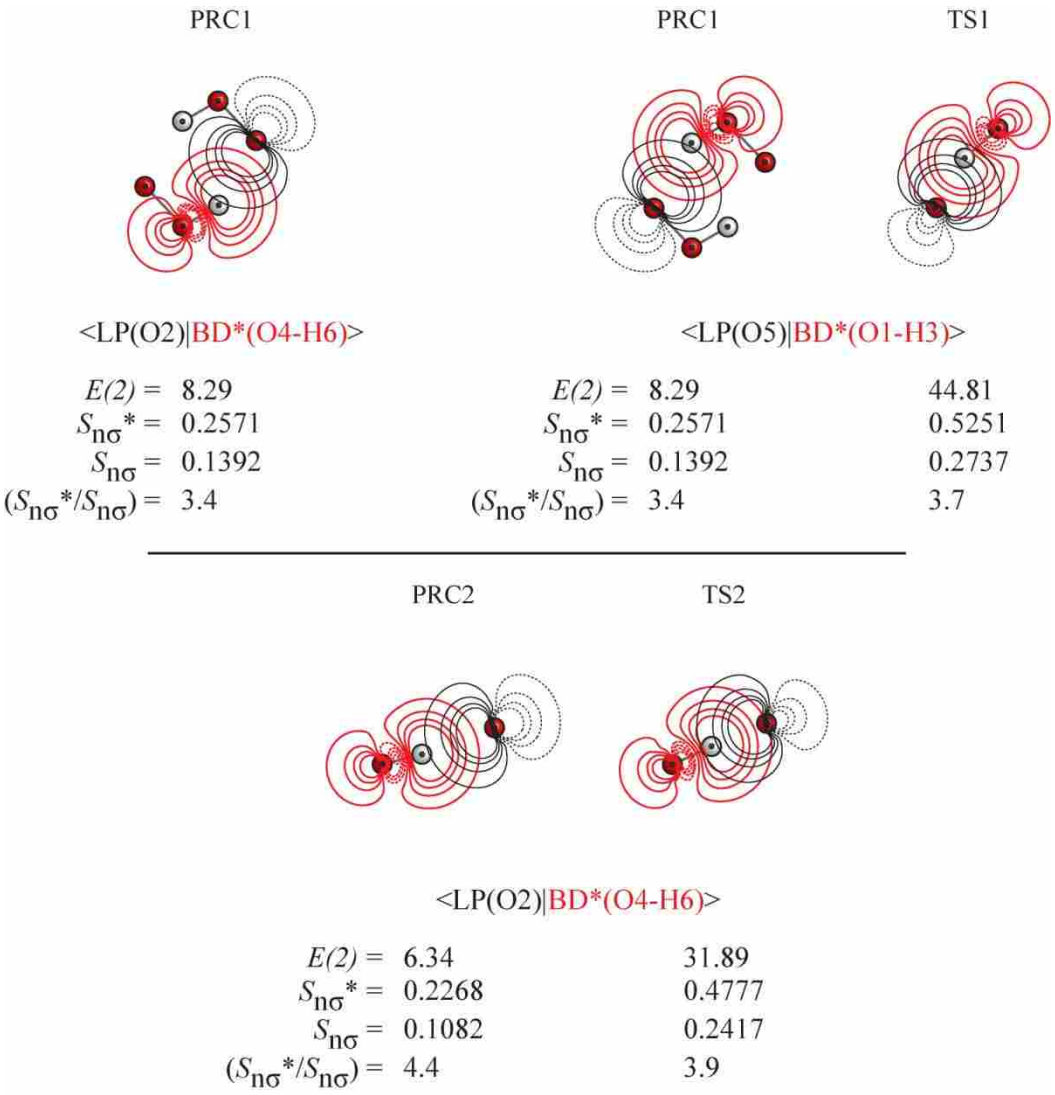

Figure 2.3. The leading n→σ* donor-acceptor interactions of the HO_2–HO_2 PES as calculated at the MP2/6-311+G(3df,2p) level. *E(2)* values are reported in kcal mol^{-1}. The atom numbering corresponds to that represented in Figure 2.1.

Table 2.2. Variations of binding energy ΔE, bond lengths R_{O3H1} and R_{H1O5}, and NRT bond orders b_{O3H1} and b_{H1O5} along the PES.

		Binding ΔE	Bond length (Å)				Bond order			
		(kcal mol^{-1})	R_{O1H3}	R_{H3O5}	R_{O4H6}	R_{H6O2}	b_{O1H3}	b_{H3O5}	b_{O4H6}	b_{H6O2}
Reactants:	$HO_2 + HO_2$	0.00	0.976	∞	0.976	∞	0.990	0.000	0.990	0.000
PRC1 (ring):	$HO_2{-}HO_2$	- 9.86	0.994	1.808	0.994	1.808	0.970	0.007	0.970	0.007
TS1 (ring):	$HO_2 \cdots HO_2$	- 0.90	1.075	1.377	0.977	2.289	0.884	0.074	0.987	0.000
Products:	$H_2O_2 + O_2$	-27.90	∞	0.966	0.966	∞	0.000	0.998	0.998	0.000
Reactants:	$HO_2 + HO_2$	0.00	0.976	∞	0.976	∞	0.990	0.000	0.990	0.000
PRC2 (linear):	$HO_2{-}HO_2$	- 3.86	0.977	∞	0.984	1.862	0.991	0.000	0.978	0.007
TS2 (linear):	$HO_2 \cdots HO_2$	1.59	0.974	∞	1.043	1.447	0.985	0.000	0.864	0.077
Products:	$H_2O_2 + O_2$	-27.90	0.966	∞	∞	0.960	0.978	0.000	0.000	0.998

Table 2.2 displays the global behavior of the bond lengths and bond orders along the reaction coordinate followed by PRC1 and PRC2, showing the progression from reactant-like to product-like values. For the path followed by PRC2, it can be seen that the O4−H6 bond length of the second HO_2 radical increases from 0.984 Å to 1.043 Å (6.0 %) resulting in the bond order decreasing from 0.978 to 0.864. Correspondingly, the H6···O2 hydrogen-bond length is shown to decrease from 1.862 Å to 1.447 Å (22.3 %) with the bond order of 0.007 increasing to 0.077. This elongation of an HO_2 H−O bond and shortening of the associated H-bond is indicative of the initial steps of a proton-transfer reaction. This change in the bonding profile of the O4−H6···O2 triad can be explained by an increase in the delocalization of electron density from the lone pair of the O2 atom into the O4−H6 anti-bonding orbital. The increase in electron density of this anti-bond results in a rise in the stabilization energy, *E(2)*, from 6.34 kcal mol^{-1} to 31.89 kcal mol^{-1}. This change in energy results from an order-of-magnitude increase in the overlap of the n→σ* (P)NBOs. As shown if Figure 2.3, PRC1 is composed of two equivalent hydrogen bonds with *E(2)* energies of 8.29 kcal mol^{-1} resulting from equal overlap between the interacting n and σ* (P)NBOs. As PRC1 passes to TS1, the H6···O2 H-bond is broken as the O4−H6 bond rotates out of the H6O4O5H3 plane. The O1−H3 and H3−O5 bond lengths of the remaining hydrogen-bond interaction see an increase of 0.081 Å (8.1 %) and a decrease of 0.431 Å (23.8 %), respectively. The *E(2)* energy of the $n_{O5}\rightarrow\sigma_{H3O1}$* interaction increases to 44.81 kcal mol^{-1}, the result of a two-fold increase in the associated (P)NBO overlap.

2.4.3 $HO_2-H_2O-HO_2$ Potential Energy Surface

The triplet potential energy surface for the HO_2 self-reaction in the presence of water, as computed at the G2M(CC5) computational level, is represented in Figure 2.4. The optimized stationary-point geometries of prominent $HO_2-H_2O-HO_2$ PES intermediates and transition states are shown in Figure 2.5. The total and relative energies for each species are assembled in Table 2.3. The product and reactant directions followed by the transition states were verified via IRC calculations. The geometry and energy of each pre-reactive complex and TS are in agreement with those previously published.[80]

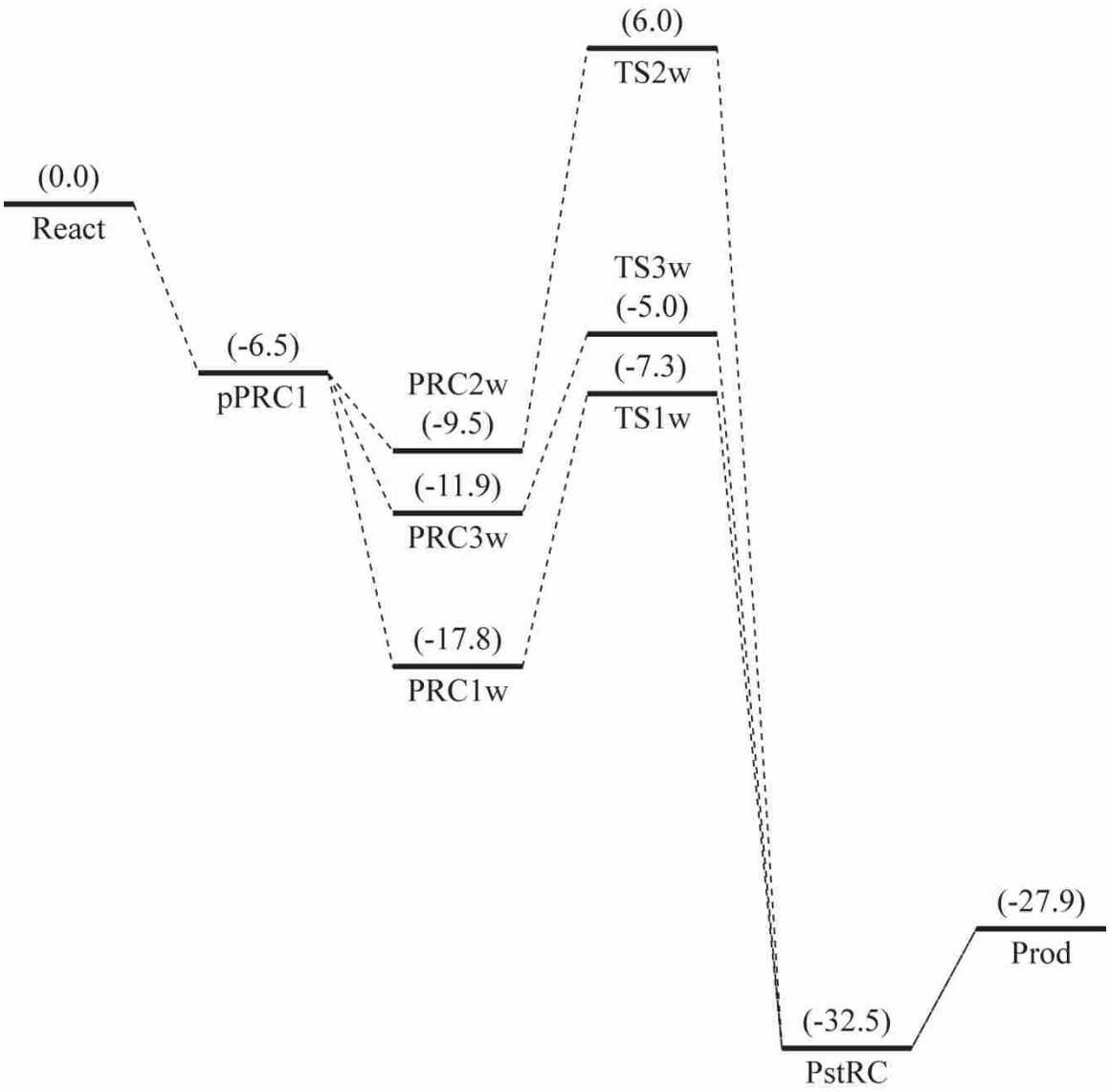

Figure 2.4. Schematic potential energy diagram of the triplet $HO_2{-}H_2O{-}HO_2$ system computed at the G2M(CC5) level**.**

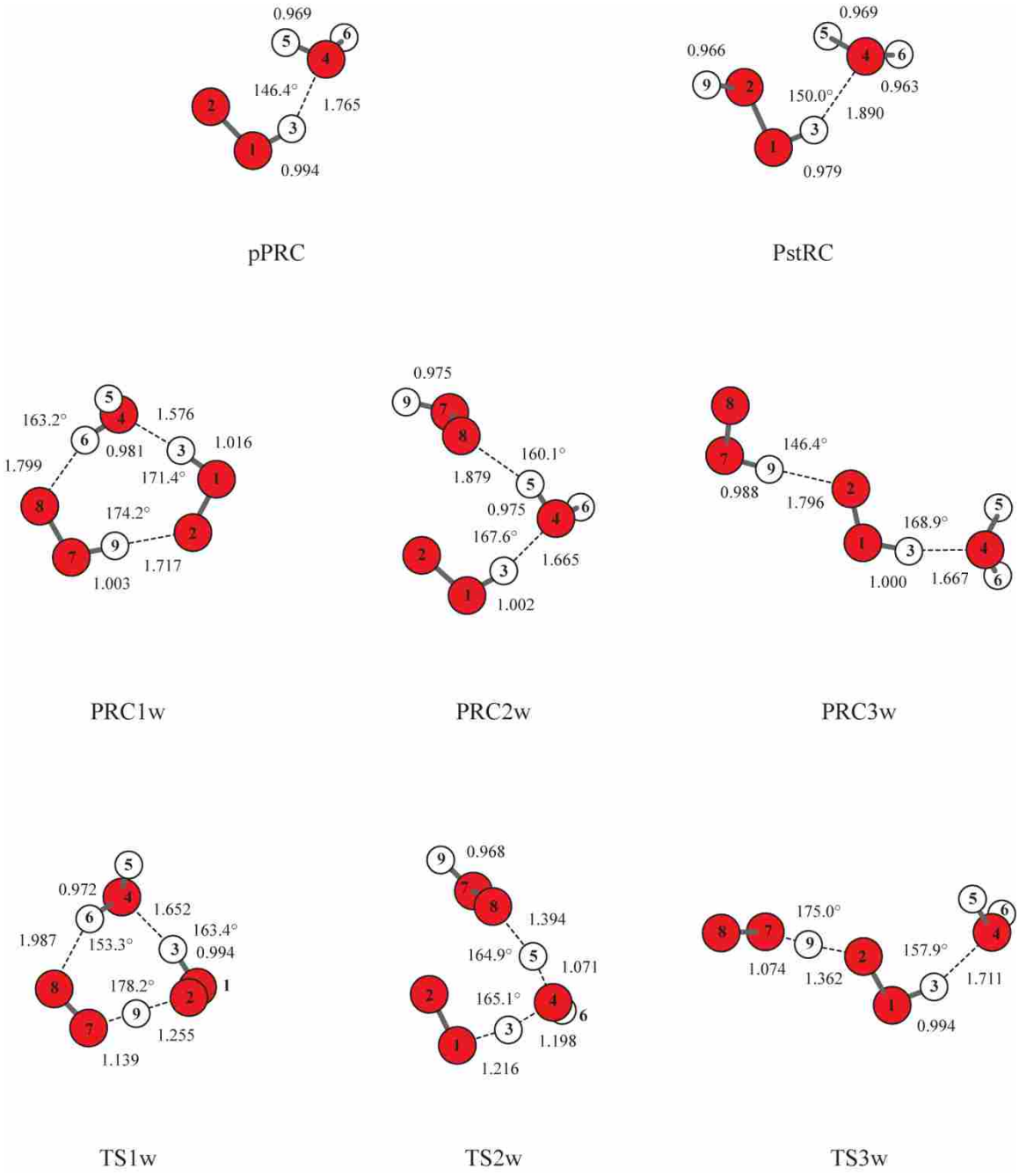

Figure 2.5. The optimized stationary-point geometries of the prominent triplet intermediates and transitions states structures of the $HO_2{-}H_2O{-}HO_2$ reaction at the B3LYP/6-311G(d,p) level.

Table 2.3. Total and relative energies of all species germaine to the dry self-reaction of HO_2 calculated at different levels of theory with B3LYP/6-311G(d,p) optimized geometries.

		Energies[b]				
Species	ZPE[a]	B3LYP/6-311G(d,p)	MP2/6-311G(d,p)	MP2/6-311+G(3df,2p)	CCSD(T)/6-311G(d,p)	G2M
$HO_2 + HO_2 + H_2O$	31.1	-378.348264	-377.434356	-377.671449	-377.505125	-377.772326
$HO_2 + H_2O$	22.2	-227.397856	-226.849118	-226.994854	-226.890621	-227.050317
pPRC	25.3	- 13.2	- 11.6	- 9.3	- 11.4	- 6.5
PRC1w	36.3	- 29.7	- 25.5	- 22.8	- 25.3	- 17.8
PRC2w	35.5	- 19.9	- 17.2	- 14.3	- 17.1	- 3.9
PRC3w	35.2	- 22.2	- 20.1	- 17.0	- 19.8	- 11.9
TS1w	32.7	- 23.1	- 10.4	- 7.2	- 11.6	- 7.3
TS2w	33.1	- 13.5	5.4	6.7	3.8	6.0
TS3w	32.6	- 19.0	- 8.2	- 5.7	- 9.1	- 5.0
PstRC	32.8	- 45.9	- 62.9	- 60.1	- 49.4	- 32.5
$H_2O_2 + {}^3O_2 + H_2O$	32.3	- 45.9	- 52.9	- 52.6	- 39.7	- 27.9

[a] Values are in units of kcal mol^{-1}.

[b]The total energies of the reactants at different levels are given in au (E^h) and the relative energies (relative to the reactants) of other species at he corresponding levels are given in units of kcal mol^{-1}, ZPE corrections are included only in the G2M energies.

Although a large number of transition state structures were identified for the triplet HO_2 self-reaction PES, they all merged to one of three main pathways upon higher-order geometry refinements. These processes which lead to the formation of H_2O_2 + $^3O_2$ reaction products include: (1) water catalyzed hydrogen abstraction; (2) formation of a linear, chain-structure; and (3) formation of an eight-membered-ring structure. All three processes involve the initial formation of the $HO_2{-}H_2O$ (pPRC) complex with a binding energy of -6.5 kcal mol^{-1}, which is within the values, -6.2 to -6.9 kcal mol^{-1}, predicted by Aloisio and Francisco.[18]

The H_2O catalyzed proton abstraction channel involves the O atom of the second HO_2 radical abstracting an H atom from the H_2O moiety of the $HO_2{-}H_2O$ complex, while the oxygen atom of the H_2O concurrently receives the H atom of the HO_2 in the complex. The result of this set of hydrogen transfers results in the formation of the $H_2O_2{-}H_2O$ and $^3O_2$ products. The structures of PRC2w and TS2w are shown in Figure 2.5 and have bonding energies D_0 of -9.5 kcal mol^{-1} and 6.0 kcal mol^{-1}, respectively. The location of the TS so far above the reactants renders the direct hydrogen abstraction kinetically unimportant.

The second channel involves the formation of a linear, chain-structure, represented by PRC3w in Figure 2.5. PRC3w has a bonding energy of 11.9 kcal mol^{-1}. In this channel, the H atom (head) of the second HO_2 molecule forms a hydrogen bond with the O atom (tail) of the HO_2 moiety in the $HO_2{-}H_2O$ complex. The transition state tying PRC3w to products, TS3w, lies -5.0 kcal mol^{-1} below the reactants; which is 4.1 kcal mol^{-1} lower than that for the formation of the H_2O_2 + $^3O_2$ products in the $HO_2{-}HO_2$ system.

The final reaction channel involves the formation of an eight-membered cyclic complex, PRC1w, and transition state, TS1w, as shown in Figure 2.5. In PRC1w and TS1w the H_2O molecule acts as a bridging molecule between the two HO_2 radicals with one HO_2 acting as an H-bond donor and the other an H-bond acceptor. PRC1w is calculated to be -5.9 kcal mol^{-1} more stable than PRC3w due to the additional hydrogen bond. The relative energies of PRC1w and TS1w are 7.9 kcal mol^{-1} and 6.4 kcal mol^{-1} below their counterparts in the self-reaction of HO_2 without H_2O. These differences clearly imply a significant catalytic effect of H_2O in enhancing the rate of the HO_2 self-reaction.

Table 2.3 displays the global behavior of the bond lengths and bond orders along the reaction coordinate followed by PRC1w, PRC2w and PRC3w, showing the progression from reactant-like to product-like values. The leading $n \rightarrow \sigma^*$ interactions for each PRC and TS are shown in Figure 2.6.

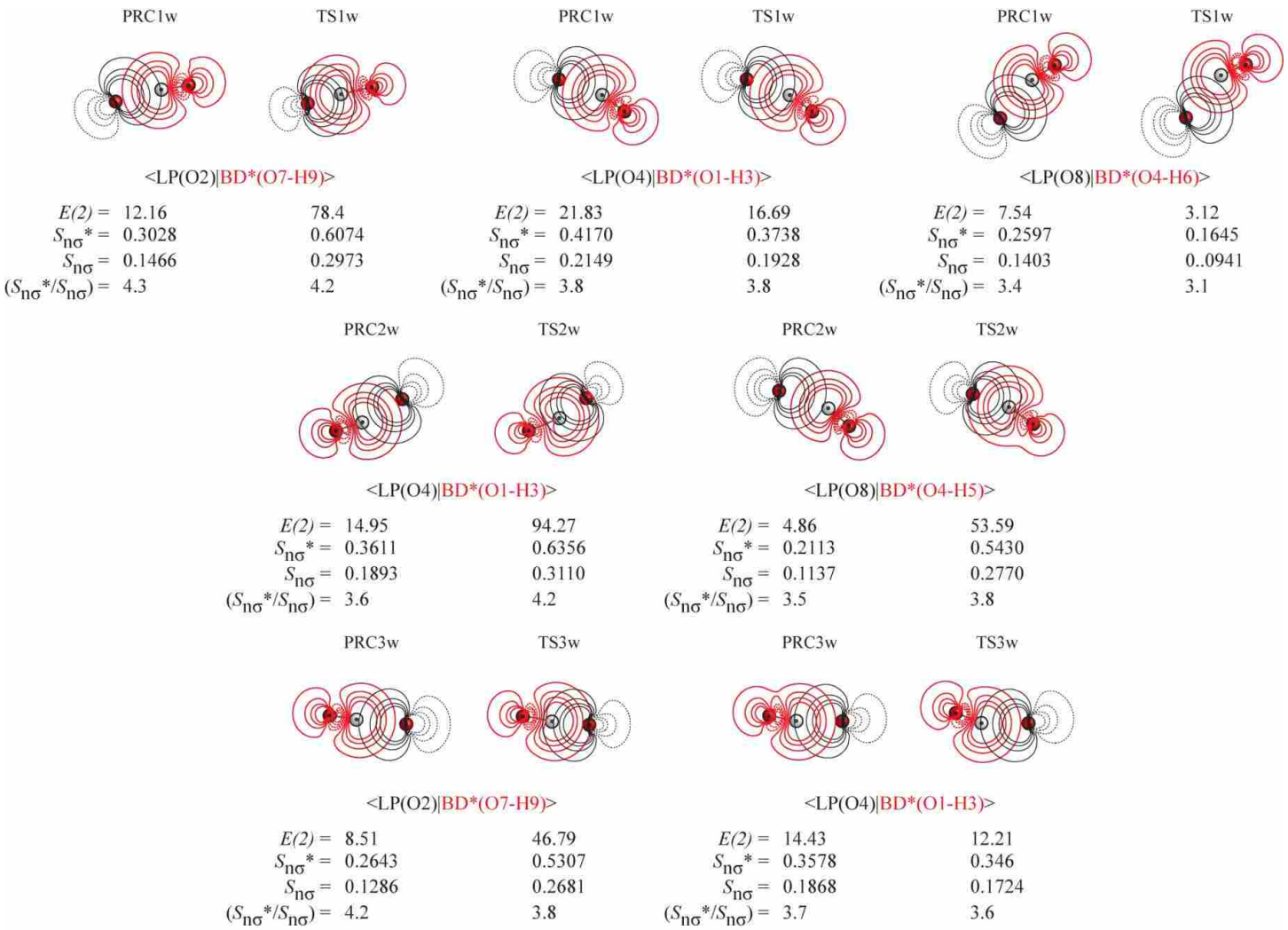

Figure 2.6. The leading n→σ* donor-acceptor interactions of PRC1, PRC2, PRC3, TS1, TS2 and TS3 as calculated at the MP2/6-311+G(3df,2p) level. $E^{(2)}$ values are reported in kcal mol^{-1}.

Table 2.4. Variations of binding energy ΔE, bond lengths R_{OH} and R_{HO}, and NRT bond orders b_{OH} and b_{HO} along the PES.

		Binding ΔE	Bond length (Å)						Bond order					
		(kcal mol^{-1})	R_{O7H9}	R_{H9O2}	R_{O1H3}	R_{H3O4}	R_{O4H6}	R_{H6O8}	b_{O7H9}	b_{H9O2}	b_{O1H3}	b_{H3O4}	b_{O4H6}	b_{H6O8}
Reactants:	HO_2 + H2O + HO_2	0.00	0.976		0.976		0.962		0.990		0.990		0.998	
pPRC:	HO_2–H_2O + HO_2	- 6.53	0.976		0.994	1.765	0.962		0.99		0.973	0.008	0.994	
PRC1w:	HO_2–HO_2	-17.79	1.003	1.717	1.016	1.576	0.981	1.799	0.961	0.012	0.955	0.035	0.977	0.014
TS1w:	HO_2 ··· HO_2	- 7.31	1.139	1.255	1.004	1.652	0.972	1.987	0.611	0.308	0.965	0.015	0.977	0.010
PstRC:	H_2O_2–H_2O + O_2	-32.51		0.970	0.979	1.890	0.963			0.997	0.984	0.005	0.994	
Products:	H_2O_2 + H_2O + O_2	-27.90		0.966	0.966		0.962			0.998	0.998		0.998	

			R_{O7H9}	R_{H9O2}	R_{O1H3}	R_{H3O4}	R_{O4H5}	R_{H5O8}	b_{O7H9}	b_{H9O2}	b_{O1H3}	b_{H3O4}	b_{O4H5}	b_{H5O8}
Reactants:	HO_2 + H2O + HO_2	0.00	0.976		0.976		0.962		0.990		0.990		0.998	
pPRC:	HO_2–H_2O + HO_2	- 6.53			0.994	1.765	0.969				0.973	0.008	0.994	
PRC2w:	HO_2–HO_2	- 9.54	0.975		1.002	1.665	0.975	1.879	0.991		0.966	0.007	0.985	0.011
TS2w:	HO_2 ··· HO_2	6.02	0.968		1.216	1.198	1.071	1.394	0.996		0.471	0.456	0.913	0.039
PstRC:	H_2O_2–H_2O + O_2	-32.51	0.966			0.963	1.890	0.979	0.997			1.000	0.005	0.984
Products:	H_2O_2 + H_2O + O_2	-27.90	0.966			0.962		0.966	0.998			0.998		0.998

			R_{O7H9}	R_{H9O2}	R_{O1H3}	R_{H3O4}	R_{O4H6}	R_{H6O8}	b_{O7H9}	b_{H9O2}	b_{O1H3}	b_{H3O4}	b_{O4H6}	b_{H6O8}
Reactants:	HO_2 + H2O + HO_2	0.00	0.976		0.976		0.962		0.990		0.990		0.998	
pPRC:	HO_2–H_2O + HO_2	- 6.53	0.976		0.994	1.765	0.962		0.99		0.973	0.008	0.994	
PRC3w:	HO_2–HO_2	-11.92	0.988	1.796	1.000	1.667	0.963		0.973	0.009	0.969	0.009	1.000	
TS3w:	HO_2 ··· HO_2	- 5.05	1.074	1.362	0.994	1.711	0.963		0.835	0.077	0.966	0.006	1.000	
PstRC:	H_2O_2–H_2O + O_2	-32.51		0.970	0.979	1.890	0.963			0.997	0.984	0.005	0.994	
Products:	H_2O_2 + H_2O + O_2	-27.90		0.966	0.966		0.962			0.998	0.998		0.998	

The pre-reactive complex of the H_2O-catalyzed H-abstraction pathway consists of two principle hydrogen bonds that participate in proton transfer processes as PRC2w passes through TS2w. The PRC2w reaction coordinate involves the passing of H3 to the water oxygen with a simultaneous transfer of the water proton H5 to the terminal oxygen of the second HO_2 radical. As PRC2w moves through TS2w, the O4···H3 H-bond length decreases from 1.765 Å (0.008) to 1.198 Å (0.456) (the associated natural bond order are shown in parentheses). This decreased bond distance results in a 2-fold increase in the n and σ* (P)NBO overlap integrals, 0.3611 to 0.6356. This results in an increase of *E(2)* from 14.95 kcal mol^{-1} to 94.27 kcal mol^{-1}. Although less pronounced, a similar increase in the stabilization energy associated with the O4−H5···O8 H-bond is seen, $\Delta E(2)$ = 48.73 kcal mol^{-1}. In this case, the increase in *E(2)* is the result of more efficient (P)NBO overlap resulting from a shortening (0.485 Å) of the O8···H5 hydrogen bond.

The linear geometry of PRC3w consists of two principal hydrogen bonds. The first is that of the HO_2−H_2O complex. The second is formed between the head (H atom) of the second HO_2 and the tail (terminal O atom) of the complexed HO_2. The hydrogen bond associated with pPRC is shown to elongate by 0.044 Å (2.6%) as PRC3w passes to TS3w. The elongation of this bond accompanied by a decrease of 10.7° in the OHO bond reduces. The direct effect of these geometric changes is to decrease the effective (P)NBO overlap of this interaction by 6.5%, resulting in a loss of 2.22 kcal mol^{-1} of stabilization energy. These new values more closely approximate those found in the H_2O_2−H_2O post-reactive product. The remaining O7−H9···O2 hydrogen bonding interaction is responsible for the proton transfer process. The hydrogen bond length decreases by 24.2% from 1.797

Å to 1.362 Å. This bond shortening coupled with an increase of 28.6° in the OHO bond angle account for an increase of 38.28 kcal mol^{-1} in *E(2)*.

The eight-membered cyclic complex, PRC1w, is composed of three hydrogen bonds, as shown in Figure 2.6. Two of the hydrogen bonds involving the H_2O molecule, O4···H3−O1 and O8···H6−O4, act to stabilize PRC1w. The H_2O moiety also acts to increase the hydrogen bonding angle the O7−H9···O2 proton transfer interaction from 150.2° in PRC1 to 174.2° in PRC1w. This increases the n→σ* interaction (P)NBO overlap from 0.2571 (PRC1) to 0.3028 (PRC1w) with a corresponding increase of *E(2)* of 8.28 kcal mol^{-1} to 12.16 kcal mol^{-1}. As PRC1w advances to TS1w, the role of these interactions remain the same, but are weakened as H_2O begins to take on its role in the H_2O_2−H_2O PstRC. The stabilization energy of the hydrogen-bond linking H_2O to the HO_2 moiety that is fated to become O_2 is reduced from 7.54 kcal mol^{-1} to 3.12 kcal mol^{-1}. This reduction is the result of a 36.7% decrease in (P)NBO overlap that results from an elongation of the H-bond from 1.799 Å in PRC1w to 1.987 Å in TS1w and a decrease in the OHO bond angle of 9.9°. The O−H···O interaction involving H_2O and the remaining HO_2 radical also decreases as the hydrogen bond length increases from 1.576 Å to 1.652 Å and the OHO bond angle decreases from 174.4° to 163.4°. Both of these changes approach the equilibrium values of 1.890 Å and 150.0°, respectively, found in the H_2O_2−H_2O product. These geometric alterations lead to a reduction in the associated (P)NBO overlap of 0.4170 to 0.3738. The attendant reduction in *E(2)* energy (21.83 kcal mol^{-1} to 16.39 kcal mol^{-1}) begins to approach that of the H-bond found in the H_2O_2−H_2O post-reaction complex (10.74 kcal mol^{-1}). The atoms of the O2H9O7 triad participate in a discrete proton transfer from O7 to O2. The increased value of *E(2)* (78.40 kcal mol^{-1} in

TS1w as compared to 12.16 kcal mol^{-1} in PRC1w), is a result of a doubling of the overlap between the n and σ* (P)NBOs that results from a shortening of the O2···H9−O7 hydrogen bond from 1.717 Å to 1.255 Å and a small increase in the OHO bond angle of 4°. The O2···H9 bond length decreases by 0.462 Å (26.9%) with the bond order increasing from 0.012 to 0.308. Concurrently, the O7···H9 bond increases from 1.003 Å to 1.139 Å, a change of 0.136 Å (13.6%) and experiences a corresponding decrease in the natural bond order of 0.961 to 0.611. Taken together, these results indicate that the primary role of the H_2O molecule is to enhance the geometry of the O7H9O2 hydrogen bond which allows for a greater delocalization of electron density into the O7H9 anti-bond, greatly facilitating proton transfer.

2.5 Conclusions

The HO_2 self-reaction potential energy surfaces in both the presence and absence of H_2O have been analyzed using geometric and NBO analysis. Three principal intermediates for the HO_2−H_2O + HO_2 reaction have been found on the triplet surface with association energies in the range of 9.5–17 kcal mol^{-1}, which are more stable than their triplet counterparts in the absence of H_2O by ~8 kcal mol^{-1}. The decomposition processes of these intermediates have been discussed and compared with the self-reaction of HO_2. The results of this work indicate that H_2O molecules can catalytically reduce the barriers to product formation by increasing the extent of electron delocalization into the σ* anti-bond of the breaking O−H bond of one of the HO_2 radicals by increasing the overlap between the relevant interacting n and σ* (P)NBOs. It accomplishes this by hydrogen bonding to each of the two HO_2 radicals and increasing the distance between them, allowing for a favorable hydrogen-bonding geometry to be reached.

Additional work performed (manuscript in preparation) indicates that NH_3 and CH_3OH act in a similar manner to H_2O to effect the enhancement of the HO_2 self-reaction.

2.6 Supplementary Material

Tables S2.1 through S2.12 represent the B3LYP/6-311G(d2p) optimized geometries and the B3LYP/6-311++G(2d,2p) harmonic vibrational frequencies.

2.6.1 Cartesian Coordinates for Each Optimized Geometry

Supplementary Table S2.1. B3LYP/6-311G(d,p) optimized reactant geometries.

	HO_2		
O	0.00000	-0.00637	0.00120
O	0.00000	1.32156	-0.00718
H	0.00000	-0.26173	0.94295
	H_2O		
O	1.92217	-4.51260	0.70817
H	1.63994	-3.59345	0.73617
H	2.18952	-4.64310	-0.20666
	HO_2−H_2O (pPRC)		
O	-0.47201	-4.82335	1.75385
O	-0.48037	-3.50129	1.63916
H	0.42140	-5.07605	1.39790
O	1.94918	-4.50570	0.72251
H	1.58158	-3.61466	0.82175
H	2.09284	-4.61948	-0.22233

Supplementary Table S2.2. B3LYP/6-311G(d,p) optimized PRC1 and PRC2 geometries.

PRC1			
O	0.00848	-4.74538	1.56281
O	0.06206	-3.42222	1.59647
H	0.09748	-5.00972	2.51712
O	0.34819	-3.23346	4.28945
O	0.29462	-4.55662	4.25578
H	0.25919	-2.96913	3.33513
PRC2			
O	-3.99980	2.18774	0.21092
O	-3.67719	0.90469	0.18023
H	-4.89240	2.23807	-0.18209
O	-1.00182	0.74135	1.12594
O	-0.32886	1.14652	0.05406
H	-1.94694	0.76928	0.85496

Supplementary Table S2.3. B3LYP/6-311G(d,p) optimized TS1 and TS2 geometries.

TS1			
O	-4.34187	1.35799	0.32245
O	-4.74294	1.76352	-0.83326
H	-4.92370	1.91627	1.03355
O	-6.77306	2.91559	0.58697
O	-5.86177	2.76930	1.57081
H	-6.28400	3.31528	-0.15797
TS2			
O	1.22807	0.15461	-4.76594
O	1.50016	-0.08464	-3.46759
H	2.02882	-0.13681	-5.23682
O	-0.33112	-1.44112	-2.46568
O	-1.00501	-0.65207	-1.69140
H	0.41757	-0.85382	-2.89285

Supplementary Table S2.4. B3LYP/6-311G(d,p) optimized PRC1w, PRC2w, and PRC3w geometries.

	PRC1w		
O	-0.26601	-4.09359	1.93858
O	-0.72168	-2.94296	1.48165
H	0.53708	-4.32246	1.36027
O	1.73449	-4.48507	0.34928
H	2.62496	-4.41958	0.70794
H	1.66178	-3.78822	-0.33778
O	0.27840	-1.58561	-0.64866
O	1.24798	-2.27647	-1.22008
H	-0.03890	-2.12485	0.13487
	PRC2w		
O	-0.33531	-4.00584	1.37703
O	-0.09839	-2.70413	1.44552
H	0.54887	-4.40831	1.13221
O	2.12214	-4.73562	0.69560
H	2.50719	-3.84111	0.74169
H	2.23638	-5.01899	-0.21684
O	2.332455	-1.466207	-0.322732
O	2.617227	-1.970217	0.874791
H	2.054796	-0.548271	-0.147948
	PRC3w		
O	-0.315794	-4.031988	1.527637
O	-0.216523	-2.936982	0.790238
H	0.555257	-4.498672	1.376256
O	2.085124	-5.010458	0.957062
H	2.609306	-4.26256	0.649464
H	2.158838	-5.681648	0.270457
O	-2.523681	-1.421639	1.142822
O	-2.094039	-0.377109	1.842581
H	-1.724588	-1.988213	1.013423

Supplementary Table S2.5. B3LYP/6-311G(d,p) optimized TS1w, TS2w, and TS3w geometries.

	TS1w		
O	-0.37569	-4.70747	2.09716
O	-0.71680	-3.41796	1.88059
H	0.47812	-4.81585	1.58070
O	1.64665	-4.72448	0.41615
H	2.34289	-4.07481	0.55755
H	1.12318	-4.39416	-0.33296
O	-1.43381	-3.15463	-0.38743
O	-0.51238	-3.61654	-1.14943
H	-1.09240	-3.26117	0.69377
	TS2w		
O	-0.47089	-4.01907	1.39390
O	0.22005	-3.31140	2.21645
H	0.34165	-4.76251	0.87756
O	1.33609	-5.35276	0.56612
H	2.01016	-4.78669	1.17606
H	1.55561	-5.20314	-0.36027
O	3.136049	-2.921235	1.22932
O	2.579339	-3.875406	2.064262
H	3.426458	-2.239423	1.852548
	TS3w		
O	-0.447446	-4.943015	1.984474
O	-0.561452	-3.607731	2.160688
H	0.3899	-5.011454	1.45297
O	1.784504	-4.480816	0.615979
H	1.740828	-3.540785	0.828907
H	1.791543	-4.528515	-0.345594
O	-2.707314	-2.835366	1.312056
O	-3.299598	-2.203488	2.268192
H	-1.786545	-3.20838	1.719388

Supplementary Table S2.6. B3LYP/6-311G(d,p) optimized product geometries.

H_2O_2−H_2O (PstRC)			
O	-4.87763	1.87989	0.25249
H	-4.89348	2.82827	0.07003
O	-3.45129	1.67263	0.46313
H	-3.27652	1.06009	-0.28002
O	-4.04032	0.02309	-1.66264
H	-4.82828	0.48445	-1.33967
H	-4.16003	-0.89041	-1.38388
H_2O_2			
O	-4.79021	1.65758	0.23709
H	-4.96177	2.48146	-0.23709
O	-3.33660	1.66157	0.23709
H	-3.16504	0.83769	-0.23709
$^3O_2$			
O	0.00000	-1.85030	0.68085
O	0.00000	-3.05598	0.68085

2.6.2 Harmonic Vibrational Frequencies

Supplementary Table S2.7. B3LYP/6-311G(d,p) reactant harmonic vibrational frequencies.

Species						
H_2O	1638.2703	3810.6100	3907.7302			
HO_2	1164.0743	1428.6417	3606.0618			
HO_2−H_2O	170.3310	297.2995	555.5555	1193.4771	1636.8096	3740.0273
	243.1252	334.7524	749.1907	1573.9763	3293.197	3879.1761

Supplementary Table S2.8. B3LYP/6-311G(d,p) PRC1 and PRC2 harmonic vibrational frequencies.

Species						
PRC1	118.0	276.3	590.2	1198.7	1547.7	3250.4
	228.7	307.8	714.5	1209.2	1562.1	3339.1
PRC2	29.1	97.9	263.9	1185.3	1442.0	3481.2
	62.2	207.5	584.9	1187.9	1510.3	3616.2

Supplementary Table S2.9. B3LYP/6-311G(d,p) TS1 and TS2 harmonic vibrational frequencies.

Species						
TS1	-892.1	184.8	361.4	934.6	1427.5	1724.9
	133.6	280.6	843.1	1227.1	1456.8	3617.1
TS2	-416.6	127.5	384.1	983.3	1420.0	1986.6
	21.9	154.6	916.4	1219.8	1507.0	3659.7

Supplementary Table S2.10. B3LYP/6-311G(d,p) PRC1w, PRC2w and PRC3w harmonic vibrational frequencies.

Species						
PRC1w	65.6	239.2	469.1	1224.7	1633.6	3162.6
	84.7	282.4	697.7	1236.7	1679.4	3500.9
	149.9	304.9	797.4	1591.6	2907.0	3871.1
	194.0	366.4	931.1			
PRC2w	42.6	145.3	318.8	1145.7	1603.8	3620.7
	60.3	210.6	422.6	1204.0	1664.3	3639.5
	72.7	302.0	699.7	1439.2	3143.1	3871.7
	82.2	311.5	832.5			
PRC3w	22.6	88.8	327.9	1191.4	1587.5	3402.4
	30.7	120.3	400.0	1216.5	1638.0	3807.5
	36.3	248.4	656.7	1532.7	3209.4	3903.0
	60.4	306.1	850.8			

Supplementary Table S2.11. B3LYP/6-311G(d,p) TS1w, TS2w and TS3w harmonic vibrational frequencies.

Species						
TS1w	-1591.9	190.9	380.8	1077.4	1526.7	3096.4
	58.0	273.0	597.7	1172.5	1573.6	3678.8
	122.5	289.5	612.6	1348.2	1646.0	3870.6
	136.9	330.6	909.9			
TS2w	-1408.9	215.4	565.0	1150.4	1397.4	2156.6
	78.9	278.3	640.7	1303.7	1704.2	3742.8
	120.1	389.2	691.6	1372.7	1791.4	3845.8
	149.3	501.1	1026.1			
TS3w	-843.1	137.0	328.8	1056.7	1573.6	3286.1
	22.3	152.2	427.4	1226.9	1623.6	3797.7
	38.9	219.3	734.3	1463.0	1632.8	3896.6
	65.7	305.3	826.1			

Supplementary Table S2.12. B3LYP/6-311G(d,p) product harmonic vibrational frequencies.

Species						
PstRC	177.0	274.2	700.8	1552.0	3555.8	3785.6
	205.8	347.6	935.4	1645.7	3742.0	3875.2
	241.8	588.9	1330.9			
H_2O_2	346.0	943.3	1302.7	1456.1	3783.5	3784.7
$^3O_2$	1640.9					

CHAPTER 3: COMPUTATIONAL STUDY ON THE EXISTENCE OF ORGANIC PEROXY-WATER COMPLEXES (RO_2-H_2O)

3.1 Abstract

The existence of a series of organic peroxy radical-water complexes [CH_3O_2-H_2O (methyl peroxy); $CH_3CH_2O_2$-H_2O (ethyl peroxy); $CH_3C(O)O_2$-H_2O (acetyl peroxy); $CH_3C(O)CH_2O_2$-H_2O (acetonyl peroxy); $CH_2(OH)O_2$-H_2O (hydroxymethyl peroxy); $CH_2(OH)CH_2O_2$-H_2O (2-hydroxyethyl peroxy); $CH_2(F)O_2$-H_2O (fluoromethyl peroxy); $CH_2(F)CH_2O_2$-H_2O (2-fluoroethyl peroxy)] is evaluated using high level *ab initio* calculations. A wide range of binding energies is predicted for these complexes, in which the difference in binding energies can be explained by examination of the composition of the R group attached to the peroxy moiety. The general trend in binding energies has been determined to be as follows: fluorine ≈ alkyl < carbonyl < alcohol. The weakest bound complex, CH_3O_2-H_2O, is calculated to be bound by 2.3 kcal mol^{-1}, and the strongest, the $CH_2(OH)O_2$-H_2O complex, is bound by 5.1 kcal mol^{-1}. The binding energy of the peroxy radical-water complexes which contain carbonyl and alcohol groups indicates that these complexes may perturb the kinetics and product branching ratios of reactions involving these complexes.

3.2 Introduction

Organic peroxy radicals (RO_2) are products of the atmospheric oxidation of hydrocarbons, and they represent an important class of intermediates[82,83] leading to the formation of tropospheric ozone, as well as playing a role in managing the HO_x (OH and HO_2) radical budget. Organic peroxy radicals are formed from the reaction of hydrocarbons with OH, Cl, or NO_3 radicals, followed by the subsequent addition of O_2 to the hydrocarbon radical.[47,84]

$$RH + OH, Cl \text{ or } NO_3 \rightarrow R\cdot + H_2O, HCl \text{ or } HNO_3 \quad (3.1)$$

$$R\cdot + O_2 + M \rightarrow RO_2 + M \quad (3.2)$$

One mechanism for the production of tropospheric ozone as well as the major loss process for peroxy radicals under polluted conditions is the reaction of RO_2 radicals with NO.

$$RO_2 + NO \rightarrow RO + NO_2 \quad (3.3)$$

$$NO_2 + h\nu \rightarrow NO + O \quad (3.4)$$

$$O + O_2 \rightarrow O_3 \quad (3.5)$$

A second association/isomerization product path to produce alkyl nitrates has been observed. The mechanism is postulated to be:[85]

$$RO_2 + NO \rightarrow ROONO^* \quad (3.6)$$

$$ROONO^* + M \rightarrow RONO_2 \quad (3.7)$$

The product branching ratio ($k_{3.3}/k_{3.7}$) has been shown to depend on the size of the RO_2 radical as well as exhibit both a pressure and negative temperature dependence.[86]

Recent work by Butkovskaya et al.[87] probing the effects of temperature and water vapor on the HO_2 + NO reaction kinetics and product branching ratio has shown that the yield of HNO_3 (the association/isomerization) product increases by 90% in the presence of modest amounts of water vapor. The increased HNO_3 production as a function of

increasing water vapor was explained as occurring because of the formation of a HO_2-H_2O complex during the reaction mechanism.

Under conditions indicative of the upper troposphere, the formation of HNO_3 from the HO_2 + NO reaction in the presence of water vapor would contribute 23% to the total loss process of HO_x radicals. This study highlights the necessity of understanding the rates and products of peroxy radical reactions under atmospheric conditions where peroxy-water complexes may exist.

The simplest RO_2 radical is the HO_2 radical. Experimental measurements on the kinetics of the HO_2 self-reaction indicate a water vapor dependence to the reaction rate coefficient. The water vapor enhancement is shown to increase with decreasing temperatures, which has been explained by the formation of a HO_2-H_2O complex which is speculated to form during the reaction mechanism. Recently, the existence of this peroxy water complex has been confirmed by Suma et al.,[49] who were able to observe pure rotational transitions for the complex in a supersonic jet by means of a Fourier transform microwave spectrometer. Kanno et al.,[48] using frequency modulated diode laser spectroscopy, have successfully measured the equilibrium constant of the HO_2−H_2O complex. These experimental results are complemented by *ab initio* computational studies that have reported the lowest energy conformer vibrational frequencies and binding energies for the HO_2-H_2O and HO_2-$(H_2O)_n$ complexes.

Recent results suggest that upward of 30% of HO_2 radicals in the atmosphere are complexed with water under typical atmospheric conditions.[18,48] Modeling studies indicate that the water vapor enhancement cannot be ignored when modeling atmospheric processes.[88] We propose that RO_2 radicals in the presence of water may form similar

RO_2-H_2O complexes. The existence of RO_2-H_2O would serve to perturb the reactivity of RO_2 radicals and consequently affect their kinetics and product branching ratios. This has not yet been considered in models incorporating RO_2 radicals.

Recently, organic films and reverse micelle formation have been proposed as one mechanism for atmospheric aerosol production.[89-92] These mechanisms suggest that water is encapsulated by organic molecules with hydrophilic heads directed inward and hydrophobic ends directed outward. Processing of these ultra-fine aerosols is initiated by reactions with atmospheric radicals that transform the surface of these aerosols into hydrophilic surfaces which can grow by water accretion and form cloud condensation nuclei. The formation of the peroxy radical-water complexes investigated in this study may represent the first stages of this proposed mechanism for the process of aerosol formation under atmospheric conditions.

The work presented here is the first study involving six of the most prominent atmospherically relevant RO_2 radicals and their water complexes. The important question raised by this work is whether organic peroxy radical water complexes exist. This work will illustrate the possible influence that RO_2-H_2O complexes may have on the spectroscopy, kinetics and measurement of RO_2 radicals.

3.3 Methods

The Gaussian 98, revision A.11.316[93] suite of programs was used to carry out *ab initio* calculations for H_2O and each of the RO_2 and RO_2-H_2O complexes under consideration in this paper. Electron correlation was included and evaluated using unrestricted second-order Møller-Plesset perturbation theory (MP2),[94] quadratic configuration interaction with single, double, and triple excitations, QCISD(T),[95,96]

coupled cluster with single, double, and perturbative triple excitations, CCSD(T),[97,98] and Brueckner doubles, BD(T).[99,100] Initial geometry and optimization work was performed using density functional methods (DFT), involving Hartree-Fock (HF)[101-103] and Becke three parameter exchange functional with the Lee, Yang, and Parr correlation functional (B3LYP).[104-107]

Basis sets used for the currently considered computations are of the general types, 6-31G and 6-311G.[108-112] Initial search optimizations and computations, including frequency calculations, used the 6-31G with the addition of diffuse functions on second-row atoms, as well as d- and p- polarization functions being added to the second-row atoms and the hydrogen atom, respectively. All other calculations involved the 6-311G basis set with added diffuse functions to both the hydrogen and second-row atoms, in addition to various combinations of polarization functions [6-311++G(d,p), 6-311++G(2d,2p), and 6-311++G(2df,2p)].

Interaction energies for the complexes were computed by taking the difference between the complex and isolated monomer sum. Zero-point vibrational energy[113,114] corrections computed at the B3LYP/6-31+G(d,p) level were applied to each interaction energy. The counterpoise (CP) procedure[71,115] was used at the MP2(full)/6-311++G(2d,2p) level to correct the interaction energy for basis set superposition error (BSSE).[72] Charges on individual atoms were calculated via the natural population method.[116]

The lowest energy peroxy radical conformation for each complex was found through a systematic evaluation of the potential energy surface defined by rotations of all bonds within each radical that, when rotated, would define a different molecular

conformation. For each considered, bond rotations increments of 30° were used. These initial geometry calculations were performed at the HF/6-31G(d,p) level, followed by a frequency calculation to verify the absence of imaginary frequencies, and finished with an MP2(full)/6-31G(d,p) single point calculation. Once a group of lowest energy structures was identified, optimizations using B3LYP and MP2(full) levels of theory with 6-311++G(d,p) and 3-11++G(2d,2p) basis sets were performed to identify the lowest energy structure. Identification and optimization of the lowest energy complex for each peroxy radical species was performed using proprietary software developed on site.[117] This software arrived at each lowest energy RO_2-H_2O complex by first optimizing each of the lowest energy RO_2 molecules in the presence of a randomly oriented water molecule, placed within a sphere surrounding the radical with a volume, in part, defined by the size of the radical species. Constraints were placed on each randomly generated complex as to ignore nonsensical geometries, such as those that might arise having two hydrogen atoms occupying the same space. Five hundred initial geometries were optimized for each peroxy radical as per the procedure for the monomer species, and a lowest energy structure was identified. All of the lowest energy structures were further evaluated at the QCISD(T), CCSD(T), and BD(T) levels of theory via single-point calculations, each with the 6-311++G(2d,2p) set of basis functions.

Calculations defining the contribution of the C-H ··· O hydrogen bonds to complex stabilization were performed by generating a series of RO_2-H_2O geometries that incrementally removed the interacting water oxygen from the vicinity of the contributing C-H proton donating groups. Optimizations carried out were at the HF/6-311++G(d,p) level followed by an MP2-(full)/6-311++G(2d,2p) single point calculation.

All optimized geometries and harmonic vibrational frequencies are given in supplemental Tables S3.1-S3.16.

3.4 Results

3.4.1 Foreword

The stabilization of atmospheric complexes comprising peroxy radical and water moieties is anticipated to arise primarily from traditional A-H···B hydrogen bonding (where A and B are highly electronegative atoms) and van der Waals interactions. The primary hydrogen bond formed in the molecular complexes, within the context of the present work, see Figure 3.1, has water acting as the hydrogen donor and an oxygen in the peroxy radical acting as the hydrogen acceptor through either the peroxy functionality itself (see Figure 3.1, panels A and B and E-H) or through other oxygen containing functionalities present in the radical, such as a carbonyl group (see Figure 3.1C, 3.1D). Each of the geometries in Figure 3.1 also seem to indicate additional molecular stabilization via significant, albeit weaker C-H···O_w hydrogen bonding interactions, with the water oxygen acting as the hydrogen acceptor and a C-H group acting as the hydrogen donor. The nomenclature of such an interaction is still in general debate, but recent work by Scheiner[118] et al. as well as that by Popelier[119] et al. has indicated that such a distinction is appropriate. For the sake of discussion here, reference to C-H···O interactions will be referred to as CHO bonds. The importance of CHO bond interactions is not limited to small molecular complexes, like those of interest here, but has been recognized as an essential part to the geometric determination of larger systems that include, but are not limited to, nucleic acids,[120-123] proteins,[124-127] and carbohydrates.[128,129] The role of CHO_w hydrogen bonds in the coordination of water molecules has been

demonstrated through an extensive review of neutron diffraction data extracted from the Cambridge Database[130] that provide hydrogen positions that have been experimentally determined to be 0.01 Å and better.[129] This later information demonstrates that any CHO_w bonds present in the peroxy radical/water complexes cannot be neglected in any description of the factors leading to complex stabilization.

3.4.2 Calibration

In addition to the eight peroxy radical/water complexes investigated herein, two calibration systems were also studied as a means to validate the methodologies used and to place the results presented in this work into a workable context. These two systems, hydroperoxy/water (HO_2-H_2O) and hydroperoxy/methanol (HO_2-CH_3OH) have been examined via computational and experimental means[18,58,131] and therefore present a reasonable basis for calibration. Table 3.1 contains the calculated binding energies for the two complexes compared to previously published results.

Table 3.1. Relative binding energies (kcal mol^{-1}) for the HO_2-H_2O and HO_2-CH_3OH complexes.

	HO_2-H_2O binding energy	
Levels of Theory	D_e	D_o
UMP2/6-311++G(2df,2p)	9.6	7.5
QCISD(T)/6-311++G(2df,2p)//UMP2/6-311++G(2df,2p)	9.3	7.2
CCSD(T)/6-311++G(2df,2p)//UMP2/6-311++G(2df,2p)	9.3	7.2
BD(T)/6-311++G(2df/2p)//UMP2/6-311++G(2df,2p)	9.3	7.2
CCSD(T)/6-311++G(2df,2p)//B3LYP/6-311++G(2df,2p)[10]	9.4	6.9
Experiment[55]		8.6±3.8
	HO_2-CH_3OH binding energy	
	D_e	D_o
UMP2/6-311++G(2df,2p)	10.6	8.8
QCISD(T)/6-311++G(2df,2p)//UMP2/6-311++G(2df,2p)	10.2	8.4
CCSD(T)/6-311++G(2df,2p)//UMP2/6-311++G(2df,2p)	10.2	8.4
BD(T)/6-311++G(2df/2p)//UMP2/6-311++G(2df,2p)	10.2	8.4
CCSD(T)/6-311++G(3df,3pd)//UMP2/6-311++G(3df,3pd)[54]	10.5	8.5
Experiment[54]		8.9±1.1

For the HO_2-H_2O system, the minimum energy structure binding energy was calculated at the CCSD(T)/6-311++G(2df,2p)//MP2(full)/6-311++G(2df,2p) level, to be 9.3 or 7.2 kcal mol^{-1} when corrected for the vibrational zero point energy. Aloisio et al.[18] reported a zero-point binding energy for the same hydroperoxy-water complex of 6.9 kcal mol^{-1}, optimized at the CCSD(T)/6-311++G(2df,2p)//B3LYP/6-311++G(2df,2p) level. In another paper, Aloisio et al.[131] report an experimentally determined value of 8.6 ± 3.8 kcal mol^{-1}. Although this experimental value deviates by more than 1.4 kcal mol^{-1} from the calculated value, our reported value falls within the reported experimental error.

Christensen et al.[58] have reported both calculated and experimental values for the binding energy of the CH_3OH-HO_2 system. In their determination, the CCSD(T)/6-311++G(3df,3pd)//MP2/6-311++G(3df,3pd) calculation of the binding energy gave an

energy of 10.5 kcal mol^{-1} and a vibrational zero-point corrected energy of 8.5 kcal mol^{-1}, which are both in very good agreement with our values, calculated at the CCSD(T)/6-311++G(2df,2p)//MP2(full)/6-311++G(2df,2p), of 10.2 and 8.4 kcal mol^{-1}, respectively. The reported experimental value of 8.9 ± 1.1 kcal mol^{-1} is again in excellent agreement with our numbers.

3.4.3 Geometry

A review of the optimized structures in Figure 3.1 reveals two significant structural similarities, regardless of functionalization. The first is the tendency for the RO_2 radical and water molecules to form 6 to 8 member cyclic structures upon complexation. In reference to this cyclization, there is clearly a preference for six member structures with nearly two thirds of the perceived ring assemblies having this organization. Both seven- and eight-member ring geometries also exist, but within the scope of the structures covered in this work, they are only present in geometries that also contain a six membered group. One rationalization for the observed cyclic organization of these complexes arises from the ability of the water molecule to simultaneously act as a proton donor and acceptor. Examination of Figure 3.1 shows that each water molecule invests in an O_w-H···O_c type hydrogen bond with various acceptor functionalities within the monomer. With the exception of structures C and D, where the acceptor moiety is a carbonyl oxygen, the involved acceptor atom is the terminal oxygen of the $–O_2$ (peroxy) functionality. If this interaction constituted the sole point of interaction between the two monomers, the coordination potential of the water would be left unsatisfied, resulting in an "available" acceptor potential.[129] In the event that no other group is present in the relevant locality, such a potential would, of necessary, remain unfulfilled. Typically,

however, there are eligible groups on hand that are able to coordinate with water and fulfill this potential. Commonly, such groups include NH, OH, and M^+. The structures herein presented also demonstrate the ability of CH groups (second structural similarity) to coordinate with water in the same way as NH and OH groups (Figure 3.1)[129] do, although this phenomenon is by no means germane to the present context.

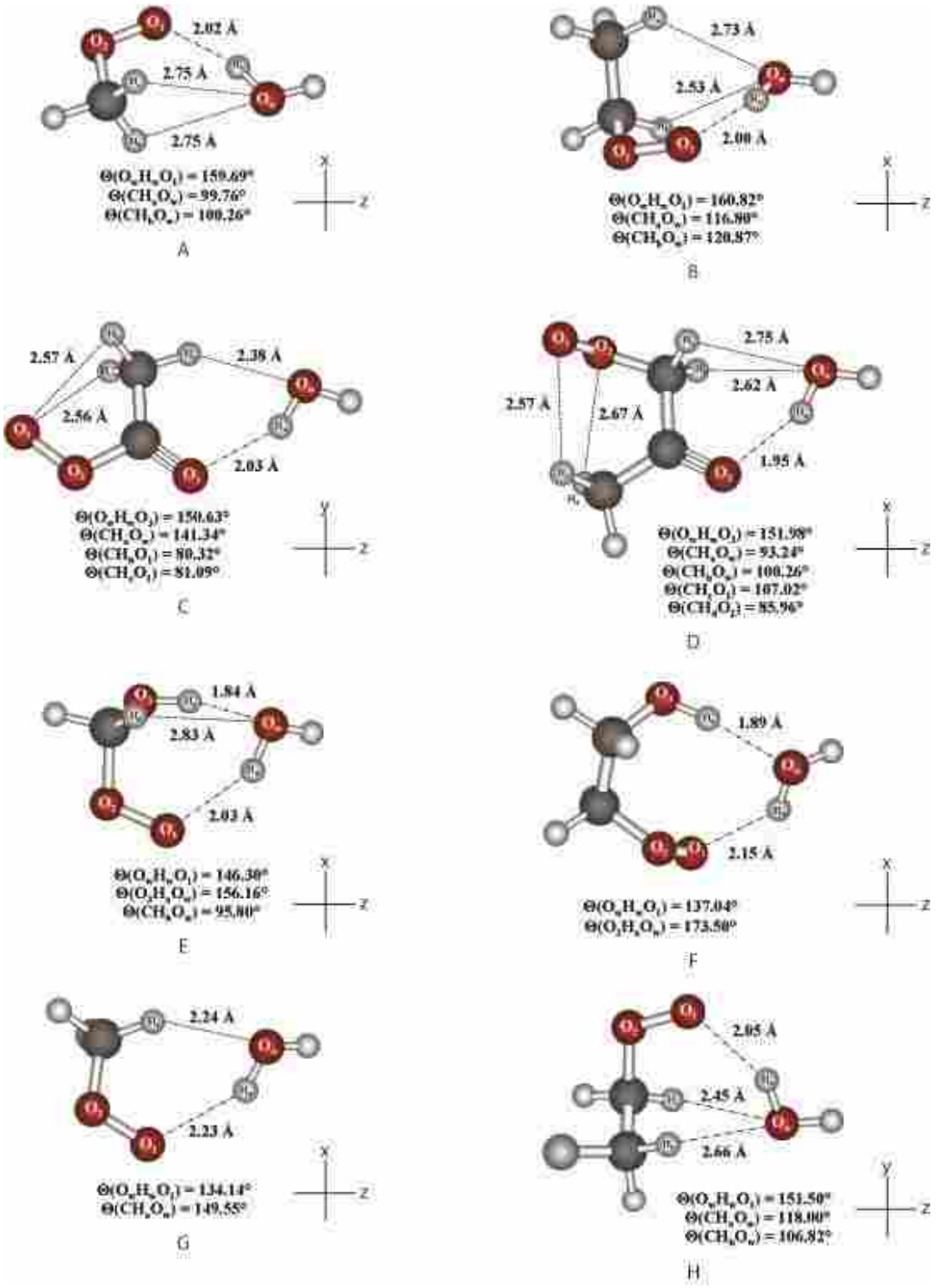

Figure 3.1. Optimized structures are at the MP2(full)/6-311++G(2df,2p) level. Bond lengths are reported in Angstroms. A = CH_3O_2-H_2O; B = $CH_3CH_2O_2$-H_2O; C = $CH_3C(O)O_2$-H_2O; D = $CH_3C(O)CH_2O_2$-H_2O; E = $CH_2(OH)O_2$-H_2O; F = $CH_2(OH)CH_2O_2$-H_2O; G = FCH_2O_2-H_2O; H = $FCH_2CH_2O_2$-H_2O.

In their review of neutron diffraction data, Steiner and Saenger[129] point out that a water molecule most frequently accepts two hydrogen bonds, preferably one from XH (X = O or N) and one from CH. The resulting coordinated geometry, although variable, is often tetrahedral. Steiner and Saenger conclude that one of the main functions of CH donors is the completion of tetrahedral coordination geometries when stronger donating species are not present. The most strongly bound complex (E), unlike the other seven structures in Figure 3.1, contains both OH and CH donor groups and manifests a distorted tetrahedral configuration. Complex F shares the strong OH donor group of E, but lacks a second coordinating CH species, which may explain the lower relative stability of this complex in relation to E. The remaining complexes are either 1 or 2 proton donating complexes, solely through CH functionalities. Complexes A and B both possess two CH proton contributing groups and each has a similarly distorted tetrahedral coordination geometry, which is reflected in their nearly identical binding energies. Complexes C and D both have CH groups that contribute to water coordination, but they also have CH groups involved in the coordination of the $-RO_2$ group. The interactions most likely in play are demonstrated in Figure 3.1C,D. The distribution of CH groups involved in CH complexation in C and D is 1:2, which is also reflected in the relative binding energies of the two complexes, although the manner of $-RO_2$ complexation most likely plays in the difference between the two. A similar 1:2 situation is evident in structures G and H. Complex H has two coordinating CH groups, similar to structure B, but demonstrates greater complex stability. In all likelihood, the dissimilarity arises from the augmented proton donating capacity of the CH groups as a result of the F atom being present. Structure G, distinguished as the least stable compound of the group, has but one CH

coordinating group. The nature of hydrogen bonds, in general, tends toward a linear geometry[118,132,133] and deviation from linearity frequently translates into a weakening of the interaction.[118] It has also been demonstrated that CHO bonds are less susceptible to weakening than their O-H···O counterparts[134,135] when bent. In the case of water, the weakening of the interaction energy for O-H···O interaction is on the order of 1-1.5 kcal mol^{-1} for a range of 120-240°.[118] Outside this range, the energy can change by as much as 3 kcal mol^{-1}. In contrast, the CHO interaction energy changes by ~0.2-1 kcal mol^{-1} over this same range, making it a faithful coordinating partner if present. The variation in the range depends in a large part upon the nature of any functional groups that may be acting upon the CH moiety. This sensitivity to geometry is demonstrated again in the eight complexes shown in Figure 3.1. Analyzed collectively, the O-H···O and C-H···O interactions show a definite statistical correlation between the bond angle of the interacting triad and the associated H—O bond length, which itself is a reflection of the magnitude of the stated interaction. Additionally, within each complex O-H···O interactions are seen to depart less from the optimum (180°) than C-H···O do, consistent with the developed paradigm. This relationship is helpful in describing the relative stabilities of hydrogen-bonded complexes. For example, structures A and B have roughly identical binding energies, with that of B being only slightly higher. This deviation, however, is not wholly unexpected. Both complexes have a similar number and type of hydrogen bonds. Each has a O_w-H···O bond angle of 159.69° and 160.82°, respectively. The difference in the two geometries is the bond angles of the two C-H···O interactions. In complex A, the two C-H···O bonds make angles of 99.76° and 100.26°, whereas in structure B, the angles are 116.80° and 120.87°. The later angles are more linear and are

expected to attribute to a more stable binding interaction, as they are observed to do. With the exception of complex G, each RO_2-H_2O species can be described in this manner. On examination, it can be seen that the most linear interaction within this complex is the CHO bond, with an angle of 149.55°, as compared to the 134.14° O-H···O bond. The stronger proton donating ability of the FC-H···O likely plays a role in this phenomenon. The overall result is a destabilization of the complex relative to A.

3.4.4 Binding Energy

The CCSD(T)/6-311++G(2d,2p) zero-point adjusted binding energies corrected for BSSE for the CH_3O_2-H_2O and $CH_3CH_2O_2$-H_2O complexes are found to be 2.3 and 2.5 kcal mol^{-1}, respectively. The binding energy increases with the addition of a carbonyl moiety in the R group of the peroxy radical. The corresponding corrected binding energies for the $CH_3C(O)O_2$-H_2O and $CH_3C(O)CH_2O_2$-H_2O complexes are calculated to be 2.9 and 4.0 kcal mol^{-1}, respectively. Further strengthening of the binding energy is observed for complexes that include an –OH moiety in the R group of the peroxy radical. The CCSD(T) level corrected binding energies are found to be 5.1 and 3.7 kcal mol^{-1} for the $CH_2(OH)O_2$-H_2O and $CH_2(OH)CH_2$-H_2O complexes, respectively. Finally, the corrected binding energies for the FCH_2O_2-H_2O and $FCH_2CH_2O_2$-H_2O complexes were computed to be 2.1 and 3.5 kcal mol^{-1}, respectively.

Analysis of results from Table 3.2 shows the following trend of stabilization based on the attached functional groups to the peroxy radical: fluorine alkyl < carbonyl < alcohol.

Table 3.2. Relative binding energies for all complexes. Relative energies are reported in kcal mol^{-1}.

	D_E[a]				D_O[a]				$D_{O,CP}$[a]			
	MP2	QCISD(T)	CCSD(T)	BD(T)	MP2	QCISD(T)	CCSD(T)	BD(T)	MP2	QCISD(T)	CCSD(T)	BD(T)
CH_3O_2-H_2O	5.3	5.1	5.1	5.1	4.4	4.1	4.1	4.1	2.6	2.3	2.3	2.4
$CH_3CH_2O_2$-H_2O	5.8	5.5	5.5	5.5	4.6	4.3	4.3	4.3	2.8	2.5	2.5	2.5
$CH_3C(O)O_2$-H_2O	5.6	5.5	5.5	5.5	4.5	4.5	4.5	4.5	2.9	2.9	2.9	2.9
$CH_3C(O)CH_2O_2$-H_2O	7.0	6.9	6.9	6.9	5.9	5.8	5.8	5.8	4.0	4.0	4.0	4.0
$CH_2(OH)O_2$-H_2O	9.8	9.4	9.4	9.4	7.9	7.5	7.5	7.5	5.5	5.1	5.1	5.1
$CH_2(OH)CH_2O_2$-H_2O	8.3	7.7	7.7	7.7	6.4	5.9	5.9	5.9	4.3	3.8	3.7	3.7
FCH_2O_2-H_2O	4.5	4.6	4.6	4.6	3.5	3.6	3.6	3.6	2.1	2.1	2.1	2.1
$FCH_2CH_2O_2$-H_2O	7.0	6.9	6.9	6.9	5.6	5.5	5.5	5.5	-3.7	3.5	3.5	3.5

3.4.5 Electron Density Shifts

A useful method for describing how the electron density of the peroxy-radical and water molecules shifts throughout the entire space occupied by the newly formed complexes is through electron density difference maps. Maps for the eight complexes of topic are provided in Figure 3.2, with a contour of 0.0007 e/au^3 computed at the MP2(full)/6-311++G-(2d,2p) level. Areas of electron gain are represented by light (yellow) regions and those of electron loss, dark (black) regions. Generally, O-H ··· O hydrogen bonds and CHO interactions are evidenced by a region of electron density loss around the proton acceptor atom.[118] Moving along the axis of the hydrogen bond toward the bridging hydrogen atom, a region of electron density gain is then observed followed by another region of electron density loss around the bridging proton. In the context of the work presented here, each hydrogen bond interaction within the eight complexes in Figure 3.2 can be demonstrated to exhibit this electron density shift pattern. In addition, these maps describe no fundamental difference in the two types of hydrogen bonding interactions.

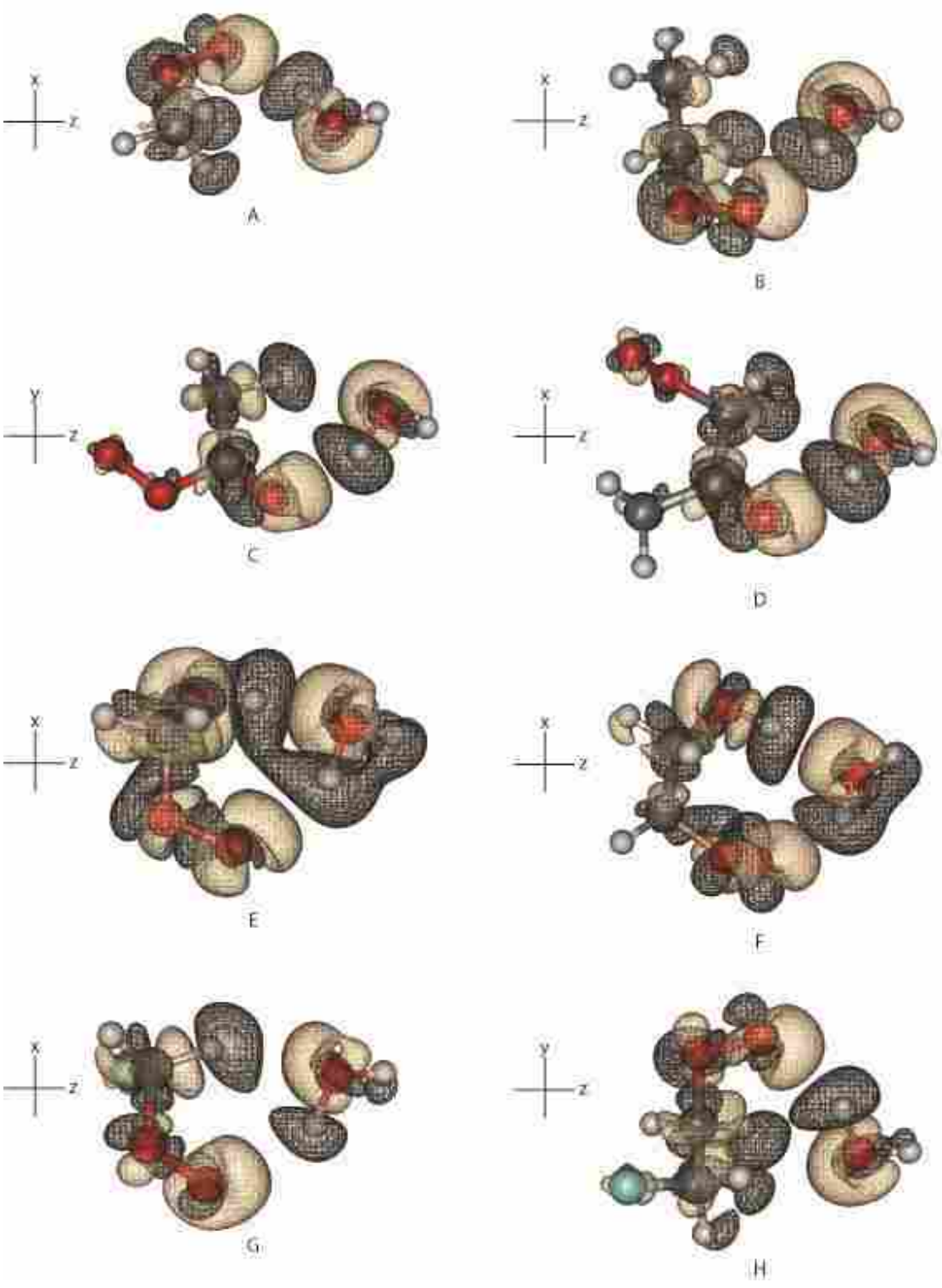

Figure 3.2. Electron density difference maps for the optimized structures. Dark and light regions represent electron density loss and gain, respectively, upon complex formation, relative to the isolated subunits. The contour shown is 0.0007 e/au^3, calculated at the MP2/6-311++G(2d,2p) level.

3.4.6 Vibrational Spectra

Changes in the vibrational spectra of each radical species may also provide evidence for the existence of these weaker C-H ··· O stabilizing interactions. In the case of conventional hydrogen bonds, changes in the vibrational spectra, upon complexation, typically demonstrate a red-shift in the frequency associated with the O-H stretch and experience an enhancement in intensity.[118] In contrast, experimental observations seem to indicate that the reverse pattern is generally true for stabilizing interactions involving the CH group;[136-139] that is, they show a blue-shift in the frequency associated with the C-H stretch and experience a reduction in intensity. Such trends can be useful in the formulation of models describing hydrogen bond and CHO bond behavior, but it should be remembered that, in practice, the assignment of a particular stretching frequency to a single molecular OH or CH vibration is not always straight forward. In the case of CHO interactions, it is often the case that multiple hydrogens are bonded to the carbon atom of the CHO triad and that the stretching vibrations of these additional hydrogens are described by the same stretching frequency as the CH stretch of interest. It follows that the sum vibrational frequency describing the various CH vibrations will be a result of not only the CHO interaction but any additional interactions the other hydrogens may be involved in. Consequently, a CHO interaction may be found to deviate from the general model of behavior expected of such interactions. Table 3.3 lists the changes in the asymmetric stretching frequencies and intensities related to the O-H (shown in bold) and C-H stretches in each of the complexes pictured in Figure 1. Each of the OH stretching frequencies, as expected, is shifted toward the red and shows a marked increase in intensity. Faithful adherence to the characteristics of CH stretching frequency and

intensity behavior upon formation of CHO bond interactions is demonstrated for the majority of the complexes of interest here. The observed range of CH blue-shifted frequencies (1.10-24.01 cm^{-1}) is consistent with those observed by Yanliang et al.[118] in their *ab initio* computational study of F_nCH-X complexes (n = 1, 2, or 3; X = H_2O, CH_3OH, H_2CO; angle CHX constrained to be 180°), where blue-shifted frequency values of 7-47 cm^{-1} were observed. Deviation from the CH stretching frequency model arises in the instances of complexes C and D. In both cases, the frequencies describing the vibrations of the CH involved in coordination of the water molecule through CHO_w interactions are coupled with additional hydrogens involved in similar interactions with the peroxy group of each complex.

Table 3.3. Changes in the frequency and intensity ration of the asymmetric CH stretch and the OH stretch (where applicable) in the peroxy radical subunit.

Complex	$\Delta\upsilon$, cm^{-1}[a]	I/Io[b]
CH_3O_2-H_2O	7.91	0.56
	10.09	0.42
$CH_3CH_2O_2$-H_2O	10.28	0.43
	10.02	0.48
$CH_3C(O)O_2$-H_2O	-1.67	5.48
$CH_3C(O)CH_2O_2$-H_2O	1.72	20.70
$CH_2(OH)O_2$-H_2O	1.10	0.97
	-272.29	**8.99**
$CH_2(OH)CH_2O_2$-H_2O	**-172.32**	**7.52**
$CH_2(F)O_2$-H_2O	7.79	0.45
$CH_2(F)CH_2O_2$-H_2O	24.01	0.52
	23.81	0.22

[a]Bold values represemt OH stretches

[b]Intensity of complex (I) over that of the isolated unit (Io)

3.4.7 CHO Bond Contribution to Stabilization

To help understand the significance CHO bonds make to the stabilization of

RO_2 species, the geometry of each complex was scanned in a stepwise optimization in such a way as to isolate the CHO bond as the sole intermolecular interaction. Comparison of the energy of this new structure with that of the original complex shown in Figure 3.1 can provide an estimate of the portion of the relative binding energy arising from the CHO bond interaction. The results of this scan analysis are given in Table 3.4. For the complexes surveyed, the CHO bond contributes between 21% (CH_3O_2-H_2O) and 33% ($CH_3C(O)O_2$-H_2O and $FCH_2CH_2O_2$-H_2O). In general, complexes without additional electronegative groups (A and B) have CHO bonds that account for ~20% of the stabilization energy of the molecule. Addition of a hydroxyl or fluoro- group tends to increase the significance of the CHO interaction by presumably making the CH group a better proton donor in CHO bond formation. The structures in which a carbonyl group is present, and which share a different form of stabilization than do those complexes that do not, have CHO bonds that account for ~35% of the stabilization energy. These results give further evidence to the significance and presence of CHO bond interactions in the stabilization of RO_2-H_2O complexes.

Table 3.4. CHO bond contribution to complex stabilization.

	C−H···O, %
CH_3O_2-H_2O	21%
CH_3O_2-H_2O	23%
$CH_3C(O)O_2$-H_2O	33%
$CH_3C(O)CH_2O_2$-H_2O	36%
$CH_2(OH)O_2$-H_2O	25%
FCH_2O_2-H_2O	29%
$FCH_2CH_2O_2$-H_2O	33%

3.5 Discussion

The stability of molecular complexes is a function of the population of gas-phase molecules with sufficient kinetic energy to overcome the binding energies of such complexes through gas-phase collisions. At atmospheric temperatures (200-300 K), a first approximation of the average kinetic energy of molecules and molecular complexes ($3/2kBT$) can range between 0.60 and 0.89 kcal mol^{-1}. All of the molecular peroxy/water complexes herein investigated have binding energies that are greater than this average by at least 2.5 kcal mol^{-1}. In addition to average kinetic energy considerations, if one assumes that all collisions between two collisional partners take place as they approach each other at an angle of 180° and that all of the kinetic energy involved is transferred to the breaking of the molecular complex, the minimum kinetic energy required by a molecule to break up a molecular complex will be one-half of the binding energy of that complex. Since the kinetic energy distribution of molecules is described by a Boltzmann distribution, the population of gas-phase molecules with sufficient energy for complex dissociation can be approximated by integrating this distribution over the appropriate limits (minimum energy required to infinity). In the case of the weakest peroxy-water complex considered (CH_3O_2-H_2O), ~3.6% of the kinetic energy distribution at 200 K has the required energy for complex dissociation. This percentage increases to ~12.7% at 300 K. For the strongest complex studied [$CH_2(OH)O_2$-H_2O], these percentages at 200 and 300 K become ~0.05% and 0.77%, respectively. The binding energies reported for each of the peroxy-water complexes suggest that, at tropospheric temperatures, these radical complexes can exist and may play an important role in modifying the peroxy reaction

kinetics in much the same way as the HO_2 self-reaction is enhanced in the presence of water.

To further place this consideration into perspective, the lifetimes for the four most prevalent peroxy radical complexes have been calculated as a function of temperature and according to the following relationship:

$$\tau(T) = \frac{1}{\beta_c k_{diss,0}^{sc}[M_T]} \qquad \text{(EQ 3.1)}$$

where β_c is the collisional efficiency (taken to be unity), $[M_T]$ is the number density of nitrogen molecules at a temperature T, and $k_{diss,0}^{sc}$ is the dissociation constant, as described by Patrick and Golden,[140] using theoretical considerations advanced by Troe.[141] The dissociation constant, $k_{diss,0}^{sc}$, is calculated using eq 3.2.

$$k_{diss,0}^{sc} = Z_{LJ} \frac{\rho(E_0)RT}{Q_{VIB}} \exp\left(\frac{-E_0}{RT}\right) F_E F_{ANH} F_{ROT} F_{CORR} \qquad \text{(EQ 3.2)}$$

where Z_{LJ} is the Lennard-Jones collisional frequency (cm^3/molecule s), $\rho(E_0)$ is the density of states calculated using the Whitten-Rabinovitch assumptions,[142,143] R is the gas constant, T is temperature, Q_{VIB} is the vibrational partition function, E_0 is the critical energy, and F_E, F_{ANH}, and F_{ROT} are correction terms for the energy dependence of the density of states, anharmonicity, and rotation, respectively. F_{CORR} is not calculable and is a correction for the coupling that exists between the different types of degrees of freedom as described by Troe[141] and is usually set equal to unity.

Figure 3.3 shows the *ab initio* derived lifetimes of hydro peroxy, methyl peroxy, ethyl peroxy, and acetyl peroxy radical complexes as a function of temperature and altitude, respectively. It also includes that of the hydro peroxy radical complex for perspective. Lifetime calculations for the remaining complexes could not easily be performed as critical thermodynamic quantities are unavailable from the literature. Analysis of Figure 3.3 shows that as the temperature decreases, the lifetime of the peroxy radical/water complexes increases. This is expected, owing to the decrease in the average kinetic energy of the molecules (assumed to be N_2) colliding with the complex. It is tempting and desirable to demonstrate that a direct relationship exists between the lifetime of each peroxy radical/water complex and its associated binding energy, lifetimes get longer as binding energies increase. This appears to be the case when there is a large difference in binding energies (>1 kcal mol-1), as can be seen by comparing the lifetimes and binding energies of the three RO_2-H_2O complexes with those of the HO_2-H_2O complex. When binding energies differ by less than 1 kcal mol^{-1}, it appears that the manner of complexation may determine complex lifetime. The methyl and ethyl peroxy radical/water complex both follow the general trend of forming a complex through hydrogen bond interactions that involve the peroxy functionality itself, and their lifetimes are seen to increase with increasing binding energy. In contrast, the acetyl peroxy complex does not share the common mechanism of complex formation, and its lifetime is shorter than that of the ethyl peroxy complex even though it has a larger binding energy. Each of the calculated lifetimes suggests that these radical-water complexes may have lifetimes of sufficient magnitude as to allow them to perturb their kinetics.

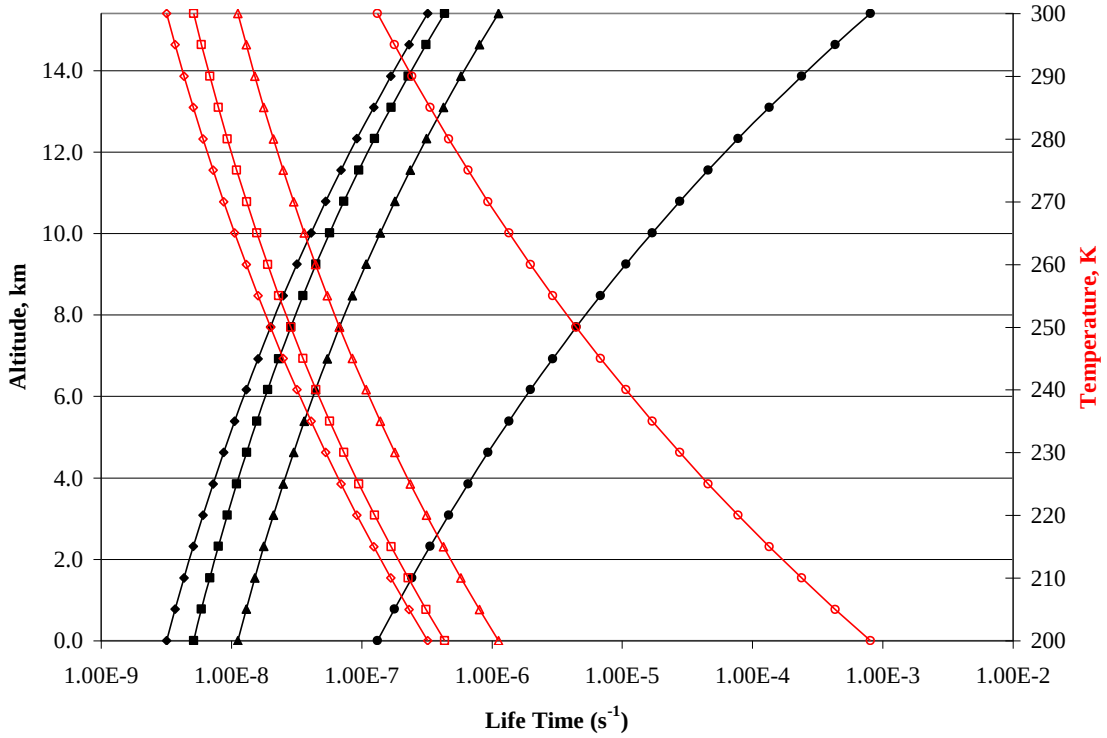

Figure 3.3. Temperature and altitude versus calculated atmospheric lifetime for the RO_2-H_2O complexes. Temperature profile as a function of altitude is calculated assuming a standard atmospheric profile as described by Arguado and Burt.[144] The black data represent the "altitude vs. lifetime" data and the red data represent the "temperature vs. lifetime" data. ♦ = CH_3O_2-H_2O; ▲ = $CH_3CH_2O_2$-H_2O; ■ = $CH_3C(O)O_2$-H_2O; ● = HO_2-H_2O.

Equilibrium constants were calculated for each of the RO_2-H_2O complexes in accordance to theoretical formulations found in McQuarrie et al.[144] and in Steinfeld et al.[145] (see eq 3.3)

$$K_{eq} = \frac{\left(\frac{q(V,T)}{V}\right)_{complex}}{\left(\frac{q(V,T)}{V}\right)_{water}\left(\frac{q(V,T)}{V}\right)_{RO_2}} \qquad \text{(EQ 3.3)}$$

where $q(V,T)/V$ is the product of the translational, rotational, vibrational, and electronic partition functions for H_2O, the RO_2 moiety, and the RO_2-H_2O complex, as shown in eq 3.4

$$\frac{q(V,T)}{V} = \left(\frac{2\pi M k_B T}{h^2}\right)^{3/2} \frac{\pi^{1/2}}{\sigma} \left(\frac{T^3}{\Theta_{rot,A}\Theta_{rot,B}\Theta_{rot,C}}\right)^{1/2} \left[\prod_{j=1}^{3n-6} \frac{1}{\left(1-e^{-\Theta_{vib,j}/T}\right)}\right] g_{e1} e^{-D_e/k_B T} \quad \text{(EQ 3.4)}$$

For the group of radical/water complexes under consideration, the magnitude of the equilibrium constant increases with increased binding energy and decreasing temperature. For CH_3O_2-H_2O and $HOCH_2O_2$-H_2O at 300 K, *K*eq was calculated to be 1.54×10^{-21} and 1.91×10^{-19} cm^3 $molecule^{-1}$, respectively. At 200 K, these values increase to 1.02×10^{-19} cm^3 $molecule^{-1}$ for CH_3O_2-H_2O and to 6.25×10^{-16} cm^3 $molecule^{-1}$ for $HOCH_2O_2$-H_2O.

Useful information regarding the atmospheric abundance of these peroxy radical/water complexes at different values for the relative humidity can be obtained in terms of a ratio between complexed and uncomplexed peroxy radicals by multiplying the equilibrium constant by the relevant [H_2O] concentration, as shown in eq 3.5

$$K_{eq}[H_2O] = \frac{[RO_2 \cdot H_2O]}{[RO_2]} \quad \text{(EQ 3.5)}$$

Figure 3.4 plots this ratio as a function of temperature at 100% humidity. As expected, the relative abundance of the complex increases relative to the uncomplexed peroxy radical as the abundance of atmospheric moisture increases with temperature. When the logarithm of this ratio is plotted against the complex binding energies, a linear

relationship is obtained. Figure 3.5 is such a plot for the eight RO_2-H_2O complexes reviewed, as well as HO_2-H_2O. A plot such as this is a powerful indicator of expected ratios ([complex]/[RO_2])of atmospherically present peroxy radicals as a function of binding energy. Many atmospheric modeling studies have ignored the water influence on RO_2 abundances and RO_2 chemistry; our findings suggest that water will play an important role in influencing the abundances of RO_2.

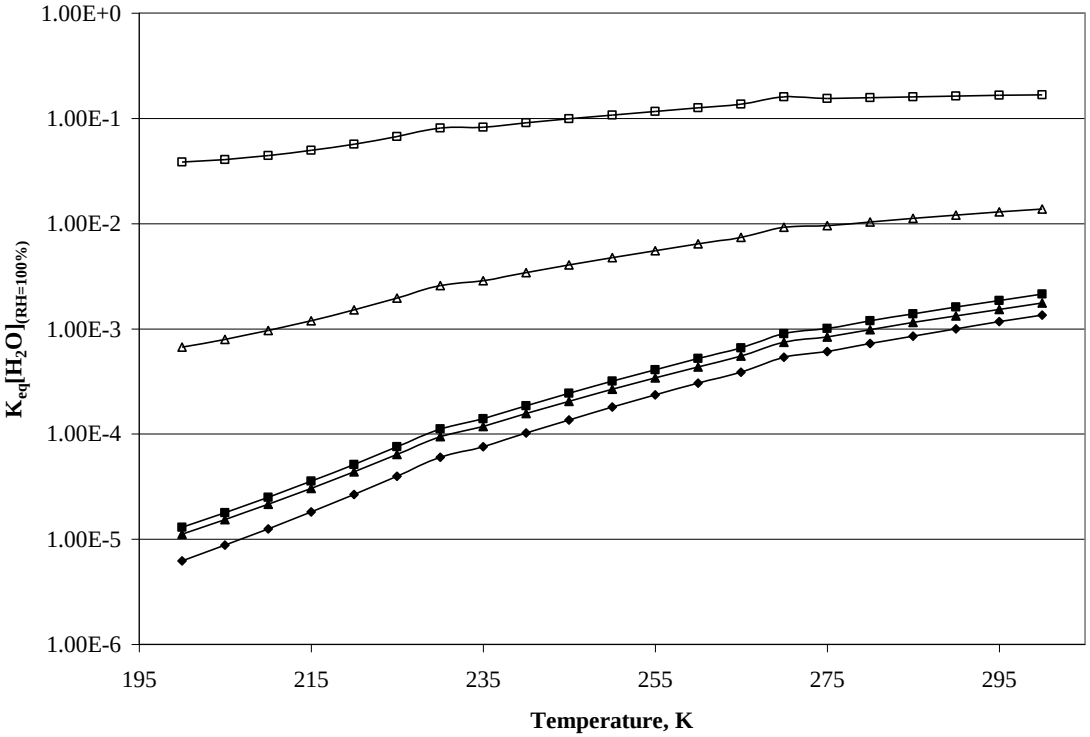

Figure 3.4. log [K_{eq}*[H_2O]] ([H_2O] at a relative humidity of 100%) as a function of temperature. ♦ = CH_3O_2-H_2O; ▲ = $CH_2CH_2O_2$-H_2O; ■ = $CH_3C(O)O_2$-H_2O; □ = $CH_2(OH)O_2$-H_2O; Δ = $CH_2(OH)CH_2O_2$-H_2O.

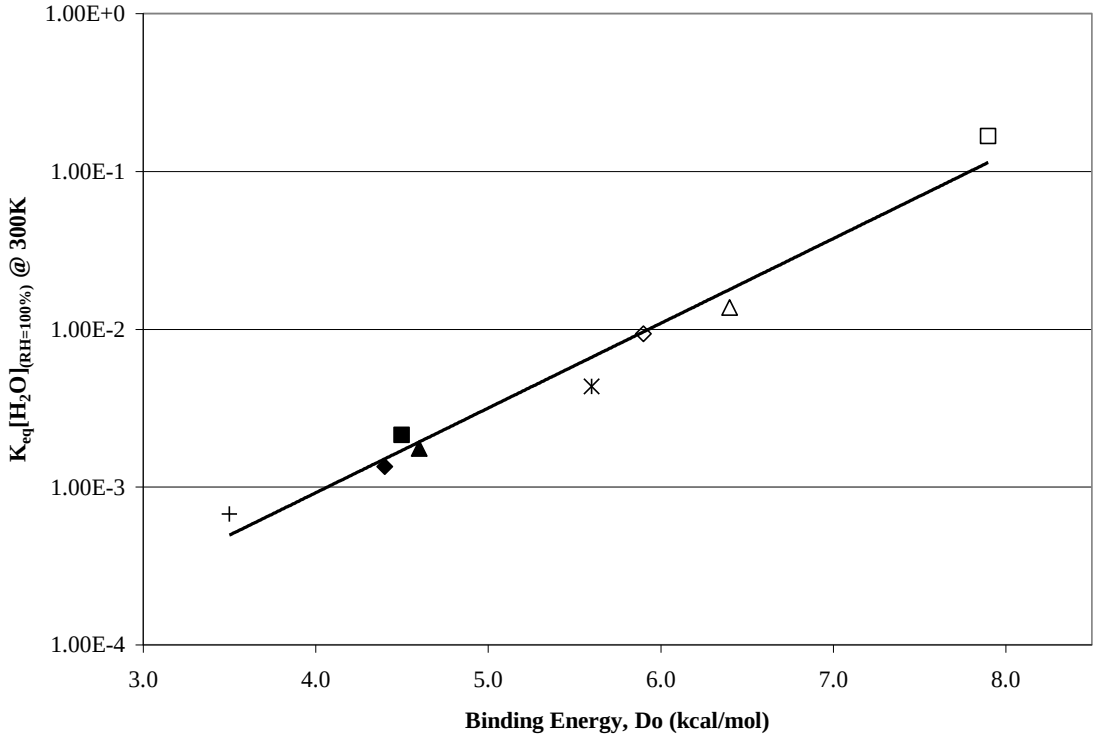

Figure 3.5. log [K_{eq}*[H_2O]] ([H_2O] at a relative humidity of 100%) versus zero point corrected binding energy (D_o) (D_o calculated at the MP2/6-311++G(2df,2p) level) at 300 K. ♦ = CH_3O_2-H_2O; ▲ = $CH_2CH_2O_2$-H_2O; ■ = $CH_3C(O)O_2$-H_2O; ◊ = $CH_3C(O)CH_2O_2$-H_2O; □ = $CH_2(OH)O_2$-H_2O; Δ = $CH_2(OH)CH_2O_2$-H_2O; + = $CH_2(F)O_2$-H_2O; * = $CH_2(F)CH_2O_2$-H_2O.

3.6 Conclusions

The existence of RO_2-H_2O complexes is postulated to play a part in the initial formation of aerosols. In order for peroxy water complexes to have significant participation as aerosol initiators through the proposed reverse micelle mechanism, they must have binding energies that are larger than 3/2*k*B*T*. Examination of the RO_2-H_2O series considered in this manuscript indicates that any member of the series may contribute, but we predict those with the largest binding energies (>5 kcal mol^{-1}) are most likely to play a significant contributing role because of their longer atmospheric lifetimes. Based on this trend, these results suggest that the kinetics of organic peroxy radical water complexes will be perturbed in relation to the magnitude of their respective binding

energies. Moreover, hydroxyl containing organic peroxy radicals would more likely modify the kinetics and the resulting product branching ratio for peroxy self-reactions, peroxy cross-reactions, and reactions with NO_x. As such, the product branching ratios of RO_2 + NO reactions in the presence of water will deviate from those run in the absence of water, much like the recent results published by Butkovskaya et al.[87]

This work illustrates the potential importance of organic peroxy radical-water complexes by their range of binding energy and atmospheric lifetime for a series of organic peroxy radicals. The spread in binding energies can be explained by the composition of the R group attached to the peroxy moiety. The general trend in binding energies has been determined to be: fluorine ≈ alkyl < carbonyl < alcohol. The weakest bound complex, FCH_2O_2-H_2O, is calculated to be bound by 2.1 kcal mol^{-1} and the strongest, [$CH_2(OH)O_2$-H_2O], is bound by 5.1 kcal mol^{-1}. The modest binding energy of the peroxy radical-water complexes which contain carbonyl and alcohol groups indicates that these complexes may play important chemical roles under low-temperature conditions, as for example in atmospheric or interstellar chemical processes.

3.7 Supplementary Material

Tables S3.1 through S3.16 represent the MP2(full)/6-311++G(2d,2p) optimized geometries and the B3LYP/6-311++G(2d,2p) harmonic vibrational frequencies.

3.7.1 Cartesian Coordinates for Each Optimized Geometry

Supplementary Table S3.1. MP2(full)/6-311++G(2d,2p) optimized geometries of the methyl peroxy radical and the methyl peroxy radical and water complex.

CH_3O_2				CH_3O_2-H_2O			
O	0.0012	0.0002	-0.0100	O	-0.1573	-0.2001	0.1799
O	-0.0140	-0.0001	1.2910	O	-0.0098	0.2531	1.3828
C	1.3359	0.0000	1.8159	C	1.3183	-0.0345	1.9040
H	1.8435	-0.8919	1.4728	H	1.4594	-1.1062	1.9226
H	1.8429	0.8925	1.4738	H	2.0518	0.4370	1.2650
H	1.2257	-0.0007	2.8922	H	1.3241	0.3874	2.8991
				O	2.3397	-1.5281	-0.6439
				H	1.4533	-1.1551	-0.5864
				H	2.3889	-1.9198	-1.5156

Supplementary Table S3.2. MP2(full)/6-311++G(2d,2p) optimized geometries of the ethyl peroxy radical and the ethyl peroxy radical and water complex.

$CH_3CH_2O_2$				$CH_3CH_2O_2$-H_2O			
C	0.0000	0.0000	0.0000	C	-0.0629	-0.2972	0.1010
C	0.0000	0.0000	1.5074	C	-0.0949	0.1787	1.5301
H	1.0222	0.0000	-0.3667	H	0.9135	-0.0832	-0.3233
H	-0.5038	-0.8813	-0.3824	H	-0.2382	-1.3664	0.0473
H	-0.5024	0.8844	-0.3736	H	-0.8069	0.2238	-0.4888
H	0.4490	-0.8946	1.9235	H	0.6161	-0.3428	2.1600
H	0.4704	0.8820	1.9256	H	0.0360	1.2501	1.6168
O	-1.3673	-0.0344	2.0163	O	-1.3851	-0.1521	2.1459
O	-1.9488	1.1174	1.8549	O	-2.3301	0.6317	1.7399
				H	-1.8046	2.2197	0.6440
				H	-1.8097	3.6217	0.0419
				O	-1.2654	2.8407	0.1408

Supplementary Table S3.3. MP2(full)/6-311++G(2d,2p) optimized geometries of the acetyl peroxy radical and the acetyl peroxy radical and water complex.

$CH_3C(O)O_2$				$CH_3C(O)O_2$-H_2O			
C	0.0000	0.0000	0.0000	C	0.0000	0.0000	0.0000
H	0.0000	0.0000	1.0811	H	0.0000	0.0000	1.0839
H	1.0144	0.0000	-0.3810	H	1.0105	0.0000	-0.3857
H	-0.4903	-0.8879	-0.3811	H	-0.5345	-0.8860	-0.3232
C	-0.7231	1.2255	-0.4467	C	-0.6830	1.2203	-0.5099
O	-0.8261	1.4074	-1.8780	O	-2.0458	1.4129	-0.0975
O	-0.2538	0.4412	-2.5613	O	-2.4871	0.4529	0.6876
O	-1.2294	2.0795	0.2092	O	-0.2579	2.0796	-1.2242
				O	2.4159	1.1646	-1.9074
				H	3.0929	1.7011	-2.3190
				H	1.6364	1.7276	-1.8635
				O	-1.2654	2.8407	0.1408

Supplementary Table S3.4. MP2(full)/6-311++G(2d,2p) optimized geometries of the acetonyl peroxy radical and the acetonyl peroxy radical and water complex.

$CH_3C(O)CH_2O_2$				$CH_3C(O)CH_2O_2$-H_2O			
C	1.3657	0.1684	0.9314	C	1.6600	-0.0435	-1.2908
H	1.6293	1.1371	0.5140	H	1.5683	0.9506	-1.7201
H	1.7597	0.0650	1.9341	H	2.6931	-0.2683	-1.0604
H	1.8012	-0.5836	0.2791	H	1.2795	-0.7400	-2.0329
C	-0.1242	0.0060	0.9692	C	0.8429	-0.1440	-0.0409
O	-0.7443	-0.3152	1.9644	O	1.3030	-0.5378	1.0195
C	-0.9286	0.2868	-0.2924	C	-0.6142	0.2842	-0.0733
H	-1.4923	1.2047	-0.1574	H	-0.7420	1.1774	0.5297
H	-1.6007	-0.5397	-0.4911	H	-1.2483	-0.5033	0.3159
O	-0.1118	0.5160	-1.4644	O	-1.0652	0.6402	-1.4002
O	0.4112	-0.6042	-1.8804	O	-1.2681	-0.4299	-2.1183
				O	-0.6958	0.1302	2.9306
				H	-0.5803	0.0461	3.8770
				H	0.1115	-0.2271	2.5394

Supplementary Table S3.5. MP2(full)/6-311++G(2d,2p) optimized geometries of the hydroxymethyl peroxy radical and the hydroxymethyl peroxy radical and water complex.

$HOCH_2O_2$				$HOCH_2O_2$-H_2O			
C	0.0000	0.0000	0.0000	C	0.0000	0.0000	0.0000
H	0.0000	0.0000	1.0804	H	0.0000	0.0000	1.0814
H	1.0005	0.0000	-0.4195	H	0.9996	0.0000	-0.4226
O	-0.7791	1.0458	-0.4399	O	-0.7984	1.0022	-0.4637
H	-0.7079	1.0865	-1.3972	H	-0.5734	1.1537	-1.3962
O	-0.5816	-1.2927	-0.3569	O	-0.5506	-1.3425	-0.3155
O	-0.5204	-1.4430	-1.6497	O	-0.3828	-1.6339	-1.5658
				O	0.2104	0.7838	-3.0234
				H	0.0791	-0.1632	-2.8887
				H	-0.1720	0.9835	-3.8784

Supplementary Table S3.6. MP2(full)/6-311++G(2d,2p) optimized geometries of the 2-hydroxyethyl peroxy radical and the 2-hydroxyethyl peroxy radical and water complex.

$HOCH_2CH_2O_2$				$HOCH_2CH_2O_2$-H_2O			
C	0.0000	0.0000	0.0000	C	0.0000	0.0000	0.0000
H	0.0000	0.0000	1.0857	H	0.0000	0.0000	1.0869
H	1.0374	0.0000	-0.3371	H	1.0384	0.0000	-0.3334
C	-0.6704	-1.2661	-0.4720	C	-0.6726	-1.2706	-0.4629
H	-0.2685	-2.1416	0.0256	H	-0.1945	-2.1537	-0.0500
H	-1.7475	-1.2157	-0.3585	H	-1.7380	-1.2623	-0.2720
O	-0.6809	1.1736	-0.4016	O	-0.6866	1.1555	-0.4208
H	-0.8516	1.0909	-1.3445	H	-0.5258	1.2819	-1.3677
O	-0.3860	-1.5199	-1.8819	O	-0.4999	-1.3743	-1.9095
O	-0.8814	-0.5922	-2.6429	O	-1.6082	-1.1854	-2.5563
				O	-0.2431	1.3177	-3.2357
				H	-0.7156	0.5251	-3.5099
				H	-0.6219	2.0305	-3.7517

Supplementary Table S3.7. MP2(full)/6-311++G(2d,2p) optimized geometries of the fluoromethyl peroxy radical and the fluoromethly peroxy radical and water complex.

FCH_2O_2				FCH_2O_2-H_2O			
C	0.0000	0.0000	0.0000	C	-0.1483	-0.0783	0.2774
H	0.0000	0.0000	1.0818	H	0.4654	-0.2078	1.1584
H	0.9837	0.0000	-0.4488	H	0.2926	0.5356	-0.4954
O	-0.6773	-1.1920	-0.3771	O	-0.3447	-1.4046	-0.2221
O	-0.3880	-1.5016	-1.6226	O	-0.7773	-1.3777	-1.4573
F	-0.6991	1.0804	-0.4492	F	-1.3568	0.4373	0.6412
				O	0.6879	0.9195	-2.6698
				H	-0.0123	0.2678	-2.7579
				H	0.6728	1.4173	-3.4876

Supplementary Table S3.8. MP2(full)/6-311++G(2d,2p) optimized geometries of the 2-fluoroethyl peroxy radical and the 2-fluoroethyl peroxy radical and water complex.

$FCH_2CH_2O_2$				$FCH_2CH_2O_2$-H_2O			
C	0.0000	0.0000	0.0000	C	-0.0064	-0.0004	0.0154
H	0.0000	0.0000	1.0834	H	-0.0190	0.0007	1.0985
H	1.0158	0.0000	-0.3823	H	1.0059	-0.0049	-0.3690
O	-0.6482	-1.2184	-0.4524	O	-0.6328	-1.2723	-0.3417
O	-0.0480	-2.2669	0.0313	O	-0.4557	-1.5571	-1.5917
C	-0.7820	1.1499	-0.5539	C	-0.7870	1.1537	-0.5355
H	-0.2356	2.0750	-0.3994	H	-0.2301	2.0731	-0.3843
H	-0.9811	1.0129	-1.6121	H	-0.9894	1.0230	-1.5909
F	-2.0027	1.2499	0.1030	F	-2.0008	1.2571	0.1398
				O	1.3333	0.4543	-2.7556
				H	1.7823	0.3675	-3.5964
				H	0.8007	-0.3432	-2.6641

3.7.2 Harmonic Vibrational Frequencies

Supplementary Table S3.9. B3LYP/6-31+G(d,p) harmonic vibrational frequencies for water, the methyl peroxy radical, and the methyl peroxy radical and water complex.

H_2O	CH_3O_2		CH_3O_2-H_2O	
1603.9	126.4	1444.6	41.2	1159.0
3810.4	490.2	1486.7	97.1	1235.8
3931.7	916.0	3064.6	148.8	1450.7
	1127.4	3162.9	152.8	1476.5
	1155.9	3175.5	155.7	1484.1
	1219.9		342.2	1619.4
			483.5	3069.3
			500.1	3170.8
			1475.3	3185.6
			902.0	3716.7
			1122.6	3900.8

Supplementary Table S3.10. B3LYP/6-31+G(d,p) harmonic vibrational frequencies for water, the ethyl peroxy radical, and the ethyl peroxy radical and water complex.

H_2O	$CH_3CH_2O_2$		$CH_3CH_2O_2$-H_2O	
1603.9	103.7	1374.8	37.8	1216.1
3810.4	230.7	1413.7	82.3	1311.3
3931.7	361.1	1485.5	115.7	1375.4
	523.2	1490.2	147.7	1416.6
	798.9	1508.2	151.7	1487.6
	843.4	3051.9	227.7	1492.7
	995.4	3077.9	345.6	1504.8
	1096.7	3123.0	366.5	1620.2
	1154.4	3130.7	502.9	3054.6
	1205.4	3149.7	528.8	3084.9
	1305.4		797.6	3125.2
			840.2	3141.0
			988.9	3159.7
			1095.4	3706.0
			1160.7	3900.3

Supplementary Table S3.11. B3LYP/6-31+G(d,p) harmonic vibrational frequencies for water, the acetyl peroxy radical, and the acetyl peroxy radical and water complex.

H_2O	$CH_3C(O)O_2$		$CH_3C(O)O_2$-H_2O	
1603.9	136.1	1131.4	36.2	1051.6
3810.4	154.9	1190.5	89.0	1139.2
3931.7	321.8	1404.2	94.8	1197.6
	501.4	1463.7	138.8	1409.8
	538.1	1469.7	141.1	1467.0
	549.7	1893.2	166.0	1476.2
	738.1	3074.6	308.6	1609.3
	985.3	3143.3	336.4	1869.0
	1046.4	3184.4	452.8	3069.4
			518.5	3138.6
			543.0	3182.9
			565.7	3750.5
			750.5	3911.2
			992.8	

Supplementary Table S3.12. B3LYP/6-31+G(d,p) harmonic vibrational frequencies for water, the acetonyl peroxy radical, and the acetonyl peroxy radical and water complex.

H_2O	$CH_3C(O)CH_2O_2$		$CH_3C(O)CH_2O_2$-H_2O	
1603.9	47.6	1229.5	30.5	1091.0
3810.4	96.8	1273.4	55.3	1165.6
3931.7	150.5	1334.9	80.9	1240.1
	244.5	1395.4	106.5	1278.5
	397.8	1435.6	149.8	1352.0
	463.7	1464.5	160.7	1397.7
	492.7	1472.3	162.6	1427.1
	570.4	1799.4	251.4	1463.7
	762.2	3048.5	367.8	1471.9
	860.6	3085.4	407.8	1615.9
	948.0	3111.0	461.4	1776.8
	995.0	3153.1	509.1	3050.6
	1091.6	3168.5	545.7	3090.9
	1160.5		575.5	3112.7
			768.5	3154.8
			859.5	3171.0
			953.5	3687.2
			999.1	3903.0

Supplementary Table S3.13. B3LYP/6-31+G(d,p) harmonic vibrational frequencies for water, the hydroxymethyl peroxy radical, and the hydroxymethyl peroxy radical and water complex.

H_2O	$HOCH_2O_2$		$HOCH_2O_2$-H_2O	
1603.9	112.9	1269.7	84.5	1171.1
3810.4	344.3	1381.4	118.4	1195.8
3931.7	474.7	1416.5	162.8	1289.0
	611.6	1504.8	220.8	1400.1
	817.2	3062.8	258.2	1492.5
	1052.4	3172.0	362.6	1501.9
	1140.8	3799.0	375.3	1606.7
	1165.6		505.1	3063.9
			587.7	3161.2
			753.6	3526.7
			820.2	3708.0
			1088.9	3898.9

Supplementary Table S3.14. B3LYP/6-31+G(d,p) harmonic vibrational frequencies for water, the 2-hydroxyethyl peroxy radical, and the 2-hydroxyethyl peroxy radical and water complex.

H_2O	$HOCH_2CH_2O_2$		$HOCH_2CH_2O_2$-H_2O	
1603.9	88.9	1217.1	67.2	1176.2
3810.4	173.7	1275.5	89.3	1251.2
3931.7	330.5	1366.3	122.9	1286.7
	396.3	1379.5	147.9	1360.2
	457.6	1429.7	200.4	1402.3
	553.6	1470.2	231.8	1448.2
	799.3	1496.2	309.9	1460.5
	924.7	3009.8	354.7	1489.4
	965.0	3076.6	434.7	1621.5
	1080.3	3093.7	481.4	3014.6
	1112.5	3144.9	506.5	3069.0
	1168.4	3774.1	738.5	3079.1
			810.2	3158.4
			891.7	3601.8
			963.7	3740.5
			1088.2	3900.8
			1118.8	

Supplementary Table S3.15. B3LYP/6-31+G(d,p) harmonic vibrational frequencies for water, the fluoromethyl peroxy radical, and the fluoromethyl peroxy radical and water complex.

H_2O	FCH_2O_2		FCH_2O_2-H_2O	
1603.9	117.1	1183.9	39.4	1131.3
3810.4	414.6	1284.6	101.0	1196.1
3931.7	570.1	1420.4	108.2	1295.6
	935.2	1489.9	120.5	1433.4
	1072.6	3096.9	144.1	1503.4
	1123.7	3184.9	261.0	1600.4
			373.1	3098.6
			419.2	3192.7
			574.4	3776.4
			912.7	3915.0
			1070.6	

Supplementary Table S3.16. B3LYP/6-31+G(d,p) harmonic vibrational frequencies for water, the 2-fluoroethyl peroxy radical, and the 2-fluoroethyl peroxy radical and water complex.

H_2O	$FCH_2CH_2O_2$		FCH_2CH2O_2-H_2O	
1603.9	55.9	1230.0	48.5	1119.8
3810.4	138.4	1287.7	84.6	1178.8
3931.7	279.3	1378.1	99.4	1259.9
	386.1	1426.0	140.9	1299.7
	543.8	1473.5	167.4	1375.4
	829.1	1493.2	183.5	1413.4
	877.0	3064.7	284.2	1467.1
	1038.8	3074.0	337.9	1490.1
	1077.3	3121.5	463.4	1609.0
	1118.9	3141.9	483.1	3080.1
	1197.5		552.3	3094.4
			813.9	3145.5
			879.4	3165.8
			996.8	3723.4
			1070.3	3904.1

CHAPTER 4: COMPUTATIONAL STUDY OF ISOPRENE HYDROXYALKYL PEROXY RADICAL-WATER COMPLEXES ($C_5H_8(OH)O_2$-H_2O)

4.1 Abstract

Herein we report an extensive *ab initio* study on the existence of eight *β*-hydroxy isoprene peroxy radical-water complexes. Binding energies calculated at the MP2(full)/6-311++G(2d,2p)//CCSD(T)/6-311++G(d,p) level of theory range between 3.85 to 5.66 kcal mol^{-1}. The results of natural bond orbital (NBO) calculations are presented to help rationalize complex formation. Atmospheric lifetimes, equilibrium constants, heats of formation and the relative abundance of complexed to uncomplexed peroxy radicals are also reported and discussed.

4.2 Introduction

Isoprene (2-methyl-1,3-butadiene) is the most abundant biogenically emitted non-methane hydrocarbon with an annual estimated global emission of 500 Tg yr^{-1},[146] representing approximately 44% of the total volatile organic compound (VOC) emissions by vegetation.[147] As a result of the high chemical reactivity of isoprene, it has been the focus of a number of computational and experimental studies.[148-151] They have investigated the kinetics and mechanism of OH radical attack and subsequent steps in the oxidation of isoprene under atmospheric conditions. The reaction between a hydroxyl radical and an isoprene molecule proceeds exclusively by addition of OH radical across one of the double bonds to yield an OH-isoprene adduct.

$$\cdot OH + C_5H_8 \rightarrow \cdot C_5H_8(OH) \quad (4.1)$$

Under atmospheric conditions, the newly formed hydroxy alky radical reacts quickly with O_2 to produce the hydroxy alkyl peroxy radical:

$$\cdot C_5H_8(OH) + O_2 \rightarrow C_5H_8(OH)O_2\cdot \quad (4.2)$$

In the presence of NO, two possible products have been shown to form:

$$C_5H_8(OH)O_2\cdot + NO \rightarrow C_5H_8(OH)O\cdot + NO_2 \quad (4.3a)$$

$$\rightarrow C_5H_8(OH)ONO_2 \quad (4.3b)$$

Reaction 4.3a, the oxidation of NO to NO_2 and the production of an alkoxy radical, is an important step in the formation of tropospheric ozone via photolysis of NO_2. Reaction 4.3b, the production of an organic nitrate, results in a net loss of NO_x and serves as a radical termination mechanism. In addition, the reaction has been shown to serve as an effective nitrogen oxide transport mechanism in much the same way that PAN has been implicated. Several experimental studies have reported on the organic nitrate yield from the reaction of OH radical with isoprene in the presence of NO.[151-153] The reported yields range between 4 and 13%.

The effect of water vapor on the kinetics and product branching ratios of organic peroxy radicals has been the subject of a number of papers and reviews. Recent work by Butkovskaya et al.[87,154] probing the effects of temperature and water vapor on the HO_2 + NO reaction kinetics and product branching ratio have shown that the yield of HNO_3 (the

association/isomerization) product increases by 90% in the presence of modest amounts of water vapor:

$$HO_2 + NO \rightarrow NO_2 + OH \quad (4.4a)$$

$$\rightarrow HNO_3 \quad (4.4b)$$

Increased HNO_3 production as a function of increasing water vapor has been explained as occurring due of the formation of an HO_2-H_2O complex during the reaction mechanism. Integrating the work of Butkovskaya et al. into 2D- and 3D-models significantly impacts the tropospheric concentrations of HNO_3, HO_x, NO_x, and ozone species.[155]

The simplest RO_2 radical is the HO_2 radical. Experimental measurements of the kinetics of the HO_2 self-reaction indicate a water vapor dependence on the reaction rate coefficient. The water vapor enhancement was observed to increase with decreasing temperatures and has been explained by the formation of an HO_2-H_2O complex. The existence of a complex has been confirmed by Suma et al.,[49] who measured the microwave spectrum of the complex in a supersonic jet by means of a Fourier transform microwave spectrometer. Kanno et al.,[48] using frequency modulated diode laser spectroscopy, successfully measured the equilibrium constant of the HO_2-H_2O complex at 298 K. These measurements combined with known water vapor and HO_2 radical concentrations suggest an upper limit of approximately 30% of HO_2 radicals may be complexed under typical atmospheric conditions.[131]

In complement to the experimental studies, *ab initio* computational analysis have reported the lowest energy geometries, vibrational frequencies, binding energies and

equilibrium constants for the HO_2-H_2O and HO_2-$(H_2O)_n$ complexes.[16,18,156] Modeling studies indicate that the water vapor enhancement of the HO_2 self-reaction kinetics cannot be ignored when modeling atmospheric processes involving the HO_2 radical.[88]

It has recently been proposed that other RO_2 radicals in the presence of water may form similar complexes. The high level *ab initio* study of Clark et al.[59] reported the optimized geometries, binding energies, and equilibrium constants for a series of organic peroxy radical-water complexes. Their work showed that for species with strong binding energies (~5 to 7 kcal mol^{-1}) a significant fraction of the RO_2 radicals can exist as a RO_2-H_2O complex. The existence of RO_2-H_2O complexes would serve to perturb the reactivity of RO_2 radicals and consequently affect their kinetics and product branching ratios in much that same manner as has been observed for the HO_2-H_2O system. The influence of RO_2-H_2O complexes has not yet been considered in models incorporating RO_2 radicals.

Reichert et al.[157] explored the effect of water vapor on the chain length (CL) of peroxy radical chemical amplifiers (PERCA). Their results indicate that radical CL is dependent on the relative humidity. The authors hypothesized that a gas reaction involving the formation of a peroxy radical and water complex is responsible for the water effect seen in the PERCA method. They further speculate that the amplifier CL is shortened as a result of such complex formation and may result from an increase in the apparent rate coefficients of non-radical chain termination reactions (e.g., reaction of HO_2 with NO to form HNO_3).

Organic films and reverse micelle formation have recently been proposed as a mechanism for atmospheric aerosol production.[89-92] This mechanism suggests that water is encapsulated by organic molecules with hydrophilic heads directed inward and

hydrophobic ends directed outward. Processing of these ultrafine aerosols is initiated by reactions with atmospheric radicals that transform the surface of these aerosols into hydrophilic surfaces that can grow by water accretion and form cloud condensation nuclei. The formation of the peroxy radical-water complexes investigated in this study may represent the first stages of this proposed mechanism for the process of aerosol formation under atmospheric conditions.

The work presented here is the first study involving the eight *β*-hydroxy isoprene peroxy radical water complexes formed as a result of the atmospheric photo-oxidation of isoprene. Optimized geometries and lifetimes and calculated equilibrium constants at 298 K for these eight complexes are reported.

4.3 Methods

4.3.1 Forward

Calculations were performed using the Gaussian 03, Revision D.01 suite of programs.[63] The geometries of the β-hydroxy isoprene peroxy monomers and their water complexes were fully optimized at the UMP2(full)/6-311++G(2d,2p) computational level. Harmonic vibrational frequency calculations performed at the B3LYP/6-311++G(2d,2p) level established the structures as minima and allowed for zero-point corrections to be made. The counterpoise procedure[71,72] was used to correct the energies for basis set superposition error. Electron correlation refinements based on the UMP2 optimized minimum energy structures were performed using quadratic configuration interaction with single, double, and triple excitations, QCISD(T) and coupled cluster with single, double, and perturbative triple excitations, CCSD(T) methods.

Natural energy decomposition analysis (NEDA) calculations were performed at the B3LYP/6-311++G(2d,2p) level using NBO.5G[77] implemented in the Firefly QC package,[78] which is partially based on the GAMESS (US)[158] source code. Natural bond orbital (NBO) analysis was performed with the B3LYP/6-311++G(2d,2p) method/basis set using the Gaussian implementation of NBO 3.1.[69,70,73-76] Electron density maps with a surface resolution of 0.0009 e/au^3 were generated at the B3LYP/6-311++G(2d,2p) level using geometries optimized at the same level. The B3LYP/6-311++G(2d,2p) method and basis set were chosen to be consistent with the corresponding method and basis used for the frequency calculations. NEDA and NBO values calculated at the MP2(full)/6-311++G(2d,2p) level did not differ significantly from those obtained at the density functional level.

The lowest energy structure for each β-hydroxy isoprene peroxy radical and its complex with water was arrived at through two search methodologies: robust systematic searching with random constrained sampling (RSS/RCS) and simulated annealing (SA).

All calculations were performed on a supercomputing Linux cluster consisting of 320 processing nodes equipped with two quad-core Intel Nehalem processors (2.8 GHz) and 24 GB of memory. All nodes are connected with Infiniband, a high-speed, low-latency copper interconnect.

All MP2(full)/6-311++G(2d,2p) optimized geometries and B3lYP/6-311++G(2d,2p) harmonic vibrational frequencies are available in supplementary Tables 4.1-4.16.

4.3.2 Robust Systematic Searching and Radom Constrained Sampling

The robust systematic search (RSS) method searches the potential energy surface of a molecule via systematic bond rotations that explore a total of *nm* possible structures, where *m* is the number of rotatable bonds, and *n* is the number of unique positions (bond rotations) for each bond. Rotatable bonds are defined as those that result in a symmetry unique molecular conformation upon a rotation of 360/*n* degrees (e.g., C-H bonds are non-rotatable). The molecular structures of interest in this work were generated by rotating each rotatable bond by 60°. In some instances, bond rotations of 180° were used owing to intrinsic bond symmetry (i.e., C-CH_3). These rotations amounted to 2592 unique structures ([360/60]4 × 360/180) for each hydroxy isoprene peroxy radical. On average, ~100 of these structures had nuclei closer than 0.5 Å and were ignored.

Initial optimization of the roughly 2500 structures for each β-hydroxy isoprene peroxy radical began with a HF/6-31+G(d,p) geometry optimization. The purpose of this initial step was to quickly generate initial force constants in the G03 environment and to decrease the overall computation time. The geometry of each radical structure was then refined at the B3LYP/6-311++G(d,p) level. The energy of the optimized structure was then refined with a B3LYP/6-311++G(d,p)//MP2(full)/6-311++G(d,p) single-point calculation. To pinpoint the lowest energy structure, the geometries of the top 100 radical structures of each radical type were further refined at the MP2(full)/6-311++G(2d,2p) level. Further energy refinements were performed at the QCISD(T)/6-311++G(d,p) and CCSD(T) /6-311++G(d,p) levels using the MP(full)/6-311++G(2d,2p) optimized geometry.

The random constrained sampling (RCS) method generates radical-water complex geometries by randomly packing a water molecule within a *n* Å constrained radius sphere encompassing the entire radical or a user-defined portion of the optimized radical structure. In this work, the optimized complex geometries were determined via two iterations of the RCS method. The first iteration generated 2000 radical-water geometries by placing a water molecule within a 4.5 Å radius sphere centered over the entire radical structure. The results of this first iteration indicated that the water molecule showed a preference for the moiety of the hydroxy isoprene radical where the hydroxyl (-OH) and the peroxy (-O-O) functionalities were in head to tail (-OH ··· O-O-) proximity. The second iteration produced an additional 2000 radical-water geometries that involved placing the optimized geometry within a 3.5 Å radius sphere centered over the portion of the molecule that contained the functionality of interest. Both iterations followed a geometry and energy optimization scheme identical to that used for the identification of the radical lowest energy structure.

4.3.3 Simulated Annealing

The simulated annealing (SA) method is a thermodynamic technique in which molecules or atoms start in random locations and orientations. At each step, the search randomly perturbs the coordinates or angles of molecules and then recalculates the energy. If the new energy is favorable, the perturbation is accepted. If not, the perturbation is accepted with a certain probability based on the temperature:

$$p = e^{-\Delta E / (k_B \times T)} \qquad \text{(EQ 4.1)}$$

where ΔE is the perturbed minus the unperturbed energy, k_B is the Boltzmann constant, and T is temperature in Kelvin. At the start of each run, the temperature and the probability of accepting bad perturbations is very high. The temperature decreases slowly over the course of the run. At the end, the temperature and the probability of accepting bad perturbations is very low. Essentially, simulated annealing is a slow transition between a random search and a downhill search. Theoretically, if the temperature starts high enough and drops slowly enough, the global minimum should always be found.

Geometry optimization for each of the hydroxy isoprene peroxy radicals involved bond rotations of 30° for each of the five pertinent single bonds. The methyl single bond had only 360/30/3 = 4 possible positions, for a total of $4 \times (360/30)^4 = 82\,944$ structures. A small number of these had nuclei closer than 0.7 Å and were ignored. The remainder underwent a B3LYP/6-311++G(d,p) single point calculation. From these calculations, a list of structures was created with every structure differing from every other structure in the list by an rms distance of 0.3 Å measured using a previously described distance metric.[159,160] The best 100 geometries from this list were optimized with the same method and basis set.

A simulated annealing search for the lowest energy hydroxy isoprene peroxy radical water complex began by positioning water at a random angle and position relative to the radical monomer at a distance between 0.7 and 2.5 Å. This random geometry underwent 3125 simulated annealing[159,161-168] steps using single point B3LYP/6-311++G(d,p) calculations with each step performing either a center-of-mass coordinate shift of the monomer or water in a random direction or perturbation of one of three angles on the monomer or water. Coordinate and angle perturbations started at 0.25 Å and 25°. After

200 iterations, these were decreased by multiplying each by $(0.9995)^{0.5}$ after every iteration for ending coordinate and angle perturbations of 0.1203 Å and 12.03°. During the simulation, maximum and minimum distance constraints of 0.7 and 2.5 Å were observed between the monomer and water to reduce the size of the search space. The starting simulated annealing temperature was 3000 K. After the first 200 steps, the temperature was decreased by multiplying it by 0.9995 after each step, for an ending temperature of 694.7 K. Although the ending temperature was above room temperature, the search was performed 32 times for a total of 100 000 B3LYP/6-311++G(d,p) single-point calculations for each of the 8 *β*-hydroxy isoprene peroxy radical water complexes. Since the search did not allow the internal geometries of the radical monomers or water to move, a list of structures from these 100 000 calculations was created with every structure differing from every other structure in the list by an rms distance of 0.3 Å, and the best 300 geometries from this list underwent a full B3LYP/6-311++G(d,p) geometry optimization.

4.4 Results and Discussion

4.4.1 Geometry

Searches for lowest energy β-hydroxy isoprene peroxy radicals and their complexes with water were performed using both RSS/RCS and SA methodologies. The minimum energy structures identified by these two different techniques were in good agreement with each other, suggesting that the geometries identified may indeed be global minima.

4.4.2 Isoprene Hydroxy Peroxy Radical

Isoprene is emitted largely during the day, and as a result its oxidation is initiated principally through reaction with the hydroxyl radical. Hydroxyl radical addition across

one of the isoprene double bonds results in the possibility of six distinct hydroxyl alkyl radicals being formed, see Figure 4.1. Peeters et al.[169-171] places the isomeric distribution of these OH adducts at 60% (1-OH), 30% (4-OH), 5% (2-OH), and 5% (3-OH). This distribution, within a few percent, is supported by experimental evidence[172] and is included in the master chemical mechanism (MCM).[173] Hermans et al.[174] suggests that the 1-OH* adduct collisionally stabilizes as ~50/50 *trans*/*cis*-1-OH, whereas the 4-OH* adducts gives a 30/70 *trans*/*cis*-4-OH distribution. The predominance of the 1-OH and 4-OH addition adducts can, in part, be rationalized based upon the relative stabilities of alkyl radicals in general. As can be seen in Figure 4.1, the dominance of the 1-OH addition adduct arises from the stable tertiary character of the radical, enhanced through allylic resonance between the β- and δ- carbons. The 4-OH addition adduct is next in prominence as a resonance stabilized secondary radical. The minor abundance of the 2-OH and 3-OH radicals can be easily understood on the basis of their primary radical nature.

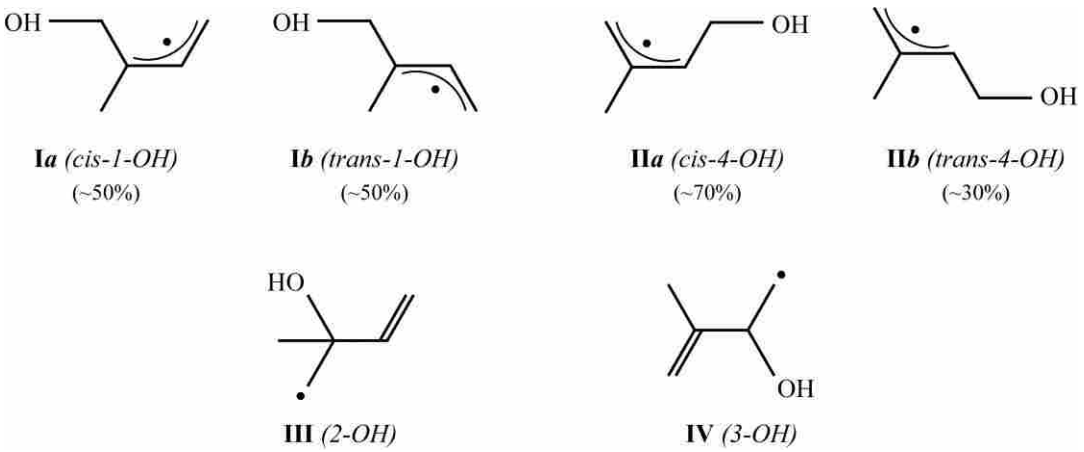

Figure 4.1. A series of six hydroxy isoprene radicals formed by the addition of an OH radical across one of the double bonds of isoprene. Isomers I and II display *cis*/*trans* isomerization that are collisionally stabilized at ~50% *trans*- (**I*a***) and ~50% *cis*- (**I*b***) and at 30% *trans*- (**II*a***) and 70% *cis*- (**II*b***)[164], respectively.

Subsequent addition of molecular oxygen leads to the formation of a series of β-hydroxy isoprene peroxy radicals, $C_5H_8(OH)O_2$, see Figure 4.2. The letters in parentheses correspond to how the different isomers are identified in this work. Addition of O_2 to the β-carbon of either **I** or **II** allows for rotation of the $-CH=CH_2$ group, uniting the contributions from cis and trans hydroxy isoprene radicals, whereas addition at the δ-OH carbon results in an trans- or cis-substituted alkene frame.

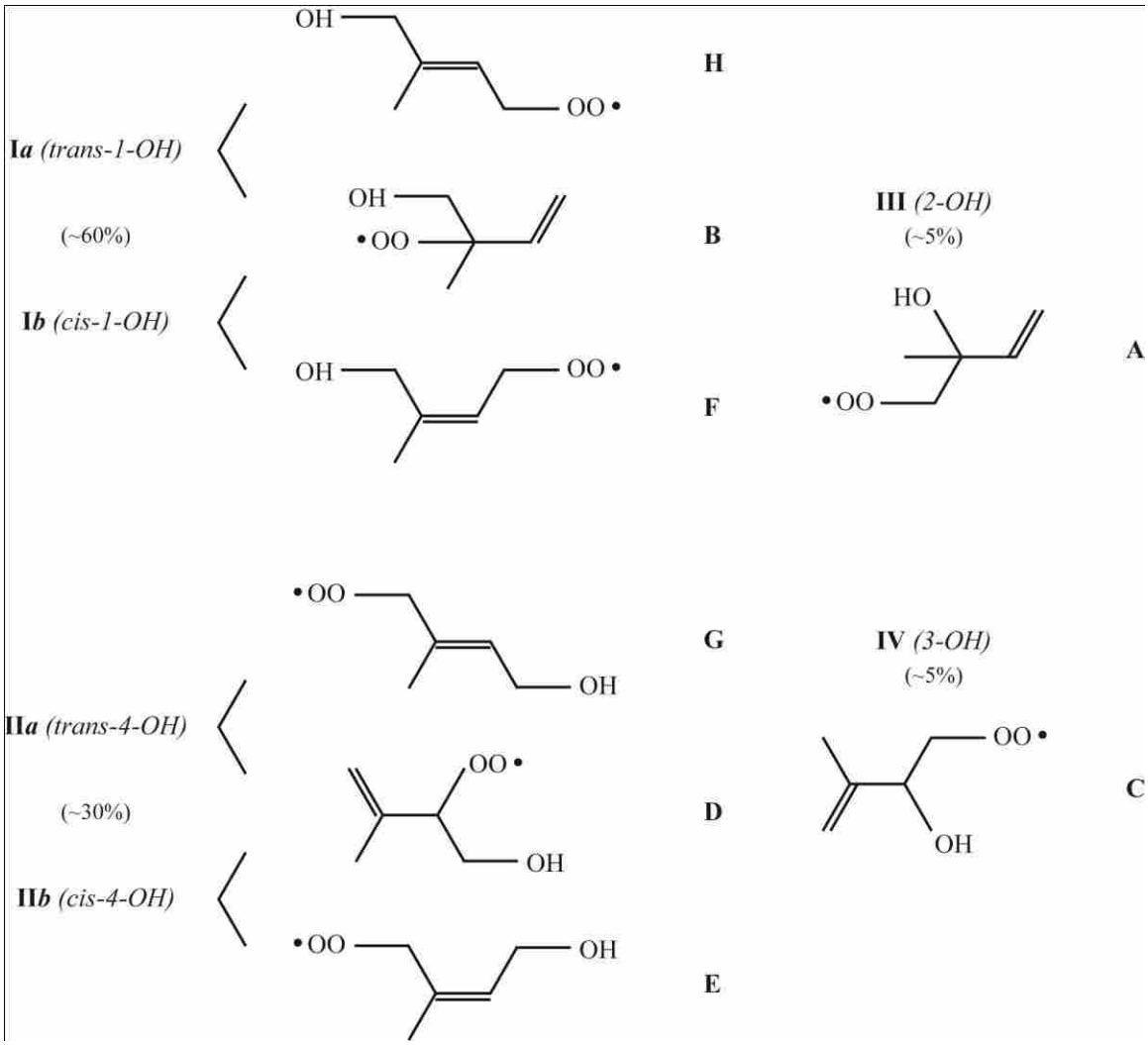

Figure 4.2. A series of eight hydroxy isoprene peroxy radicals formed by the addition of O_2 to the OH-isoprene adducts.

The addition of O_2 to the hydroxy isoprene radicals has been the generally accepted pathway followed by this family of radicals and is the pathway considered herein in relation to the formation of complexes composed of β-hydroxy isoprene peroxy radicals and water.[153,175,176] It is of note that Park et al.[172] have proposed that structures **III** and **IV** in Figure 4.1 may undergo prompt cyclic isomerization prior to the addition of O_2 and that the resulting radicals react with O_2 via hydrogen abstraction. As the overall abundance of these two isomers is low, this pathway will not be explored.

The lowest-energy conformers of the eight hydroxy isoprene peroxy radicals are shown at the left in each pairing in Figure 4.3. The β-hydroxy isoprene peroxy radical structures, optimized at the MP2(full)/6311++G(2d,2p) level, are in good agreement with those calculated in previous studies.[177,178] β-hydroxy isoprene peroxy radicals **A**-**F** are characterized by the pairing of the alcohol and peroxy moieties forming an intramolecular hydrogen bond. This arrangement is consistent with other organic peroxy radicals reported to date.[59] The proximity of the proton donor and acceptor groups of all eight radicals creates a hydrophilic zone that is capable of accepting and forming multiple strong hydrogen bonds with water molecules. The minimum-energy structure for each radical-water complex, found using the RCS method, is shown at the right of each paring in Figure 4.3, and the binding energies are tabulated in Table 4.1.

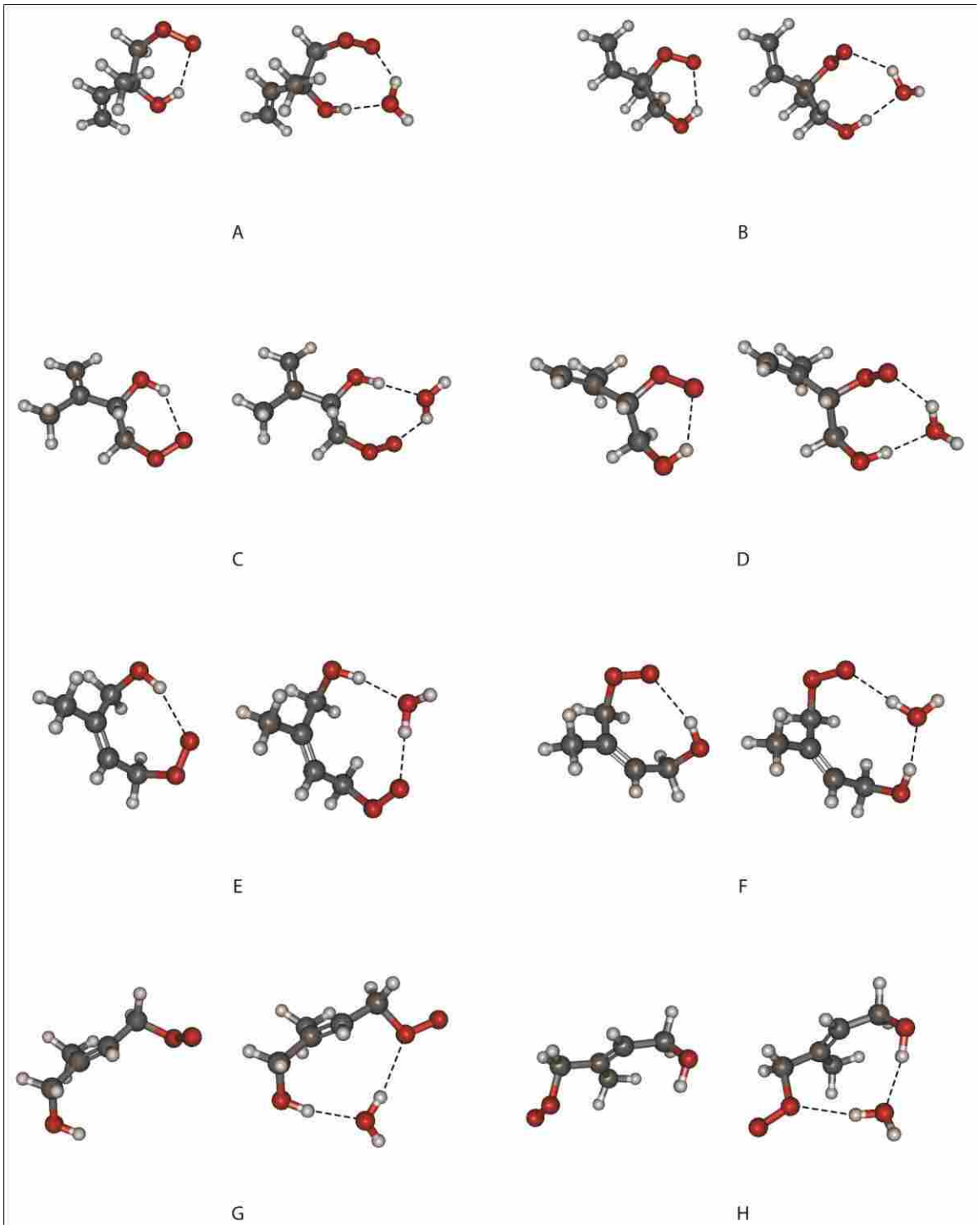

Figure 4.3. Optimized structures for the isoprene peroxy radicals and the associated water complexes as determined at the MP2(full)/6-311++G(2d,2p) level.

Table 4.1. Zero-point energy corrected binding energies for the eight β-hydroxy isoprene peroxy water comomplexes, adjusted for basis set super-position error (BSSE). Energies are in kcal/mol.

$\Delta E_{zpe,BSSE}$	mp2(full)/6311++G(2d,2p)	*//qcisd(t)/6-311++G(d,p)	*//ccsd(t)/6311++G(d,p)
A	-5.6	-5.6	-5.6
B	-5.6	-5.4	-5.4
C	-5.3	-5.3	-5.3
D	-5.8	-5.8	-5.7
E	-6.4	-6.1	-6.2
F	-6.3	-6.2	-6.2
G	-7.0	-6.8	-6.8
H	-6.5	-6.3	-6.3

* Denotes single-point calculations based on the mp2(full)/6-311++G(2d,2p) geometries.

The most notable feature of the optimized monomer structures is the formation of an intramolecular ring structure held together by classical hydrogen bonding motifs, with isomers **A**-**D** forming 6-membered rings and isomers **E** and **F** forming 8-membered rings. The proximity of the hydroxyl and peroxy groups on structures **G** and **H** are such that no intramolecular hydrogen bonding occurs. The 6-membered rings of radicals **A**-**D** all adopt the more stable chair conformation. The 8-membered rings of isomers **E** and **F** take on a structure that approximates the boat-chair conformation. Cyclo-octyl groups are conformationally among the most complex cyclic architectures owing to the existence of numerous structural forms of comparable energy, but it has been suggested that the boat-chair conformation is the most stable form.[179,180]

4.4.3 Isoprene Hydroxy Peroxy Radical-Water Complex

Complex formation results in structural perturbations to the β-hydroxy isoprene peroxy radical, suggesting that a portion of the stabilization energy arises from charge transfer (CT) processes. A useful method for describing how the electron density of the β-hydroxy isoprene peroxy radical and water molecules shifts throughout the entire integrated space defined by each newly formed complex is through electron density

difference maps. Maps for the eight hydroxy isoprene peroxy water complexes are provided in Figure 4.4, with a contour of 0.009 e/au^3 computed at the B3LYP/6-311++G(2d,2p) level. Areas of electron gain are represented by blue regions, and those of electron loss by red regions. Generally, O-H ··· O hydrogen bonds are evidenced by a region of electron density loss around the proton acceptor atom.[181] Moving along the axis of the hydrogen bond toward the bridging hydrogen atom, a region of electron density gain is then observed followed by another region of electron density loss around the bridging proton. In the context of the work presented here, each hydrogen bond interaction within complexes **A**-**H** can be demonstrated to exhibit this electron density shift pattern.

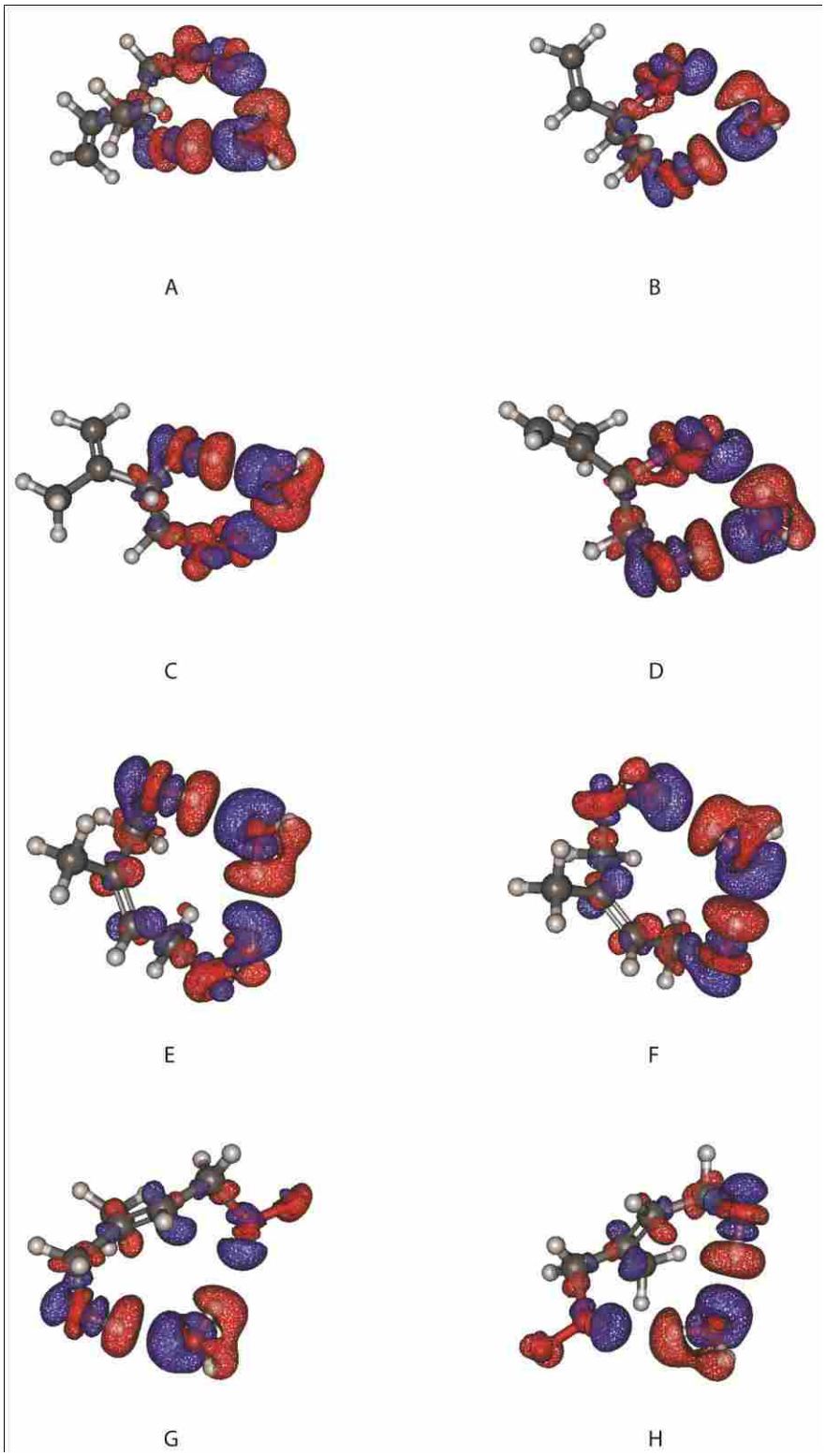

Figure 4.4. Electron density difference maps for the optimized structures. Blue represents regions of electron density gain and red regions those of electron density loss upon complex formation, relative to the isolated subunits. The contour shown is 0.0009 e/au^3, calculated at the B3LYP/6-311++G(2d,2p) level.

A survey of the optimized structures in Figure 4.3 suggests that each complex is stabilized by the formation of two intermolecular hydrogen bonds that delocalize electron density principally through Lewis-like lone pair (LP) donor NBOs to non-Lewis-like acceptor anti-bond (BD*) NBOs. The energy ($E^{(2)}$) of such stabilizing interactions can be estimated as:

$$E^{(2)} = q_i \left(\frac{\left(F_{i,j}\right)^2}{\varepsilon_j - \varepsilon_i} \right) \qquad \text{(EQ 4.2)}$$

Here, qi is the donor orbital occupancy, εj and εi are diagonal elements that describe the energy splitting (in atomic units) of the donor and acceptor orbitals, and Fi,j is the off-diagonal NBO Fock matrix element that describe the donor-acceptor interaction. Additionally, the amount of charge transferred from donor NBOs to acceptor NBOs can be approximated by:

$$Q_{CT} = q_i \left(\frac{\left(F_{i,j}\right)}{\varepsilon_j - \varepsilon_i} \right)^2 \qquad \text{(EQ 4.3)}$$

The degree to which CT happens depends upon the amount of NBOD/NBOA overlap, which can be estimated from the pre-orthogonal NBO overlap integrals (S_n), $\langle NBO_D|NBO_A\rangle$. The quantities $E^{(2)}$, Q_{CT}, and S_n are given in Table 4.2. The $E^{(2)}$ values indicate the LP(O_{water}) → BD*($O_{isoprene}$-H) to be the primary hydrogen bond interaction for complexes **A**-**D**, with an average α/β-spin summed value of ~11.02 kcal mol^{-1}. This is

consistent with an almost linear O-H ··· O bond angle of ~175° that optimizes the NBO_D/NBO_A orbital overlap. The O_{water}-H· · ·$O_{isoprene}$ bond angle in **A**-**D** is ~35° more acute, constricting effective NBO overlap by ~66% and reducing $E^{(2)}$ by an order of magnitude. This difference results in an average hydrogen bond distance that is elongated by 0.25 Å. Although weaker, this second interaction is strengthened by a small CT interaction from the lone pair electron on the terminal peroxy oxygen that contributes roughly 0.80 kcal mol^{-1} of additional stabilization energy. The similarities of these quantities for complexes **A**-**D** help to explain the similar binding energies of these structures. Whereas structures **A**-**D** have the alcohol and peroxy functionalities vicinal to each other, complexes **E**-**G** have them oriented α/*δ*. This greater separation allows the *β*-hydroxy isoprene peroxy radical to more readily accommodate the water molecule and tolerates two relatively large hydrogen bond angles, both on the order of 170°. Although the expectation is that both bonds would be roughly equivalent, a survey of Table 4.3 suggests that this is not the case. In contrast with **A**-**D**, the $O_{isoprene}$ ··· H-O_{water} appears the stronger of the two interactions and is almost solely the result of better NBO overlap. For complexes **E**-**G**, this hydrogen bond is estimated to have NBO overlap that is greater by a factor of 2 over the O_{water} ··· H-$O_{isoprene}$ interaction. This disparity results in a 0.14 Å average difference in the two hydrogen bond lengths. Although weaker, the O_{water} ···H-$O_{isoprene}$ has approximately 1.5 times better overlap than it does in **A**-**D**. The greater NBO overlap explains the larger binding energies of the α/*δ* structures compared to those oriented α/*β*.

Table 4.2. Stabilization energies, charge transfer and overlap integrals for selected $NBO_{donor}/NBO_{acceptor}$ interactions. Values calculated at the B3LYP/6-311++G(2d,2p) level. Occupancy in e, $E^{(2)}$ in kcal/mol, and Q_{CT} in a.u.

		occupancy	$\varepsilon_j - \varepsilon_i$	F(i,j)	$E^{(2)}$	Q_{CT}	$<NBO_{don.}\|NBO_{acc}>$
$LP(O_{HIP,up}) \rightarrow BD^*(OH_{water})$							
A		0.98457	0.87	0.037	0.97	0.0018	0.1039
B		0.99356	0.86	0.034	0.84	0.0016	0.0934
C		0.98457	0.87	0.035	0.87	0.0016	0.0982
D		0.98337	0.86	0.033	0.78	0.0014	0.0935
E		0.97866	0.79	0.063	3.09	0.0062	0.1903
F		0.98033	0.8	0.052	2.08	0.0041	0.1521
G							
H							
$LP(O_{HIP,p}) \rightarrow BD^*(OH_{water})$							
A	**α**	0.99605	0.83	0.028	0.59	0.0011	0.0876
	β	0.98286	0.84	0.033	0.80	0.0015	0.0930
B	**α**	0.98298	0.85	0.038	1.05	0.0020	0.1219
	β	0.98098	0.82	0.029	0.63	0.0012	0.0757
C	**α**	0.99623	0.83	0.028	0.59	0.0011	0.0859
	β	0.98278	0.83	0.032	0.76	0.0015	0.0888
D	**α**	0.99642	0.83	0.025	0.47	0.0009	0.0784
	β	0.98124	0.83	0.03	0.67	0.0013	0.0841
E	**α**	0.99355	1.29	0.048	1.11	0.0014	0.1352
	β	0.97554	0.77	0.066	3.46	0.0072	0.1958
F	**α**	0.99428	1.37	0.047	1.01	0.0012	0.1326
	β	0.97745	0.78	0.056	2.47	0.0050	0.1608
G	**α**	0.9934	1.17	0.037	0.73	0.0010	0.1169
	β	0.99259	1.14	0.039	0.83	0.0012	0.1204
H	**α**	0.99317	1.16	0.032	0.55	0.0008	0.1027
	β	0.99228	1.14	0.034	0.63	0.0009	0.1066
$LP(O_{water}) \rightarrow BD^*(OH_{HIP})$							
A	**α**	0.98703	0.94	0.091	5.46	0.0093	0.2781
	β	0.98702	0.94	0.091	5.46	0.0093	0.2779
B	**α**	0.98675	0.94	0.091	5.45	0.0092	0.2764
	β	0.98667	0.93	0.091	5.51	0.0094	0.2763
C	**α**	0.98623	0.94	0.094	5.82	0.0099	0.2845
	β	0.98623	0.94	0.094	5.82	0.0099	0.2844
D	**α**	0.98742	0.95	0.09	5.28	0.0089	0.2713
	β	0.98744	0.95	0.09	5.28	0.0089	0.2713
E	**α**	0.9896	1.06	0.086	4.33	0.0065	0.2577
	β	0.98904	1.04	0.086	4.41	0.0068	0.2572
F	**α**	0.98837	1.04	0.09	4.83	0.0074	0.2658
	β	0.98831	1.03	0.089	4.77	0.0074	0.2682
G	**α**	0.99086	1.04	0.078	3.64	0.0056	0.2362
	β	0.99083	1.04	0.078	3.64	0.5573	0.2361
H	**α**	0.99112	1.02	0.077	3.62	0.0056	0.2329
	β	0.99112	1.02	0.077	3.62	0.0056	0.2329

Table 4.3. Changes in radical and water bond lengths (ΔÅ) upon complexation. Hydrogen bond lengths (Å) and angles (deg). Based on MP2 optimized structures.

	Δr, O─H	Δr, O─Op	Δr, Ow─H1	Δr, Ow─H2	r, O─H ⋯ Ow	r, Ow─H1 ⋯ Op	Θ, O─H ⋯ Ow	Θ, Ow─H1 ⋯ Op
A	0.0057 (0.59%)	-0.0017 (0.13%)	0.0059 (0.62%)	0.0010 (0.11%)	1.895	2.124	174.634	136.099
B	0.0063 (0.66%)	-0.0039 (0.30%)	0.0055 (0.58%)	0.0008 (0.08%)	1.885	2.072	174.497	137.000
C	0.0058 (0.60%)	-0.0027 (0.21%)	0.0056 (0.59%)	0.0009 (0.10%)	1.874	2.141	176.277	136.219
D	0.0065 (0.68%)	-0.0024 (0.18%)	0.0055 (0.57%)	0.0009 (0.10%)	1.897	2.172	174.117	139.359
E	0.0023 (0.24%)	-0.0040 (0.31%)	0.0102 (1.06%)	0.0003 (0.03%)	1.898	1.919	156.368	167.301
F	0.0037 (0.39%)	-0.0069 (0.53%)	0.0086 (0.90%)	0.0006 (0.06%)	1.886	1.968	163.067	172.182
G	0.0076 (0.79%)	0.0020 (0.16%)	0.0057 (0.60%)	0.0009 (0.10%)	1.955	2.178	165.412	168.864
H	0.0054 (0.57%)	0.0017 (0.13%)	0.0054 (0.57%)	0.0012 (0.13%)	1.970	2.218	167.483	162.235

Natural energy decomposition analysis was used to estimate the contributions of charge transfer (CT), electrostatic (ES), and deformation interactions to the binding energy of each β-hydroxy isoprene peroxy radical water complex. The results are listed in Table 4.4. The amount of the stabilization energy that results from CT interactions is determined from the ratio of CT to CT + ES. For all of the β-hydroxy isoprene peroxy radical water complexes surveyed, this ratio is around 0.39, suggesting that 61% of the stabilization energy results from electrostatic interactions.

TABLE 4.4. NEDA results, reported in kcal mol^{-1}.

$\Delta E_{zpe,BSSE}$	CT	ES	CT/(CT + ES)	DEF(SE) Isoprene	DEF(SE) H_2O
A	-19.33	-30.43	0.39	20.45	22.33
B	-18.81	-27.21	0.41	18.40	20.91
C	-19.42	-28.80	0.40	19.57	21.47
D	-17.95	-27.86	0.39	19.12	19.79
E	-26.04	-36.22	0.42	28.53	24.85
F	-23.64	-32.64	0.42	25.35	23.08
G	-12.56	-22.76	0.36	`14.16	14.44
H	-13.05	-23.57	0.36	14.77	14.97

4.4.4 Thermodynamics

The enthalpy of formation for each complex was calculated. Following the procedure outlined by Ochterski[182] $\Delta H_f°$(0 K) and $\Delta H_f°$(298 K) were extracted from Gaussian 03 frequency calculations. Values of $\Delta H_f°$(298 K) are listed in Table 4.5. Heats and entropy of reaction for the formation of each water complex are also tabulated in Table 4.5. This data indicates that complexation of β-hydroxy isoprene peroxy radicals with water is enthalpically favorable.

Table 4.5. Calculated thermondynamic properties for the HIP radical water complexes.

	$\Delta E_{zpe,BSSE}$	τ	K*eq*	K*eq* $\times[H_2O]_{100\%}$	$\Delta H_{f,complex}$	ΔH_{rxn}	ΔS_{rxn}
A	-5.6	6.80E-03	1.76E-20	0.014	-5.29	-4.70	-0.03
B	-5.6	4.48E-03	1.21E-20	0.009	-5.44	-4.85	-0.03
C	-5.3	5.34E-03	1.04E-20	0.008	-5.24	-4.65	-0.03
D	-5.8	1.46E-03	3.28E-20	0.025	-5.71	-5.12	-0.03
E	-6.4	2.66E-04	9.54E-20	0.073	-6.36	-5.76	-0.03
F	-6.3	2.59E-04	6.37E-20	0.049	-6.39	-5.80	-0.03
G	-7.0	9.47E-04	2.60E-19	0.200	-5.72	-5.13	-0.03
H	-6.5	4.11E-03	1.11E-19	0.086	-5.17	-4.58	-0.03

Note: The lifetime is reported in seconds.
Keq is reported as cm^3 $molecule^{-1}$. Enthalpies and entropy are reported in kcal/mol.
All values are at 298 K.

The lifetime of each *β*-hydroxy isoprene peroxy radical water complex at 298 K was calculated according to EQ 4.1 and 4.2 Lifetimes are found in Table 4.5. The expected lifetime of *β*-hydroxy isoprene peroxy radical water complexes average around 3 ms. Such a long lifetime indicates that such complexes are likely to play a significant role in the chemistry of *β*-hydroxy isoprene peroxy radicals.

The equilibrium constants for the formation of each *β*-hydroxy isoprene peroxy radical water complex, Table 4.5, are estimated from partition functions using statistical thermodynamics. At 298 K, the equilibrium constants are calculated to be on the order of 10^{-19} cm^3 $molecule^{-1}$. The atmospheric abundance of each water complex at different relative humidity values can be expressed in terms of a ratio between complexed and uncomplexed peroxy radicals. As seen in Table 4.5, this ratio for structures **A**-**D** averages about 1.0%. The more strongly bound geometries of **E**-**H** have abundances on the order of 5.0-20.0%.

4.5 Conclusions

Understanding of the role *β*-hydroxy isoprene peroxy radicals in the chemistry of the troposphere is essential in modeling concentrations of HO_x, NO_x, HNO_3, and ozone

species. It is essential to properly recognize the importance that water vapor may have on reactions of β-hydroxy isoprene peroxy radicals with other radicals and with NO. An increase in the formation of organic nitrates as the result of complexation with water may help explain missing NO_y. The work presented here demonstrates that β-hydroxy isoprene peroxy radicals water complexes are expected to exist and have chemically relevant lifetimes.

4.6 Supplementary Material

Tables S4.1 through S4.16 represent the MP2(full)/6-311++G(2d,2p) optimized geometries and the B3LYP/6-311++G(2d,2p) harmonic vibrational frequencies of the isoprene radicals and water complexes.

4.6.1 Cartesian Coordinates for Each Optimized Geometry

Supplementary Table S4.1. MP2(full)/6-311++G(2d,2p) optimized geometries for ISOPRENE A and the ISOPRENE A and water complex.

ISOPRENE A				ISOPRENE A/H_2O			
C	-0.7067	-0.1410	-2.6832	C	-2.6985	-0.7418	-0.1545
H	-1.4101	0.6520	-2.4850	H	-2.5001	-1.4237	0.6557
H	-0.7120	-0.6108	-3.6547	H	-3.6653	-0.7668	-0.6310
C	0.1666	-0.5225	-1.7489	C	-1.7674	0.1255	-0.5514
H	0.8788	-1.3121	-1.9583	H	-1.9743	0.8134	-1.3618
C	0.2519	0.0844	-0.3747	C	-0.4024	0.2336	0.0637
O	-0.6008	1.2236	-0.3377	O	-0.3106	-0.6944	1.1259
C	-0.2532	-0.9853	0.5915	C	0.5883	-0.1462	-1.0345
H	0.2701	-1.9266	0.4534	H	0.5071	0.5109	-1.8954
H	-1.3259	-1.1150	0.4840	H	0.4808	-1.1885	-1.3081
C	1.6933	0.4838	-0.0649	C	-0.1605	1.6570	0.5569
H	1.7645	0.9251	0.9255	H	0.8304	1.7474	0.9928
H	2.3573	-0.3781	-0.1100	H	-0.2517	2.3729	-0.2566
H	2.0157	1.2162	-0.7989	H	-0.8998	1.8933	1.3152
H	-0.7992	1.3952	0.5906	H	0.5100	-0.5256	1.6156
O	0.0189	-0.6529	1.9898	O	1.9494	0.0314	-0.5402
O	-0.6619	0.3840	2.3772	O	2.5446	-1.1005	-0.3191
				O	2.1996	-0.2568	2.4299
				H	2.4362	-0.7508	3.2162
				H	2.7697	-0.5972	1.7323

Supplementary Table S4.2. MP2(full)/6-311++G(2d,2p) optimized geometries for ISOPRENE B and the ISOPRENE B and water complex.

ISOPRENE B				ISOPRENE B/H_2O			
C	0.0766	-0.5379	2.5564	C	2.3049	0.4141	-0.5724
H	1.0831	-0.8816	2.3783	H	2.0846	1.4678	-0.5349
H	-0.3305	-0.6555	3.5486	H	3.2653	0.1142	-0.9590
C	-0.6517	0.0329	1.5953	C	1.4367	-0.5039	-0.1609
H	-1.6574	0.3714	1.8127	H	1.7068	-1.5510	-0.2206
C	-0.2217	0.2398	0.1752	C	0.0788	-0.2662	0.4186
O	1.2532	0.0696	0.1925	O	-0.1557	1.1890	0.5929
C	-0.8435	-0.8519	-0.6985	C	-1.0050	-0.8409	-0.4888
H	-1.8993	-0.9140	-0.4455	H	-0.7835	-1.8996	-0.6076
H	-0.3763	-1.8010	-0.4260	H	-0.9327	-0.3685	-1.4655
C	-0.5204	1.6434	-0.3131	C	-0.0238	-0.7898	1.8355
H	-0.0527	2.3717	0.3438	H	0.6978	-0.2880	2.4726
H	-0.1594	1.7764	-1.3266	H	-1.0279	-0.6363	2.2140
H	-1.5964	1.8025	-0.3104	H	0.1908	-1.8544	1.8401
O	1.7565	-0.0498	-0.9971	O	-0.3447	1.8135	-0.5238
O	-0.7842	-0.6090	-2.0906	O	-2.2986	-0.7345	0.0604
H	0.1492	-0.5147	-2.3056	H	-2.6604	0.1332	-0.1733
				O	-3.1941	1.8823	-0.6315
				H	-2.3488	2.3369	-0.5565
				H	-3.7862	2.3511	-0.0422

Supplementary Table S4.3. MP2(full)/6-311++G(2d,2p) optimized geometries for ISOPRENE C and the ISOPRENE C and water complex.

ISOPRENE C				ISOPRENE C/H_2O			
C	-0.6082	0.6159	-0.7452	C	-0.7734	-0.3644	0.3485
H	-1.5973	0.8290	-0.3542	H	-0.6185	-1.4371	0.3926
H	-0.0188	1.5239	-0.8347	H	-0.8406	0.0780	1.3350
C	0.1319	-0.4140	0.0930	C	0.2785	0.3452	-0.4887
H	-0.3620	-1.3825	-0.0445	H	0.1973	-0.0162	-1.5186
C	0.0199	-0.0150	1.5433	C	1.6387	-0.0237	0.0429
C	1.0271	0.6079	2.1644	C	2.3495	0.8468	0.7640
H	0.9373	0.8951	3.2018	H	3.3232	0.5769	1.1432
H	1.9514	0.8120	1.6484	H	1.9722	1.8357	0.9627
C	-1.2704	-0.3714	2.2259	C	2.1365	-1.3979	-0.2975
H	-1.2891	0.0125	3.2416	H	3.1226	-1.5639	0.1236
H	-2.1367	0.0280	1.6993	H	1.4781	-2.1786	0.0779
H	-1.3936	-1.4533	2.2642	H	2.1989	-1.5258	-1.3767
O	-0.8829	0.1195	-2.0944	O	-2.0703	-0.1896	-0.2992
O	0.2105	-0.0443	-2.7778	O	-2.8656	0.5804	0.3767
O	1.4957	-0.4919	-0.2855	O	0.0864	1.7396	-0.4300
H	1.5208	-0.4711	-1.2495	H	-0.7017	1.9681	-0.9479
				O	-2.2891	2.3416	-1.8711
				H	-2.5736	3.2534	-1.9471
				H	-2.9324	1.9209	-1.2913

Supplementary Table S4.4. MP2(full)/6-311++G(2d,2p) optimized geometries for ISOPRENE D and the ISOPRENE D and water complex.

ISOPRENE D				ISOPRENE D/H_2O			
C	-1.0583	0.4424	-0.8391	C	-0.5026	-1.3339	0.6332
H	-2.0019	0.4210	-0.2996	H	-0.1414	-2.1992	0.0835
H	-0.7089	1.4761	-0.8794	H	-0.1173	-1.3939	1.6518
C	-0.0548	-0.3933	-0.0592	C	0.0469	-0.0907	-0.0418
H	-0.1917	-1.4470	-0.2905	H	-0.4808	0.1001	-0.9695
C	-0.0795	-0.1466	1.4198	C	1.5318	-0.0782	-0.2198
C	-0.3257	-1.1580	2.2480	C	2.0395	0.0509	-1.4438
H	-0.3836	-1.0029	3.3155	H	3.1059	0.0378	-1.6088
H	-0.4787	-2.1613	1.8782	H	1.4001	0.1685	-2.3050
C	0.1494	1.2635	1.8873	C	2.3820	-0.2336	1.0069
H	0.1605	1.3097	2.9721	H	3.4324	-0.1187	0.7615
H	1.0980	1.6431	1.5130	H	2.1179	0.5101	1.7548
H	-0.6329	1.9289	1.5253	H	2.2434	-1.2124	1.4603
O	-1.3253	-0.0692	-2.1332	O	-1.9107	-1.3738	0.6055
H	-0.4730	-0.1423	-2.5747	H	-2.2539	-0.7172	1.2301
O	1.3236	-0.0509	-0.4841	O	-0.3159	1.0259	0.8584
O	1.4798	-0.1392	-1.7703	O	-1.0725	1.9070	0.2827
				O	-2.8458	0.7040	2.3384
				H	-3.7851	0.8782	2.4115
				H	-2.4806	1.4655	1.8765

Supplementary Table S4.5. MP2(full)/6-311++G(2d,2p) optimized geometries for ISOPRENE E and the ISOPRENE E and water complex.

ISOPRENE E				ISOPRENE E/H_2O			
C	-0.5374	0.1155	1.0401	C	1.0754	-0.3562	-0.0727
C	-1.2433	0.0749	-0.0913	C	-0.1323	-0.9169	-0.1978
H	-2.1581	-0.5046	-0.1130	H	-0.2160	-1.8568	-0.7290
C	0.7930	0.8152	1.1625	C	1.3483	0.9215	0.6746
H	0.9030	1.2243	2.1635	H	2.0623	0.7109	1.4686
H	0.8908	1.6388	0.4570	H	0.4503	1.3207	1.1419
C	-0.9779	-0.6237	2.2681	C	2.2883	-1.0012	-0.6714
H	-0.1843	-1.2951	2.5913	H	2.8008	-0.2947	-1.3173
H	-1.1616	0.0751	3.0835	H	2.9894	-1.2839	0.1120
H	-1.8808	-1.2010	2.0917	H	2.0301	-1.8871	-1.2424
C	-0.8415	0.7106	-1.3728	C	-1.4130	-0.3995	0.3485
H	-0.1129	1.5042	-1.2639	H	-1.3838	0.6420	0.6440
H	-1.6919	1.0636	-1.9473	H	-1.8048	-1.0077	1.1583
O	1.8580	-0.1223	1.0059	O	1.9570	1.8957	-0.1612
H	1.7706	-0.4692	0.1098	H	1.2427	2.2396	-0.7151
O	-0.2305	-0.2820	-2.2909	O	-2.4777	-0.5295	-0.6676
O	0.9310	-0.6695	-1.8665	O	-2.2909	0.2611	-1.6721
				O	-0.5530	2.5099	-1.2680
				H	-1.0679	1.7328	-1.5265
				H	-0.8915	3.2308	-1.7996

Supplementary Table S4.6. MP2(full)/6-311++G(2d,2p) optimized geometries for ISOPRENE F and the ISOPRENE F and water complex.

ISOPRENE F				ISOPRENE F/H_2O			
C	-0.8735	0.1312	0.5857	C	0.6378	-0.6191	0.0575
C	-1.2311	-0.0397	-0.6838	C	-0.6454	-0.8198	-0.2576
H	-2.0750	-0.6892	-0.8857	H	-0.8604	-1.5279	-1.0486
C	0.3187	0.9463	0.9721	C	1.0575	0.2903	1.1625
H	0.1433	1.5269	1.8738	H	1.5191	-0.2527	1.9828
H	0.6991	1.5835	0.1841	H	0.2664	0.9271	1.5367
C	-1.5896	-0.5311	1.7281	C	1.7515	-1.3563	-0.6287
H	-0.9013	-1.1534	2.2989	H	2.4281	-0.6681	-1.1283
H	-1.9958	0.2132	2.4125	H	2.3415	-1.9221	0.0909
H	-2.4036	-1.1552	1.3721	H	1.3562	-2.0454	-1.3668
C	-0.5124	0.4981	-1.8874	C	-1.8666	-0.1785	0.3243
H	-0.0063	1.4380	-1.6693	H	-1.6164	0.5846	1.0612
H	-1.2187	0.6898	-2.6892	H	-2.4618	-0.9325	0.8334
O	1.4332	0.0607	1.3700	O	2.1497	1.1841	0.7329
O	1.9209	-0.5686	0.3439	O	1.7759	1.9792	-0.2143
O	0.4066	-0.4668	-2.4028	O	-2.6966	0.3510	-0.6978
H	0.9996	-0.6846	-1.6742	H	-2.1784	1.0447	-1.1307
				O	-0.7793	2.2081	-1.6260
				H	0.0518	2.0450	-1.1620
				H	-0.8326	3.1596	-1.7211

Supplementary Table S4.7. MP2(full)/6-311++G(2d,2p) optimized geometries for ISOPRENE G and the ISOPRENE G and water complex.

ISOPRENE G				ISOPRENE G/H_2O			
C	0.8309	1.0048	1.4575	C	0.8095	1.0460	1.6941
C	1.0309	2.2057	0.8976	C	1.1491	2.0264	0.8534
H	2.0462	2.5636	0.7873	H	2.1207	1.9886	0.3811
C	2.0208	0.2074	1.9113	C	1.7678	-0.0882	1.9322
H	2.9294	0.8023	1.8269	H	2.7254	0.1302	1.4587
H	1.9023	-0.0887	2.9502	H	1.9354	-0.2246	2.9980
C	-0.4959	0.3489	1.6903	C	-0.5116	0.9254	2.3866
H	-0.4510	-0.6844	1.3591	H	-0.9513	-0.0399	2.1520
H	-0.7200	0.3342	2.7557	H	-0.3661	0.9537	3.4651
H	-1.3158	0.8383	1.1783	H	-1.2149	1.7018	2.1091
O	2.1401	-1.0210	1.1887	O	1.2223	-1.3146	1.4610
H	2.2851	-0.7960	0.2666	H	0.9644	-1.1698	0.5395
C	-0.0183	3.1263	0.3912	C	0.2281	3.1085	0.4206
H	-1.0224	2.7394	0.5058	H	-0.4659	3.4344	1.1852
H	0.0550	4.1176	0.8251	H	0.7394	3.9631	-0.0045
O	0.1338	3.3049	-1.0580	O	-0.5876	2.5262	-0.6680
O	1.0936	4.1411	-1.3219	O	-1.3371	3.4223	-1.2432
				O	0.3279	-0.4253	-1.1525
				H	-0.1656	-0.8610	-1.8487
				H	-0.0546	0.4555	-1.0804

Supplementary Table S4.8. MP2(full)/6-311++G(2d,2p) optimized geometries for ISOPRENE H and the ISOPRENE H and water complex.

ISOPRENE H				ISOPRENE H/H_2O			
C	2.4477	-1.1728	3.2471	C	2.1006	-1.3781	3.0609
C	3.3509	-0.7220	4.1314	C	3.3206	-0.9856	3.4254
C	2.2345	-2.6477	3.1379	C	1.8061	-2.8406	3.0359
H	2.8151	-3.1950	3.8722	H	2.5264	-3.4272	3.5949
H	1.1877	-2.9300	3.1777	H	0.7922	-3.0941	3.3256
C	1.6049	-0.3310	2.3368	C	0.9910	-0.4971	2.5686
H	0.5569	-0.4087	2.6201	H	0.1627	-0.5055	3.2747
H	1.8847	0.7149	2.3560	H	1.3052	0.5280	2.4209
H	1.6828	-0.6896	1.3140	H	0.6116	-0.8703	1.6200
O	2.7274	-3.1182	1.8377	O	1.9397	-3.2328	1.6194
O	1.7592	-3.2977	0.9878	O	1.3660	-4.3750	1.3691
C	3.7488	0.6957	4.3741	C	3.8800	0.3972	3.3369
H	3.6232	0.9468	5.4228	H	4.3752	0.6667	4.2648
O	5.1437	0.8853	4.1134	O	4.8849	0.4404	2.3267
H	3.1469	1.3903	3.7935	H	3.1003	1.1329	3.1510
H	5.3098	0.5924	3.2144	H	4.4883	0.0727	1.5244
H	3.8871	-1.4493	4.7287	H	4.0303	-1.7455	3.7302
				O	3.4037	-0.8547	0.1661
				H	3.0605	-1.6996	0.4744
				H	3.6659	-1.0047	-0.7435

4.6.2 Harmonic Vibrational Frequencies

Supplementary Table S4.9. B3LYP/6-311++G(2d,2p) harmonic frequencies for ISOPRENE A and the ISOPRENE A and water complex.

ISOPRENE A		ISOPRENE A/H_2O	
71.2513	1152.9993	61.1248	1051.2779
106.4951	1168.8628	78.4100	1137.8684
156.1725	1230.6805	87.7019	1163.8763
229.5739	1297.0392	111.6962	1172.2634
251.1033	1335.9611	127.1895	1233.6554
293.4816	1351.9591	158.1978	1302.2567
299.3656	1389.9518	226.3882	1335.7770
363.3959	1413.2192	233.2486	1346.7057
402.1519	1450.7631	254.0542	1413.2648
430.7198	1466.7837	297.5995	1414.1919
439.2159	1497.3138	307.2275	1457.7739
526.8774	1504.4541	332.6998	1462.1979
633.0852	1699.1826	355.2651	1503.2006
679.1935	3044.6732	413.4377	1508.9324
761.4837	3082.0686	428.8815	1649.1301
869.2094	3110.2450	463.2255	1699.6894
912.4604	3129.3281	524.9418	3044.3825
957.0052	3141.7576	609.2680	3074.3070
962.5787	3147.2340	681.4386	3109.2293
982.3266	3156.9259	712.0666	3126.0147
1028.0070	3242.0947	761.1975	3140.5652
1046.1076	3748.5658	873.7410	3155.5634
1135.1593		901.5321	3159.0668
		951.0516	3241.3399
		975.3803	3620.9951
		979.6195	3736.9593
		1027.7712	3887.1542

Supplementary Table S4.10. B3LYP/6-311++G(2d,2p) harmonic frequencies for ISOPRENE B and the ISOPRENE B and water complex.

ISOPRENE B		ISOPRENE B/H_2O	
70.5139	1174.1650	40.3405	1083.8012
78.0777	1208.6665	84.2155	1138.4615
146.2402	1214.4998	99.2587	1181.9992
208.7223	1267.6683	103.8485	1190.5167
231.2972	1337.1986	174.7946	1235.6614
240.6352	1377.0056	187.5812	1291.2643
311.8125	1414.5248	203.7187	1338.7364
317.4732	1436.2086	208.1568	1391.2815
379.5784	1459.3169	223.6045	1415.6542
435.9380	1488.9698	264.5040	1460.3625
488.8890	1492.2319	300.9194	1470.4488
511.0255	1499.1518	318.2707	1485.9245
578.3701	1698.7256	325.9975	1493.7912
672.1857	3017.7023	355.3852	1503.8855
741.9152	3056.6195	409.3587	1642.2600
836.3658	3089.6697	461.9916	1699.7625
913.5918	3119.7255	527.1732	3045.3756
966.4112	3146.2404	609.3606	3056.8301
976.8896	3148.0199	674.7289	3087.7010
1027.8394	3158.4121	676.6523	3120.2653
1047.8999	3239.6141	731.8199	3140.1282
1074.0800	3782.3478	831.3971	3141.4721
1135.7488		904.9740	3156.7677
		950.0761	3237.7933
		969.6757	3632.7544
		1022.9327	3753.7445
		1050.0088	3888.5071

Supplementary Table S4.11. B3LYP/6-311++G(2d,2p) harmonic frequencies for ISOPRENE C and the ISOPRENE C and water complex.

ISOPRENE C		ISOPRENE C/H_2O	
59.6	1170.0	41.7	1084.2
62.5	1248.3	57.7	1118.8
146.4	1275.0	84.3	1174.2
166.8	1295.6	87.2	1255.1
206.3	1343.1	129.9	1281.4
268.3	1373.9	159.5	1307.0
331.6	1420.5	170.6	1338.3
361.6	1429.6	194.9	1364.0
430.5	1448.5	228.5	1421.9
471.2	1465.6	284.3	1442.2
520.7	1490.2	321.7	1457.9
548.9	1498.7	344.4	1472.7
573.8	1709.3	378.1	1491.4
732.1	2968.8	428.0	1502.1
858.7	3024.3	467.5	1647.9
894.2	3061.5	509.4	1708.5
920.3	3082.5	530.9	2983.0
959.3	3115.9	577.0	3024.5
968.7	3149.2	712.9	3061.9
1019.5	3151.5	730.1	3083.2
1047.3	3243.5	859.3	3113.9
1078.6	3747.6	879.5	3150.8
1120.1		912.8	3158.5
		954.3	3242.6
		969.7	3611.0
		1021.2	3740.2
		1058.3	3887.3

Supplementary Table S4.12. B3LYP/6-311++G(2d,2p) harmonic frequencies for ISOPRENE D and the ISOPRENE D and water complex.

ISOPRENE D		ISOPRENE D/H_2O	
55.6	1195.0	31.6	1081.3
72.7	1229.0	52.8	1097.7
131.5	1282.7	71.2	1204.8
186.1	1303.1	106.0	1246.9
190.3	1325.4	133.9	1294.9
209.4	1384.9	172.4	1304.6
303.8	1422.1	190.2	1334.9
355.9	1438.2	194.8	1399.9
405.7	1459.9	219.9	1422.7
476.7	1487.4	232.1	1457.9
519.8	1499.6	300.5	1461.7
535.3	1504.5	331.4	1488.3
542.2	1706.8	352.5	1493.6
724.0	3009.4	433.2	1505.0
804.3	3035.9	454.9	1650.1
866.1	3081.1	501.2	1702.9
954.7	3086.4	534.8	3019.2
977.6	3098.7	543.5	3036.9
995.6	3119.2	712.1	3077.9
1046.0	3142.5	724.9	3082.6
1070.1	3223.8	806.3	3118.0
1079.5	3766.5	859.7	3126.7
1086.2		949.4	3141.3
		970.4	3222.3
		997.0	3618.5
		1034.5	3741.6
		1072.7	3888.0

Supplementary Table S4.13. B3LYP/6-311++G(2d,2p) harmonic frequencies for the ISOPRENE E and the ISOPRENE E and water complex.

ISOPRENE E		ISOPRENE E/H_2O	
72.8	1195.3	27.5	1107.9
89.2	1252.1	55.8	1173.1
117.2	1283.8	90.2	1204.0
152.9	1350.1	97.2	1265.7
198.1	1370.4	151.7	1282.1
234.8	1397.4	158.5	1346.9
306.6	1415.8	183.8	1382.0
377.0	1438.6	195.6	1403.8
388.4	1482.1	214.2	1417.8
498.0	1485.5	260.9	1476.9
543.9	1495.8	269.0	1478.4
547.1	1528.0	347.4	1482.9
634.9	1706.0	397.9	1499.5
762.6	3027.2	417.9	1509.5
811.6	3031.5	502.8	1663.6
892.2	3074.4	514.8	1711.2
955.2	3086.0	549.9	3027.9
979.4	3088.7	623.4	3031.3
1033.0	3114.1	674.0	3060.3
1060.8	3138.4	778.3	3068.8
1069.1	3154.3	825.9	3085.1
1110.1	3746.7	873.4	3118.5
1167.3		955.2	3133.4
		994.5	3148.3
		1042.6	3628.2
		1063.3	3673.2
		1074.9	3888.1

Supplementary Table S4.14. B3LYP/6-311++G(2d,2p) harmonic frequencies for the ISOPRENE F and the ISOPRENE F and water complex.

ISOPRENE F		ISOPRENE F/H_2O	
78.2	1185.4	36.4	1107.2
82.2	1253.4	63.7	1175.7
119.2	1283.2	99.1	1195.8
145.9	1347.4	108.0	1264.2
194.5	1367.3	139.2	1282.6
224.8	1387.3	148.7	1346.4
304.7	1423.1	185.0	1373.2
383.2	1436.4	191.3	1401.1
426.9	1482.9	216.6	1425.4
460.4	1490.5	240.4	1471.0
506.6	1500.2	273.2	1474.4
539.9	1527.0	345.4	1487.9
635.6	1712.6	375.6	1499.8
782.5	3022.5	418.8	1508.1
820.8	3024.0	465.3	1656.2
904.8	3066.2	510.7	1713.9
954.2	3084.7	564.1	3013.6
981.8	3090.1	630.2	3026.3
1029.4	3117.1	687.9	3053.3
1054.8	3143.6	775.5	3068.0
1075.2	3155.1	842.8	3073.7
1115.6	3762.6	887.0	3119.9
1164.4		968.3	3139.9
		992.7	3148.6
		1045.6	3639.4
		1054.5	3700.8
		1082.5	3887.4

Supplementary Table S4.15. B3LYP/6-311++G(2d,2p) harmonic frequencies for the ISOPRENE G and the ISOPRENE G and water complex.

ISOPRENE G		ISOPRENE G/H_2O	
39.7	1206.5	40.5	1127.4
64.4	1232.8	46.9	1180.8
79.1	1281.8	49.9	1194.6
129.9	1341.2	82.2	1230.5
168.9	1362.3	96.8	1253.4
243.9	1401.1	124.6	1347.5
275.5	1407.7	145.3	1374.3
323.8	1426.2	156.1	1398.0
370.9	1475.4	176.9	1426.3
420.9	1484.1	254.9	1459.3
489.1	1502.3	298.4	1481.7
554.4	1506.8	311.8	1488.3
601.9	1717.0	358.6	1507.6
802.7	3026.5	403.8	1513.2
843.5	3032.2	415.7	1645.1
888.2	3074.0	438.3	1707.0
944.5	3076.1	568.3	3013.4
986.8	3087.4	599.1	3033.9
1024.1	3128.0	638.9	3067.3
1044.9	3140.6	781.2	3086.4
1064.1	3154.2	838.4	3091.3
1116.1	3823.6	912.4	3128.7
1163.1		961.2	3141.8
		978.7	3157.0
		1037.8	3673.8
		1040.3	3771.0
		1065.1	3893.8

Supplementary Table S4.16. B3LYP/6-311++G(2d,2p) harmonic frequencies for the ISOPRENE H and the ISOPRENE H and water complex.

ISOPRENE H		ISOPRENE H/H_2O	
39.4	1187.7	40.5	1118.5
68.0	1245.8	42.9	1177.8
71.9	1274.7	55.9	1204.1
142.6	1346.0	85.6	1214.1
171.5	1353.5	93.3	1260.8
238.8	1390.8	134.2	1352.1
277.9	1420.4	149.9	1362.3
328.7	1430.7	154.3	1405.2
340.5	1474.2	178.5	1428.5
437.9	1489.6	230.1	1459.8
492.8	1493.5	285.8	1487.6
538.6	1512.3	302.6	1493.2
595.5	1713.1	374.7	1499.1
808.6	3034.1	392.1	1519.3
830.2	3041.5	396.2	1645.3
902.9	3072.9	476.1	1715.5
958.8	3074.0	533.7	3027.8
984.0	3081.5	593.8	3031.7
1022.4	3132.8	623.4	3067.7
1042.7	3135.3	794.6	3071.0
1072.6	3140.8	860.0	3077.9
1121.3	3825.3	921.1	3134.0
1163.8		952.2	3139.8
		993.9	3140.0
		1034.6	3680.3
		1044.8	3775.1
		1073.1	3893.7

CHAPTER 5: COMPUTATIONAL STUDY OF E-2-HEXANAL PEROXY RADICAL-WATER COMPLEXES

5.1 Abstract

Herein is reported the results of an *ab initio* study on a family of hydroxy peroxy radical-water complexes that are formed from the oxidation of E-2-hexenal, which constitutes an important component of biogenic atmospheric emissions. Binding energies for the β-hydroxy-γ-peroxy hexanal (β- and γ-positions are relative to the carbonyl) radical water complex and the γ-hydroxy-β-peroxy hexanal radical water complex are predicted to be to 3.8 kcal mol^{-1} and 3.6 kcal mol^{-1}, respectively, computed at the MP2/6-311++G(2d,2p)//B3LYP/6-311++G(2d,2p) computational level. Natural bond orbital (NBO) reveals that conventional hydrogen bonding between the water and the hydroxy and aldehyde functional groups of the radical are primarily responsible for the stability of the complex. It can be shown that the peroxy moiety contributes very little to the stability of the radical-water complexes. Thermochemistry calculations reveal estimated equilibrium constants that are comparable to those recently reported for several hydroxy isoprene radical water complexes. The results of this report suggest that the hexanal peroxy radical-water complexes are expected to play a significant role in the complex chemistry of the atmospheric.

5.2 Introduction

Organic peroxy radicals are formed from the oxidation of hydrocarbons under atmospheric conditions and they represent an important class of intermediates leading to the formation of tropospheric ozone and nitrogen oxides (NO_x), demonstrated below:

$$RO_2 + NO \rightarrow RO + NO_2 \quad (5.1)$$

$NO_2 + h\nu \rightarrow NO + O$ (5.2)

$O + O_2 \rightarrow O_3$ (5.3)

A number of studies have both theoretically predicted the presence of peroxy radical-water complexes and confirmed their existence in the laboratory. The simplest of these, the $HO_2{-}H_2O$ complex, was first detected in a supersonic jet using Fourier transform microwave (FTMW) spectroscopy.[49] Using high level *ab initio* calculations, Francisco et al. reported the binding energy (-6.9 kcal mol^{-1} for the complex) for the $HO_2{-}H_2O$ complex with the associated minimum energy structure.[18] Kinetic studies using laser flash photolysis coupled with UV time-resolved absorption spectroscopy have demonstrated that the HO_2 self-reaction rate increases in the presence of water vapor.[183] It is speculated that the measured increase in the reaction rate coefficient is due to the formation of the $HO_2{-}H_2O$ complex as one step in the reaction mechanism. This result is complemented by turbulent flow reactor experiments that demonstrate rate enhancement for the $NO + HO_2 \rightarrow HNO_3$ reaction in water vapor.[184] A similar rate enhancement is also observed for the HO_2 self-reaction in the presence of CH_3OH and NH_3, but not CH_4,[16,50,52] suggesting that such enhancements are likely the result of O−H···O or N−H···O hydrogen bond interactions between the radical and the interacting species.

The role of the $HO_2{-}H_2O$ complex has also been found to play an important part in the chemistry of other atmospheric systems. The $HO_2{-}H_2O$ complex is thought to play a role in the reaction of HO_2 with NO. Turbulent flow reactor experiments have been reported that demonstrate an enhancement of the HNO_3 production channel of the $NO + HO_2 \rightarrow HNO_3$ reaction in the presence of water vapor.[184] The results further indicate that the obtained branching fraction of the HNO_3 forming channel increases from ~0.2% to

~7%. $HO_2{-}H_2O$ has also been investigated in the context of the SO_3 + HO_2 reaction.[185] The primary product of this reaction is the formation of the HSO_5 radical. In the presence of water vapor, the product channel is reported to shift towards the formation of H_2SO_4, which accounts for ~66% of the products formed. Additionally, *ab inito* methods employed by Long et al.[186] predict that the $HO_2{-}H_2O$ complex serves to lower the decomposition barrier of CF_3OH in the atmosphere from 45.7 kcal mol^{-1} to ~0. The rate constant calculated from this work suggests that the decomposition of CF_3OH by $HO_2{-}H_2O$ is the main sink for this molecule in the atmosphere.

Computational studies clarify the nature of these specific interactions. Recent computational results by Clark et al. suggest that many methyl- and ethyl-sized peroxy radicals exhibit binding energies between -2.5 kcal mol^{-1} and -5.1 kcal mol^{-1} with water vapor.[59] These strong binding energies are traced to the formation of hydrogen bonds between the radical's peroxy- and hydroxy- moieties and water, as well as surprisingly strong CH-O interactions between the radical and water that contribute up to 36% of the overall stabilization energy.[59]

Using the previous studies as a foundation, theoretical investigations have focused on larger organic molecules that play essential roles in atmospheric chemistry. In recent work, Clark et al. reported the binding energies and minimum energy structures for six different hydroxy isoprene peroxy (HIP) radicals that form complexes with water, with binding energies ranging from 3.9 to 5.7 kcal mol^{-1}.[187] Using a combination of the binding energies and NBO analyses, they hypothesized that water complexation could potentially perturb the kinetics and product branching ratios of reactions involving these species. Their results showed that larger molecular weight organic peroxy radicals could

form complexes with water in much the same way that smaller radicals such as HO_2 can complex with water.

While isoprene is the single greatest non-methane biogenically emitted hydrocarbon, many other large organic peroxy radicals are present at significant quantities in the atmosphere. One of these species is E-2-hexenal (E2HEX), a natural product of trees, algae and other vegetation, as well as a common flavor additive in the food industry.[188] Global volatile organic carbon (VOC) emissions studies estimate that 1,150 Tg of biogenic VOC emissions are produced annually, with 10-50 Tg C of this being 2-E-hexanal.[146,189] For a complete understanding of the effect of atmospheric processes involving organic peroxy radicals, the effects of water vapor upon the derivatives of E2HEX should not be ignored.

As with isoprene, we expect the first step in the photo-oxidation of E2HEX under atmospheric conditions to be addition of an OH radical to the double bond.[187] The hydroxylated 2-(E)-hexenal radical then reacts with O_2 to form a family of β-hydroxy peroxy radicals. The general mechanism is described below:

$$OH + C_5H_9CHO \rightarrow C_5H_9(OH)CHO \quad (5.4)$$

$$C_5H_9(OH)CHO + O_2 \rightarrow C_5H_9(OH)(O_2)CHO \quad (5.5)$$

Addition of the OH radical can occur on carbons 2 or 3, and the subsequent addition of the peroxy moiety on the opposing carbon results in two chiral centers that may be in either rectus (R) or sinister (S) orientations, resulting in the formation of a family of eight isomers. A second mechanism, although with a much smaller yield, suggests that the OH

radical may participate in organic radical formation through hydrogen abstraction,[190] as shown below:

$$OH + C_5H_9CHO \rightarrow C_5H_9CO + H_2O \quad (5.6)$$

While the present work does not rule out the possibility of this mechanism, the examination of this species will be left to further study. Certainly, comparisons between mechanisms would provide some insight as to the relative abundances of each radical species.

The aim of the present work is to demonstrate to existence of E2HEX-H_2O complexes and evaluates the effect of complexation on two representative β-hydroxy peroxy radical isomers derived from E2HEX. The optimized radical geometries and complex binding energies for both isomers are presented.

5.3 Methods

The Gaussian 03, Revision D.0110 suite of programs[63] was used to carry out geometry optimizations, vibrational frequency calculations, and high level configuration interaction molecular energy calculations. The geometry for each radical and radical-water complex was fully optimized at the B3LYP/6-311++G(2d,2p) computational level. The energy of the optimized structures were refined at the MP2(full)/6-311++G(2d,2p) level. Harmonic vibrational frequency calculations performed at the B3LYP/6-311++G(2d,2p) level established each structure as a minimum and allowed for the correction of zero-point energy.

The robust systematic searching method of Clark et al.[187] was used to identify the lowest energy structure for the two hexanal radical isomers (2-hydroxy-3-peroxy hexanal and 2-peroxy-3-hydroxy hexanal radicals). The lowest energy structures of interest in this work were identified by rotating bonds C1—C2, C2—C3, C2—O2(OH), and C3—OH(O2) by 90°, and by rotating bond C3—C4 by 180°. These rotations amounted to 512 unique structures ($[360/90]^4 \times 2$) for each peroxy radical. Structures having nuclei closer than 0.5 Å were ignored. As with Clark et al., the initial optimizations were performed using the HF/6-31G (d,p) method and basis set, followed by further refinement at the B3LYP/6-311++G(d,p) level. The geometry of the 50 lowest energy structures were further refined at the B3LYP/6-311++G(2d,2p) level, and the lowest structure of this group was taken to be the global minimum. Upon identifying the lowest energy geometry of each radical, the optimal complexation arrangement with water was determined using the random constrained sampling method of Clark et al., where 2000 random radical-water complexes were generated within a 3.5 Å sphere around the aldehyde end of each radical. These complex geometries were then optimized at successively higher methods and basis sets, similar to the process illustrated above, until a lowest energy complex geometry was identified for each radical species. Basis set superposition error (BSSE) was corrected for using the counterpoise procedure.

The optimized geometries and harmonic vibrational frequencies are given in supplementary Tables S5.1-S5.4.

Electron density maps with a surface resolution of 0.001 e/au^3 were generated at the MP2(full)/6-311++G(2d,2p)//B3LYP/6-311++G(2d,2p) level for both radical−water complexes. Subtraction of the electron density map computed for the complex from maps

for the radical and water alone produced an electron density difference map that reveals the presence of significant electron density shifts that take place upon complexation.

A natural bonding orbital (NBO) analysis is instrumental in examining specific intermolecular interactions associated with complex stability. NBO interactions are characterized by donor-acceptor relationships, in which a Lewis-like donor NBO (e.g., lone pair) donates electron density to a non-Lewis-like acceptor NBO (e.g., anti-bonding orbital). The energy of stabilization, $E^{(2)}$, that arises from electron delocalization can be estimated by 2nd-order perturbation theory that gives a 2nd-order energy, $E^{(2)}$, associated with this interaction may be calculated as:

$$E^{(2)} = q_i \left(\frac{\left(F_{i,j}\right)^2}{\varepsilon_i - \varepsilon_j} \right) \qquad \text{(EQ 5.1)}$$

where q_i is the donor orbital occupancy, ε_i and ε_j are the diagonal Fock matrix elements describing the energy of the donor and acceptor orbitals, and $F_{i,j}$ is the off-diagonal Fock matrix element describing the energy of interaction between the donor and acceptor orbitals. The 2nd-order perturbation correction for the α- and β-spin orbital components of a given interaction may be summed to provide a reasonable estimate of the interaction energy. $E^{(2)}$ is directly related to the overlap integral Si,j = $\left\langle NBO_{i,donor} \middle| NBO_{j,acceptor} \right\rangle$ that is estimated from the corresponding pre-orthogonal NBO, (P)NBO, matrix element. In the present work, NBO calculations were conducted at the MP2(full)/6-311++G(2d,2p)//B3LYP/6-311++G(2d,2p) level of theory using the Firefly software package[78] implementation of NBO 5.0.[77]

Thermochemistry data for the radical-water complexes may be extracted from calculated harmonic oscillator frequencies through a standard statistical mechanical treatment.[144,182] Frequencies for the complexes were calculated at the B3LYP/6-311++G(2d,2p) level and were used to calculate the values of ΔH_{rxn}, ΔS_{rxn}, and ΔG_{rxn} of radical−water complex over the 220 K to 300 K temperature range.

5.4 Results and discussion

5.4.1 β-hydroxy peroxy hexanal radicals

Analysis of the original eight β-hydroxy peroxy hexanal radical conformers, shown in Figure 5.1, led to the identification of the 2-hydroxy-3-peroxy hexanal (2h3pHEX) and the 2-peroxy-3-hydroxy hexanal (2p3hHEX) radicals. Both 2h3pHEX and 2p3hHEX were chosen to represent the lowest energy structure of each group of four optical isomers. The minimum energy radical-water complex for 2h3pHEX and 2p3hHEX was then identified. The B3LYP/6-311++G(2d,2p) optimized geometries of each radical and radical-water complex are shown in Figure 5.2. The binding energies of 2h3pHEX and 2p3hHEX, corrected for zero-point error and basis set superposition error, are shown in Table 5.1.

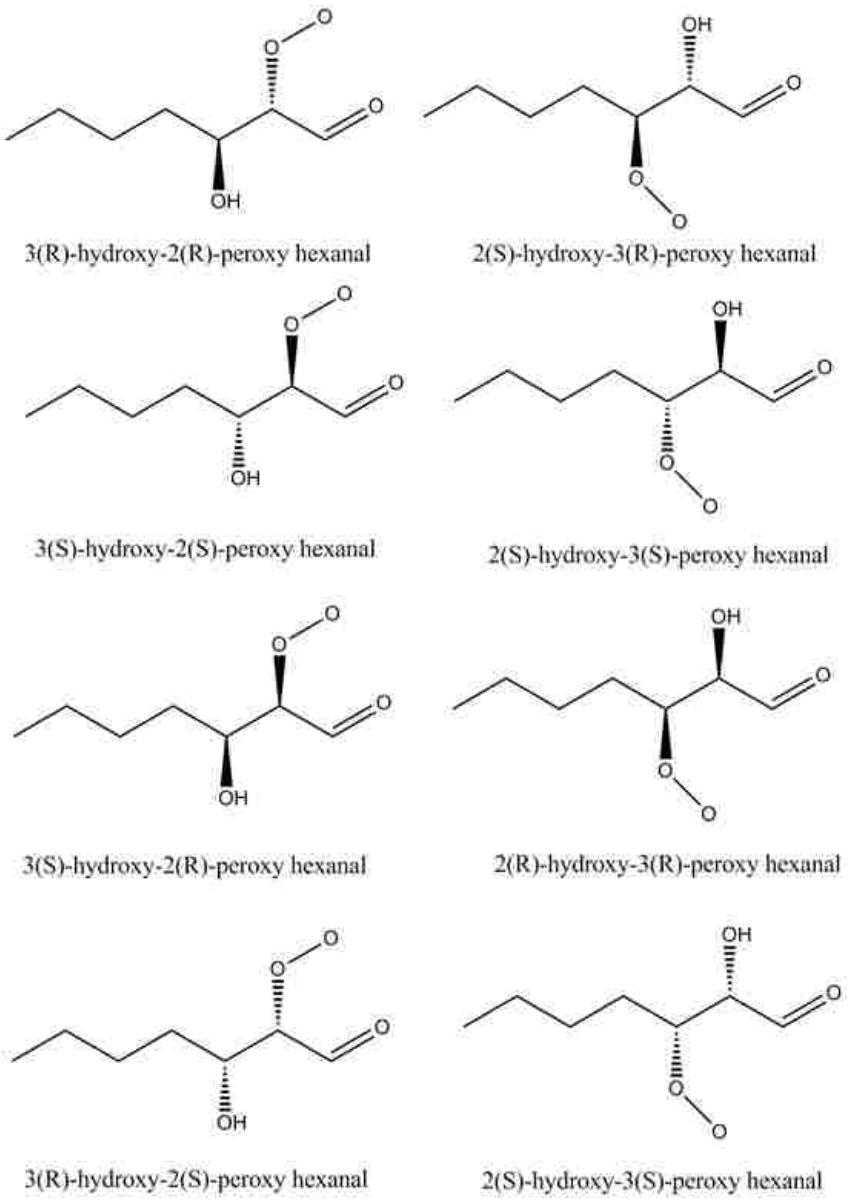

Figure 5.1. Representations of eight possible conformers formed upon serial addition of OH radical and O_2 to 2-E-hexenal. The existence of two chiral center carbons produces a set of four enantiomers with orientations of (R, R), (R, S), (S, R), and (S, S) for both 2h3pHEX and 2p3hHEX radicals.

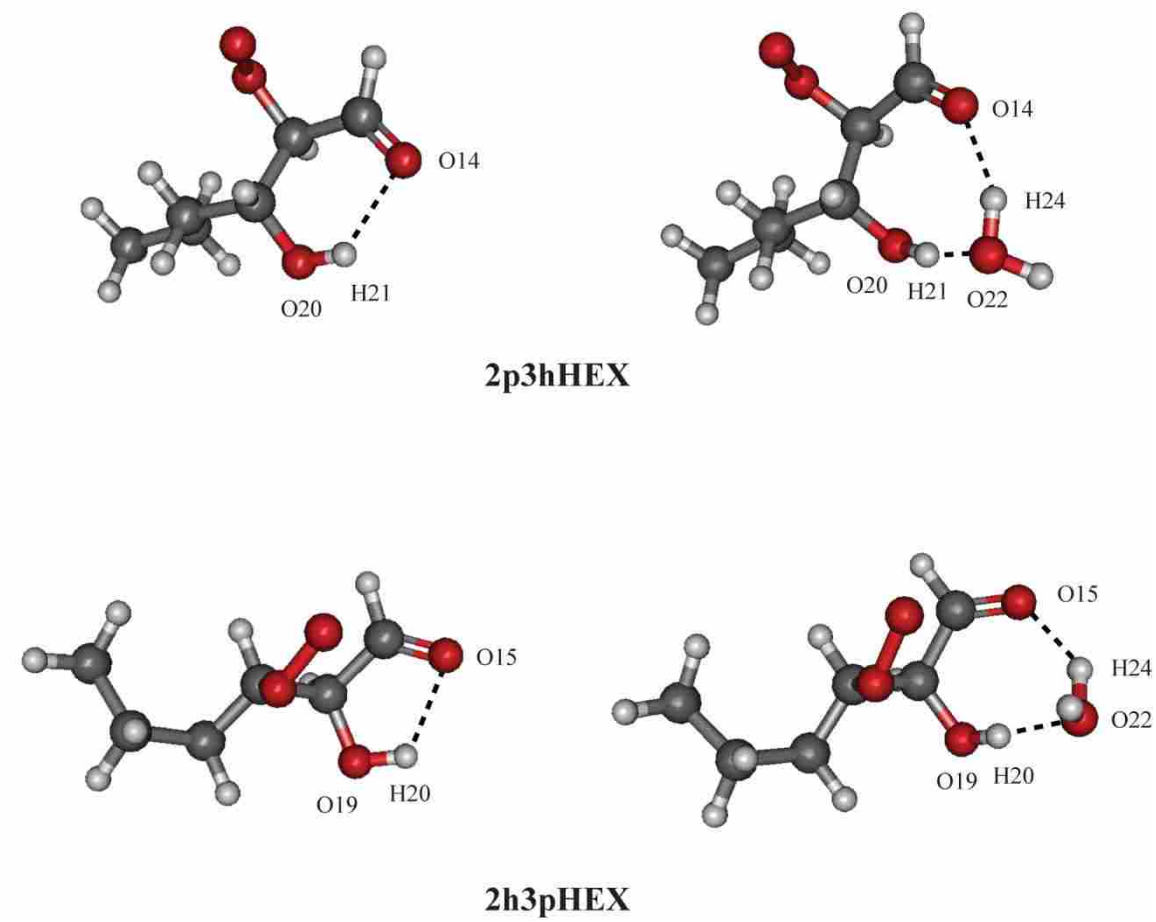

Figure 5.2. Optimized geometries of the 2p3hHEX and 2h3pHEX and the associated water complexes as determined at the B3LYP/6-311++G (2d,2p) level.

Table 5.1. Zero point energy (ZPE) corrected binding energies of hydroxy peroxy hexanal-water complexes, adjusted for basis set superposition error (BSSE).

	ΔE, kcal/mol				
Complex	ZPVE	BSSE	B3LYP/*	MP2(full)/*	MP2(full)corr
2p3hHEX + H_2O	120.6				0.0
2p3hHEX−H_2O	122.6	2.0	- 6.0	- 7.8	- 3.8
2h3pHEX + H_2O	120.6				0.0
2h3pHEX−H_2O	122.6	2.2	- 6.1	- 7.8	- 3.6

* Denotes 6-311++G(2d,2p).

Complex formation results in structural perturbations to the 2p3hHEX and 2h3pHEX peroxy radical, suggesting that a portion of the stabilization energy arises from

charge transfer (CT) processes. A useful method for describing how the electron density of each radical delocalizes throughout the entire integrated space defined by the newly formed complex is through electron density difference maps. Maps for the two radical-water complexes discussed here are shown in Figure 5.3, each with a contour of 0.001 e/au^3, computed at the MP2(full)/6-311++G(2d,2p) level. Blue regions represent areas of electron gain, while those of electron loss by red regions. Generally, O-H···O hydrogen bonds are indicated by a region of electron density loss around the proton acceptor atom.[181] Moving along the axis of the hydrogen bond toward the bridging hydrogen atom, a region of electron density gain is then observed followed by another region of electron density loss around the bridging proton. As seen from the electron density shift patterns in Figure 5.3, two principal H-bonds are present. The first exists between the O atom of H_2O (donor) and the hydroxy function group of the peroxy radical (acceptor). The second is between the aldehyde oxygen atom (donor) and one of the O−H bonds of water. The hydrogen bond lengths and angles of each interaction are listed in Table 5.2. The formation of these new H-bonds breaks the weak interaction that exists between the O−H moiety and the aldehyde in the monomer by rotating the OH proton out of the CCOH plane by ~45° to accommodate the H_2O molecule.

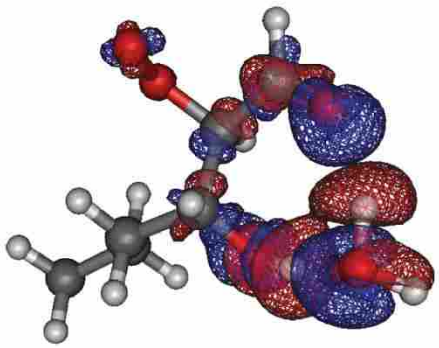

2p3hHEX

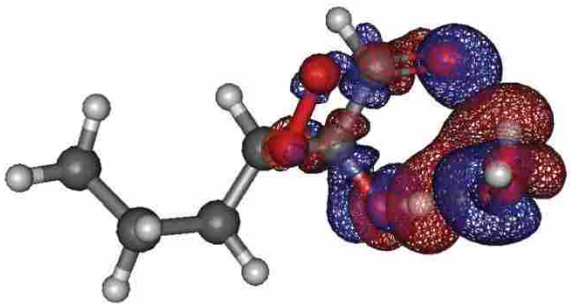

2h3pHEX

Figure 5.3. Electron density difference maps for 2p3hHEX and 2h3pHEX, with a contour of 0.001 *e*/au^3 calculated at the UMP2(full)/6-311G++(2d,2p) level. Blue shaded regions represent areas of electron density gain, and red shaded regions represent areas of electron loss, relative to the isolated subunits.

Table 5.2. Hydrogen bond lengths and angles for 2p3hHEX and 2h3pHEX and the associated water complexes.

Complex	Interaction	*r(H···O)*, Å	θ(OHO), deg
2p3hHEX	O20−H21···O14	2.082	132.4
2p3hHEX−H_2O	O20−H21···O14	2.844	98.3
	O20−H21···O22	1.844	168.8
	O22−H24···O14	1.955	151.6
2h3pHEX	O19−H20···O15	2.052	118.1
2h3pHEX−H_2O	O19−H20···O15	2.587	93.6
	O19−H20···O22	1.831	170.3
	O22−H24···O15	2.020	143.2

The O···H−O interactions of the monomers can be described as a weak hydrogen-bonding interaction, with bond lengths that are ~5% (0.1 Å) longer than that found in the H_2O-dimer and with bond angles that are strongly acute (i.e. angles that are closer to 90° than 180°). Although the bond lengths for the original hydrogen bonds are close in magnitude, the bond angles differ markedly. As seen in Figure 5.1, this is the result of the proximity of the hydroxyl group to the carbonyl oxygen. The placement of OH is in the α-position for 2h3pHEX and is in the β-position for 2p3hHEX. Upon complexation, the nascent hydrogen bonds are replaced by stronger interactions that have shorter bond lengths and bond angles that are closer to the ideal value of 180°. Second-order perturbative estimates, $E^{(2)}$, of the stabilization energy of each hydrogen-bond are listed in Table 5.3. In addition, the values of the (P)NBO overlap integrals, which give a measure of the extent of donor NBO and acceptor NBO overlap, are also listed. This data indicates that the hydrogen-bond between the water oxygen and the hydroxyl functionality of the radical forms the strongest interaction of the two newly formed H-bonds. The data also indicate that, while present, the second hydrogen bond interaction

between the carbonyl oxygen and the water molecule is fairly weak, providing ~1 kcal mol^{-1} of stabilization energy. The magnitude of this interaction accounts for approximately 70 % of the stabilization energy lost upon cleavage of the O−H···O_{ald} interaction originally present in the monomer. It can be concluded that the stability of the 2p3hHEX−H_2O and 2h3pHEX−H_2O complexes arises principally from the radical−OH···O_w hydrogen bond. The values of the binding energies for these complexes, 3.8 kcal mol^{-1} and 3.6 kcal mol^{-1}, may appear low, but they are a reflection of the balance between the stabilization lost from the monomer and that gained by the presence of water upon complex formation.

Table 5.3. The $E^{(2)}$ and $S_{n\sigma}$* descriptors of the hydrogen bonds in 2p3hHEX and 2h3pHEX radicals and the associated water complexes.

Complex	Interaction	$E^{(2)}$, kcal mol^{-1}	$S_{n\sigma}$*
2p3hHEX	O20−H21···O14	1.43	0.1388
2p3hHEX−H_2O	O20−H21···O14	–	–
	O20−H21···O22	6.95	0.2732
	O22−H24···O14	1.01	0.1141
2h3pHEX	O19−H20···O15	1.48	0.1482
2h3pHEX−H_2O	O19−H20···O15	–	–
	O19−H20···O22	7.78	0.2844
	O22−H24···O15	1.07	0.1186

Interestingly, the electron density difference maps, Figure 5.3, indicate a lack of significant intermolecular interactions between the water and the peroxy moiety in either of the 2h3pHEX or 2p3hHEX radicals. While small electron density shifts are evident in the O-O-C region of the radical, there is no significant interaction observed between these shifts and those associated with the two primary hydrogen bonds. The NBO analysis

indicates that the peroxy moiety plays no role in the overall stability of the radical-water complexes, which is in stark contrast with interactions observed in HIPs and smaller organic peroxy radical complexes where the peroxy moiety plays a central role complex stabilization. It is of note that smaller peroxy radicals containing an aldehyde group, such as the acetyl and acetonyl peroxy radicals also indicate a lack of interaction between the carbonyl carbon and the peroxy functionalities (see Chapter 3 for more details), indicating that the optimized radical structures presented here should not be considered out of the common way.

5.4.2 Thermochemistry

The relevance of the 2p3hHEX and 2h3pHEX complex systems at atmospherically relevant temperatures is analyzed through thermochemical calculations. The resulting data are presented in Table 5.4.

Table 5.4. Thermodynamic properties, ΔHrxn, ΔSrx , and ΔGrxn, calculated for the formation of the 2p3hHEX−H_2O and 2h3pHEX−H_2O complexes at the B3LYP/6-311++G(2d,2p) level.

TEMP, (K)	ΔH_{rxn}, (kcal mol^{-1})	ΔS_{rxn}, (cal mol^{-1} K^{-1})	ΔG_{rxn}, (kcal mol^{-1})
2h3pHEX−H_2O			
220	-4.51	-0.03	-4.51
230	-4.50	-0.03	-4.50
240	-4.49	-0.03	-4.48
250	-4.47	-0.03	-4.47
260	-4.46	-0.03	-4.45
270	-4.44	-0.03	-4.43
280	-4.42	-0.03	-4.41
290	-4.40	-0.03	-4.40
300	-4.38	-0.03	-4.37
2p3hHEX−H_2O			
220	-4.51	-0.03	-4.51
230	-4.50	-0.03	-4.50
240	-4.49	-0.03	-4.48
250	-4.47	-0.03	-4.47
260	-4.46	-0.03	-4.45
270	-4.44	-0.03	-4.43
280	-4.42	-0.03	-4.41
290	-4.40	-0.03	-4.40
300	-4.38	-0.03	-4.37

As expected, complex formation requires a loss of entropy as the radical and the H_2O molecule form a stable bound complex. The loss of entropy is minor, amounting to ~0.03 kcal mol^{-1} K^{-1}. It is also apparent from the data in Table 5.4 that the formation of both complexes is enthalpically favored over the temperature range of interest. The magnitude of the Gibb's free energy at each temperature point indicates that the formation of 2h3pHEX−H_2O and 2p3hHEX−H_2O can readily occur.

Useful information regarding the atmospheric abundance of these peroxy radical−water complexes at different values for the relative humidity can be obtained in terms of a ratio between complexed and uncomplexed peroxy radicals by multiplying the equilibrium constant by the relevant [H_2O] concentration, as shown in EQ 5.2:

$$K_{eq}[H_2O] = \frac{[RO_2 \cdot H_2O]}{[RO_2]} \qquad \text{(EQ 5.2)}$$

The equilibrium constant for the formation of each complex and the $K_{eq}[H_2O]$ ratio are tabulated in Table 5.5 and the results of (EQ 5.2) are displayed in Figure 5.4, which shows a plot of this ratio as a function of temperature at 100% humidity.

Table 5.5. Equilibrium constants and the $K_{eq}[H_2O]$ ration calculated for the formation of the 2p3hHEX−H_2O and 2h3pHEX−H_2O complexes at the B3LYP/6-311++G(2d,2p) level.

TEMP, (K)	K_{eq}	K_{eq}*[H2O](RH=100%)
2h3pHEX−H_2O		
220	1.46E-20	1.68E-05
230	8.11E-21	2.56E-05
240	4.76E-21	4.00E-05
250	2.92E-21	6.55E-05
260	1.86E-21	1.03E-04
270	1.23E-21	1.57E-04
280	8.42E-22	2.19E-04
290	5.92E-22	2.87E-04
300	4.27E-22	3.68E-04
2p3hHEX−H_2O		
220	3.87E-20	4.46E-05
230	2.18E-20	6.87E-05
240	1.29E-20	1.08E-04
250	7.97E-21	1.79E-04
260	5.13E-21	2.84E-04
270	3.42E-21	4.37E-04
280	2.36E-21	6.12E-04
290	1.67E-21	8.09E-04
300	1.21E-21	1.04E-03

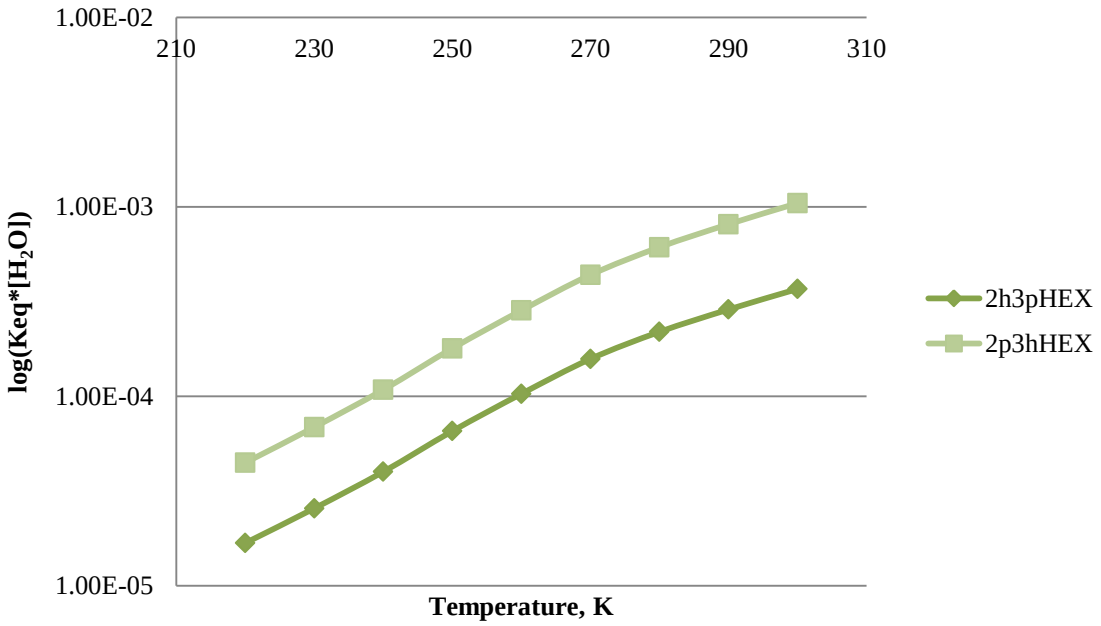

Figure 5.4. The ratio of [radical−H_2O]/[radical] as calculated for 2h3pHEX and 2p3hHEX at the B3LYP/6-311++G(2d,2p) level. The water concentration used was that that exists at a relative humidity of 100% at the included temperatures.

As expected, the relative abundance of the complex increases relative to the uncomplexed peroxy radical as the abundance of atmospheric moisture increases with temperature. The K_{eq}*[H_2O] ratio values are indicative of other peroxy−water systems, such as the methyl peroxy, ethyl peroxy, and the acetyl peroxy radicals, See Chapter 3. One noticeable difference between the 2h3pHEX−H_2O and 2p3hHEX−H_2O complexes and those mentioned from Chapter 3 is the larger corrected binding energies, ~1 kcal mol^{-1}, of the E2HEX derived peroxy radicals. The larger binding energies can be attributed to the presence of the hydroxyl group and not the carbonyl. In addition, the extra carbon bulk of the E2HEX peroxy radicals distant from the hydrogen bonding region seems to play no role in the stabilization of RO_2 radicals. When the logarithm of the K_{eq}*[H_2O] ratio is plotted against temperature an almost linear relationship is

observed. This is in line with the water vapor concentration increasing exponentially with warming temperatures. Many atmospheric modeling studies have ignored the water influence on RO_2 abundances and RO_2 chemistry. If the presence of water can be shown to perturb either of the reaction rate constant of any reactions involving 2h3pHEX or 2p3hHEX or any of the resulting product branching ratios, the formation of these complexes will be important in our understanding of atmospheric oxidative pathways. While experimental studies will be necessary to corroborate these theoretical findings, it is anticipated that these complexes will play a primary role in the atmospheric stability of hydroxy-peroxy hexanal radicals.

5.5 Conclusions

Owing to the significant contribution of 2-(E)-hexenal to the total biogenic VOC emissions in the atmosphere, the contribution of radicals derived from this species is an important step toward understanding tropospheric chemistry. This work demonstrates an expected binding energy between hydroxy peroxy hexanal radicals and water that is comparable with previous organic radical studies. Primary intermolecular interactions within the complex are attributed to hydrogen bonds between water and the hydroxy and aldehyde moieties of the radical, with the peroxy group playing only a slight role in complex stability. The additional carbon bulk of the 2h3pHEX and 2p3hHEX radicals seems to play no part, for good or bad, in the stabilization of the radicals, indicating that binding motifs identifies for smaller RO_2 radicals are relevant to larger molecular weight peroxy radicals. Thermochemical calculations demonstrate that the formation of these complexes is favorable, with the Gibb's free energy of formation in excess of 4 kcal mol^{-1}, and that they are likely to exist at all of the atmospherically relevant temperatures

studied. The ratio of complexed radical to non-complexed radical is similar to less functionalized smaller RO_2 radicals that have been studies previously.

5.6 Supplementary Material

Tables S5.1 through S5.4 represent the B3LYP/6-311++G(2d,2p) optimized geometries and the B3LYP/6-311++G(2d,2p) harmonic vibrational frequencies of the 2h3pHEX and 2p3hHEX radicals and radical−water complexes.

5.6.1 Cartesian Coordinates for Each Optimized Geometry

Supplementary Table S5.1. B3LYP/6-311++G(2d,2p) optimized geometries for 2h3pHEX and the 2h3pHEX and water complex.

2h3pHEX				2h3pHEX−H_2O			
C	0.7187	-0.0256	-0.0102	C	0.8249	0.0183	-0.0804
C	0.1802	-0.9723	-1.0728	C	0.1438	-0.9103	-1.0792
C	0.3079	-0.4240	-2.4981	C	0.3368	-0.4085	-2.5274
H	1.3528	-0.1726	-2.6856	H	1.3902	-0.1878	-2.7011
C	-0.2538	-1.3578	-3.5597	C	-0.2319	-1.3544	-3.5728
H	-1.3136	-1.5018	-3.3501	H	-1.2954	-1.4788	-3.3699
H	0.2243	-2.3312	-3.4216	H	0.2284	-2.3321	-3.4066
C	-0.0559	-0.8858	-5.0071	C	-0.0115	-0.9207	-5.0288
H	-0.6073	-1.5704	-5.6545	H	-0.5656	-1.6131	-5.6655
H	-0.5214	0.0925	-5.1367	H	-0.4618	0.0606	-5.1877
C	1.4030	-0.8309	-5.4662	C	1.4526	-0.8965	-5.4737
H	1.4666	-0.5498	-6.5174	H	1.5310	-0.6427	-6.5308
H	1.9853	-0.0988	-4.9048	H	2.0389	-0.1584	-4.9243
H	1.8909	-1.8015	-5.3544	H	1.9264	-1.8702	-5.3326
O	0.0696	0.2337	0.9730	O	0.2933	0.5032	0.8879
H	1.7452	0.3474	-0.1477	H	1.9002	0.1847	-0.2746
O	-0.4380	0.8370	-2.6227	O	-0.3736	0.8695	-2.6940
O	0.0687	1.7787	-1.8569	O	0.1940	1.8354	-2.0017
O	-1.1309	-1.3602	-0.7728	O	-1.1711	-1.2465	-0.7741
H	-1.3575	-0.9307	0.0672	H	-1.6774	-0.4616	-0.4828
H	0.8534	-1.8456	-1.0407	H	0.7387	-1.8339	-1.0263
				O	-2.4670	0.9774	0.3286
				H	-2.5124	1.7812	-0.1974
				H	-1.6507	1.0515	0.8457

Supplementary Table S5.2. B3LYP/6-311++G(2d,2p) optimized geometries for 2p3hHEX and the 2p3hHEX and water complex.

2p3hHEX				2p3hHEX−H_2O			
C	-0.0315	-0.8753	-2.71457	C	0.3142	-0.7549	-2.61779
C	-0.6242	0.0029	-1.62082	C	-0.5407	-0.1085	-1.53582
C	-0.1653	-0.4041	-0.1971	C	0.0031	-0.2232	-0.08685
C	-0.6196	0.5620	0.89372	C	-0.6052	0.8068	0.86786
H	-0.1360	1.5269	0.73032	H	-0.3217	1.8103	0.54453
H	-0.2207	0.1685	1.83155	H	-0.1232	0.6412	1.83399
C	-2.1338	0.7492	1.02818	C	-2.1242	0.7210	1.04162
H	-2.5347	1.2127	0.12266	H	-2.6202	0.9390	0.09216
H	-2.6104	-0.2276	1.11882	H	-2.3957	-0.3003	1.31203
C	-2.5025	1.6183	2.23195	C	-2.6408	1.6922	2.10463
H	-3.5821	1.7484	2.30932	H	-3.7237	1.6223	2.21173
H	-2.1552	1.1666	3.16277	H	-2.1970	1.4800	3.07895
H	-2.0529	2.6102	2.15792	H	-2.3984	2.7254	1.84909
O	0.1624	-2.0571	-2.57961	O	1.0971	-1.6541	-2.44614
H	0.1983	-0.3572	-3.66062	H	0.1491	-0.3386	-3.62607
O	-0.3122	1.3836	-1.91852	O	-0.7721	1.2631	-1.95097
H	-1.7137	-0.0507	-1.67711	H	-1.5324	-0.5670	-1.56195
O	0.9866	1.5322	-2.14353	O	0.3703	1.8532	-2.27515
H	0.9290	-0.4317	-0.20571	H	1.0845	-0.0737	-0.1201
O	-0.6938	-1.6887	0.08685	O	-0.3028	-1.5303	0.36355
H	-0.3579	-2.3033	-0.57916	H	0.4899	-2.0916	0.30321
				O	2.0568	-2.9704	-0.11325
				H	2.0941	-3.9296	-0.07981
				H	1.9314	-2.7313	-1.04358

5.6.2 Harmonic Vibrational Frequencies

Supplementary Table S5.3. B3LYP/6-311++G(2d,2p) harmonic frequencies for 2h3pHEX and the 2h3pHEX and water complex.

2h3pHEX		2h3pHEX−H_2O	
42.1	1207.5	25.5	1158.3
67.4	1250.2	40.1	1172.5
90.7	1267.4	48.0	1205.4
117.8	1293.3	84.7	1255.7
124.0	1319.6	115.8	1270.7
185.5	1338.4	125.7	1290.2
234.4	1358.6	161.2	1315.4
251.7	1385.9	178.4	1348.7
268.8	1391.5	186.2	1355.8
298.6	1411.1	235.1	1387.1
341.3	1425.4	248.6	1403.3
389.5	1430.4	258.6	1421.0
437.8	1485.4	278.2	1424.4
474.6	1500.0	295.7	1455.3
526.9	1510.5	302.5	1487.0
694.3	1515.0	336.7	1499.6
719.6	1777.9	382.0	1510.2
768.5	2935.5	436.7	1514.6
808.9	2976.9	517.4	1655.0
843.1	3030.7	528.5	1783.3
874.5	3036.2	679.7	2924.7
910.0	3040.9	723.7	2979.8
957.1	3063.8	763.5	3030.8
1007.6	3066.6	781.8	3036.1
1036.8	3091.5	807.9	3040.3
1065.6	3094.5	836.5	3064.7
1114.1	3097.0	872.3	3070.8

Supplementary Table S5.4. B3LYP/6-311++G(2d,2p) harmonic frequencies for 2p3hHEX and the 2p3hHEX and water complex.

2p3hHEX		2p3hHEX−H_2O	
51.1	1160.8	41.2	1130.3
70.9	1249.5	50.8	1142.6
78.3	1264.9	65.3	1160.3
98.4	1290.7	82.9	1259.4
147.9	1328.4	89.6	1278.7
185.1	1335.4	127.2	1294.3
209.7	1350.8	136.6	1322.6
245.2	1370.5	154.3	1335.6
264.8	1409.9	202.1	1355.2
272.0	1413.4	215.3	1370.8
345.1	1422.5	240.5	1410.2
383.6	1437.1	252.8	1421.4
421.5	1484.9	258.8	1425.6
534.6	1501.8	278.2	1464.9
554.6	1506.7	341.2	1487.8
648.0	1516.8	352.7	1501.5
670.6	1789.3	381.2	1505.6
748.1	2960.2	431.6	1515.9
798.7	3010.8	458.1	1641.4
867.0	3021.2	552.1	1798.3
891.6	3030.2	649.0	2955.0
945.0	3042.6	682.8	3024.9
980.7	3061.6	746.2	3028.6
1017.0	3071.3	762.3	3036.3
1039.0	3077.1	785.4	3047.6
1049.8	3093.9	868.7	3060.0
1108.5	3095.3	888.2	3065.5

CHAPTER 6: THE EFFECT OF WATER ON THE $HOCH_2CH_2O_2$ SELF-REACTION RATE COEFFICIENT. AN EXPERIMENTAL INVESTIGATION

6.1 Abstract

The gas phase reactions of the 2-hydroxyethyl peroxy (2HEP) radical in the presence and absence of water vapor are studied at temperatures between 286 and 292 K using laser flash photolysis coupled with UV time-resolved absorption detection between 220 and 300 nm. Water vapor concentrations were quantified using IR wavelength modulated diode laser spectroscopy. At 286 K, the 2HEP self-reaction rate constant is enhanced by the presence of water vapor ($[H_2O] = 4.23 \times 10^{16}$ molecule cm^3) by as much as a factor of 2 (2.45×10^{-12} cm^3 $molecule^{-1}$ s^{-1} versus 5.35×10^{-12} cm^3 $molecule^{-1}$ s^{-1}), similar to the HO_2 self-reaction. The enhancement in the 2HEP self-reaction rate coefficient is thought to occur as a result of the formation of a 2HEP−H_2O complex during the reaction mechanism.

6.2 Introduction

Organic peroxy radicals (RO_2) play a significant role as reaction intermediates in the tropospheric oxidation of volatile organic compounds (VOCs). The first step in the oxidation of organics in the atmosphere involves the abstraction of a hydrogen atom to from an alkyl radical, R. The abstracting molecule may include the hydroxy radical (OH), the nitrate radical (NO_3) or atomic chlorine (Cl):

$$OH + R{-}H \rightarrow R + H_2O \quad (6.1a)$$

$$NO_3 + R{-}H \rightarrow R + HNO_3 \quad (6.1b)$$

$$Cl + R{-}H \rightarrow R + HCl \quad (6.1c)$$

In air, the predominant reaction for the alkyl radical is reaction with O_2, forming the alkylperoxy radical:

$$R + O_2 \rightarrow RO_2 \quad (6.2)$$

In the presence of NO_x, O_3 is formed as a byproduct since RO_2 radicals react with NO to produce NO_2, which is rapidly photolyzed to yield O_3:

$$RO_2 + NO \rightarrow RO + NO_2 \quad (6.3)$$

$$NO_2 + h\nu(\lambda \leq 420 \text{ nm}) \rightarrow NO + O \quad (6.4)$$

$$O + O_2 + M \rightarrow O_3 + M \quad (6.5)$$

When concentrations of NO and NO_2 are sufficiently high, RO_2 radicals react exclusively with NO leading to O_3 formation. Since the oxidation of organics is usually initiated by attach of the OH radical (6.1a), the O_3 potential of any organic molecule is governed by its rate of reaction with OH. When concentrations of NO_x are low, reactions of RO_2 radicals with themselves, HO_2, or other RO_2 can compete with (6.3):

$$RO_2 + R_yO_2 \text{ (y = H, R or } R_1) \rightarrow \text{products} \quad (6.6)$$

These reactions are considered to be terminating as they lead to the production of a non-radical, relatively stable products (e.g., hydroperoxides (ROOH), alcohols, and

aldehydes). These pathways alter the O_3 potential of a particular organic as its rate is not governed solely by reaction with OH, but by the relative rate of reaction of RO_2 with NO (6.3) and HO_2 (6.6).

The rate of oxidation of non-methane hydrocarbons, although present in lower concentrations, is expected to be significant since the rate coefficients for their reaction with HO are much larger.[191] As an example, the rate of reaction of ethene (C_2H_4) with OH can be as high as 5.4×10^{-2} s^{-1} (assuming a C_2H_4 concentration of 0.5 ppb and temperature of 270 K indicative of a height of 5 km in the troposphere), as compared with that of methane, 9×10^{-2} s^{-1} (at a concentration of 1.7 ppm at 270 K and 5 km).[192] Although present at a much higher concentration, the relative rate of OH with CH_4 is within a factor of 2 of the C_2H_4 + OH reaction, reflective of the difference in the rate constant of each reaction, 4.4×10^{-15} versus 9×10^{-12} cm^3 $molecule^{-1}$ s^{-1}, respectively.[193] A number of studies investigating the rates of hydrogen atom abstraction from various compounds by radicals indicate that the reactivity of C−H hydrogens is affected by resonance, steric, polar, and solvent effects.[194-197] The methane C−H bond is least affected by these considerations resulting in a slower OH + CH_4 rate constant as compared to higher alkanes. The slow rate of this reaction has resulted has resulted in a focus on “non-methane hydrocarbons” (NMHC) as they relate to the production of ozone in urban areas. The formation of the hydroxyethyl radical is quickly followed by the addition of O_2 to form the 2-hydroxyethylperoxy radical (2HEP):

$$OH + C_2H_4 + M \rightarrow HOCH_2CH_2 + M \quad (6.7)$$

$$HOCH_2CH_2 + O_2 \rightarrow HOCH_2CH_2O_2 \quad (6.8)$$

The rate of reaction of 2HEP with NO and HO_2 may be also play an important role in O_3 formation, as discussed above.

To date, a variety of kinetic studies aimed at studying the reactions of RO_2 with itself and other RO_2 radicals have been performed.[192,198-210] However, it is not feasible or practical to carry out kinetic studies on every RO_2 radical that can be derived from the oxidation of each organic compound believed to be present in the atmosphere. Nonetheless, it is possible and instructive to establish structure-reactivity relationships for peroxy radicals with different substituent functional groups (e.g., the –OH group of the $HOCH_2O_2$ radical). This may be achieved by studies on the kinetics of peroxy radicals representative of a particular class. 2HEP is the simplest example of the class of peroxy radicals that is derived from the atmospheric oxidation of alkenes.

The presence of water vapor has been shown to have an effect on the rate of reaction for the simplest RO_2 radical, HO_2. Experimentally, the presence of water has been shown to introduce a significant enhancement (k_{wet} is faster than k_{dry} by a factor of 1.6) in the HO_2 self-reaction rate.[47,48,211,212] This factor of 1.6 was observed at 295 K and a water vapor concentration of 2.9×10^{17} molecules cm^{-3} and is the result of a change in the HO_2 self-reaction rate constant from $(2.7 \pm 0.5) \times 10^{-12}$ to $(4.3 \pm 0.4) \times 10^{-12}$ cm^3 $molecule^{-1}$ s^{-1}. The underlying mechanism of the water enhancement of the HO_2 self-reaction is discussed in detail in Chapter 2.

Computational methods have predicted strong complex formation between 2HEP and H_2O, with a zero-point energy corrected value of 6.4 kcal mol^{-1}, calculated at the

MP2(full)/6-311++G(2d,2p) level of theory.[59] The optimized structure of the 2HEP−H_2O complex is shown in Figure 6.1.

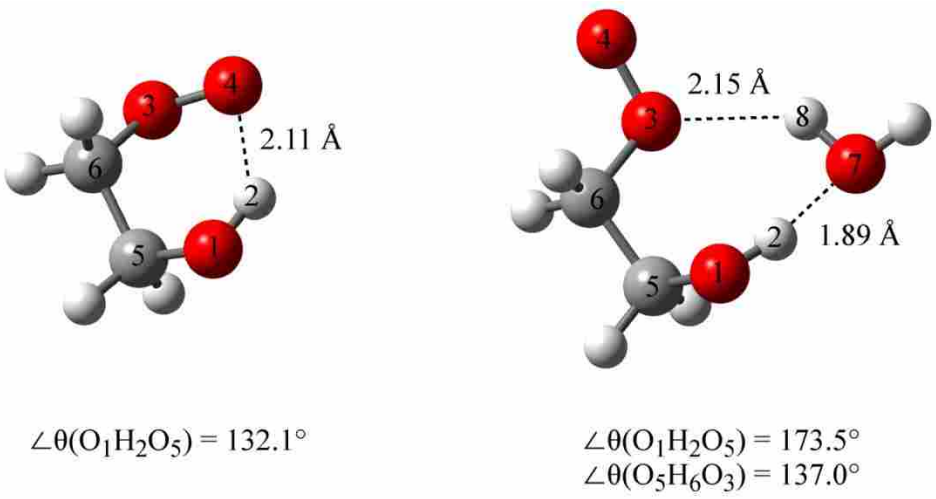

Figure 6.1. MP2(full)/6-311++G(2d,2p) optimized structures of 2HEP and 2HEP−H_2O.

As shown, the 2HEP−H_2O complex is stabilized by the formation of two inter-molecular hydrogen bonds. Complex formation breaks the O1H2O4 intra-molecular hydrogen and causes the terminal peroxy oxygen atom to rotate to a position between the two hydrogen atoms of the second 2HEP carbon (C6). Natural population calculations indicate that the population of the radical electron located on the terminal peroxy oxygen atom increases by 8.3×10^{-4} e. This increase in electron density is likely to increase the rate of 2HEP combination to form the expected (ROOOOR)* excited intermediate.[176] The presence of H_2O may continue to have an effect on the decomposition of the tetroxide intermediate. The present work is an experimental study regarding the effects of H_2O on the 2HEP self-reaction.

6.3 Methods

To investigate the dependence on water vapor on the 2HEP radical self-reaction, the kinetics of the self-reactions of 2HEP + 2HEP were measured over 286-292 K at ~200 Torr. Flash photolysis/UV spectroscopy is used to create/monitor the radicals, while wavelength modulated infrared diode laser spectroscopy is used to quantify the water vapor concentration. Figure 6.2 presents a schematic representation of this system showing the components used for both the UV and IR spectroscopy measurements. All of the experiments are performed in a Pyrex cylindrical reaction cell (187 cm in length, 5.1 cm in diameter). The reaction tube was surrounded by a Pyrex jacket through which methanol, or a glycol/water mixture is circulated, allowing for temperature regulation. K-type thermocouples are placed at the ends of the cell to monitor the temperature of the system. MgF_2 windows are used at both ends of the cell because they transmit both UV and IR light over the range of interest. The use of kinematically mounted mirrors in the optical path of the system makes it possible to switch between UV and IR detection methods without changing the position, and hence alignment, of the flow cell, light sources or detectors.

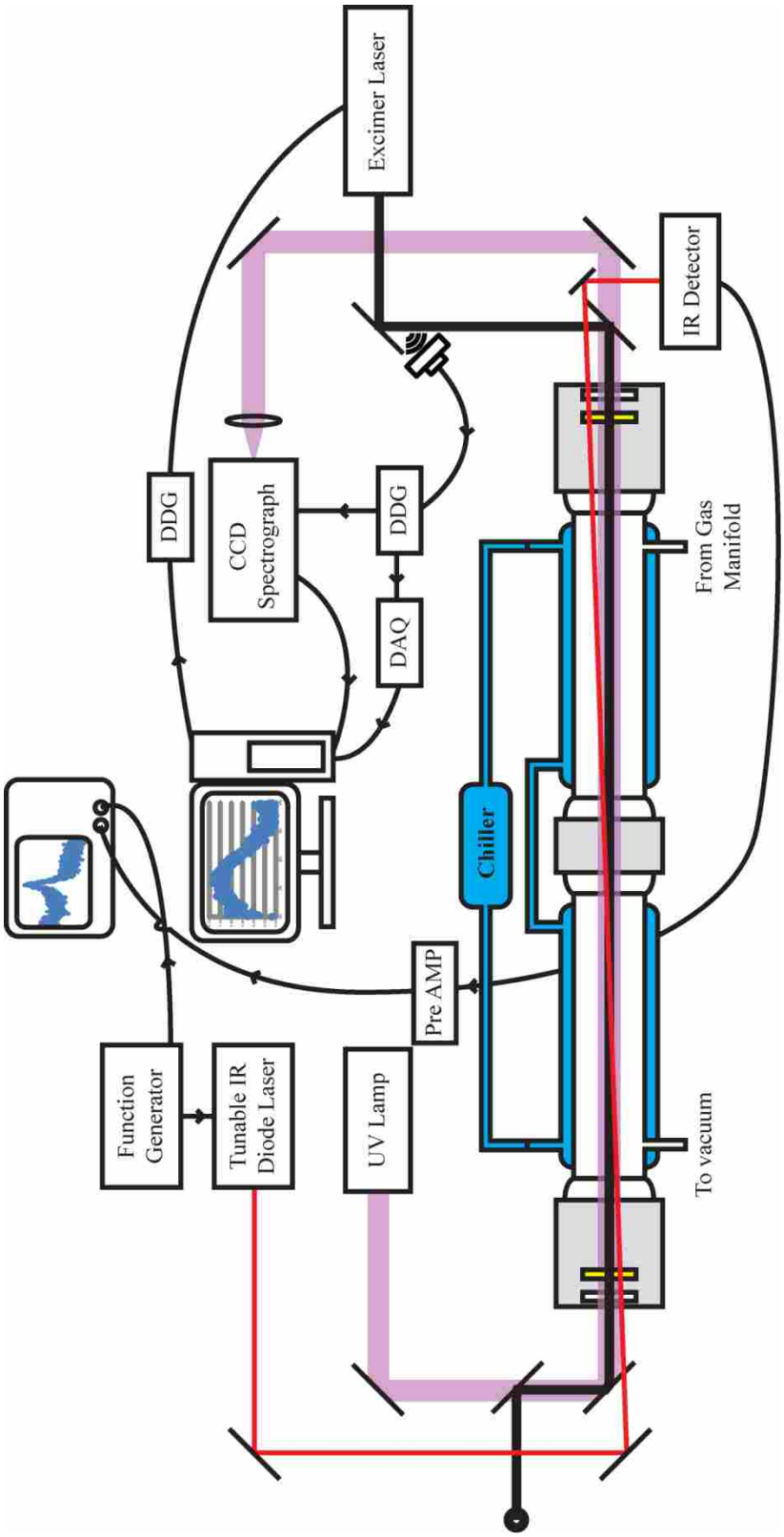

Figure 6.2. Schematic of UV/flash-photolysis system for kinetic measurements.

6.3.1 $HOCH_2CH_2O_2$ Self-Reaction Kinetics Measurements.

2HEP is formed in the reaction cell by introducing a gas mixture containing 10 Torr of 98% $HOCH_2CH_2Br$ carried by N_2, 64 Torr of O_2, and enough N_2 to reach a total pressure of 200 Torr. Hasting Teledyne mass flow controllers adjust the gas flows of $HOCH_2CH_2Br/N_2$, O_2 and N_2 to achieve the appropriate partial pressures. The flow rate was maintained at 3150 sccm resulting in a total gas mixture residence time of ~1 s in the reaction cell. An excimer beam was used to photolyze an area with dimensions 2.5 cm (width) × 1 cm (height) area. The excimer was fired at 1 Hz allowing for a fresh mixture of gas to be probed with every laser shot. $HOCH_2CH_2Br$ is introduced into the gas mixture via a dual 100 mL bubbler system using N_2 as the carrier gas. The first bubbler in the series is filled with ~80 ml of $HOCH_2CH_2Br$ and the second bubbler acts as a trap to avoid liquid reactant from entering the reaction tube. The bubbler's temperature is maintained by emersion in a constant temperature bath set to 303 K. The concentration of $HOCH_2CH_2Br$ is adjustable by changing the carrier gas flow rate, but was set at 1000 sccm for the work presented here.

A photolysis pulse from an excimer laser (Lamda Physik, model EMG201MSC) initiates the radical chemistry. The laser employs a ArF mixture to produce 193 nm light at a pulse rate of 1 Hz and energy of 300 ± 20 mJ $pulse^{-1}$. This pulse is used to photolyze a small fraction (1-3%) of the $HOCH_2CH_2Br$ molecules to produce $HOCH_2CH_2$ and Br radicals. The typical range observed for the concentration of the $HOCH_2CH_2$ radical is between 2.0×10^{13} and 4.0×10^{13} molecules cm^{-3}. Subsequent reaction of the $HOCH_2CH_2$ alkyl radical with O_2 produces the 2HEP radical as per (6.8). Following the

formation of 2HEP, the simplified reaction mechanism for the peroxy radical reactions studied here are:

$$HOCH_2CH_2O_2 + HOCH_2CH_2O_2 \rightarrow 2\ HOCH_2CH_2O + O_2 \quad (6.9)$$

$$\rightarrow HOCH_2CHO + HOCH_2CH_2OH + O_2 \quad (6.10)$$

$$HOCH_2CH_2O_2 + HOCH_2CH_2O_2{-}H_2O \rightarrow \text{Products} \quad (6.11)$$

Table 6.1 lists the detailed reaction mechanism used to model the chemistry of 2HEP + 2HEP.

Figure 6.2 shows the main components and layout of the experimental apparatus. Time-resolved detection of the 2HEP radical is made by directing the output from a 30 Watt D_2 lamp (Oriel model 60010) through the center of the reaction cell. The excimer laser photolysis beam path is aligned to pass coaxially with the UV probe beam path by the use of dielectric mirrors which reflect the 193 nm photolysis beam while passing all other UV wavelengths (with the exclusion of a ±15 nm band centered around 193 nm). UV light absorption is detected by a monochromator (Andor model SR-303i-B, grating 600 l/mm) and intensified and gated CCD camera (Andor model CCD30-11). Collection of dark counts, blank (Io) and response (I) is controlled through a LABVIEW routine written in-house. The concentration of 2HEP radicals is determined by monitoring the CCD signal from 225 nm to 300 nm at discrete time points after the excimer laser pulse. Using established UV cross-sections for 2HEP[213] and O_3,[214] the concentration of 2HEP is determined by a two-parameter least-square fit:

$$A_{tot} = l*(\varepsilon_{2HEP}c*c_{2HEP} + \varepsilon_{O3}*c_{O3}) \quad \text{(EQ 6.1)}$$

2HEP self-reaction kinetics are determined by fitting the 2HEP time-dependent concentrations to the kinetic model described in Table 6.1. Examples of typical fits to (EQ 6.1) and the kinetic model described in Table 6.1 are shown in Figure 6.3.

Table 6.1. Reactions used to predict peroxy radical reaction rate constants in the kinetic model.

Reaction	k (cm^3 $molecule^{-1}$ s^{-1})
$HOCH_2CH_2O_2 + HOCH_2CH_2O_2 \rightarrow 2\ HOCH_2CH_2O + O_2$	1.1×10^{-12}
$HOCH_2CH_2O_2 + HO_2 \rightarrow HOCH_2CH_2OOH + O_2$	1.5×10^{-11}
$HOCH_2CH_2O \rightarrow CH_2O + CH_2OH$	5.5×10^{-14}
$HOCH_2CH_2O + O_2 \rightarrow HOCH_2CHO + HO_2$	$5.0 \times 10^{-26}\ e^{(34.92/RT)}$
$CH_2OH + O_2 \rightarrow CH_2O + HO_2$	9.6×10^{-12}
$CH_2O + HO_2 \rightarrow HCO + H_2O_2$	$1.5 \times 10^{-13}\ (T/298)\ 2.70\ e^{(-48.20.92/RT)}$
$CH_2O + HO_2 \rightarrow HOCH_2O_2$	$9.7 \times 10^{-15}\ e^{(5.20/RT)}$
$HOCH_2O_2 + HOCH_2O_2 \rightarrow 2\ HOCH_2O + O_2$	5.5×10^{-12}
$HOCH_2O_2 + HO_2 \rightarrow$ products	5.65×10^{-15}
$HOCH_2O + O_2 \rightarrow HC(O)OH + HO_2$	3.5×10^{-14}
$O + O_2 \rightarrow O_3$	2.8×10^{-12}
$HO_2 + HO_2 \rightarrow H_2O_2 + O_2$	$2.2 \times 10^{-13}\ e^{(4.99/RT)}$
$HO_2 + O_3 \rightarrow OH + 2\ O_2$	$1.1 \times 10^{-14}\ e^{(-4.16/RT)}$

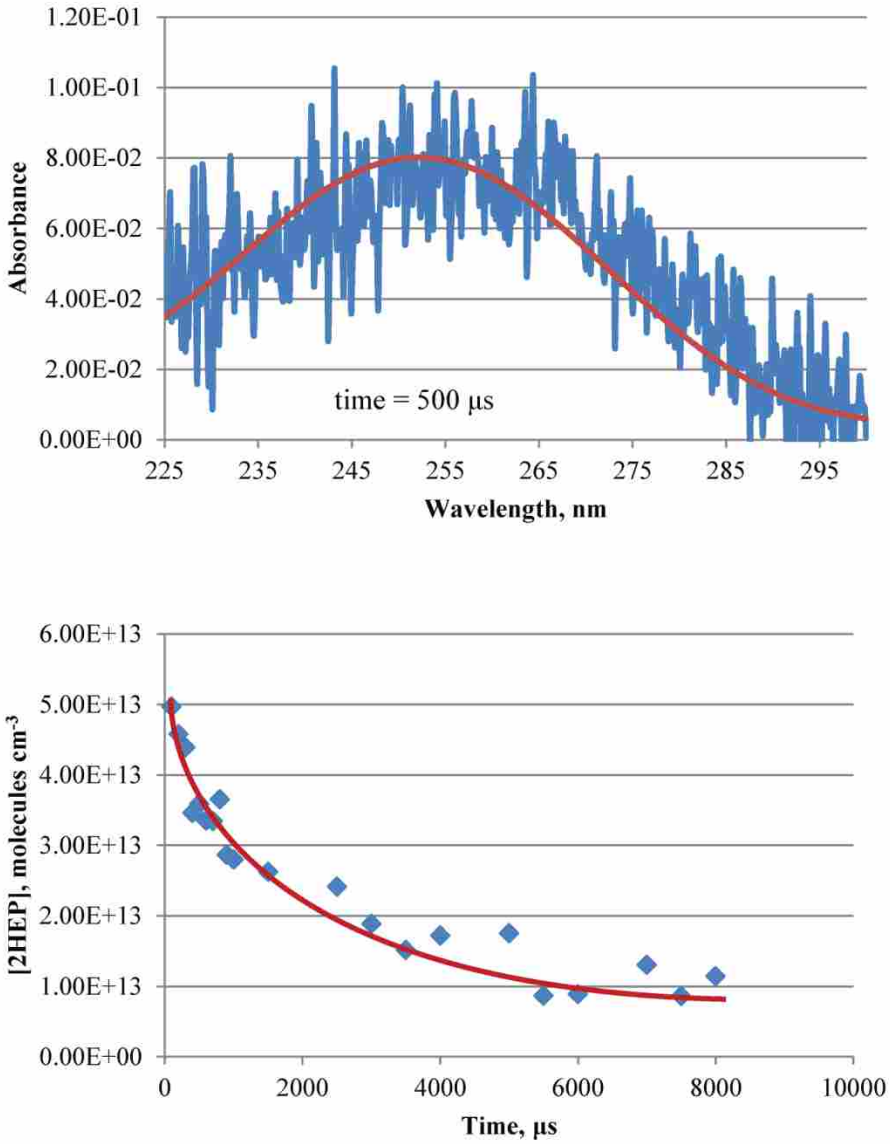

Figure 6.3. The top graph is an example of a fit of (EQ 6.1) to the CCD data obtained at 289 K and 500 µs. The bottom graph is an example of the fit of the values of [2HEP] derived from (EQ 6.1) as a function of time at 289 K to the kinetic model detailed in Table 6.1.

6.3.2 Water Concentration Measurements

Water vapor is introduced into the reaction cell by N_2 carrier gas passing through a bubbler immersed in a constant temperature bath. The amount of water vapor is controlled by both the temperature of the water and the flow rate of the carrier gas. The water vapor concentration was varied between 6.04×10^{15} and 6.08×10^{16} molecules cm^{-3}. Efforts were made to introduce water vapor as close as possible to the saturation vapor pressure, but uncertainties in the exact water concentrations likely contribute to some of the scatter in the data.

Wavelength modulated IR diode laser spectroscopy is used to quantify the water in the cell. Figure 6.2 show the IR system components. Water absorbs IR light that is scanned over a narrow frequency band (150 Hz) centered at the 1486.19 nm line such that the entire peak of the selected rovibration transition can be observed. The IR beam is produced by a New Focus TLB-6326 tunable diode laser with a line width of <300 kHz. With the use of Herriott cell optics, the IR beam is passed five times through the reaction cell, and finally directed towards an IR 1 GHz low noise photoreceiver. The signal from the detector is synchronized with the 150 Hz modulation frequency and visualized and recorded by a digital oscilloscope (Textronix model TDS 3024B).

6.4 Discussion

The reaction model in Table 6.1 is run to produce predictions of 2HEP concentration decays (using Micromath Scientist version 3.0 to solve the coupled differential equations that describe the kinetics) based upon the experimental decays determined by calculating 2HEP concentrations at different time points. The best fit of this model to the data yields self-reaction rate constants that demonstrate both a

temperature and H_2O dependence. The rate constants, as a function of water vapor and temperature, are listed in Table 6.2 and depicted graphically in Figure 6.4. Columns 2 and 3, Table 6.2, of each temperature set represent the raw rate constant and the fit rate constant, respectively.

Figure 6.2. 2HEP rate constants as a function of H_2O vapor concentration and temperature.

286 K			289 K			292 K		
$[H_2O]^a$	$k_9{}^b$ (Data)	$k_9{}^b$ (Fit)	$[H_2O]^a$	$k_9{}^b$ (Data)	$k_9{}^b$ (Fit)	$[H_2O]^a$	$k_9{}^b$ (Data)	$k_9{}^b$ (Fit)
0.00E+00	2.45E-12 ± 5.39E-13	2.64E-12	0.00E+00	2.52E-12 ± 4.79E-13	2.28E-12	0.00E+00	1.72E-12 ± 2.74E-13	1.76E-12
6.04E+15	3.37E-12 ± 4.37E-13	3.08E-12	7.26E+15	2.51E-12 ± 3.88E-13	2.62E-12	8.69E+15	2.00E-12 ± 2.22E-13	1.80E-12
1.21E+16	3.41E-12 ± 3.53E-13	3.51E-12	1.45E+16	2.72E-12 ± 3.13E-13	2.97E-12	1.74E+16	1.84E-12 ± 1.79E-13	1.85E-12
1.81E+16	3.62E-12 ± 3.02E-13	3.94E-12	2.18E+16	3.00E-12 ± 2.68E-13	3.32E-12	2.61E+16	1.90E-12 ± 1.54E-13	1.89E-12
2.42E+16	4.82E-12 ± 3.02E-13	4.37E-12	2.90E+16	3.91E-12 ± 2.68E-13	3.67E-12	3.47E+16	1.63E-12 ± 1.54E-13	1.93E-12
3.02E+16	4.62E-12 ± 3.53E-13	4.80E-12	3.63E+16	4.30E-12 ± 3.13E-13	4.02E-12	4.34E+16	1.86E-12 ± 1.79E-13	1.97E-12
3.63E+16	5.60E-12 ± 4.37E-13	5.24E-12	4.36E+16	4.62E-12 ± 3.88E-13	4.36E-12	5.21E+16	2.20E-12 ± 2.22E-13	2.02E-12
4.23E+16	5.35E-12 ± 5.39E-13	5.67E-12	5.08E+16	4.38E-12 ± 4.79E-13	4.71E-12	6.08E+16	2.12E-12 ± 2.74E-13	2.06E-12

[a]molecule cm^{-3}; [b]cm^3 $molecule^{-1}$ s^{-1}

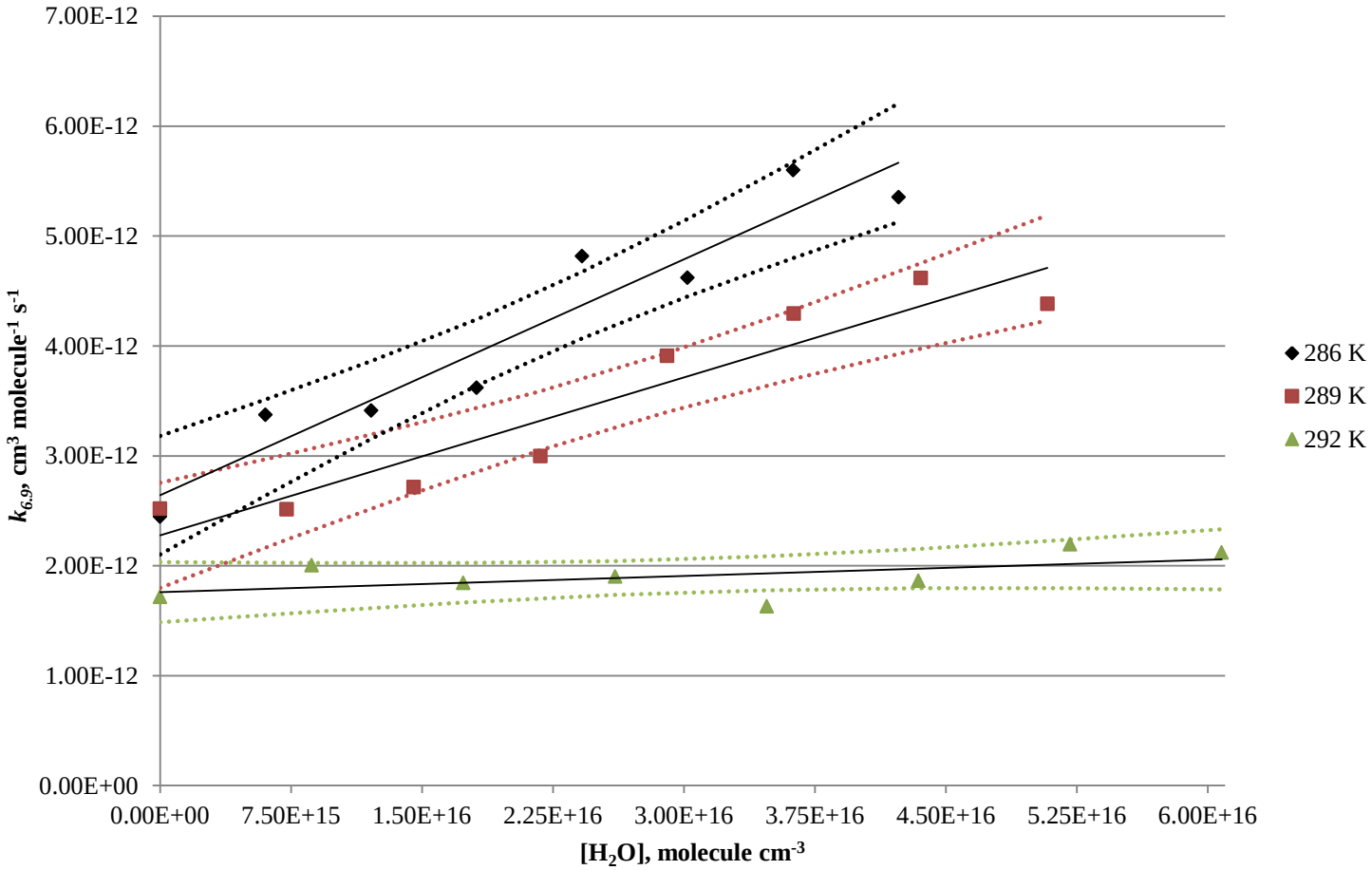

Figure 6.4. Plot of k_9 as a function of temperature and water vapor.

The 2HEP self-reaction rate constants determined in the absence of H_2O are in good agreement with values published previously. Jenkin and Cox, who formed 2HEP via the 254 nm photolysis of 2-iodoethanol, reported the value of $k_{6.9}$ to be $(1.6 \pm 0.17) \times 10^{-12}$ cm^3 $molecule^{-1}$ s^{-1} at 298 K and 760 torr.[192] Murrells and co-workers, generating 2HEP by the 248 nm photolysis of H_2O_2 in the presence of C_2H_4 and O_2, determined $k_{6.9}$ to be $(2.2 \pm 0.5) \times 10^{-12}$ cm^3 $molecule^{-1}$ s^{-1} at 296 K and 740 torr.[215] The H_2O enhancement of the 2HEP self-reaction rate constants is supported by the work of Anastasi et al. who reported k_9 to be $(7.7 \pm 1.2) \times 10^{-12}$ cm^3 $molecule^{-1}$ s^{-1}.[201] Although unintentional, the method by which they produced 2HEP involved the presence of a copious amount of water vapor, 1.2×10^{18} molecules cm^{-3}, which is a factor of 20 greater than the largest amount of H_2O vapor used in this study (6.08×10^{16} molecules cm^{-3}). The method of 2HEP generation used by Anastasi[201] is outlined below:

$$\text{2-MeV } e^- + SF_6 \rightarrow SF_4 + 2F + e^- \quad (6.12a)$$

$$\rightarrow SF_5 + F + e^- \quad (6.12b)$$

$$F + H_2O \rightarrow OH + HF \quad (6.13)$$

$$OH + C_2H_4 + M \rightarrow CH_2CH_2OH + M \quad (6.14)$$

In this scheme, H_2O is the source of the OH radical (6.13) that then adds across the double bond of ethene (6.14) to form the 2-hydroxyalkyl radical. The subsequent addition of O_2 (6.8) to CH_2CH_2OH results in the formation of the 2HEP radical. The large amount of water vapor used and the relatively large value of $k_{6.9}$ may represent a saturation limit for the effect of water on the self-reaction of the 2HEP radical.

The results of k_9 reported herein, for a given temperature, indicate a negative temperature dependence. This is expected as the amount of a 2HEP−H_2O complex, analogous to the HO_2−H_2O complex, will be greater at lower temperatures owing to a reduction in thermal decomposition. The largest observed value of k_9, 5.35×10^{-12} cm^3 $molecule^{-1}$ s^{-1}, is observed with $[H_2O] = 4.23 \times 10^{16}$ molecules cm^{-3} at 286 K and 200 torr total pressure, which corresponds to an enhancement of the 2HEP self-reaction rate constant by a factor of 2.1. This value is similar to the H_2O enhancement of the HO_2 self-reaction, 1.6, indicating that water may play a similar role in both peroxy radical systems. The rate enhancement at 289 K and 292 K, as calculated from the best fit of k_9 is 1.7 and 1.2, respectively. An *ab initio* analysis of the effect of H_2O on the 2HEP self-reaction system is currently underway.

The Arrhenius plot for k_9 is shown if Figure 6.5. The Arrhenius parameters for the self-reaction of 2HEP at different water concentrations are shown in Table 6.3.

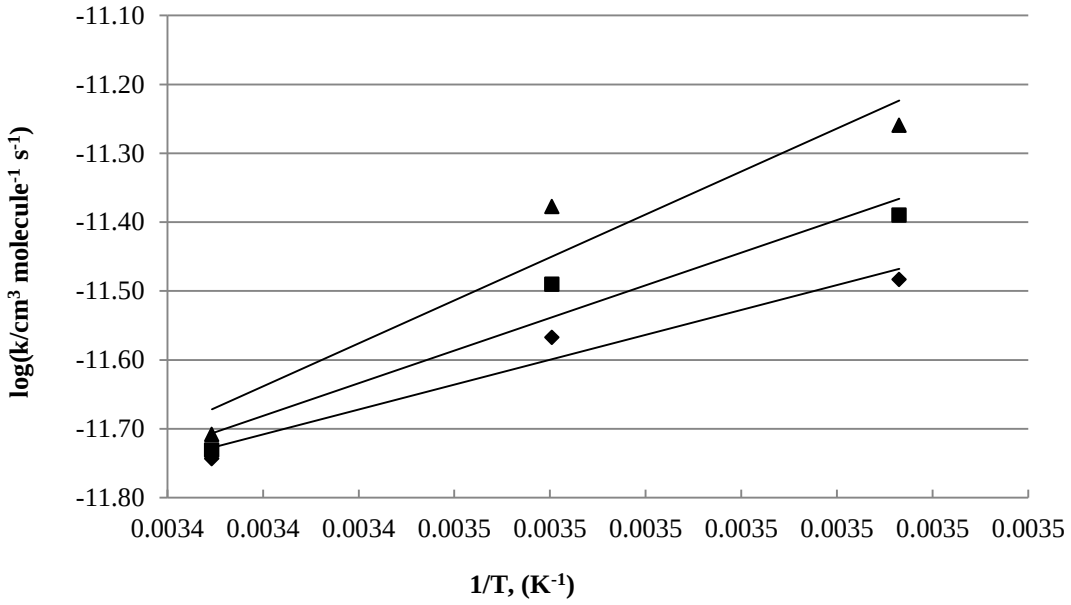

Figure 6.5. Arrhenius plots for the self-reaction of 2HEP at three different $[H_2O]$ levels: (♦) $[H_2O] = 9.0 \times 10^{15}$ molecules cm^{-3}; (■) $[H_2O] = 2.0 \times 10^{16}$ molecules cm^{-3}; (▲) = $[H_2O] = 4.0 \times 10^{16}$ molecules cm^{-3}.

Table 6.3. Arrhenius parameters for the 2HEP self-reaction as a function of [H_2O].

[H_2O][a]	A[b]	E/R[c]	E[d]
9.00E+15	3.33E-11	-3619.6	- 7.19
2.00E+16	7.45E-13	-4735.7	- 9.40
4.00E+16	4.48E-15	-5239.3	-10.40

[a] Units, molecules cm^{-3}

[b] Units, cm^3 $molecule^{-1}$ s^{-1}

[c] Units, K

[d] Units, kcal mol^{-1}

As determined from the slope of the Arrhenius plots as a function of [H_2O], the activation energy for the 2HEP self-reaction becomes more negative with increasing water vapor. This is indicative of a shift from reaction (6.9) to (6.11), increasingly involving the 2HEP−H_2O complex.

6.5 Conclusions

The value for the overall rate of the self-reaction of 2HEP radicals has been shown to experience a water vapor enhancement and a negative temperature dependence. At 286 K and 200 torr total pressure, the value of k_9 is shown to increase by a factor of 2, from 2.45×10^{-12} cm^3 $molecule^{-1}$ s^{-1} to 5.35×10^{-12} cm^3 $molecule^{-1}$ s^{-1}. At warmer temperatures, the rate enhancement as a function of water decreases to 1.7 at 289 K and to 1.2 at 292 K. The reduced sensitivity to water vapor at 292 K may be indicative of the moderate binding energy predicted for the 2HEP−H_2O complex, -4.3 kcal mol^{-1}.[59]

The effect of temperature and water vapor on the 2HEP self-reaction system will be furthered by increasing the temperature range over which the 2HEP system is studied and by introducing larger concentrations of H_2O to ascertain if the value of k_9 reported by

Anastasi can be considered saturated. Computational work is also being performed to ascertain possible mechanisms for the role of H_2O in the self-reaction of 2HEP.

CHAPTER 7: NH_x−HNO_3, NH_x−H_2SO_4, NH_x−CH(O)OH, AND NH_x−$CH_3C(O)OH$ COMPLEXES AND THEIR ROLE IN THE FORMATION OF ATMOSPHERIC AEROSOLS

7.1 Abstract

The formation of sulfuric acid (H_2SO_4), nitric acid (HNO_3), acetic acid ($CH_3C(O)OH$) and formic acid (HC(O))H) complexes with ammonia (NH_3), amidogen radical (NH_2) and imidogen radical (NH) was studied using Natural Bond Orbital (NBO) calculations. The equilibrium structures, binding energies, and harmonic frequencies were calculated for each acid−NH_x complex using the hybrid density functional (B3LYP) and the second-order Møller-Plesset perturbation approximation (MP2) methods with the 6-311++G(3df,3pd) basis set. The results presented here suggest that the effects of NH_3 on the formation of new aerosol particles will be imitated by NH_2, but to a lesser degree and confined primarily to complexes with H_2SO_4 and HNO_3. The NH radical is not expected to play a noticeable role in the formation of new atmospheric aerosols.

7.2 Introduction

Tropospheric aerosol particles directly affect the radiative balance of the Earth through processes such as light absorption and scattering. Furthermore, aerosol particles indirectly affect the terrestrial radiation budget because they are the precursors to the formation of clouds. Aerosols have also been implicated in adverse human health effects,[216] in the reduction of visibility in urban and regional areas,[217-219] and in acid deposition.

Sulfuric acid (H_2SO_4), nitric acid (HNO_3) and ammonia (NH_3) are important precursors in the formation of tropospheric aerosol particles. Atmospheric H_2SO_4 is largely the result of SO_2 emissions resulting from anthropogenic and natural means. SO_2

is readily oxidized in the atmosphere by OH radicals and other oxidizing agents to form SO_3. In the presence of water vapor, SO_3 is quickly converted to H_2SO_4.[220] Nitric acid is a final product of the NO_x oxidation process that is involved in photochemical smog formation.[176] Ammonia is primarily the result of animal waste, nitrogen based fertilizers and industrial emissions.[221]

It is commonly accepted that the formation of atmospheric aerosols is the result of gas phase acid base reactions that take place in the presence of water vapor. The reaction of H_2SO_4 and NH_3 is responsible for the creation of a family of sulfur containing particulates (e.g. NH_4HSO_4 and $(NH_4)_2SO_4$), whilst the reaction of HNO_3 and NH_3 leads to the formation of particulate ammonium nitrate (NH_4HNO_3).

The role of water appears to be the stabilization of the forming acid-ammonia ion pairs. In the case of sulfuric acid, the presence of one molecule of water was shown to be sufficient to convert the $H_2SO_4{-}(NH_3)$ system from a hydrogen bonded system to one that exists only as an ion pair, the result of complete proton transfer from acid to base.[222] A similar effect was shown for nitric acid, with the exception that two or more water molecules were required to convert the hydrogen bonded $NH_3{-}HNO_3$ system to an ion pair.[222,223]

The oxidation of NH_3 by a hydroxyl radical (OH) leads to the formation of an amidogen radical (NH_2)[224]:

$$NH_3 + OH \rightarrow NH_2 + H_2O \qquad (7.1)$$

The formation of NH_2 is not only an important step in the oxidation of NH_3 but is known to be important in the combustion of fossil fuels.[225] NH_2 also plays a key role in the NO_x cycle.[176] When the concentration of NH_3 is elevated, NH_2 may also play a role in the formation of aerosol particulates.

The purpose of the present work is to identify NH_2−acid [acid = H_2SO_4, HNO_3, HC(O)OH, and $CH_3C(O)OH$] complexes and to compare them to the NH_3-acid complexes. In addition, acid complexes of the imidogen radical (NH) are also explored. NH concentrations are expected to be low under normal atmospheric conditions and are not expected to play a significant role in the formation of atmospheric aerosols, but are included for completeness and to help elucidate the manner in which NH_x species affect gas phase acids. Complex formation is analyzed through geometric and natural bond orbital (NBO) analysis. The Gibb's free energy of formation, ΔG_f, is estimated for each complex over the temperature range of 220 – 300 K. Equilibrium and dissociation constants, as well as, atmospheric lifetime estimates are also presented spanning the same temperatures.

7.3 Methods

Calculations were performed using the Gaussian 03, Revision D.01 system of codes.[63] All geometries were fully optimized at the UMP2(full)/6-311++G(3df,3pd) computational level. Harmonic vibrational frequency calculations performed at the B3LYP/6-311++G(3df,3pd) level established the structures as minima and allowed for zero-point corrections to be made to the optimized energies. The counterpoise (CP) procedure[72] was used to further correct the energies for basis set superposition error (BSSE). Electron correlation refinements based on the UMP2 optimized global minimum

structures were performed using quadratic configuration interaction with single, double, and triple excitations, QCISD(T), coupled cluster with single, double, and perturbative triple excitations, CCSD(T) methods, and Brueckner Doubles with a triples contribution, BD(T).

Natural energy decomposition analysis (NEDA) calculations were performed at the UB3LYP/6-311++G(3d,3p) level using NBO.5G[77] implemented in Firefly QC package,[78] which is partially based on the GAMESS (US)[158] source code.

Electron density maps with a surface resolution of 0.0009 e/a.u^3 were generated at the MP2(full)/6-311++G(3df,3pd) level using geometries optimized at the same level. Natural bond orbital (NBO) analysis was performed under UMP2(full)/6-311++G(3df,3pd) conditions using the Gaussian implementation of NBO 3.1.[69,70,73-76]

The global minimum structure for each complex was arrived at through an extensive RCS methodology. The RCS method generates NH_x−acid complex geometries by randomly packing a previously optimized NH_x molecule within a constrained 3.5-Å radius sphere encompassing the entire optimized acid structure. Each of the twelve complexes presented herein was arrived at via 2,000 random NH_x−acid.

All calculations were performed on a super-computing Linux cluster consisting of 320 processing nodes equipped with two quad-core Intel Nehalem processors (2.8 GHz) and 24 GB of memory. All nodes are connected with Infiniband, a high-speed, low-latency copper interconnect

The optimized geometries and harmonic vibrational frequencies are given in supplementary Tables S7.1-S7.24.

7.4 Results and Discussion

7.4.1 Calibration Structures

The gas-phase reactions of H_2SO_4 and HNO_3 with NH_3 are responsible for the creation of sulfur- and nitrogen-containing particulates such as NH_4HSO_4, $(NH_4)_2SO_4$, and NH_4NO_3. Together with H_2SO_4 and HNO_3, these species represent the major forms of sulfur- and nitrogen-containing aerosols[222,223] and play a key role in the formation of cloud condensation nuclei. H_2SO_4 and HNO_3 form hydrogen bonded complexes with ammonia that may facilitate the formation of aerosol particles, especially in the presence of water.

Figure 7.1 schematically represents the MP2(full)/6-311++G(3df,3pd) optimized structures for the $NH_3{-}H_2SO_4$ and $NH_3{-}HNO_3$ complexes, lists the hydrogen bond length and angle, gives the change in the O—H bond length, and corrected (zero-point and basis set superposition error) molecular binding energy. Both complexes are primarily stabilized through strong hydrogen bond interactions with the inorganic acid acting as the hydrogen bond donor and the NH_3 as the acceptor. The bond distances of the main hydrogen bond interactions, r(OH···N) for the $NH_3{-}H_2SO_4$ and $NH_3{-}HNO_3$ systems are 1.56 Å and 1.66 Å, respectively. Both bond lengths are considerably shorter than the 1.96 Å hydrogen bond length of the water dimer, considered the prototypical hydrogen bonding system.[226,227] Although they look the part, the $O_4{\cdots}H_{10}{-}N_8$ interaction in $NH_3{-}H_2SO_4$ and the $O_5{\cdots}H_7{-}N_6$ interaction in $NH_3{-}HNO_3$ are not true hydrogen bonding interactions. This will be discussed later on. All energy and geometry values are in good agreement with previously published work for the $NH_3{-}H_2SO_4$[222] and $NH_3{-}HNO_3$[223] systems.

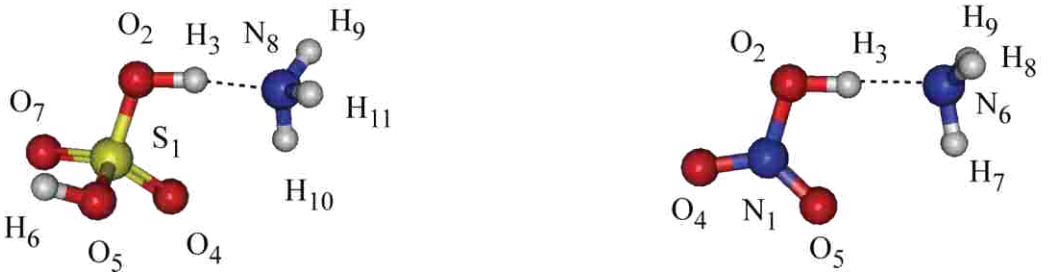

NH_3–H_2SO_4
(-13.6 kcal/mol)

$r(H_3N_8)$ = 1.56 Å
$\Theta(O_2H_3N_8)$ = 172.5°
$r(O_2H_3)$ = 1.04 Å (+ 0.07 Å)

NH_3–HNO_3
(-10.5 kcal/mol)

$r(H_3N_6)$ = 1.65 Å
$\Theta(O_2H_3N_6)$ = 179.4°
$r(O_2H_3)$ = 1.02 Å (+ 0.05 Å)

Figure 7.1. MP2(full)/6-311++G(3df,3pd) optimized structures for the NH_3–H_2SO_4 and NH_3–HNO_3 complexes. Hydrogen bond lengths and angles for each complex are listed along with the change in the acid-O—H bond length.

Qualitatively, the presence and strength of the hydrogen bond present in each complex can be visualized through electrostatic potential difference maps (EPDMs). EPDMs for the NH_3–H_2SO_4 and NH_3–HNO_3 complexes are shown in Figure 7.2. Each map has a surface contour resolution of 0.002 e/au^3. Areas of electron density gain are represented by blue regions and those of electron density loss by red regions. Generally, O—H···N hydrogen bonds are evidenced by a region of electron density loss around the proton acceptor atom.[59,118] Moving along the axis of the hydrogen bond towards the bridging hydrogen atom, a region of electron density gain is observed and is followed by another region of electron density loss around the bridging proton. The relative strength of the O—H···N hydrogen bond for each complex can be assessed by comparing the extent of change in the electrostatic potential that results from complex formation. As

observed from Figure 7.2, the amount of electron density change is most severe in the $NH_3{-}H_2SO_4$ complex and is less so in $NH_3{-}HNO_3$, consistent with the hydrogen bond lengths of the two complexes. It is of note that the EPDMs do not indicate H-bonding for the $O_4{\cdots}H_{10}$ and $O_5{\cdots}H_7$ interactions.

Figure 7.2. EPDMs for the $NH_3{-}H_2SO_4$ and $NH_3{-}HNO_3$ complexes, shown with surface contour resolution of 0.002 e/au^3.

Quantitatively, the presence and strength of the hydrogen bond interaction can be satisfactorily assessed using Natural Bond Orbital (NBO) theory. From an NBO point of view, a hydrogen bond corresponds to a two-electron intermolecular donor-acceptor interaction of the type, nB → σAH*, where nB typically represents a lone pair of the Lewis base B and σAH* is the unfilled anti-AH bond of the Lewis acid. This type of interaction results in the change of certain geometric, energetic, and dielectric observables that can be used to assess the extent of hydrogen bonding. Table 7.1

represents details of the interacting nB (in this instance, nB represents lone pair, bonding, and anti-bonding orbitals) and σAH* NBOs and their diagonal and off-diagonal Fock matrix elements. Figure 7.3 depicts the nB → σAH* (P)NBO 2D-contour diagrams of the leading overlap interaction for each complex and the associated second-order perturbation stabilization energies, $E^{(2)}$, arising from them. The contour diagrams in Figure 7.3 shows only the atoms that lie in the plane of the O—H···N bonding system. The donating nB (P)NBOs are show in red and the acceptor σAH* (P)NBOs are shown in black. The contours of the $O_4\cdots H_{10}-N_8$ and $O_5\cdots H_7-O_6$ interactions are also shown in Figure 7.3 to demonstrate that these interactions to not represent hydrogen bonding interactions. The (P)NBO overlap integral of the $O_4H_{10}N_8$ is 0.0175 and that of the $O_5H_7O_6$ is 0.0082.

Table 7.1. Summary of the major stabilizing NBO interactions between HNO_3 and NH_x.

	Donor		Acceptor				
Complex	n_B	ε_n (a.u.)	σ_{AH}^*	ε_{σ^*} (a.u.)	$F_{n\sigma^*}$	$E^{(2)}$	$\Sigma(E^{(2)})$
$NH_3{-}H_2SO_4$							
major	$(sp^{3.62})_{N(8)}$	-0.5565			0.261	73.7	
minor	$0.84(sp^{2.75})_{N(8)} + 0.55(s)_{H(10)}$	-0.888			0.063	3.5	
other	$0.84(sp^{3.31})_{S(1)} - 0.55(s)_{O(2)}$	0.4526			0.045	2.5	
other	$0.83(sp^{2.86})_{N(8)} + 0.56(s)_{H(9)}$	-0.8909	$0.43(sp^{2.11})O_{(2)} - 0.91(s)H_{(3)}$	0.5423	0.042	1.6	83.8
other	$0.83(sp^{2.87})_{N(8)} + 0.56(s)_{H(11)}$	-0.8907			0.040	1.4	
other	$0.91(sp^{2.11})_{O(2)} + 0.43(s)_{H(3)}$	-1.0361			0.029	0.6	
other	$0.57(sp^{2.35})_{S(1)} + 0.82(s)_{O(7)}$	-1.3278			0.0283	0.5	
$NH_3{-}HNO_3$							
major	$(sp^{3.50})_{N(6)}$	-0.5625			0.223	52.5	
minor	$0.83(sp^{2.82})_{N(6)} + 0.56(s)_{H(7)}$	-0.8839	$0.44(sp^{2.16})_{O(2)} - 0.90(s)_{H(3)}$	0.5791	0.050	2.1	59.7
other	$0.83(sp^{2.87})_{N(6)} + 0.56(s)_{H(8)}$	-0.8864			0.032	0.9	
other	$0.83(sp^{2.87})_{N(6)} + 0.56(s)_{H(9)}$	-0.8864			0.032	0.9	

Note: $E^{(2)}$ values reported in kcal mol^{-1}.

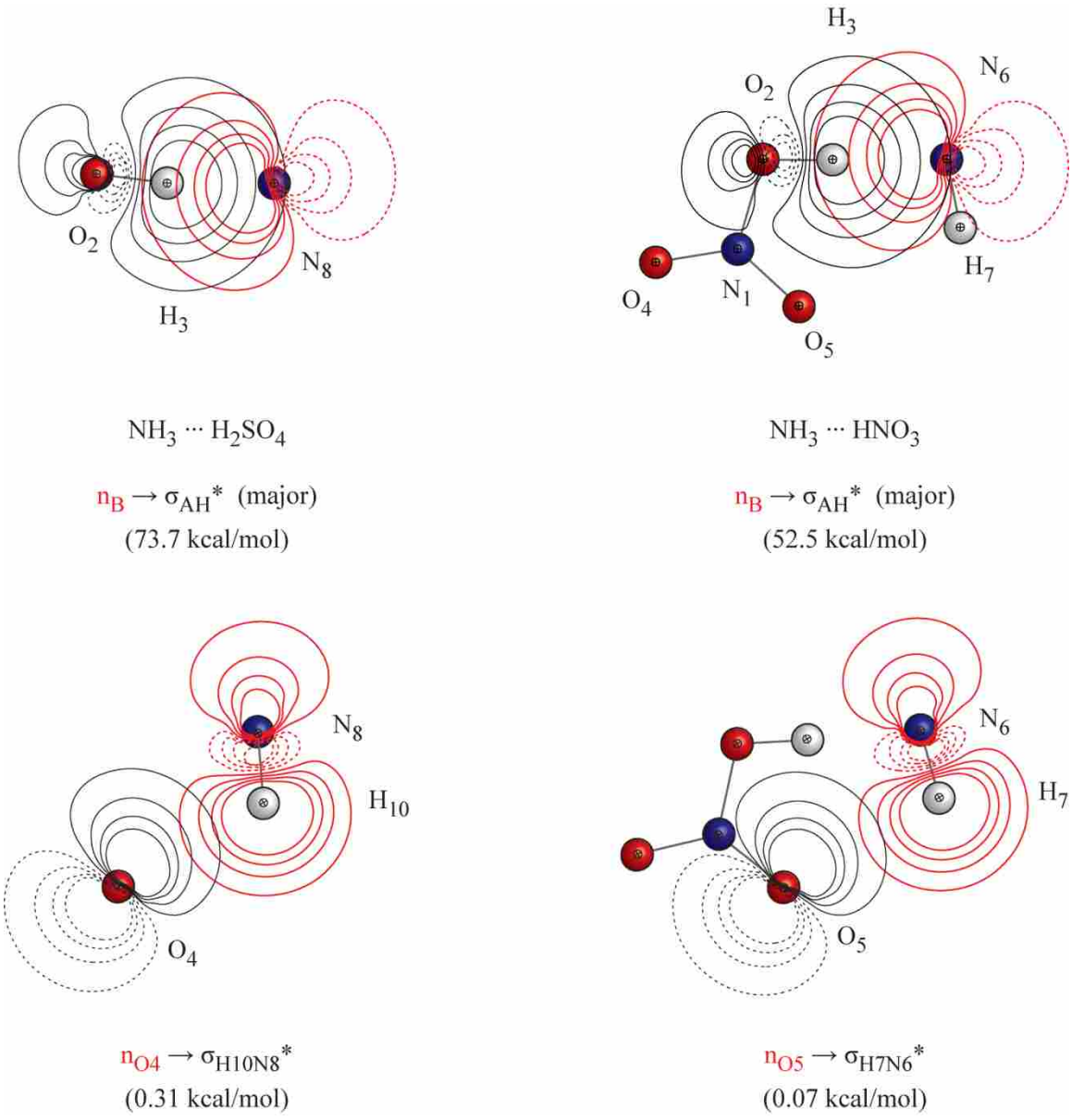

Figure 7.3. 2D-(P)NBO contour maps of the primary NBO interaction for each complex. The contours of the $O_4\cdots H_{10}–N_8$ and $O_5\cdots H_7–N_6$ are also included (bottom half).

The Lewis base and acid of a hydrogen bonded complex will tend towards a linear geometry, as this corresponds to the strongest intermolecular interaction between the acid/base pair as a consequence of maximum nB/σAH* orbital overlap. As can be seen in Figure 7.1, the (O—H)···N angle for each complex is nearly linear. The bond angle for

the O2H3N8 interaction is 172.5° and that of the O2H3N6 interaction is 179.4°. Additionally, the O—H bond length of the Lewis acid will lengthen as a result of the increased occupancy of the σOH* anti-bonding orbital. This lengthening of the O—H bond, shown in Figure 7.1, leads to the characteristic red-shifting of the O—H vibrational frequency and bond weakening; a change of -1398.8 cm^{-1} and -925.3 cm^{-1} for $NH_3{-}H_2SO_4$ and $NH_3{-}HNO_3$, respectively. These frequency shifts are in good agreement with those published previously.[222,223]

Table 7.2 summarizes the charge transfer, (P)NBO overlap integral for the leading nN→σHO* interaction and the A—H bond ionicity for each complex. In hydrogen bonding, the Lewis acid is expected to become slightly anionic as the Lewis base becomes equally cationic; a result of the nN→σHO* intermolecular charge transfer. The extent of charge transfer from nN to σOH* can be correlated with the extent of overlap between the interacting NBOs. The $NH_3{-}H_2SO_4$ complex demonstrates the largest amount of charge transfer as a result of the greatest nN/σOH* overlap. Consequently, the σOH* anti-bond will attempt to repolarize in order to maximize the overlap between the nN and σOH* NBOs, resulting in a withdrawal of electron density from the proton, increasing the ionicity of the O—H bond ($\Delta i_{OH} > 0$). As expected, both complexes experience a positive change in O—H bond ionicity, with that of the $NH_3{-}H_2SO_4$ complex being most pronounced.

Table 7.2. NBO descriptors showing net intermolecular charge transfer ($\Delta Q_{B\rightarrow A}$), bond ionicity ($i_{AH}$), and the (P)NBO overlap integrals for attractive nB-σAH* (Snσ*) interactions.

Complex	$\Delta Q_{B\rightarrow A}$	$S_{n\sigma}$*	Δi_{AH}
NH_3−H_2SO_4			
major	0.1101	0.6078	0.1209
NH_3−HNO_3			
major	0.0803	0.5536	0.1047

The formation of H_2SO_4 and HNO_3 hydrogen bonded complexes of NH_3 weakens the O—H bond of the acid. The net result is that the inorganic acid becomes more anionic while the ammonia becomes more cationic, making each complex resemble the ionic forms found in aerosol particles.

7.4.2 NH_x−acid Complexes

As the concentration of NH_3 becomes more elevated in the atmosphere through increases in agricultural activities, on-road vehicle use and other processes,[228] the importance of the gas-phase oxidation products of ammonia become more significant. These products include the amidogen (NH_2) and imidogen (NH) radicals. As the concentration of these radicals increase, so does the likelihood that they may play a more pronounced role in the formation of atmospheric aerosols. In an effort to ascertain the importance NH_x radicals in the formation of atmospheric aerosols, the gas-phase structures of NH_x−H_2SO_4 and NH_x−HNO_3 have been identified and are presented here for the first time. In addition, the NH_x complexes of formic acid [HC(O)OH] and acetic acid [$CH_3C(O)OH$] are presented here for the first time.

7.4.3 Equilibrium Structures

Figure 7.4 presents the three-dimensional structures of the twelve minimum energy NH_x−acid complexes presented in this work. Each complex can be easily described as a typical hydrogen bonded structure stabilized by the presence of a single O—H···N interaction. The hydrogen bond length *r*(O—H) and angle Θ(O—H···N) of each complex are tabulated in Table 7.3 (columns 1 and 2). As expected, the hydrogen bond angle approaches linearity, consistent with a maximum in the overlap of n_B and σ_{AH}*. The extent of this overlap is manifest in the magnitude of the corresponding hydrogen bond lengths. In the present context, hydrogen bond length are shortest for those complexes of NH_3 and longest for those of NH, suggesting that the overlap of n_B and σ_{OH}* is greater for NH_3.

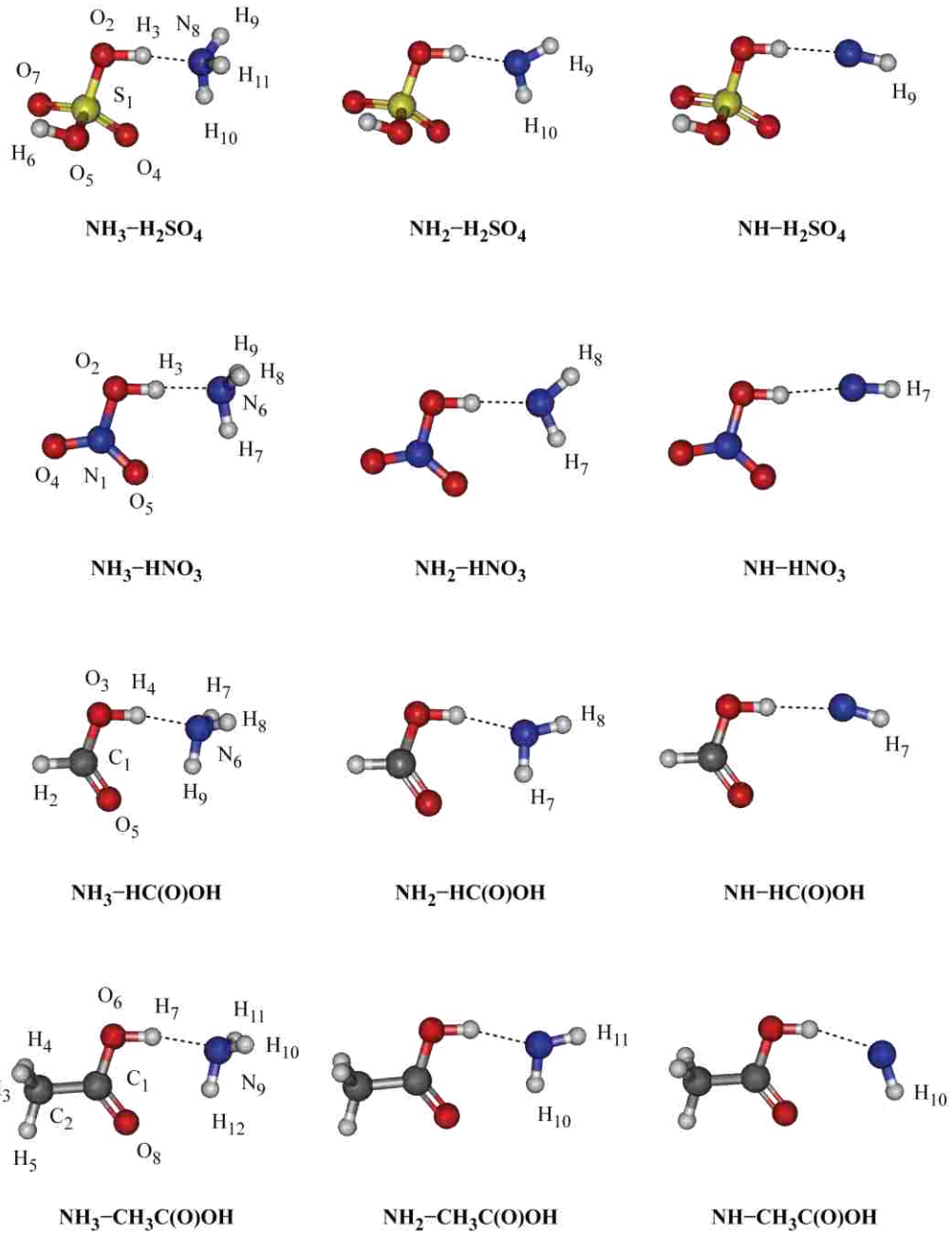

Figure 7.4. Lowest energy NH_x−acid complexes optimized at the MP2(full)/6-311++G(3df,3pd).

Table 7.3. Geometric parameters for the NH_x−acid complexes.

	r (H ··· N), Å	Θ(O—H ··· N), deg.	r (O—H), Å	Δr (O—H), Å	Δν(O—H), cm^{-1}
NH_3−HNO_3	1.65	179.4	1.02	0.05	-925.3
NH_2−HNO_3	1.74	179.6	1.00	0.03	-542.5
NH−HNO_3	1.91	172.5	0.98	0.01	-200.5
NH_3−H_2SO_4	1.56	172.5	1.04	0.07	-1398.8
NH_2−H_2SO_4	1.67	170.3	1.00	0.04	-779.2
NH−H_2SO_4	1.84	176	0.98	0.01	-297.6
NH_3−CHO(OH)	1.73	169.0	1.00	0.03	-724.0
NH_2−CHO(OH)	1.81	166.2	0.99	0.02	-407.8
NH−CHO(OH)	1.96	180.0	0.97	0.01	-155.8
NH_3−$CH_3CO(OH)$	1.75	168.5	1.00	0.03	-651.5
NH_2−$CH_3CO(OH)$	1.83	165.9	0.98	0.02	-365.7
NH−$CH_3CO(OH)$	1.98	161.8	0.97	0.01	-148.9
H_2O−H_2O	1.93	173.1	0.97	0.01	-101.3

Table 7.3 also lists the r(O—H) bond length and the change in this bond length compared with that of the monomer structure (columns 3 and 4). For a given acid series, the r(O—H) bond length increases and the hydrogen bond length decreases. The largest change in r(O—H) bond length is seen in the NH_3−H_2SO_4 complex, 0.07Å. Such a large change in the O—H bond length results in the weakening of the bond and sets up a scenario where proton transfer from H_2SO_4 is facilitated. Previous work by Larson et al.[222] has shown that the addition of a single water molecule to the system, increases r(O—H) by 0.42 Å to 1.46 Å. Such a large r(O—H) bond distance indicates that the O—H bond is broken. The net result is the transfer of a proton from H_2SO_4 to NH_3, giving the ion pair, NH_4^+ and HSO_4^-. This suggests that the nucleation of H_2SO_4 in the presence of H_2O is enhanced by the presence of NH_3 because the NH_3−H_2SO_4 structure strongly resembles the ion pair. To a first approximation, the r(O—H) bond distance can be taken as a rough indictor as to the effect NH_x has on the nucleation of atmospheric acids.

The final column of Table 7.3 lists the change in the vibrational frequency of the O—H bond. As expected, the most significant change takes place with the NH_3−H_2SO_4

complex, $\Delta\nu$ = -1398.8 cm^{-1}. This is significant, especially when viewed against the change computed for the water dimer, -101 cm^{-1} (also shown in Table 7.3 for comparison). This discrepancy can be explained in terms of the magnitude of electron density delocalized into the $O_2{-}H_3$ anti-bond. In the case of the $NH_3{-}H_2SO_4$ complex, an increase of 0.10553 e is observed compared to an increase of only 0.00015 e for the H−O bond of the water dimer.

7.4.4 Binding Energies

Table 7.4 presents the total corrected binding energy for each complex. The binding energy D_e is determined as the difference between the total energy of the complex and the sum of the total energies of the isolated monomers. The zero-point energy correction is added to D_e to give the zero point energy corrected binding energy D_0. Finally, the basis set superposition error, calculated via the counterpoise method is added to D_o to give the final total corrected binding energy $D_{0,cp}$. As expected, those complexes that manifest the shortest intermolecular hydrogen bond have the largest stabilization energy. The binding energy reveals the stability of each complex. Of all the NH_x complexes examined, the $NH_3{-}H_2SO_4$ complex is the most stable, as indicated by the large binding energy, $D_{0,cp}$ = -13.6 kcal/mol. For comparison, a typical hydrogen bond energy, such as in the water dimer, is $D_{0,cp}$ = -2.3 kcal/mol (as calculated and corrected for at the MP2(full)/6-311++G(3df,3pd) level). This large stabilization energy is indicative of a strong hydrogen bond interaction between H_2SO_4 and NH_3, which is in agreement with the unusually short hydrogen bond distance discussed earlier.

Table 7.4. Binding energies (kcal/mol) of the NH_x−acid complexes. Energies are zero-point energy and BSSE corrected.

			MP2(full)/*//	
	MP2(full)/*	QCISD(T)/*	CCSD(T)/*	BD(T)/*
NH_3−HNO_3	-10.5	-10.1	-10.2	-10.2
NH_2−HNO_3	-7.5	-7.1	-7.1	-7.2
NH−HNO_3	-3.8	-3.5	-3.5	-3.5
NH_3−H_2SO_4	-13.6	-12.8	-12.8	-12.8
NH_2−H_2SO_4	-9.8	-9.1	-9.1	-9.1
NH−H_2SO_4	-4.8	-4.4	-4.4	-4.4
NH_3−CHO(OH)	-8.8	-8.3	-8.2	-8.3
NH_2−CHO(OH)	-6.3	-5.8	-5.8	-5.8
NH−CHO(OH)	-2.9	-2.6	-2.6	-2.6
NH_3−CH_3CO(OH)	-8.3	-7.9	-7.9	-7.9
NH_2−CH_3CO(OH)	-6.0	-5.6	-5.6	-5.6
NH−CH_3CO(OH)	-2.9	-2.9	-2.9	-2.9

* Denotes the 6-311++G(3df,3pd) basis set.

7.4.5 Electron Density Difference Maps

As shown before in the case of the NH_3−H_2SO_4 and NH_3−HNO_3 complexes, a qualitative way of viewing the extent of the hydrogen bond interaction is by viewing the relevant electron density difference maps. The maps for the 12 NH_x complexes are shown in Figure 7.5. Looking across an acid series, it is immediately apparent that the extent of change in the electron density is most pronounced in the NH_3 complexes and less so as the multiplicity of the NH_x species increases. This decrease in change as one moves from NH_3 to NH indicates that the n_B and σ_{OH}* overlap is more efficient in the case of complexes of NH_3. These maps also corroborate that each complex is stabilized through the formation of a hydrogen bond, indicated by a region of electron gain around the nitrogen, a region of loss around the proton, and a sequence of regions of electron gain, loss, an gain.[59] The extent of this hydrogen bonding is correlated with the amount of electron density shared between the two monomer units.

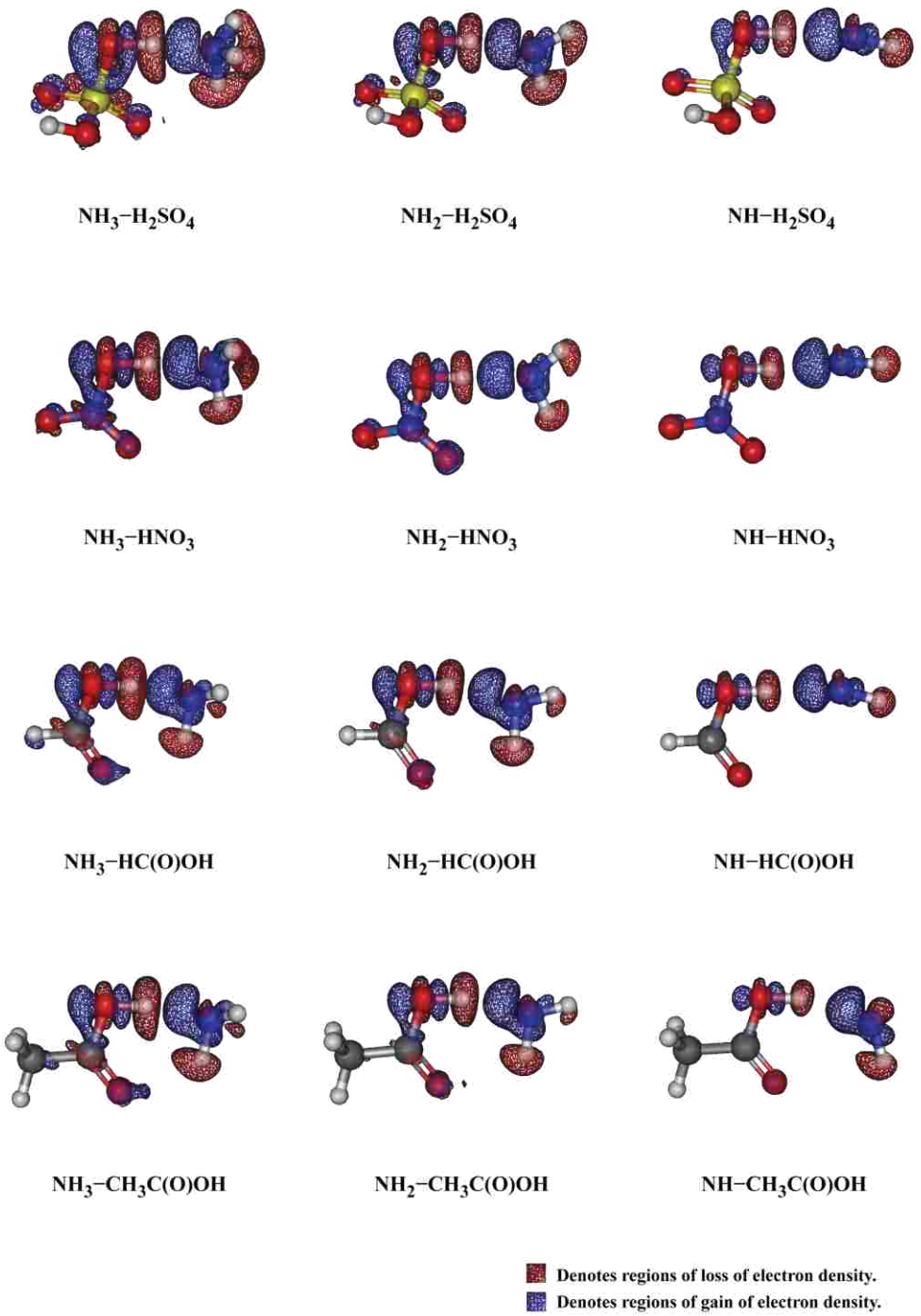

Figure 7.5. EPDMs for the $NH_x{-}H_2SO_4$ and $NH_x{-}HNO_3$ complexes, shown with surface contour resolution of 0.002 e/au^3.

7.4.6 Orbital Overlap Diagrams

The leading $n_N \rightarrow \sigma_{XH}^*$ interaction for each complex is illustrated in Figure 7.6 (only those atoms that lie in the X—H···N plane are depicted). In the case of the NH_2 and NH complexes, only the leading α-spin interaction is depicted. Listed with each overlap image is the second-order perturbative estimate *E(2)* of the stabilization energy arising from the shown interaction and the associated overlap integral $S_{n\sigma}^*$. For the NH_2 and NH complexes, the *E(2)* estimate is the total of the α- and β-spin contributions; whereas, $S_{n\sigma}^*$ represents the interaction shown and is comparable for both spin states. As a point of reference, *E(2)* and $S_{n\sigma}^*$ for the water dimer are 8.1 kcal/mol and 0.2048, respectively. It is clear from Figure 7.6 that the short hydrogen bond distances of these complexes is the result of ideal orbital overlap.

As can be seen in Figure 7.6, the $n_N \rightarrow \sigma_{XH}^*$ interaction becomes less pronounced as the radical nature of the NH_x species increases. As an example, *E(2)* for the NH_3−H_2SO_4 is estimated to be 52.5 kcal mol^{-1}. This interaction is lowered to 39.3 kcal mol^{-1} for NH_2 and 16.7 kcal mol^{-1} for NH. The decrease is a result of poorer overlap between the interacting orbitals. The orbital overlap integral for the $n_N \rightarrow \sigma_{XH}^*$ interaction of the NH_x−H_2SO_4 complexes is reduced by 14.7% and 46.2% for NH_2− and NH−, respectively. The result of this reduction is a complex that is less "salt-like" than NH_3-H_2SO_4. However, the resulting NH_x−acid complexes are more "salt like" than the acid monomers taken alone. The result of this reduction is a complex that is less "salt-like" than NH_3−H_2SO_4. However, the resulting NH_x−acid complexes are more "salt like"

than the acid monomers taken alone with the result that both NH_2 and NH are expected to play a role in the enhancement of the nucleation of each acid.

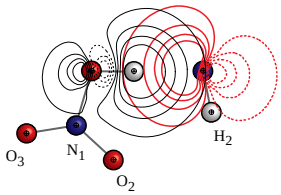

$n_N \rightarrow \sigma_{HO}^*$ (52.5 kcal/mol)

$S_{n\sigma}^*$ (0.5536)

$NH_3 \cdots HNO_3$

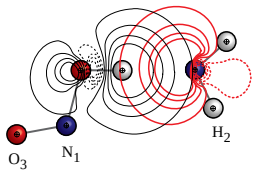

$n_N \rightarrow \sigma_{HO}^*$ (39.3 kcal/mol)$_{total}$

$S_{n\sigma}^*$ (0.4721)

$NH_2 \cdots HNO_3$

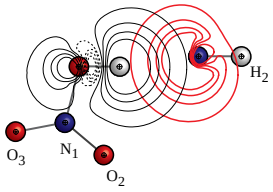

$n_N \rightarrow \sigma_{HO}^*$ (16.7 kcal/mol)$_{total}$

$S_{n\sigma}^*$ (0.2978)

NH $\cdots$ HNO_3

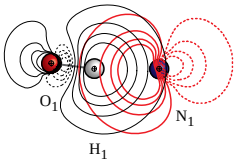

$n_N \rightarrow \sigma_{HO}^*$ (73.7 kcal/mol)

$S_{n\sigma}^*$ (0.6078)

$NH_3 \cdots H_2SO_4$

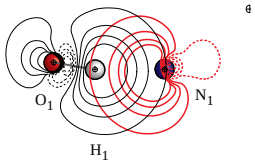

$n_N \rightarrow \sigma_{HO}^*$ (50.4 kcal/mol)$_{total}$

$S_{n\sigma}^*$ (0.5201)

$NH_2 \cdots H_2SO_4$

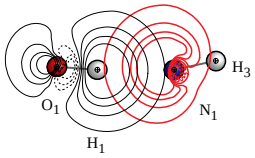

$n_N \rightarrow \sigma_{HO}^*$ (23.1 kcal/mol)$_{total}$

$S_{n\sigma}^*$ (0.3400)

NH $\cdots$ H_2SO_4

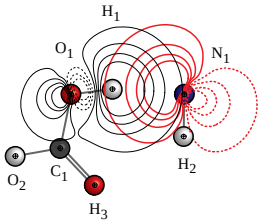

$n_N \rightarrow \sigma_{HO}^*$ (38.7 kcal/mol)

$S_{n\sigma}^*$ (0.4968)

$NH_3 \cdots CHO(OH)$

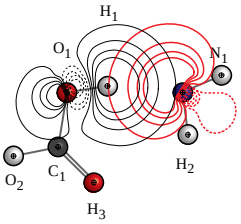

$n_N \rightarrow \sigma_{HO}^*$ (26.9 kcal/mol)$_{total}$

$S_{n\sigma}^*$ (0.4042)

$NH_2 \cdots CHO(OH)$

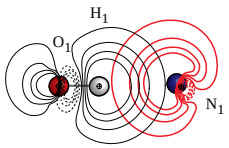

$n_N \rightarrow \sigma_{HO}^*$ (12.5 kcal/mol)$_{total}$

$S_{n\sigma}^*$ (0.2718)

NH $\cdots$ CHO(OH)

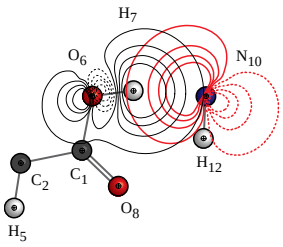

$n_N \rightarrow \sigma_{HO}^*$ (35.4 kcal/mol)

$S_{n\sigma}^*$ (0.4860)

$NH_3 \cdots CH_3CO(OH)$

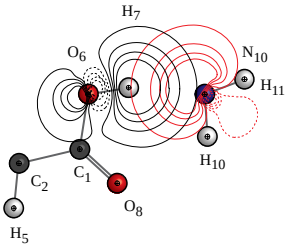

$n_N \rightarrow \sigma_{HO}^*$ (24.0 kcal/mol)$_{total}$

$S_{n\sigma}^*$ (0.3881)

$NH_2 \cdots CH_3CO(OH)$

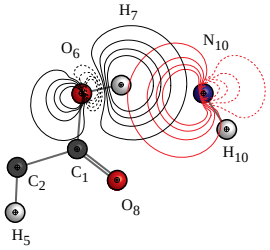

$n_N \rightarrow \sigma_{HO}^*$ (11.2 kcal/mol)$_{total}$

$S_{n\sigma}^*$ (0.2918)

NH $\cdots$ $CH_3CO(OH)$

Figure 7.6. 2D (P)NBO contour maps of the leading interactions between NH_x and the corresponding acid. The 2nd-order purterbative stabilization energy for each interaction is listed in parenthesis. The orbital overlap integral sum is also listed for each interaction.

7.5 Thermodynamics

7.5.1 Gibb's Free Energy

The binding energies listed in Table 7.4 represent the BSSE corrected Gibb's free energy of formation, ΔG_f for each of the NH_x−acid complexes as determined at 0 K ($\Delta G = \Delta H - \Delta S(0\ K)$). To ascertain the importance of complex formation at more elevated, atmospherically relevant temperatures, estimations of ΔG_f for each complex in the temperature range of 220-300 K were made and are listed in Table 7.5. Complexes of NH_3 will all acids have strong ΔG_f, even at temperatures as high as 300 K. This is significant because the formation of atmospheric aerosols may be enhanced by complex formation even at elevated temperatures. The Gibb's energy for complexes of NH_2 is significant for HNO_3 and H_2SO_4 at all of the temperatures listed. Complexes of formic acid and acetic acid are expected to form at temperatures below ~260 K. Above this temperature, the Gibb's energy is only slightly positive and it may be argued that complex formation is probable for those temperatures within the error of the calculations. Complexes of NH are only predicted to be significant within the temperature range probed for sulfuric acid, and only then at temperatures colder than ~260 K. The data suggest that in general NH complexes are not going to be significant under atmospheric conditions.

Table 7.5. Gibb's free energy of formation for the NH_x−acid complexes, as determined at the MP2(full)/6-311++G(3df,3pd) computational level.

	HNO_3			H_2SO_4			HC(O)OH			$CH_3C(O)OH$		
	NH_3	NH_2	NH	NH_3	NH_2	NH	NH_3	NH_2	NH	NH_3	NH_2	NH
220	-6.3	-3.2	0.2	-9.8	-5.7	-1.2	-4.2	-1.7	0.9	-3.6	-1.3	1.4
230	-6.1	-2.9	0.4	-9.5	-5.4	-0.9	-3.9	-1.4	1.2	-3.3	-1.0	1.7
240	-5.8	-2.6	0.7	-9.2	-5.1	-0.7	-3.6	-1.1	1.4	-3.0	-0.7	1.9
250	-5.5	-2.3	0.9	-8.9	-4.8	-0.4	-3.4	-0.8	1.6	-2.7	-0.4	2.2
260	-5.2	-2.1	1.2	-8.6	-4.5	-0.2	-3.1	-0.6	1.9	-2.5	-0.1	2.4
270	-4.9	-1.8	1.4	-8.3	-4.2	0.1	-2.8	-0.3	2.1	-2.2	0.2	2.6
280	-4.6	-1.5	1.6	-8.0	-3.9	0.3	-2.5	0.0	2.3	-1.9	0.5	2.9
290	-4.4	-1.2	1.9	-7.7	-3.6	0.6	-2.2	0.3	2.5	-1.6	0.7	3.1
300	-4.1	-1.0	2.1	-7.4	-3.4	0.8	-1.9	0.6	2.8	-1.3	1.0	3.4

Note: Values are reported in kcal/mol.

7.5.2 Equilibrium and Dissociation Constants

The equilibrium and dissociation constants were determined for each NH_x complex and are reported in Table 7.6. For complexes of NH_3, both nitric acid and sulfuric acid have equilibrium constants that lay orders of magnitude below the dissociations constants at temperatures colder then ~260 K for nitric acid and for all temperatures considered for sulfuric acid. This reflects strong complex formation as represented in the respective binding energies. For complexes of NH_2, the ration of K_{EQ} to k_{DISS} (K_{EQ}/k_{DISS}) is greater than one for only H_2SO_4 at temperatures at or below 240 K. This ratio is less than for all complexes of NH, an indication of the minimal role NH is expected to play in the formation of new atmospheric aerosols.

Table 7.6. Equilibrium an Dissociation Constants for the NH_x−acid complexes.

	HNO_3						H_2SO_4					
	NH_3		NH_2		NH		NH_3		NH_2		NH	
T, K	$\mathbf{K_{EQ}}$	$\boldsymbol{k}_{\mathbf{DISS}}$	$\mathbf{K_{EQ}}$	$\boldsymbol{k}_{\mathbf{DISS}}$	$\mathbf{K_{EQ}}$	$\boldsymbol{k}_{\mathbf{DISS}}$	$\mathbf{K_{EQ}}$	$\boldsymbol{k}_{\mathbf{DISS}}$	$\mathbf{K_{EQ}}$	$\boldsymbol{k}_{\mathbf{DISS}}$	$\mathbf{K_{EQ}}$	$\boldsymbol{k}_{\mathbf{DISS}}$
220	1.01E-14	1.54E-18	1.04E-17	2.65E-16	8.74E-20	3.40E-14	8.27E-12	3.81E-20	3.79E-15	2.19E-17	1.48E-19	9.25E-15
230	3.11E-15	4.51E-18	4.44E-18	5.60E-16	5.08E-20	4.94E-14	1.85E-12	1.54E-19	1.22E-15	5.84E-17	8.39E-20	1.47E-14
240	1.06E-15	1.19E-17	2.05E-18	1.10E-15	3.10E-20	6.91E-14	4.69E-13	5.47E-19	4.30E-16	1.41E-16	4.99E-20	2.22E-14
250	3.95E-16	2.90E-17	1.01E-18	2.03E-15	1.98E-20	9.33E-14	1.33E-13	1.73E-18	1.66E-16	3.15E-16	3.10E-20	3.21E-14
260	1.59E-16	6.51E-17	5.24E-19	3.55E-15	1.31E-20	1.22E-13	4.16E-14	4.96E-18	6.88E-17	6.51E-16	2.00E-20	4.45E-14
270	6.88E-17	1.37E-16	2.87E-19	5.90E-15	8.92E-21	1.56E-13	1.42E-14	1.30E-17	3.06E-17	1.26E-15	1.34E-20	5.96E-14
280	3.16E-17	2.70E-16	1.64E-19	9.39E-15	6.27E-21	1.94E-13	5.25E-15	3.13E-17	1.44E-17	2.30E-15	9.22E-21	7.75E-14
290	1.54E-17	5.05E-16	9.82E-20	1.44E-14	4.53E-21	2.36E-13	2.08E-15	7.02E-17	7.17E-18	3.99E-15	6.53E-21	9.79E-14
300	7.86E-18	9.00E-16	6.08E-20	2.12E-14	3.35E-21	2.82E-13	8.79E-16	1.48E-16	3.75E-18	6.59E-15	4.75E-21	1.21E-13

	HC(O)OH						$CH_3C(O)OH$					
	NH_3		NH_2		NH		NH_3		NH_2		NH	
T, K	$\mathbf{K_{EQ}}$	$\boldsymbol{k}_{\mathbf{DISS}}$	$\mathbf{K_{EQ}}$	$\boldsymbol{k}_{\mathbf{DISS}}$	$\mathbf{K_{EQ}}$	$\boldsymbol{k}_{\mathbf{DISS}}$	$\mathbf{K_{EQ}}$	$\boldsymbol{k}_{\mathbf{DISS}}$	$\mathbf{K_{EQ}}$	$\boldsymbol{k}_{\mathbf{DISS}}$	$\mathbf{K_{EQ}}$	$\boldsymbol{k}_{\mathbf{DISS}}$
220	3.99E-19	1.54E-17	2.56E-19	9.33E-16	1.70E-21	8.57E-14	1.27E-19	1.07E-16	1.15E-19	2.40E-15	1.15E-21	2.75E-14
230	1.87E-19	3.78E-17	1.26E-19	1.76E-15	1.21E-21	1.12E-13	6.23E-20	2.35E-16	5.85E-20	4.15E-15	8.18E-22	3.38E-14
240	9.35E-20	8.51E-17	6.58E-20	3.12E-15	8.97E-22	1.43E-13	3.26E-20	4.80E-16	3.16E-20	6.78E-15	5.98E-22	4.04E-14
250	4.96E-20	1.78E-16	3.63E-20	5.25E-15	6.80E-22	1.77E-13	1.80E-20	9.14E-16	1.79E-20	1.05E-14	4.50E-22	4.71E-14
260	2.77E-20	3.50E-16	2.11E-20	8.41E-15	5.29E-22	2.14E-13	1.04E-20	1.64E-15	1.07E-20	1.56E-14	3.47E-22	5.38E-14
270	1.62E-20	6.49E-16	1.28E-20	1.29E-14	4.20E-22	2.54E-13	6.32E-21	2.78E-15	6.63E-21	2.22E-14	2.74E-22	6.02E-14
280	9.85E-21	1.14E-15	8.04E-21	1.91E-14	3.40E-22	2.96E-13	3.98E-21	4.50E-15	4.27E-21	3.06E-14	2.20E-22	6.64E-14
290	6.21E-21	1.92E-15	5.23E-21	2.74E-14	2.80E-22	3.40E-13	2.59E-21	6.98E-15	2.84E-21	4.09E-14	1.80E-22	7.21E-14
300	4.05E-21	3.11E-15	3.52E-21	3.81E-14	2.34E-22	3.84E-13	1.74E-21	1.04E-14	1.94E-21	5.31E-14	1.50E-22	7.73E-14

* k_{DISS} is reported in cm^3 $molecules^{-1}$ s^{-1}.

7.5.3 Lifetime and Collisional Frequency

Atmospheric lifetimes and collisional frequencies for each NH_x complex were calculated over the same 220-300 K temperature range and the results are listed in Table 7.7. For complexes of NH_x to have an effect on the formation of atmospheric aerosols, they need to exist long enough to experience sufficient collisions with water as to form condensation nuclei. It can be seen by comparison of Tables 7.4 and 7.7 that those complexes with the largest binding energies have the longest atmospheric lifetimes. The lifetime of $NH_3{-}H_2SO_4$ at 220 K is quite large, 4 s. The collisional frequency will be dependent on the amount of water vapor present and this is in large part dependent of the prevalent temperature. For the estimates given here, a relative humidity of 50% at each temperature was assumed. The lifetime for $NH_2{-}H_2SO_4$ complexes are in the millisecond timeframe from 240 – 220 K. This should have both *in situ* and laboratory significance for their direct observation.

Table 7.7. Lifetime and collisional frequencies for the NH_x−acid complexes.

	HNO_3						H_2SO_4					
	NH_3		NH_2		NH		NH_3		NH_2		NH	
T, K	**τ**	υ_{coll}	**τ**	υ_{coll}	**τ**	υ_{coll}	**τ**	υ_{coll}	**τ**	υ_{coll}	**τ**	υ_{coll}
220	1.03E-01	8.85E+03	5.99E-04	1.02E+04	4.67E-06	1.10E+04	4.17E+00	9.89E+03	7.25E-03	1.05E+04	1.72E-05	1.10E+04
230	2.91E-02	3.66E+04	2.34E-04	4.23E+04	2.65E-06	4.55E+04	8.51E-01	4.09E+04	2.25E-03	4.36E+04	8.92E-06	4.54E+04
240	9.18E-03	8.84E+04	9.94E-05	1.02E+05	1.58E-06	1.10E+05	2.00E-01	9.88E+04	7.74E-04	1.05E+05	4.93E-06	1.10E+05
250	3.18E-03	2.34E+05	4.53E-05	2.71E+05	9.87E-07	2.92E+05	5.31E-02	2.62E+05	2.92E-04	2.79E+05	2.87E-06	2.91E+05
260	1.20E-03	6.19E+05	2.19E-05	7.16E+05	6.37E-07	7.71E+05	1.57E-02	6.92E+05	1.19E-04	7.37E+05	1.75E-06	7.68E+05
270	4.86E-04	1.44E+06	1.12E-05	1.67E+06	4.26E-07	1.80E+06	5.12E-03	1.61E+06	5.26E-05	1.72E+06	1.11E-06	1.79E+06
280	2.10E-04	2.99E+06	6.05E-06	3.46E+06	2.93E-07	3.72E+06	1.82E-03	3.34E+06	2.47E-05	3.56E+06	7.33E-07	3.71E+06
290	9.68E-05	5.70E+06	3.41E-06	6.60E+06	2.07E-07	7.10E+06	6.97E-04	6.37E+06	1.23E-05	6.79E+06	4.99E-07	7.08E+06
300	4.70E-05	1.03E+07	2.00E-06	1.19E+07	1.50E-07	1.28E+07	2.86E-04	1.15E+07	6.42E-06	1.23E+07	3.50E-07	1.28E+07

	HC(O)OH						$CH_3C(O)OH$					
	NH_3		NH_2		NH		NH_3		NH_2		NH	
T, K	**τ**	υ_{coll}	**τ**	υ_{coll}	**τ**	υ_{coll}	**τ**	υ_{coll}	**τ**	υ_{coll}	**τ**	υ_{coll}
220	1.03E-02	8.57E+03	1.70E-04	9.95E+03	1.85E-06	1.06E+04	1.49E-03	1.21E+04	6.62E-05	1.37E+04	5.77E-06	1.07E+04
230	3.47E-03	3.54E+04	7.45E-05	4.11E+04	1.17E-06	4.39E+04	5.57E-04	5.02E+04	3.16E-05	5.65E+04	3.88E-06	4.43E+04
240	1.29E-03	8.56E+04	3.51E-05	9.94E+04	7.67E-07	1.06E+05	2.28E-04	1.21E+05	1.62E-05	1.37E+05	2.71E-06	1.07E+05
250	5.16E-04	2.27E+05	1.75E-05	2.63E+05	5.20E-07	2.81E+05	1.01E-04	3.22E+05	8.76E-06	3.62E+05	1.95E-06	2.84E+05
260	2.22E-04	5.99E+05	9.25E-06	6.95E+05	3.63E-07	7.42E+05	4.75E-05	8.49E+05	4.99E-06	9.55E+05	1.45E-06	7.49E+05
270	1.02E-04	1.40E+06	5.13E-06	1.62E+06	2.61E-07	1.73E+06	2.39E-05	1.98E+06	2.98E-06	2.23E+06	1.10E-06	1.75E+06
280	4.97E-05	2.89E+06	2.97E-06	3.36E+06	1.92E-07	3.59E+06	1.26E-05	4.10E+06	1.85E-06	4.61E+06	8.55E-07	3.62E+06
290	2.54E-05	5.52E+06	1.78E-06	6.40E+06	1.44E-07	6.84E+06	7.00E-06	7.82E+06	1.20E-06	8.80E+06	6.78E-07	6.90E+06
300	1.36E-05	9.97E+06	1.11E-06	1.16E+07	1.10E-07	1.24E+07	4.06E-06	1.41E+07	7.97E-07	1.59E+07	5.47E-07	1.25E+07

* Lifetime is reported in s. υ_{coll} is reported in collisions/s^{-1}.

7.6 Conclusions

The present work has demonstrated the existence of hydrogen bond stabilized complexes of NH_x with HNO_3, H_2SO_4, formic and acetic acid. The calculated binding energies of all the acid complexes of NH_3 and NH_2 are greater than or equivalent to that of the water dimer, which has a binding energy of -5.0 kcal mol^{-1}.[229] The water dimer is a useful comparison as it is broadly held as the standard for atmospheric hydrogen bonded complexes. The acid−NH complexes have weaker binding energies between -2.9 kcal mol^{-1} and -4.8 kcal mol^{-1}, a result of the double radical nature of the NH diradical.

The results presented here suggest that the effect of NH_3 of the formation of new aerosol particles will be imitated by NH_2 and NH, although to a lesser degree. This can be seen by observing the trend in the change of electron density for a given acid as a function of the multiplicity of NH_x. As the radical nature of NH_x increases, the extent to which electron density is delocalized into a hydrogen bond interaction is decreased. This decrease in electron delocalization is quantitatively expressed by the trend in the (P)NBO overlap integrals and in the 2^{nd}-order perturbative estimates of the stabilization energy.

A mitigating factor for the relevance of NH_2 and NH in the formation of new aerosol particles will be their respective concentrations at temperatures relevant to the atmosphere. The binding energies expressed for each NH_x−acid complex are based on *ab initio* calculations that assume a temperature of 0 K. The actual formation of each complex will involve interplay between the enthalpies and entropies of formation. The Gibb's free energy of formation for complexes of NH_3 is found to be favorable at all temperatures between 220 and 300 K. The NH_2−H_2SO_4 and NH_2−HNO_3 complexes are also expected to be of importance within the same temperature range and must be

considered in nucleation models germane to these acids. The remaining complexes of NH_2 are only expected to be relevant at temperatures below 280 K. The NH radical is only expected to play a role in nucleation in the case of H_2SO_4 and at temperatures below 270 K. However, the full importance of the NH radical in nucleation is expected to be minimal as the atmospheric concentration of this radical species is expected to be very low.

7.7 Supplementary Tables

Tables S7.1 through S7.6 represent the MP2(full)/6-311++G(3df,3pd) optimized geometries and S7.7 through S7.12 represent the B3LYP/6-311++G(3df,3pd) harmonic vibrational frequencies.

7.7.1 Cartesian Coordinates for Each Optimized Geometry

Table S7.1. MP2(full)/6-311++G(3df3,dp) optimized geometries for NH_3, NH_2, and NH.

NH_3				
	N	-2.4015	-1.2103	-0.1686
	H	-2.8309	-0.3889	-0.5709
	H	-2.9646	-1.4774	0.6267
	H	-2.4855	-1.9508	-0.8510
NH_2				
	N	1.9584	2.7608	0.1381
	H	1.3377	3.4071	-0.3507
	H	2.7734	3.3357	0.3549
NH				
	N	-1.7910	1.2362	2.3826
	H	-2.7594	1.3074	2.7235

Table S7.2. MP2(full)/6-311++G(3df3,dp) optimized geometries for H_2SO_4, HNO_3, HC(O)OH and $CH_3C(O)OH$.

H_2SO_4				
	S	-0.1158	0.4446	-0.0874
	O	-0.4142	-0.9882	0.5081
	H	0.3801	-1.3029	0.9581
	O	0.8656	1.0768	0.7150
	O	0.6144	0.0932	-1.4440
	H	-0.0571	-0.0999	-2.1106
	O	-1.3846	1.0007	-0.3831
HNO_3				
	N	0.2770	-0.0788	-0.2241
	O	0.6465	0.6738	0.8904
	H	-0.2038	0.8173	1.3324
	O	1.1956	-0.3771	-0.9312
	O	-0.9024	-0.3231	-0.3218
HC(O)OH				
	C	0.2939	-1.7676	2.1457
	H	-0.0933	-2.7870	2.2023
	O	0.0614	-1.2619	0.9273
	H	0.4203	-0.3640	0.9276
	O	0.8446	-1.1884	3.0406
$CH_3C(O)OH$				
	C	0.8359	0.0000	0.0536
	C	0.7660	0.0000	-1.4382
	H	0.2201	-0.8767	-1.7762
	H	0.2201	0.8767	-1.7762
	H	1.7672	0.0000	-1.8493
	O	-0.3985	0.0000	0.6020
	H	-0.2628	0.0000	1.5583
	O	1.8406	0.0000	0.7189

Table S7.3. MP2(full)/6-311++G(3df3,dp) optimized geometries for NH_3-H_2SO_4, NH_2-H_2SO_4, and NH-H_2SO_4.

$NH_3-H_2SO_4$				
	S	-0.3714	0.0573	-0.1700
	O	-0.2340	-1.3400	-0.8034
	H	0.6989	-1.7278	-0.5631
	O	0.4973	0.1606	0.9562
	O	0.2914	1.0089	-1.2616
	H	-0.3749	1.1928	-1.9345
	O	-1.7539	0.3763	-0.0943
	N	2.0904	-2.1917	-0.0381
	H	2.1159	-3.1237	0.3542
	H	2.2316	-1.5281	0.7163
	H	2.8654	-2.1041	-0.6821
$NH_2-H_2SO_4$				
	S	-0.2320	-0.1661	0.9821
	O	1.1096	-0.3595	0.2278
	H	1.6958	0.4352	0.4084
	O	-0.0242	0.6654	2.1180
	O	-1.0701	0.7365	-0.0214
	H	-1.4512	0.1586	-0.6937
	O	-0.8568	-1.4381	1.0625
	N	2.5140	1.7919	0.9414
	H	3.3378	2.3470	0.7252
	H	2.0767	2.2023	1.7649
$NH-H_2SO_4$				
	S	-0.1412	0.4547	-0.0858
	O	-0.3834	-0.9615	0.5313
	H	0.4379	-1.2559	0.9773
	O	0.8052	1.1583	0.7034
	O	0.6246	0.1117	-1.4317
	H	-0.0315	-0.1418	-2.0927
	O	-1.4221	0.9668	-0.4161
	N	2.0108	-1.6841	1.8225
	H	2.9195	-1.7109	2.2955

Table S7.4. MP2(full)/6-311++G(3df3,dp) optimized geometries for $NH_3{-}HNO_3$, $NH_2{-}HNO_3$, and $NH{-}HNO_3$.

$NH_3{-}HNO_3$				
	N	0.1805	0.8755	-0.0099
	O	0.1030	-0.4208	0.3849
	H	-0.8467	-0.7118	0.1722
	O	1.2507	1.3999	0.1661
	O	-0.8245	1.3662	-0.4938
	N	-2.3927	-1.2032	-0.1683
	H	-2.7829	-0.3585	-0.5682
	H	-2.9623	-1.4590	0.6277
	H	-2.4828	-1.9397	-0.8559
$NH_2{-}HNO_3$				
	N	-0.0156	0.0295	0.0004
	O	1.2224	0.1412	0.5662
	H	1.4857	1.0888	0.4097
	O	-0.5125	-1.0632	0.0873
	O	-0.4705	1.0302	-0.5198
	N	1.9582	2.7447	0.1421
	H	1.2741	3.3095	-0.3581
	H	2.7470	3.3562	0.3404
$NH{-}HNO_3$				
	N	0.2918	-0.0793	-0.2279
	O	0.6075	0.6666	0.8871
	H	-0.2567	0.8084	1.3246
	O	1.2353	-0.3644	-0.9137
	O	-0.8798	-0.3507	-0.3761
	N	-1.8149	1.2130	2.3503
	H	-2.7206	1.3622	2.8075

Table S7.5. MP2(full)/6-311++G(3df3,dp) optimized geometires for NH_3−HC(O)OH, NH_2−HC(O)OH, and NH−HC(O)OH.

NH_3−HC(O)OH				
	C	-1.5449	1.8578	0.4549
	H	-2.0929	2.6793	-0.0159
	O	-1.4791	0.8134	-0.3514
	H	-0.9713	0.0907	0.1202
	O	-1.0744	1.9290	1.5677
	N	-0.0735	-0.9381	1.1808
	H	-0.5194	-1.7617	1.5623
	H	0.8746	-1.1910	0.9360
	H	-0.0305	-0.2382	1.9142
NH_2−HC(O)OH				
	C	-1.6582	2.0378	0.1982
	H	-2.3334	2.8427	0.5009
	O	-1.9604	0.9149	0.8335
	H	-1.3309	0.2173	0.5333
	O	-0.7685	2.1803	-0.6062
	N	-0.0172	-0.7401	-0.2608
	H	0.4157	-0.0412	-0.8650
	H	0.4940	-1.6084	-0.4020
NH−HC(O)OH				
	C	-1.6186	2.1011	0.2985
	H	-2.6729	2.2935	0.5139
	O	-1.4269	0.8005	0.0844
	H	-0.4804	0.6651	-0.1037
	O	-0.7677	2.9510	0.2636
	N	1.4269	0.3923	-0.4828
	H	2.4307	0.5286	-0.6450

Table S7.6. MP2(full)/6-311++G(3df3,dp) optimized geometries for $NH_3{-}CH_3C(O)OH$, $NH_2{-}CH_3C(O)OH$, and $NH{-}CH_3C(O)OH$.

$NH_3{-}CH_3C(O)OH$				
	C	-0.2910	-0.7729	0.9480
	C	0.8669	-1.4982	0.3355
	H	0.6080	-1.8062	-0.6742
	H	1.7177	-0.8259	0.2628
	H	1.1217	-2.3616	0.9370
	O	-0.6405	0.2984	0.2399
	H	-1.4116	0.7313	0.7004
	O	-0.8497	-1.1172	1.9708
	N	-2.7275	1.2292	1.7386
	H	-3.6820	1.1642	1.4115
	H	-2.6489	2.0774	2.2832
	H	-2.5522	0.4421	2.3553
$NH_2{-}CH_3C(O)OH$				
	C	-1.6582	2.0378	0.1982
	H	-2.3334	2.8427	0.5009
	O	-1.9604	0.9149	0.8335
	H	-1.3309	0.2173	0.5333
	O	-0.7685	2.1803	-0.6062
	N	-0.0172	-0.7401	-0.2608
	H	0.4157	-0.0412	-0.8650
	H	0.4940	-1.6084	-0.4020
$NH{-}CH_3C(O)OH$				
	C	0.1155	0.0676	0.4336
	C	-0.0795	-1.3348	0.9136
	H	-1.0807	-1.6699	0.6562
	H	0.6247	-1.9913	0.4095
	H	0.0672	-1.3789	1.9851
	O	-0.0588	0.1625	-0.8934
	H	0.0829	1.0954	-1.1300
	O	0.3952	1.0138	1.1331
	N	0.4691	3.0347	-0.9927
	H	0.6946	3.5889	-0.1592

7.7.2 Harmonic Vibrational Frequencies

Table S7.7. B3LYP/6-311++G(3df3,dp) harmonic vibrational frequencies for NH_3, NH_2, and NH.

NH_3	1021.4	1657.4	3685.0
	1657.4	3537.6	3685.0
NH_2	1532.1	3482.5	3582.3
NH	3449.3		

Table S7.8. B3LYP/6-311++G(3df3,dp) harmonic vibrational frequencies for H_2SO_4, HNO_3, HC(O)OH, and $CH_3C(O)OH$.

H_2SO_4	261.6	549.2	1160.0
	346.0	563.6	1255.1
	383.0	848.2	1506.6
	448.0	897.4	3829.2
	500.9	1140.4	3833.7
HNO_3	502.4	793.3	1349.3
	597.0	916.7	1867.2
	681.5	1339.8	3774.5
HC(O)OH	631.1	1140.9	1815.9
	683.8	1306.6	3130.0
	1065.6	1415.4	3799.2
$CH_3C(O)OH$	96.3	1011.5	1497.7
	428.0	1077.5	1829.8
	558.5	1210.2	3088.5
	589.7	1347.6	3176.8
	671.9	1428.8	3220.7
	883.8	1487.4	3810.8

Table S7.9. B3LYP/6-311++G(3df3,dp) harmonic vibrational frequencies for $NH_3{-}H_2SO_4$, $NH_2{-}H_2SO_4$, and $NH{-}H_2SO_4$.

$NH_3{-}H_2SO_4$	43.2	538.2	1434.3
	94.7	565.1	1530.4
	125.8	576.9	1659.9
	251.8	841.4	1667.3
	282.8	965.9	2434.9
	351.4	1150.6	3512.8
	389.3	1153.1	3645.8
	426.8	1190.2	3669.6
	461.2	1238.6	3843.1
$NH_2{-}H_2SO_4$	46.3	445.2	1244.2
	104.7	532.8	1387.6
	143.7	559.1	1490.5
	242.6	568.8	1523.5
	278.0	847.1	3054.5
	331.5	942.6	3513.7
	381.2	965.7	3625.5
	408.3	1152.0	3839.9
$NH{-}H_2SO_4$	41.4	435.7	1151.5
	56.4	517.7	1250.5
	199.1	552.4	1271.3
	252.3	565.7	1496.2
	269.6	746.2	3501.2
	291.8	851.1	3536.1
	390.7	920.9	3837.7

Table S7.10. B3LYP/6-311++G(3df3,dp) harmonic vibrational frequencies for $NH_3{-}HNO_3$, $NH_2{-}HNO_3$, and $NH{-}HNO_3$.

$NH_3{-}HNO_3$	61.9	710.3	1656.7
	76.5	809.7	1664.9
	121.6	987.4	1823.3
	254.2	1130.3	2849.2
	326.3	1135.3	3520.4
	408.2	1355.2	3658.3
	668.8	1550.0	3666.9
$NH_2{-}HNO_3$	74.2	652.5	1496.0
	96.4	709.9	1534.6
	105.0	801.6	1840.7
	232.4	963.0	3232.0
	321.6	993.1	3511.7
	370.3	1396.9	3618.2
$NH{-}HNO_3$	67.4	624.3	1351.2
	68.4	697.4	1412.7
	180.3	777.2	1847.6

Table S7.11. B3LYP/6-311++G(3df3,dp) harmonic vibrational frequencies for NH_3−HC(O)OH, NH_2−HC(O)OH and NH−HC(O)OH.

NH_3−HC(O)OH	116.0	1057.0	1671.4
	122.9	1110.1	1780.4
	183.9	1144.6	3075.2
	253.6	1245.6	3115.2
	326.4	1405.8	3508.6
	424.2	1492.6	3646.0
	710.0	1653.3	3672.5
NH_2−HC(O)OH	113.8	691.3	1513.1
	163.7	970.5	1790.2
	184.6	1084.7	3111.1
	227.3	1224.2	3391.4
	324.5	1394.0	3495.4
	375.9	1453.7	3610.4
NH−HC(O)OH	43.5	661.0	1427.6
	141.2	858.6	1804.3
	178.6	1074.1	3114.1
	235.8	1186.6	3487.5
	254.2	1351.2	3643.4

Table S7.12. B3LYP/6-311++G(3df3,dp) harmonic vibrational frequencies for $NH_3{-}CH_3C(O)OH$, $NH_2{-}CH_3C(O)OH$ and $NH{-}CH_3C(O)OH$.

$NH_3{-}CH_3C(O)OH$	73.8	908.9	1651.4
	91.9	1029.2	1673.7
	125.6	1076.7	1789.9
	130.4	1094.3	3085.5
	222.1	1099.8	3159.3
	297.2	1317.7	3173.9
	406.3	1408.3	3215.4
	466.4	1478.3	3505.2
	607.7	1492.9	3644.0
	637.0	1497.6	3674.3
$NH_2{-}CH_3C(O)OH$	71.8	625.2	1497.4
	92.9	903.6	1508.9
	117.6	947.2	1800.2
	183.8	1026.8	3086.6
	200.5	1077.5	3175.0
	314.5	1295.6	3216.9
	362.5	1394.1	3445.1
	449.9	1455.1	3491.8
	603.0	1486.9	3609.1
$NH{-}CH_3C(O)OH$	61.7	606.2	1486.7
	75.5	802.5	1497.4
	93.1	894.3	1810.6
	153.4	1020.9	3087.7
	235.4	1077.4	3176.3
	243.6	1253.9	3219.1
	438.3	1367.8	3488.1
	593.1	1434.9	3661.9

CHAPTER 8: STUDY ON THE POTENTIAL ENERGY SURFACE OF THE OH + Cl_2O REACTION

8.1 Abstract

Theoretical methods are used to examine OH−OCl_2 and OH−ClOCl adduct formation as wells as the potential energy surfaces leading to the HOCl + ClO (8.1a) and Cl + HOOCl (8.1d) products in reaction (8.1) using the hybrid density functional UMPW1K/6-311++G(2df,p) level of theory. The OH−OCl_2 and OH−ClOCl adducts were found to have binding energies of ~0.2 kcal mol^{-1}. The reaction proceeds through pre-reactive complexes that are 1.4 kcal mol^{-1} below and 0.1 kcal mol^{-1} above the reactant energy for channels (8.1a) and (8.1d), respectively. Transition state energies were calculated to be ~1.4 and ~3.3 kcal mol^{-1} above the energy of the reactants.

8.2 Introduction

Although Cl_2O is thought to be of only minor atmospheric importance, an understanding of 8.1:

		D_rH^0(298 K) (kcal mol^{-1})	
OH + Cl_2O	→ HOCl + ClO	- 21.9	(8.1a)
	→ HCl + OClO	- 27.8	(8.1b)
	→ Cl_2 + HO_2	- 25.0	(8.1c)
	→ Cl + HOOCl	+ 0.9	(8.1d)

including the overall rate coefficient, $k_{8.1}$ (as a function of temperature and pressure), and the reaction mechanism provides a benchmark for studies of other chlorine oxides (e.g. ClO, OClO, and ClOOCl) that are important to the study of atmospheric chemistry and

stratospheric ozone depletion. Each of the reaction channels (8.1a—8.1d) can possible occur on separate potential energy surfaces by means of different reaction intermediates. It might be expected, therefore, that each channel might have significantly different temperature and pressure dependent behaviors.

The OH + Cl_2O reaction rate coefficient is also of particular interest for the interpretation of laboratory studies of the reaction:

$$OH + HOCl \rightarrow H_2O + ClO \quad (8.2)$$

Here, HOCl serves as a temporary reservoir for reactive chlorine in the atmosphere and can be removed via reaction (8.2) and UV/vis photolysis[230]:

$$HOCl + h\nu \rightarrow OH + Cl \quad (8.3)$$

It is important to note that the rate of reaction 8.1, $k_{8.2}$, has been proven difficult to measure accurately in the laboratory because of interference from Cl_2O that is present because of the equilibrium established with HOCl in reaction 8.4:

$$2\ HOCl \leftrightarrow Cl_2O + H_2O \quad (8.4)$$

where $K_{eq}(298\ K) = 0.09$ [214] and because Cl_2O reacts more efficiently with the OH radical than HOCl. The current JPL recommendation for $k_{8.2}$ at 298 K is 5.6×10^{-13} cm^3 $molecule^-$

^{1} s^{-1}. It is of note, however, that the JPL 06-2 estimated uncertainty in this value is a factor of 3.[214]

Here, the theoretical methods presented in Hansen et al.[231] was used in this work to gain further insight into the potential energy surfaces for reaction (8.1) and the product channels.

8.3 Methods

Calculations were performed using the Gaussian 03, Revision D.01 suite of programs.[63] The geometries of all the OH + Cl_2O reaction scheme participants were fully optimized at the UMPW1K[71,232] computational level employing the 6-311++G(2df,p) basis set. Harmonic vibrational frequency calculations performed at the UMPW1K/6-311++G(2df,p) level established the optimized structures as reactants, products, intermediate or transition state geometries and allowed the energies of all species to be zero-point energy corrected. The counterpoise procedure[72,187] was used to correct the energies for basis set superposition error. The expectation value $<s^2>$ was monitored for all species. The expectation value never exceeded 0.76, before spin-annihilation, for any of the open shell species, indicating that the wave functions were not contaminated by higher multiplicity states.

Each transition state and pre-reactive complex was identified via the random constrained sampling (RCS) methodology.[187] This method generates transition state geometries by randomly packing one reactant within a n-Å constrained radius sphere encompassing the second reactant. In this work, 1000 random geometries were generated by placing the OH radical within a 3.5-Å radius sphere centered over the Cl_2O molecule.

All calculations were performed on a supercomputing Linux cluster consisting of 320 processing nodes equipped with two quad-core Intel Nehalem processors (2.8 GHz) and 24 GB of memory. All nodes are connected with Infiniband, a high-speed, low-latency copper interconnect.

All UMPW1K/6-311++G(2df,p) optimized geometries and harmonic vibrational frequencies are available in supplementary Tables S8.1-S8.10.

8.4 Discussion

A RCS search of the doublet potential energy surface of the OH + Cl2O reaction revealed two of the possible reaction paths, those leading to the production of ClO + HOCl (8.1a) and ClOOH + Cl (8.1d) as product pairs. Although the RCS doesn't explicitly rule out the production of HCl + OClO (8.1b) and Cl_2 + HO_2 (8.1c) as reaction products, none of the 1,000 calculations resulted in transition state structures that would indicate their production. It is of note that the product channel (8.1d) has not previously been considered for this reaction. Francisco et al.[233] have previously identified HOOCl as the lowest energy isomer of $HClO_2$ and set the HOOCl molecule as a model for HOOBr.[234] In addition, HOOCl has been proposed as a product[235] in the heterogeneous reaction of the ClO dimer (ClOOCl) with HCl and as a reaction intermediate in the reactions of OH + ClO[236-238] and HO_2 + Cl.[239] To date, no direct experimental evidence for HOOCl has been published and merits future investigation.

On the basis of the optimized geometries, we have constructed potential energy surfaces for reactions (8.1a) and (8.1d), using energy values calculated at the UMPW1K/6-311++G(2df,p) level with zero-point energy and basis set superposition error corrections (Figures 8.1 and 8.2). For each reaction, the minimum energy path to

products was found to proceed through a pre-reactive complex (PRC), which was calculated to be 1.4 and 0.1 kcal mol^{-1}, respectively, below and above the reactant energy.

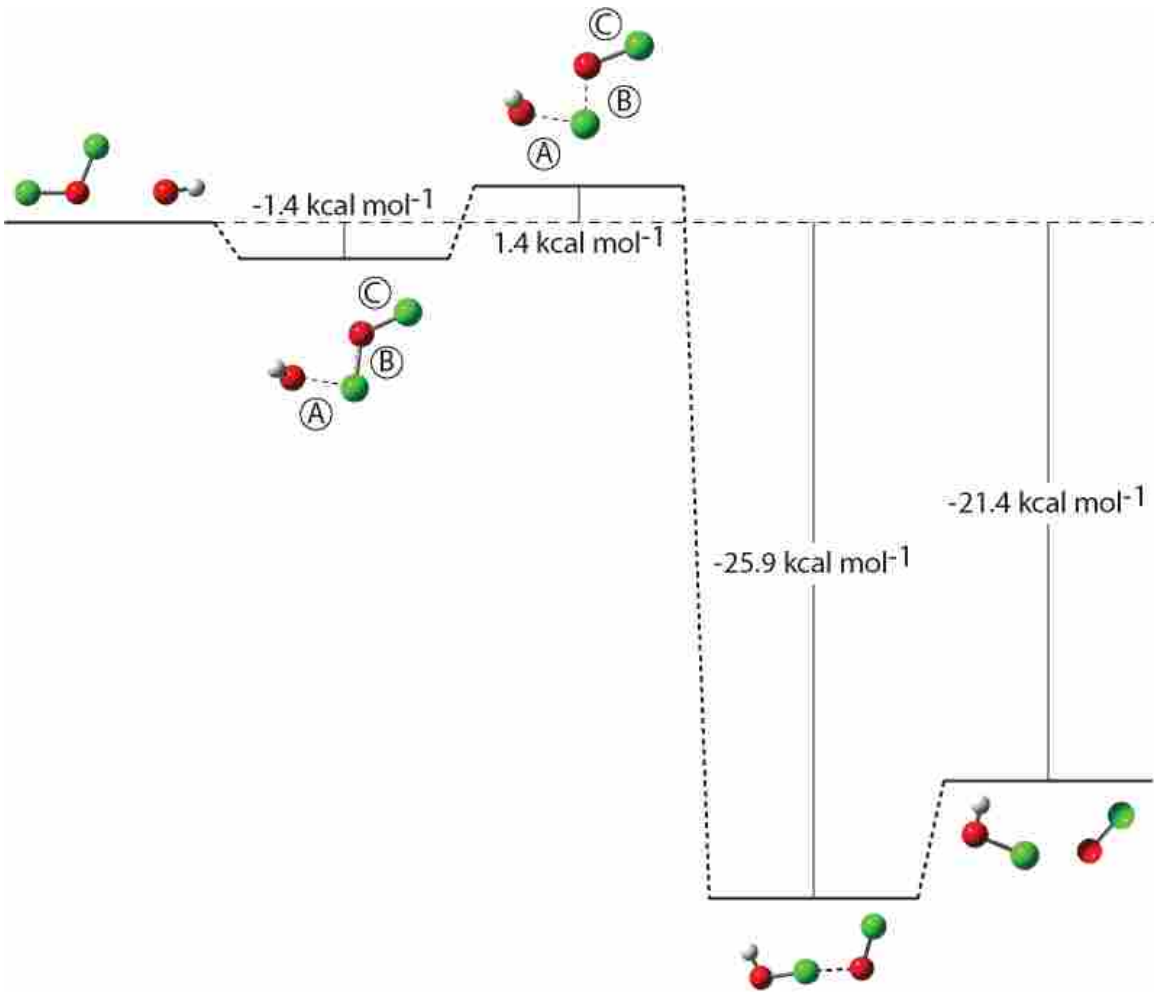

Figure 8.1. Calculated potential energy surface for the OH + Cl_2O reaction leading to the formation of ClO and HOCl. Energies are calculated at the UMPW1K/6-311++G(2df,p) level.

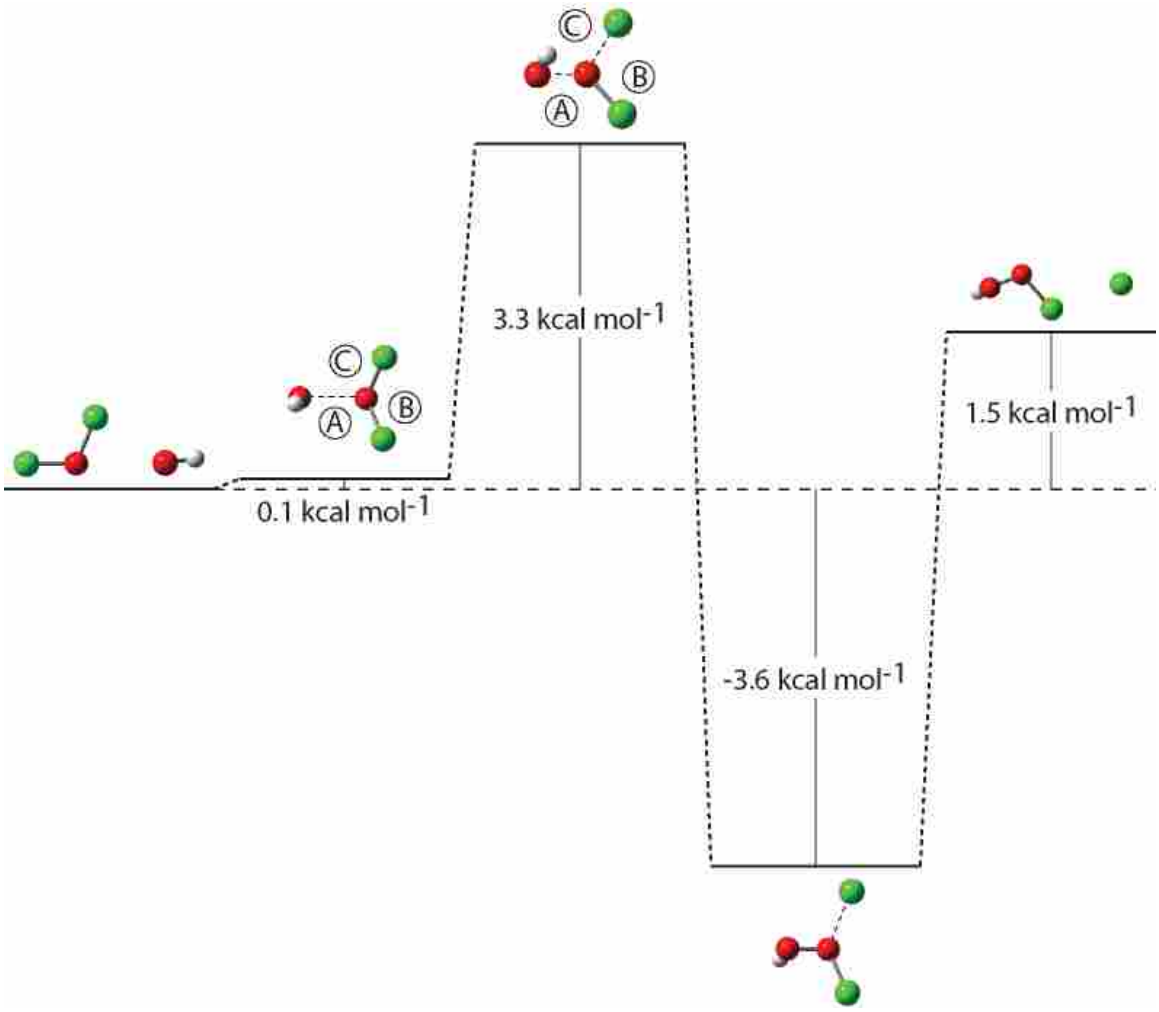

Figure 8.2. Calculated potential energy surface for the OH + Cl_2O reaction leading to the formation of HOOCl and Cl products. Energies are calculated at the UMPW1K/6-311++G(2df,p) level.

For reaction (8.1a) the PRC, shown in Figure 8.1, is characterized by a loose interaction (A) between one of the Cl_2O chlorine atoms and the hydroxyl oxygen atom. In addition, there is virtually no change in the length of the internal O–Cl bonds [(B) and (C)] of the Cl_2O molecule. As the reaction progresses through the transition state the newly formed O–Cl bond (A) length decreases dramatically (2.3 Å → 1.7 Å, ~26%) along with a significant increase (1.8 Å → 2.1 Å, ~20%) in the participating Cl_2O bond (B) length. The remaining O–Cl bond (C) experiences a small decrease (~7%) in length. The resulting transition state is product-like with bond lengths that are very similar to

those of the expected products. The transition state energy is calculated to be ~1.4 kcal mol^{-1} above the energy of the reactants. Exiting from the transition state leads to the breaking of an O–Cl bond of Cl_2O and the formation of a new O–Cl bond to produce HOCl and ClO. The PES calculations suggest that the transition state may first fall into a loosely bound post-reactive complex that is ~26 kcal mol^{-1} below the reactants. A 4.5 kcal mol^{-1} barrier separates the post-reactive complex from the separated products.

Similar to reaction (8.1a), the PRC of reaction (8.1d), Figure 8.2, is also characterized by a loose interaction (A), this time between the oxygen of Cl_2O and the hydroxyl oxygen atom with similarly little change in the O–Cl bonds [(B) and (C)] lengths of Cl_2O. Passing into the transition state the forming O–O bond (A) length shortens considerably (2.4 Å → 1.7 Å, ~26%) along with an increase (1.7 Å → 2.0 Å, 13%) in the Cl_2O bond (C) length. The remaining O–Cl bond (B) experiences a small (~7%) decrease in length. The transition state energy is calculated to be 3.3 kcal mol^{-1} above the energy of the reactants. Moving from the transition state to products leads to the breaking of an O–Cl bond (C) of Cl_2O and the formation of a new O–O (A) bond to produce HOOCl and Cl. Calculations suggest the existence of a post-reactive complex that is ~3.6 kcal mol^{-1} below the energy of the reactants. A 5.1 kcal mol^{-1} barrier separates the post-reactive complex from the products (HOOCl + Cl).

The combination of a pre-reactive complex and low activation barrier for the ClO + HOCl product channel is consistent with the experimentally determined negative temperature dependence observed for the reaction rate coefficient. Decreasing the temperature increasingly favors the formation of the weakly stable pre-reactive complex. From this point on the PES, the reaction can then proceed over a small barrier and onto

products. The product branching ratio is determined by the competition between the formation of the two pre-reactive complexes and the activation barriers. An *ab initio* molecular dynamics study of this potential including a calculation of the density of states would offer additional insights into the effects of the pre-reactive complexes and small activation barriers on the temperature dependence and product distribution for this reaction.

Using the NASA/JPL[214] recommend heats of formation the overall reaction enthalpy for the formation of HOCl + ClO (8.1a) is determined to be -21.92 ± 0.14 kcal mol^{-1} and 0.88 ± 0.53 kcal mol^{-1} for the products HOOCl + Cl (8.1d). The *ab initio* reaction enthalpies are calculated to be ⁻21.4 and 1.5 kcal mol^{-1} for reaction (8.1a) and (8.1d), respectively. The difference between the NASA/JPL recommended values compared to the calculated values in this work suggests the magnitude of the uncertainty in the reported activation barriers and pre-reactive complex binding energies of the potential energy surfaces obtained in the present work to be on the order of 0.6 kcal mol^{-1}.

At reduced temperature the formation of hydrogen bonded adducts, $OH{-}Cl_2O$, is a possibility that could influence the overall temperature dependence of the rate coefficient resulting in the observed weak non-Arrhenius behavior in reaction (8.1). Two adducts, $OH{-}OCl_2$ and OH−ClOCl, were identified from among 1,000 initial geometries using the UMPW1K/6-311++G(2df,p) method/basis set. The binding energies corrected for zero-point energy and basis set superposition error were calculated to be surprisingly small, ⁻0.20 and ⁻0.19 kcal mol^{-1}, respectfully. The optimized geometries of the two adducts are shown in Figure 8.3. Second-order perturbative estimates of donor-acceptor (bond-

antibond) interactions in the natural bond order bases of the adducts indicate that approximately 5% of the stabilization energy that results from adduct formation is a consequence of hydrogen bond interactions between the OH radical and Cl_2O. The calculated binding energies are less than *k*T at room temperature and neither of the two adducts are likely to exist in appreciable amounts at temperatures greater than 100 K. In addition, adduct formation is not expected to perturb the reactivity of the OH radical as the electron density of the OH radical electron is unchanged. Rate coefficient measurements at much lower temperatures than included in this study could possibly establish the hypothesis of $OH{-}OCl_2$ and/or OH−ClOCl adduct formation in reaction 8.1.

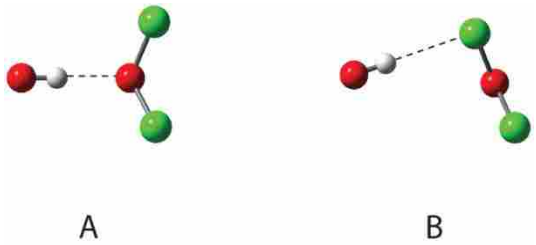

Figure 8.3. UMPW1K/6-311++G(2df,p) optimized $OH{-}OCl_2$ and OH−ClOCl adducts.

8.5 Conclusions

The theoretical calculations found that the PES leading to the formation of HOCl + ClO, reaction (8.1a), and Cl + HOOCl, reaction (8.1d), proceed through very weak pre-reactive complexes, which is consistent with a pressure independent rate coefficient and consistent with the observed negative temperature dependence. A weak non-Arrhenius behavior was observed within the precision of the present measurements made by Riffault et al.[240] suggesting the possible formation of a hydrogen bonded OH−ClOCl adduct that does not lead to reaction products. Theoretical calculations, however, suggest

that such adducts may form at low temperatures, but the weak binding energies (0.20 and 0.19 kcal mol^{-1}) of the identified complexes suggest they cannot be responsible for a measurable temperature dependence under the experimental conditions of the cited work. Natural population analysis of the unpaired electron of the OH radical indicates its reactivity will not be perturbed as a result of the formation of OH−Cl_2O complexes. In summary, the calculated hydrogen-bonded adducts are not stable enough to influence the temperature dependence of reaction (8.1). However, the calculated more stable pre-reactive complexes are consistent with the observed negative temperature dependence observed in $k_{9.1}$(T).

8.6 Supplemental Tables

Tables S8.1 through S8.10 represent the UMPW1K/6-311++G(2df,p) optimized geometries and harmonic vibrational frequencies.

8.6.1 Cartesian Coordinates for Each Optimized Geometry

Table S8.1. Reactant geometries UMPW1K/6-311++G(2df,p).

Cl_2O				
	Cl	-0.00336	0.00000	0.00428
	O	0.00888	0.00000	1.73162
	Cl	1.60140	0.00000	2.39666
HO				
	O	0.00000	0.00000	-0.00224
	H	0.00000	0.00000	0.98151

Table S8.2. Product geometries UMPW1K/6-311++G(2df,p).

ClOH				
	Cl	0.1020	0.0000	-3.7383
	O	0.0503	0.0000	-5.4549
	H	0.9975	0.0000	-5.6925
ClO				
	Cl	0.6123	0.0000	-2.9280
	O	0.6123	0.0000	-4.5179
ClOOH				
	Cl	0.8520	-0.1850	-2.1636
	O	1.2479	0.2666	-3.8362
	O	2.4386	-0.3601	-4.2589
	H	3.1257	0.2785	-3.9694
Cl				
	Cl	0.0000	0.0000	0.0000

Table S8.3. Pre-reactive complex geometries UMPW1K/6-311++G(2df,p).

PES1				
	Cl	-0.0784	-0.0910	0.0180
	O	0.0010	1.6534	-0.0723
	Cl	0.0652	2.3864	1.4850
	O	-0.2276	0.0681	-2.3107
	H	-1.2040	0.1677	-2.3089
PES2				
	Cl	-0.0410	-0.3146	0.0263
	O	-0.1432	0.1970	1.6789
	Cl	1.3377	-0.0244	2.5436
	O	-2.0362	-0.6442	2.8107
	H	-1.8487	-1.5631	2.5215

Table S8.4. Transition state geometries UMPW1K/6-311++G(2df,p).

PES1				
	Cl	-0.0821	0.0395	-1.9066
	O	-0.6068	-0.0668	-0.3074
	Cl	0.8246	-0.0238	0.9190
	O	-0.8187	-0.0889	2.1445
	H	-0.9735	0.8784	2.1898
PES2				
	Cl	-0.0749	0.0341	-0.0071
	O	-0.0512	1.8964	-0.0006
	Cl	0.0963	2.5848	1.6242
	O	0.8675	2.8341	-1.2905
	H	1.7065	2.9175	-0.7895

Table S8.5. Post-reactive complex geometries UMPW1K/6-311++G(2df,p).

PES1				
	Cl	1.0129	-0.2766	0.3195
	O	-0.1413	1.5173	0.1290
	Cl	-0.2705	2.4902	1.4235
	O	1.9388	-1.7734	0.3299
	H	2.2852	-1.8121	1.2430
PES2				
	Cl	0.0689	-0.2528	-0.0853
	O	-0.0661	1.4797	-0.4581
	Cl	-0.1902	2.9063	1.5851
	O	-1.2405	1.7486	-1.1955
	H	-0.9087	1.6852	-2.1186

8.6.2 Harmonic Vibrational Frequencies

Table S8.6. Reactant harmonic frequencies UMPW1K/6-311++G(2df,p). Frequencies are reported in cm^{-1}.

Cl_2O	HO
276.7	3611.8
573.5	
633.9	

Table S8.7. Product harmonic frequencies UMPW1K/6-311++G(2df,p). Frequencies are reported in cm^{-1}.

ClOH	ClO	ClOOH
714.9	853.4	339.3
1216.3		458.7
3668.6		566.8
		862.7
		1366.8
		3569.1

Table S8.8. Pre-reactive complex harmonic frequencies UMPW1K/6-311++G(2df,p). Frequencies are reported in cm^{-1}.

PES1	PES2
18.1	47.7
49.0	61.3
182.7	98.1
242.7	135.7
260.9	276.5
524.4	368.7
595.6	549.0
620.3	618.4
3632.8	3633.3

Table S8.9. Transition state harmonic frequencies UMPW1K/6-311++G(2df,p). Frequencies are reported in cm^{-1}.

PES1	PES2
-374.5	-277.3
80.4	78.1
152.6	112.1
245.5	239.7
292.3	261.6
458.1	378.1
666.1	482.6
858.3	854.2
3639.1	3639.7

Table S8.10. Post-reactive complex harmonic frequencies UMPW1K/6-311++G(2df,p). Frequencies are reported in cm^{-1}.

PES1	PES2
84.8	77.0
87.7	118.6
174.7	156.4
259.6	331.0
308.5	369.4
582.5	545.8
764.5	832.4
1119.6	1364.6
3658.9	3568.1

CHAPTER 9: CONCLUSIONS

9.1 Summary

This thesis represents a comprehensive study of many radical-molecule systems pertinent to atmospheric processes. Each of the studies detailed herein and the associated results add to the current understanding of the chemistry of the atmosphere. High level *ab initio* calculations have been used to study radical−molecule complex formation and the potential energy surfaces of a number of atmospherically important reactions. Experimental methods have been used to understand the effects of water vapor on the self-reaction kinetics of 2HEP, the simplest and most abundant unsaturated hydrocarbon in the atmosphere. This coupled approach of using both theory and experiment to address relevant issues in the chemistry of the atmosphere has led to insights of complex reaction mechanisms and the characterization of new complexes.

Ab inito calculations were used to study the catalytic enhancement of H_2O on the self-reaction of HO_2 at the G2M(CC5)//B3LYP/6-311G(d,p) level of theory. The calculated potential energy surface predicts a lowering of the activation barrier, 6.4 kcal mol^{-1}, for the formation of products (H_2O_2 + $^3O_2$) in the presence of an HO_2−H_2O complex. Compared with the results for the reaction without H_2O, it is noted that the H_2O molecule catalytically enhances the self-reaction rate constant of the HO_2 radical by enhancing the hydrogen bonding architecture of the HO_2−HO_2 complex. NBO and geometric analysis of this modified structure demonstrate that the presence of H_2O allows for a greater degree of delocalization of electron density from the terminal peroxy oxygen of the complexed HO_2 radical into the O−H anti-bond of the HO_2 radical fated to become

$^3O_2$. Earlier assumptions stating that water acts as an energy chaperone are unfounded based upon this work.

Due to the possible role that water may play in the reaction kinetics of small RO_2 radicals, of which HO_2 is the simplest, the existence of water complexes of the most common RO_2 radicals is verified computationally. Radical−water complexes of the methyl peroxy (CH_3O_2), ethyl peroxy ($CH_3CH_2O_2$), acetyl peroxy ($CH_3C(O)O_2$), acetonyl peroxy ($CH_3C(O)CH_2O_2$), hydroxymethyl peroxy ($CH_2(OH)O_2$), 2-hydroxyethyl peroxy ($CH_2(OH)CH_2O_2$), fluoromethyl peroxy ($CH_2(F)O_2$), 2-fluoroethyl peroxy ($CH_2(F)CH_2O_2$) radicals are evaluated using high level *ab initio* calculations. A wide range of binding energies is predicted for these complexes, in which the difference in binding energies can be explained by examination of the composition of the R group attached to the peroxy moiety. The general trend in binding energies has been determined to be as follows: fluorine ≈ alkyl < carbonyl < alcohol. The weakest bound complex, CH_3O_2-H_2O, is calculated to be bound by 2.3 kcal mol^{-1}, and the strongest, the $CH_2(OH)O_2$-H_2O complex, is bound by 5.1 kcal mol^{-1}. The binding energy of the peroxy radical-water complexes which contain carbonyl and alcohol groups indicates that these complexes may perturb the kinetics and product branching ratios of reactions involving these complexes. The formation and thermochemistry of larger peroxy radicals derived from isoprene and (E)-2-hexenal is also addressed. These two molecules represent the largest source of non-methane biogenically emitted hydrocarbons in the atmosphere. The kinetics of these radicals is important for understanding the formation of O_3 in non-urban, NO_x-limited environments.

The importance of NH_3 in the formation of new atmospheric aerosol particles has been understood since the mid-1970's. In the presence of water vapor, NH_3 forms hydrogen-bonded proton-transfer complexes that result in salts (e.g. $(NH_4)HSO_4$ and $(NH_4)_2SO_4$) that have a lower vapor pressure and that act as condensation nuclei. Although the role of NH_3 has been studies, the impact of the photolysis products of ammonia, NH_2 and NH, on new particle formation has been largely neglected. This thesis presents computational work that addressed the formation of sulfuric acid, nitric acid, acetic acid and formic acid complexes with NH_3, NH_2 and NH. The results of this study suggest that the effects of NH_3 on the formation of new aerosol particles will be imitated by NH_2, although to a lesser degree, and confined primarily to complexes with H_2SO_4 and HNO_3. The NH radical is not expected to play a noticeable role in the formation of new atmospheric aerosols.

Although Cl_2O is thought to be of only minor atmospheric importance, an understanding of the reaction of Cl_2O + OH, including the overall rate coefficient (as a function of temperature and pressure), and the reaction mechanism provides a benchmark for studies of other chlorine oxides (e.g. ClO, OClO, and ClOOCl) that are important to the study of atmospheric chemistry and stratospheric ozone depletion. Theoretical methods are used to examine OH-OCl_2 and OH-ClOCl adduct formation using the hybrid density functional UMPW1K. The reaction of Cl_2O with OH is found to proceed through these two very weak pre-reactive complexes, consistent with a pressure independent rate coefficient and consistent with the observed negative temperature dependence. Theoretical calculations, however, suggest that such adducts cannot be responsible for a measurable temperature dependence. Natural population analysis of the unpaired electron

of the OH radical indicates its reactivity will not be perturbed as a result of the formation of OH-Cl_2O complexes.

The 2HEP radical is the simplest example of the class of peroxy radicals that is derived from the atmospheric oxidation of alkenes. This thesis presents a study of the gas phase reactions of the 2HEP radical in the presence and absence of water vapor at temperatures between 286 and 292 K using laser flash photolysis coupled with UV time-resolved absorption detection between 220 and 300 nm. Water vapor concentrations were quantified using IR spectroscopy. The 2HEP self-reaction rate constant is enhanced by the presence of water vapor by as much as a factor of 2 (2.45×10^{-12} cm^3 $molecule^{-1}$ s^{-1} to 5.35×10^{-12} cm^3 $molecule^{-1}$ s^{-1}), similar to the HO_2 self-reaction. The enhancement in the 2HEP self-reaction rate coefficient is thought to occur as a result of the formation of a 2HEP−H_2O complex during the reaction mechanism.

The combination of computational and experimental techniques has been applied to a number of different and important issues in atmospheric chemistry. Some of the computational work has been aimed at providing insight into the experimental observations of others. For example, until now, the role of H_2O in the water enhancement of the HO_2 self-reaction rate constant has been poorly understood. The work provided in this dissertation provides a sound explanation for this phenomenon and forms the foundation upon which similar reaction enhancements may be made (e.g., the role of H_2O in 2HEP self-reaction kinetics). Other portions of the work has been to broaden the scope of the current understanding of the role NH_x species plays in the formation of new atmospheric aerosol particles. The experimental work has demonstrated that a water vapor dependence exists for the 2HEP self-reaction. The combination of experimental

and computational techniques used in this thesis demonstrates the necessity of using both theory and experiments in assessing the impact of atmospheric species and their myriad of complexes on atmospheric processes.

9.2 Future Considerations

The role of the $HO_2{-}H_2O$ complex has also been found to play an important part in the chemistry of many atmospheric systems. The $HO_2{-}H_2O$ complex is thought to play a role in the reaction of HO_2 with NO. Turbulent flow reactor experiments designed to measure the product branching ratio show an enhancement of the HNO_3 production channel of the $NO + HO_2 \rightarrow HNO_3$ reaction in the presence of water vapor. The results further indicate that the obtained branching fraction of the HNO_3 forming channel increases from ~0.2% to ~3%. It is of a fundamental importance to understand how the presence of H_2O perturbs the product branching ratio of the HO_2 + NO system so that this understanding can be applied to larger systems of interest, such as isoprene + NO. Computationally, this can be accomplished through the identification of critical points, or transition states, within the relevant potential energy surfaces and following those points to their products using a number of molecular dynamic simulations. This would allow for the estimation of branching ratios for reactions that are not readily experimentally probable.

The $HO_2{-}H_2O$ complex is known to be important in the context of the $SO_3 + HO_2$ reaction. The primary product channel of this reaction is the formation of the HSO_5 radical. In the presence of water vapor, the product channel is reported to shift towards the formation of H_2SO_4, which accounts for ~66% of the products formed. The increased formation of H_2SO_4, in environments high in NH_3, may lead to the formation of new

aerosol particles. A deeper understanding of this process may lead to better models and predictions about how and why particulates form in the atmosphere.

Although the self-reaction of the 2HEP radical is important, when the concentration of other radicals, such as HO_2 is elevated, the cross-reactions are likely to dominate. Further experimental studies into these cross-reactions and into the effect of water vapor on these reactions is critical to understand the full role of 2HEP in the atmosphere.

REFERENCES

(1) Donaldson, D. J.; Vaida, V.; Naaman, R. *J. Chem. Phys.* **1987**, *87*, 2522.

(2) Robinson, G. W. *J. Chem. Phys.* **1967**, *46*, 572.

(3) Rudich, Y.; Hurwitz, Y.; Frost, G. J.; Vaida, V.; Naaman, R. *J. Chem. Phys.* **1993**, *99*, 4500.

(4) Sapers, S. P.; Vaida, V.; Naaman, R. *J. Chem. Phys.* **1988**, *88*, 3638.

(5) Donaldson, D. J.; Gaines, G. A.; Vaida, V. *J. Phys. Chem.* **1988**, *92*, 2766.

(6) Donaldson, D. J.; Richard, E. C.; Strickler, S. J.; Vaida, V. *J. Phys. Chem.* **1988**, *92*, 5514.

(7) Donaldson, D. J.; Vaida, V.; Naaman, R. *J. Phys. Chem.* **1988**, *92*, 1204.

(8) Prinslow, D. A.; Vaida, V. *J. Phys. Chem.* **1989**, *93*, 1836.

(9) \Vaida, V.; Donaldson, D. J.; Sapers, S. P.; Naaman, R.; Child, M. S. *J. Phys. Chem.* **1989**, *93*, 513.

(10) Vaida, V.; Donaldson, D. J.; Strickler, S. J.; Stephens, S. L.; Birks, J. W. *J. Phys. Chem.* **1989**, *93*, 506.

(11) Hurwitz, Y.; Naaman, R. *J. Chem. Phys.* **1995**, *102*, 1941.

(12) Gillies, J. Z.; Gillies, C. W.; Suenram, R. D.; Lovas, F. J.; Schmidt, T.; Cremer, D. *J. Mol. Spec.* **1991**, *146*, 493.

(13) Schriver, L.; Barreau, C.; Schriver, A. *Chem. Phys.* **1990**, *140*, 429.

(14) Frost, G. J.; Vaida, V. *J. Geophys. Res. Lett.* **1995**, *100*, 18803.

(15) Staikova, M.; Donaldson, D. J. *Phys. Chem. Earth* **2001**, *26*, 473.

(16) Hamilton Jr, E. J. *J. Chem. Phys.* **1975**, *8*, 3682.

(17) Aloisio, S.; Li, Y.; Francisco, J. S. *J. Chem. Phys.* **1999**, *110*, 9017.

(18) Aloisio, S.; Francisco, J. S. *J. Phys. Chem. A* **1998**, *102*, 1899.

(19) Hamilton Jr, E. J.; Naleway, C. A. *J. Phys. Chem.* **1976**, *80*, 2037.

(20) Nanayakkara, A. A.; Balint-Kurti, G. G.; Williams, I. H. *J. Phys. Chem.* **1992**, *96*, 3662.

(21) Kim, K. S.; Kim, H. S.; Jang, J. H.; Kim, H. S.; Mhin, B.-J.; Xie, Y.; Schaefer Iii, H. F. *J. Chem. Phys.* **1991**, *94*, 2057.

(22) Xie, Y.; Schaefer Iii, H. F. *J. Chem. Phys.* **1993**, *98*, 8829.

(23) Li, Y.; Francisco, J. S. *J. Chem. Phys.* **2001**, *115*, 8381.

(24) Aloisio, S.; Francisco, J. S. *Chem. Phys.* **2000**, *254*, 1.

(25) Francisco, J. S.; Sander, S. P. *J. Am. Chem. Soc.* **1995**, *117*, 9917.

(26) Aloisio, S.; Francisco, J. S. *J. Am. Chem. Soc.* **2000**, *122*, 9196.

(27) Li, Y.; Francisco, J. S. *J. Chem. Phys.* **2001**, *114*, 211.

(28) Aloisio, S.; Francisco, J. S. *J. Phys. Chem. A* **1999**, *103*, 6049.

(29) Kulmala, M.; Vehkamäki, H.; Petäjä, T.; Dal Maso, M.; Lauri, A.; Kerminen, V. M.; Birmili, W.; McMurry, P. H. *J. Aeros. Sci.* **2004**, *35*, 143.

(30) Kulmala, M.; Laakso, L.; Lehtinen, K. E. J.; Riipinen, I.; Dal Maso, M.; Anttil, T.; Kerminen, V. M.; Horrak, U.; Vana, M.; Tammet, H. *Atmos. Chem. Phys.* **2004**, *4*, 2553.

(31) Doyle, G. J. *J. Chem. Phys.* **1961**, *35*, 795.

(32) Covert, D. S.; Kapustin, V. N.; Quinn, P. K.; Bates, T. S. *J. Geophys. Res.* **1992**, *97*, 20581.

(33) Hoppel, W. A.; Frick, G. M.; Fitzgerald, J. W.; Larson, R. E. *J. Geophys. Res.* **1994**, *99*, 14443.

(34) Dowd, C.; McFiggans, G.; Creasey, D. J.; Pirjola, L.; Hoell, C.; Smith, M. H.; Allan, B. J.; Plane, J. M. C.; Heard, D. E.; Lee, J. D.; Pilling, M. J.; Kulmala, M. *Geophys. Res. Lett.* **1999**, *26*, 1707.

(35) Coffman, D. J.; Hegg, D. A. *J. Geophys. Res.* **1995**, *100*, 7147.

(36) Scott, W. D.; Cattell, F. C. R. *Atmos. Environ.* **1979**, *13*, 307.

(37) Asman, W. A. H.; Drukker, B.; Janssen, A. J. *Atmos. Environ.* **1988**, *22*, 725.

(38) Gehring, M.; Hoyermann, K.; Wagner, H. G.; Wolfrum, J. *Ber. Bunsenges. Physik. Chem.* **1971**, *75*, 1287.

(39) Khe, P. V.; Soulignac, J. C.; Lesclaux, R. *J. Phys. Chem.* **1977**, *81*, 210.

(40) Zetzsch, C.; Stuhl, F. *Ber. Bunsenges. Physik. Chem.* **1981**, *85*, 564.

(41) Cohen, N.; Westberg, K. R. *J. Phys. Chem. Ref. Data* **1991**, *21*, 1211.

(42) Kimball-Linne, M. A.; Hanson, R. K. *Combust. Flame* **1986**, *64*, 337.

(43) Kanaya, Y.; Akimoto, H. *Chem. Rec.* **2002**, *2*, 199.

(44) DeMore, W. B. *J. Phys. Chem.* **1979**, *83*, 1113.

(45) Cox, R. A.; Burrows, J. P. *J. Phys. Chem.*, *83*, 2560.

(46) Lii, R. R.-.; Sauer Jr, M. C.; Gordon, J. *J. Phys. Chem.* **1981**, *85*, 2833.

(47) Kircher, C. C.; Sander, S. P. *J. Phys. Chem.* **1984**, *88*, 2082.

(48) Kanno, N.; Tonokura, K.; Tenzaki, A.; Koshi, M. *J. Phys. Chem. A* **2005**, *109*, 3153.

(49) Suma, K.; Sumiyoshi, Y.; Endo, Y. *Science* **2006**, *311*, 1278.

(50) Tang, Y.; Tyndall, G. S.; Orlando, J. J. *J. Phys. Chem. A* **2009**, *114*, 369.

(51) Aloisio, S.; Francisco, J. S.; Friedl, R. R. *J. Phys. Chem. A* **2000**, *104*, 6597.

(52) Hamilton Jr, E. J.; Lii, R. R.-. *Int. J. Chem. Kinet.* **1977**, *9*, 875.

(53) Lii, R. R.-.; Gorse Jr, R. A.; Sauer Jr, M. C.; Gordon, S. *J. Phys. Chem.* **1980**, *84*, 813.

(54) Clegg, S. M.; Abbatt, J. P. D. *Atmos. Chem. Phys.* **2001**, *1*, 73.

(55) Christensen, L. E.; Sander, S. P.; Okumura, M.; Salawitch, R. J.; Toon, G. C.; Sen, B.; Blaview, J.-F.; Jucks, K. W. *Geophys. Res. Lett.* **2002**, *29*, 1299.

(56) Andersson, B. Y.; Cox, R. A.; Jenkin, M. E. *Int. J. Chem. Kinet.* **1988**, *20*, 283.

(57) Bloss, W. J.; Rowley, D. M.; Cox, R. A.; Jones, R. L. *Phys. Chem. Chem. Phys.* **2002**, *4*, 3639.

(58) Christensen, L. E.; Okumura, M.; Hansen, J. C.; Sander, S. P.; Francisco, J. S. *J. Phys. Chem. A* **2006**, *110*, 6948.

(59) Clark, J. M.; Hansen, J. C.; English, A. M.; Francisco, J. S. *J. Phys. Chem. A* **2008**, *112*, 1587.

(60) Alongi, K. S.; Dibble, T. S.; Shields, G. C.; Kirschner, K. N. *J. Phys. Chem.* **2006**, *110*, 3686.

(61) Bil, A.; Latajka, Z. *Chem. Phys. Lett.* **2005**, *406*, 366.

(62) Zhu, R.; Lin, M. C. *Chem. Phys. Lett.* **2002**, *354*, 366.

(63) Frisch, M. J.; Trucks, G. W.; Schlegel, H. B.; Scuseria, G. E.; Robb, M. A.; Cheeseman, J. R.; Montgomery, J., J. A.; Vreven, T.; Kudin, K. N.; Burant, J. C.;

Millam, J. M.; Iyengar, S. S.; Tomasi, J.; Barone, V.; Mennucci, B.; Cossi, M.; Scalmani, G.; Rega, N.; Petersson, G. A.; Nakatsuji, H.; Hada, M.; Ehara, M.; Toyota, K.; Fukuda, R.; Hasegawa, J.; Ishida, M.; Nakajima, T.; Honda, Y.; Kitao, O.; Nakai, H.; Klene, M.; Li, X.; Knox, J. E.; Hratchian, H. P.; Cross, J. B.; Bakken, V.; Adamo, C.; Jaramillo, J.; Gomperts, R.; Stratmann, R. E.; Yazyev, O.; Austin, A. J.; Cammi, R.; Pomelli, C.; Ochterski, J. W.; Ayala, P. Y.; Morokuma, K.; Voth, G. A.; Salvador, P.; Dannenberg, J. J.; Zakrzewski, V. G.; Dapprich, S.; Daniels, A. D.; Strain, M. C.; Farkas, O.; Malick, D. K.; Rabuck, A. D.; Raghavachari, K.; Foresman, J. B.; Ortiz, J. V.; Cui, Q.; Baboul, A. G.; Clifford, S.; Cioslowski, J.; Stefanov, B. B.; Liu, G.; Liashenko, A.; Piskorz, P.; Komaromi, I.; Martin, R. L.; Fox, D. J.; Keith, T.; Al-Laham, M. A.; Peng, C. Y.; Nanayakkara, A.; Challacombe, M.; Gill, P. M. W.; Johnson, B.; Chen, W.; Wong, M. W.; Gonzalez, C.; Pople, J. A. Gaussian 2003; Gaussian 2003, revision D.01 ed.; Gaussian, Inc: Wallingford, CT, 2004.

(64) Becke, A. D. *J. Chem. Phys.* **1992**, *97*, 9173.

(65) Becke, A. D. *J. Chem. Phys.* **1992**, *96*, 2155.

(66) Becke, A. D. *J. Chem. Phys.* **1993**, *98*, 5648.

(67) Lee, C.; Yang, W.; Parr, R. G. *Physical Review B* **1988**, *37*, 785.

(68) Mebel, A. M.; Morokuma, K.; Lin, M. C. *J. Chem. Phys.* **1995**, *103*, 7414.

(69) Curtis, L. A.; Pochatko, D. J.; Reed, A. E.; Weinhold, F. *J. Chem. Phys.* **1985**, *82*, 2679.

(70) Foster, J. P.; Weinhold, F. *J. Am. Chem. Soc.* **1980**, *102*, 7211.

(71) Jensen, F. *Introduction to Computational Chemistry*, 2nd ed.; Wiley: New York, 2006.

(72) Latajka, Z.; Scheiner, S. J. *J. Chem. Phys.* **1987**, *87*, 1194.

(73) Reed, A. E.; Weinhold, F. *J. Chem. Phys.* **1983**, *78*, 4066.

(74) Reed, A. E.; Weinhold, F. *J. Chem. Phys.* **1985**, *83*, 1736.

(75) Reed, A. E.; Weinhold, F.; Curtis, L. A.; Pochatko, D. J. *J. Chem. Phys.* **1986**, *84*, 5687.

(76) Reed, A. E.; Weinstock, R. B.; Weinhold, F. *J. Chem. Phys.* **1985**, *83*, 735.

(77) Glending, E.; Lanids, C. R.; Weinhold, F. NBO.5G; NBO 5.G ed.; Theoretical Chemistry Institute and Department of Chemistry: Madison, WI, 2010.

(78) Granovsky, A. A. GAMESS; Firefly version 7.1.G; Available at: http://classic.chem.msu.su/gran/firefly/index.html ed., 2010.

(79) Anglada, J. M.; Olivella, S.; Solé, A. *J. Phys. Chem. A* **2007**, *111*, 1695.

(80) Zhu, R. S.; Lin, M. C. *PhysChemComm* **2001**.

(81) Odutola, J. A.; Dyke, T. R. *J. Chem. Phys.* **1980**, *72*, 5062.

(82) Wallington, T. J.; Dagaut, P.; Kurylo, M. J. *Chem. Rev.* **1992**, *92*, 667.

(83) Lightfoot, P. D.; Cox, R. A.; Crowley, J. N.; Destriau, M.; Hayman, G. D.; Jenkin, M. E.; Moortgat, G. K.; Zabel, F. *Atmos. Environ.* **1992**, *26A*, 1805.

(84) Blanksby, S. J.; Ramond, T. M.; Davico, G. E.; Nimlos, M. R.; Kato, S.; Bierbaum, V. M.; Lineberger, W. C.; Ellison, G. B.; Okumura, M. *J. Am. Chem. Soc.* **2001**, *123*, 9585.

(85) Darnall, K. R.; Carter, W. P. L.; Winer, A. M.; Lloyd, A. C.; Pitts, J. N. *J. Phys. Chem.* **1976**, *80*, 1948.

(86) Atkinson, R. *J. Phys. Chem. Ref. Data* **1997**, *26*, 215.

(87) Butkovskaya, N. I.; Kukui, A.; Pouvesle, N.; LeBras, G. *J. Phys. Chem. A* **2005**, *109*, 6509.

(88) Stockwell, J. *J. Geophys. Res.* **1995**, *110*, 11695.

(89) Donaldson, D. J.; Vaida, V. *Chem. Rev.* **2006**, *106*, 1445.

(90) Ellison, G. B.; Tuck, A. F.; Vaida, V. *J. Geophys. Res.* **1999**, *104*, 11633.

(91) Dobson, C. M.; Ellison, G. B.; Tuck, A. F.; Vaida, V. *Proc. Natl. Acad. Sci.* **2000**, *97*, 11864.

(92) Vaida, V.; Tuck, A. F.; Ellison, G. B. *Phys. Chem. Earth* **2000**, *25*, 195.

(93) Frisch, M. J.; Trucks, G. W.; Schlegel, H. B.; Scuseria, G. E.; Robb, M. A.; Cheeseman, J. R.; Zakrzewski, V. G.; Montgomery, J. A.; Stratmann, R. E.; Burant, J. C.; Dapprich, S.; Millam, J. M.; Daniels, A. D.; Kudin, K. N.; Strain, M. C.; Farkas, O.; Tomasi, J.; Barone, V.; Cossi, M.; Cammi, R.; Mennucci, B.; Pomelli, C.; Adamo, C.; Clifford, S.; Ochterski, J.; Petersson, G. A.; Ayala, P. Y.; Cui, Q.; Morokuma, K.; Rega, N.; Salvador, P.; Dannerberg, J. J.; Malick, D. K.; Rabuck, A. D.; Raghavachri, K.; Foresman, J. B.; J, C.; Oritz, J. V.; Baboul, A. G.; Stefanov, B. B.; Liu, G.; Liashenko, A.; Piskorz, P.; Komaromi, R.; Gomperts, R.; Martin, R. L.; Fox, D. J.; Keith, T.; Al-Laham, M. A.; Peng, C. Y.; Nanayakkara, A.; Challacombe, P. M.; Gill, P. M. W.; Johnson, B.; Chen, W.; Wong, M. W.; Andres, J. L.; Gonzalez, C.; Head-Gordon, M.; Repogle, E. S.; Pople, J. A. Gaussian 98, revision A.11.3; Gaussian 98, revision A.11.3 ed.; Gaussian, Inc.: Pittsbutgh, PA, 2002.

(94) Moller, C.; Plesset, M. S. *Phys. Rev.* **1934**, *46*, 618.

(95) Pople, J. A.; Head-Gordon, M.; Raghavachri, K. *J. Chem. Phys.* **1987**, *87*, 5968.

(96) Pople, J. A.; Head-Gordon, M.; Raghavachri, K.; Fox, D. J. *J. Chem. Phys.* **1989**, *90*, 5622.

(97) Purvis, G. D. I.; Bartlett, R. J. *J. Chem. Phys.* **1982**, *76*, 1910.

(98) Lee, T. J. *J. Chem. Phys.* **1991**, *69*.

(99) Handy, N. C.; Pople, J. A.; Head-Gordon, M.; Raghavachri, K.; Trucks, G. W. *Chem. Phys. Lett.* **1989**, *164*, 185.

(100) Scuseria, G. E. *Chem. Phys. Lett.* **1994**, *226*, 251.

(101) Slater, J. C. *Phys. Rev.* **1930**, *35*, 210.

(102) Fock, V. *Z. Physik.* **1930**, *126*, 61.

(103) Hartree, D. R.; Hartree, W. *Proc. R. Soc.* **1935**, *9*, A150.

(104) Stephens, P. J.; Devlin, F. J.; Chabalowski, C. F.; Frisch, M. J. *J. Phys. Chem.* **1994**, *98*, 11623.

(105) Becke, A. D. *J. Chem. Phys.* **1993**, *98*, 5648.

(106) Lee, C.; Yang, W.; Parr, R. G. *Phys. Rev. B* **1988**, *37*, 785.

(107) Vosko, S. H.; Wilk, L.; Nusair, M. *Can. J. Phys.* **1980**, *58*, 1200.

(108) Hariharan, P. C.; Pople, J. A. *Theor. Chim. Acta* **1973**, *28*, 213.

(109) Krishnan, R.; Binkley, J. S.; Seeger, R.; Pople, J. A. *J. Chem. Phys.* **1980**, *72*, 650.

(110) Clark, T.; Chandrasekhar, J.; Spitznagel, G. W.; Schleyer, P. v. R. *J. Comput. Chem.* **1983**, *4*, 294.

(111) Ditchfield, R.; Hehre, W. J.; Pople, J. A. *J. Chem. Phys.* **1971**, *54*, 724.

(112) Frisch, M. J.; Pople, J. A.; Binkley, J. S. *J. Chem. Phys.* **1984**, *80*, 3265.

(113) Planck, M. *Verhandlungen der Deutschen Physikalischen Gesell-schaft* **1911**, *13*, 138.
(114) Einstein, A. *Ann. Phys.* **1913**, *40*.
(115) Boys, S. F.; Bernardi, F. *Mol. Phys.* **1970**, *19*, 553.
(116) Reed, A. E.; Curtis, L. A.; Weinhold, F. *Chem. Rev.* **1988**, *88*, 899.
(117) Clark, J. jMOL; jMOL, 1.0 ed. Provo, 2006.
(118) Gu, Y.; Kar, T.; Scheiner, S. J. *J. Am. Chem. Soc.* **1999**, *121*, 9411.
(119) Popelier, P. L. A.; Koch, U. *J. Phys. Chem.* **1995**, *99*, 9747.
(120) Berger, I.; Egli, M.; Rich, A. *Proc. Natl. Acad. Sci.* **1996**, *93*, 12116.
(121) Ornstein, R. L.; Zheng, Y. J. *J. Biomol. Struct. Dyn.* **1997**, *14*, 657.
(122) Takahara, P. M.; Frederick, C. A.; Lippard, S. J. *J. Am. Chem. Soc.* **1996**, *118*, 12309.
(123) Egli, M.; Gessner, R. V. *Proc. Natl. Acad. Sci.* **1995**, *92*, 180.
(124) Jiang, L.; Lai, L. *J. Biomol. Struct. Dyn.* **2002**, *277*, 37732.
(125) Derewenda, Z. S.; Lee, L.; Derewenda, U. *J. Mol. Bio.* **1995**, *252*, 248.
(126) Bella, J.; Berman, H. M. *J. Mol. Bio.* **1996**, *264*, 734.
(127) Musah, R. A.; Jensen, G. M.; Rosenfeld, R. J.; McRee, D. E.; Goodin, D. B.; Bunte, S. W. *J. Am. Chem. Soc.* **1997**, *119*, 9083.
(128) Steiner, T.; Saenger, W. *J. Am. Chem. Soc.* **1992**, *114*, 10146.
(129) Steiner, T.; Saenger, W. *J. Am. Chem. Soc.* **1993**, *115*, 4540.
(130) Allen, F. H.; Bellard, S.; Brice, M. D.; Cartwright, B. A.; Doubleday, A.; Higgs, H.; Hummelink, T.; Hummelink-Peters, B. G.; Kennard, O.; Motherwell, W. D. S.; Rodgers, J. R.; Watson, D. G. *Acta Crystallogr. Sect. B* **1979**, *B35*, 2331.
(131) Aloisio, S.; Francisco, J. S.; Friedll, R. R. *J. Phys. Chem. A* **2000**, *104*, 6597.
(132) Steiner, T. *Chem. Commun.* **1997**, 727.
(133) van de Bovenkamp, J.; Matxain, J. M.; van Duijneveldt, F. B.; Steiner, T. *J. Phys. Chem.* **1999**, *103*, 2784.
(134) Steiner, T.; Kanters, J. A.; Kroon, J. *J. Chem. Commun.* **1996**, 1277.
(135) Brandl, M.; Linaur, K.; Meyer, M.; Suhnel, J. *Theor. Chim. Acta* **1999**, *101*, 103.
(136) Mizuno, K.; Ochi, T.; Shindo, Y. *J. Chem. Phys.* **1998**, *109*, 9502.
(137) Hobza, P.; Spirko, V.; Havlas, Z.; Buchhold, K.; Reimann, B.; Barth, H.-D.; Brutschy, B. *Chem. Phys. Lett.* **1999**, *299*, 180.
(138) Chaney, J. D.; Goss, C. R.; Folting, K.; Santarsiero, B. D.; Hollingsworth, M. D. *J. Am. Chem. Soc.* **1996**, *118*, 9432.
(139) Bedell, B. L.; Goldfarb, L.; Mysak, E. R.; Samet, C.; Maynary, A. *J. Phys. Chem.* **1999**, *103*, 4572.
(140) Patrick, R.; Golden, D. M. *Int. J. Chem. Kinet.* **1983**, *15*, 1189.
(141) Troe, J. *J. Chem. Phys.* **1977**, *66*, 4745.
(142) Tardy, D. C.; Rabinovitch, B. S.; Whitten, G. Z. *J. Chem. Phys.* **1968**, *48*, 1427.
(143) Whitten, G. Z.; Rabinovitch, B. S. *J. Chem. Phys.* **1963**, *38*, 2466.
(144) McQuarrie, G. Z.; Simon, J. D. *Physical Chemistry: A molecular Approach*, 1st ed.; University Science Books, 1997.

(145) Steinfeld, J. I.; Francisco, J. S.; Hase, W. L. *Chemical Kinetics and Dynamics*; Prentice Hall: New York, 1989.

(146) Guenther, A. *Reactive Hydrocarbons in the Atmosphere*; Academic Press: San Diego, 1999.

(147) Warneke, C.; Holzinger, R.; Hansel, A.; Jordan, A.; Lindinger, W.; Poschl, U.; WIlliams, J.; Hoor, P.; Fischer, H.; Crutzen, P. J.; Scheeren, H. A.; Lelieveld, J. *J. Atmos. Chem.* **2001**, *38*, 167.

(148) Chen, X. H.; Hulbert, D.; Shepson, P. B. *J. Geophys. Res.* **1998**, *103*, 25563.

(149) Tuazon, E. C.; Atkinson, R. *Int. J. Chem. Kinet.* **1990**, *22*, 1221.

(150) Sprengnether, M.; Demerjian, K. L.; Donahue, N. M.; Anderson, J. G. *J. Geophys. Res.* **2002**, *10*, 4268.

(151) Zhang, R.; Suh, I.; Clinkenbearn, A.; Lei, W.; North, S. W. *J. Geophys. Res.* **2000**, *105*, 24627.

(152) Zhang, D.; Zhang, R.; Church, C.; North, S. W. *Chem. Phys. Lett.* **2001**, *2001*, 49.

(153) Jenkin, M. E.; Boyd, A.; Lesclaux, R. *J. Atmos. Chem.* **1998**, *29*, 267.

(154) Butkovskaya, N. I.; Kukui, A.; LeBras, G. *J. Phys. Chem.* **2007**, *111*, 9047.

(155) Butkovskaya, N. I.; Kukui, A.; LeBras, G. *Geohpys. Res. Abstr.* **2009**, *11*, EGU20092620.

(156) Zhu, R. S.; Lin, M. C. *PhysChemComm* **2003**, *6*, 51.

(157) Reicert, L.; Andres Hernandez, M. D.; Stobener, D.; Burkert, J.; Burrows, J. P. *J. Geophys. Res.* **2003**, *2003*, 4017.

(158) Schmidt, M. W.; Baldridge, K. K.; Boatz, J. A.; Elbert, S. T.; Gordon, M. S.; Jensen, J. H.; Koseki, S.; Matsunaga, N.; Nguyen, K. A.; Windus, T. L.; Dupuis, M.; Montgomery, J. A. *J. Comput. Chem.* **1993**, *14*, 1347.

(159) Call, S. T.; Boldyrev, A. I.; Zubarev, D. Y. *J. Comput. Chem.* **2007**, *28*, 1177.

(160) Carugo, O.; Parrinello, M. *Phys. Rev. Lett.* **1985**, *55*, 2471.

(161) Car, R.; Parrinello, M. *Phys. Rev. Lett.* **1985**, *55*, 2471.

(162) Jones, R. O.; Ganterfor, G.; Hunsicker, S.; Pieperhoff, P. J. *J. Chem. Phys.* **1995**, *103*, 9549.

(163) Yourshaw, I.; Zhao, Y.; Neumark, D. M. *J. Chem. Phys.* **1996**, *105*, 351.

(164) Tomasulo, A.; Ramakrishna, M. V. *J. Chem. Phys.* **1996**, *105*, 10449.

(165) Lenzer, T.; Yourshaw, I.; Furlenetto, M. R.; Pivonka, N. L.; Neumark, D. M. *J. Chem. Phys.* **2001**, *115*, 3578.

(166) Corcelli, S. A.; Kelly, J. A.; Tully, J. C.; Johnson, M. A. *J. Chem. Phys.* **2002**, *106*, 4872.

(167) Haubein, N. C.; McMillan, S. A.; Broadbelt, L. J. *J. Chem. Inf. Comput. Sci.* **2003**, *43*, 68.

(168) Haubein, N. C.; McMillan, S. A.; Broadbelt, L. J.; Snurr, R. Q. *J. Chem. Inf. Comput. Sci.* **2003**, *43*, 1820.

(169) Peeters, J.; Nguyen, T. L.; Vereecken, L. *Phys. Chem. Chem. Phys.* **2009**, *11*, 5935.

(170) Peeters, J.; Boullart, W.; Van Hoeymissen, J. "Proc. Eurotrac. Symp."; Proc. Eurotrac. Symp., 1994, The Hauge.

(171) Peeters, J.; Boullart, W.; Pultau, V.; Vandenberk, S.; Vereecken, L. *J. Phys. Chem. A* **2007**, *111*, 897.

(172) Park, J.; Jongsma, C. G.; Zhang, R.; North, S. W. *J. Phys. Chem. A* **2004**, *108*, 10688.

(173) Jenkin, M. E.; Saunders, S. M.; Wagner, V.; Philling, M. J. *Atmos. Chem. Phys.* **2003**, *3*, 181.

(174) Hermans, I.; Muller, J. F.; Nguyen, T. L.; Jacobs, P. A.; Peeters, J. *J. Phys. Chem. A* **2005**, *109*, 4303.

(175) Jenkin, M. E.; Hayman, G. D. *J. Chem. Soc., Faraday Trans.* **1995**, *91*, 1911.

(176) Finlayson-Pitts, B. J.; Pitts, J. N. *Chemistry of the Upper and Lower Atmosphere: Theory, Experiments and Applications*, 1st ed.; Academic Press: San Diego, 2000.

(177) Wenfang, L.; Zhang, R.; McGivens, W. S.; Derecskei-Kovacs, A.; North, S. W. *J. Phys. Chem. A* **2001**, *105*, 471.

(178) Lei, W.; Derecskei-Kovacs, A.; Zhang, R. *J. Chem. Phys.* **2000**, *113* 5354.

(179) Hendreickson, J. B. *J. Am. Chem. Soc.* **1967**, *89*, 7036.

(180) Dorofeeva, O. V.; Mastryukov, V. S.; Allinger, N. L.; Almenningen, A. *J. Phys. Chem.* **1985**, *89*, 252.

(181) Yanling, G.; Tapas, K.; Scheiner, S. J. *J. Am. Chem. Soc.* **1999**, *121*, 9411.

(182) Ochterski, J. Thermochemistry in Gaussian; Thermochemistry in Gaussian ed., 2000.

(183) Lightfoot, P. D.; Veyret, B.; Lesclaux, R. *J. Phys. Chem.* **1990**, *94*, 708.

(184) Butkovskaya, N.; Rayez, M.-T. r. s.; Rayez, J.-C.; Kukui, A.; Le Bras, G. *J. Phys. Chem. A* **2009**, *113*, 11327.

(185) Gonzalez, J.; Torrent-Sucarrat, M.; Anglada, J. M. *Phys. Chem. Chem. Phys.* **2010**, *12*, 2116.

(186) Long, B.; Tan, X.-f.; Ren, D.-s.; Zhang, W.-j. *Chem. Phys. Lett.* **2010**, *492*, 214.

(187) Clark, J.; Call, S. T.; Austin, D.; Hansen, J. C. *J. Phys. Chem. A* **2010**, *114*, 6534.

(188) Lanciotti, R.; Belletti, N.; Patrignani, F.; Gianotti, A.; Gardini, F.; Guerzoni, M. E. *J. Agric. Food Chem.* **2003**, *51*, 2958.

(189) Wiedinmyer, C.; Guenther, A.; Harley, P.; Hewitt, C. N.; Geron, C.; Artaxo, P.; Steinbrecher, R.; Rasmussen, R. *Emissions of Atmospheric Trace Compounds*; Kluwer Academic Publishers: Dordrecht, 2004.

(190) Albaladejo, J.; Ballesteros, B.; Jimenez, E.; Martin, P.; Martinez, E. *Atmos. Environ.* **2002**, *36*, 3231.

(191) Atkinson, R. *Chem. Rev.* **1986**, *86*, 69.

(192) Jenkin, M. E.; Cox, R. A. *J. Phys. Chem.* **1991**, *95*, 3229.

(193) Atkinson, R.; Baulch, D. L.; Cox, R. A.; Hampson, R. F.; Kerr, J. A.; Troe, J. *Int. J. Chem. Kinet.* **1989**, *21*, 115.

(194) Huang, R. L.; Singh, S. *J. Chem. Soc. (Resumed)* **1958**, 891.

(195) Russell, G. A. *J. Org. Chem.* **1958**, *23*, 1407.

(196) Russell, G. A. *J. Am. Chem. Soc.* **1958**, *80*, 4987.
(197) Brown, H. C.; Asii, A. B. *J. Am. Chem. Soc.* **1955**, *77*, 4019.
(198) Atkinson, R.; Baulch, D. L.; Cox, R. A.; Hampson, J. R. F.; Kerr, J. A.; Troe, J. *J. Phys. Chem. Ref. Data* **1989**, *18*, 881.
(199) Veyret, B.; Lesclaux, R.; Rayez, M. T.; Rayez, J. C.; Cox, R. A.; Moortgat, G. K. *J. Phys. Chem.* **1989**, *93*, 2368.
(200) Burrows, J. P.; Moortgat, G. K.; Tyndall, G. S.; Cox, R. A.; Jenkin, M. E.; Hayman, G. D.; Veyret, B. *J. Phys. Chem.* **1989**, *93*, 2375.
(201) Anastasi, C.; Muir, D. J.; Simpson, V. J.; Pagsberg, P. *J. Phys. Chem.* **1991**, *95*, 5791.
(202) Maricq, M. M.; Szente, J. J. *J. Phys. Chem.* **1996**, *100*, 4507.
(203) Fenter, F. F.; Catoire, V.; Lesclaux, R.; Lightfoot, P. D. *J. Phys. Chem.* **1993**, *97*, 3530.
(204) Horie, O.; Crowley, J. N.; Moortgat, G. K. *J. Phys. Chem.* **1990**, *94*, 8198.
(205) Feria, L.; Gonzalez, C.; Castro, M. *Int. J. Quant. Chem.* **2004**, *99*, 605.
(206) Elrod, M. J.; Ranschaert, D. L.; Schneider, N. J. *Int. J. Chem. Kinet.* **2001**, *33*, 363.
(207) Wallington, T. J.; Dagaut, P.; Kurylo, M. J. *Chem. Rev.* **1992**, *92*, 667.
(208) McAdam, K.; Veyret, B.; Lesclaux, R. *Chem. Phys. Lett.* **1987**, *133*, 39.
(209) Bauer, D.; Crowley, J. N.; Moortgat, G. K. *J. Photochem. Photobiol. A* **1992**, *65*, 329.
(210) Villenave, E.; Lesclaux, R. *J. Phys. Chem.* **1996**, *100*, 14372.
(211) Stone, D.; Rowley, D. M. *Phys. Chem. Chem. Phys.* **2005**, *7*, 2156.
(212) Sander, S. P.; Peterson, M.; Watson, R. T.; Patrick, R. *J. Phys. Chem.* **1982**, *86*, 1236.
(213) Lightfoot, P. D.; Cox, R. A.; Crowley, J. N.; Destriau, M.; Hayman, G. D.; Jenkin, M. E.; Moortgat, G. K.; Zabel, F. *Atmos. Environ.* **1992**, *26A*, 1805.
(214) Sander, S. P.; Friedll, R. R.; Golden, D. M.; Kurylo, M. J.; Moortgat, G. K.; Keller-Rudek, H.; Wine, P. H.; Ravishankara, A. R.; Kolb, C. E.; Molina, M. J.; Finlayson-Pitts, B. J.; Huie, R. E.; Orkin, V. L. "Chemical kinetics and photochemical data for use in atmospheric studies, JPL Pub. 06-2," Jet Propulsion Laboratory, 2006.
(215) Murrells, T. P.; Jenkin, M. E.; Shalliker, S. J.; Hayman, G. D. *J. Chem. Soc., Faraday Trans.* **1991**, *87*, 2351.
(216) Dockery, D. W.; Pope III, C. A.; Xu, X.; Spengler, J. D.; Ware, J. H.; Fay, M. E.; Ferris, J., B G; Speizer, F. E. *New England J. Med.* **1993**, *329*, 1753.
(217) Ball, R. J.; Robinson, G. D. *J. Appl. Meterol.* **1982**, *21*, 171.
(218) Eldering, A.; Larson, S. M.; Hall, J. R.; Hussey, K. J.; Cass, G. R. *Environ. Sci. Technol.* **1993**, *27*, 626.
(219) Liepert, B.; Fabian, P.; Grassi, H. *Beitr. Phys. Atmos.* **1994**, *67*, 15.
(220) Castleman, A. W.; Dans, R. E.; Mukelwitz, H. R.; Tang, I. N.; Wood, W. P. *Int. J. Chem. Kinet. Symp.* **1975**, *1*, 629.
(221) Seinfeld, J. H. *Atmospheric Chemistry and Physics of Air Pollution*; Wiley & Sons: New York, 1986.
(222) Larson, L. J.; Largend, A.; Tao, F.-M. *J. Phys. Chem. A* **1999**, *103*, 6786.
(223) Nguyen, M.-T.; Jamka, A. J.; Cazar, R. A.; Tao, F.-M. *J. Chem. Phys.* **1997**, *106*, 8710.

(224) Ennis, C. P.; Lane, J. R.; Kjaergaard, H. G.; McKinley, A. J. *J. Am. Chem. Soc.* **2009**, *131*, 1358.

(225) Seinfeld, J. H.; Pandis, S. Atmospheric Chemistry and Physics In *Air Pollution to Climate Change*; Wiley & Sons: New York, 1998.

(226) Kim, K.; Jordan, K. D. *J. Phys. Chem.* **1994**, *98*, 10089.

(227) Kim, K. S.; Mhin, B. J.; Choi, U. S.; Lee, K. *J. Chem. Phys.* **1992**, *97*, 6649.

(228) CENRS "Atmospheric Ammonia: Sources and Fate A Review of Ongoing Federal Research and Future Needs," NOAA Aeronomy Laboratory, 2000.

(229) Feyereisen, M. W.; Feller, D.; Dixon, D. A. *J. Phys. Chem.* **1996**, *100*, 2993.

(230) Burkholder, J. B. *J. Geophys. Res.* **1993**, *98*, 2963.

(231) Hansen, J. C.; Friedll, R. R.; Sander, S. P. *J. Phys. Chem. A* **2008**, *112*, 9229.

(232) Perdew, J. In *Electronic Structure of Solids*; Ziesche, P., Eschig, H., Eds.; Akademie Verlag: Berlin, 1991; pp 11.

(233) Francisco, J. S.; Sander, S. P.; Lee, T. J.; Rendell, A. P. *J. Phys. Chem.* **1994**, *98*, 5644.

(234) Guha, S.; Francisco, J. S. *J. Phys. Chem. A* **1997**, *101*, 5347.

(235) De Haan, D. O.; Floisand, I.; Stordal, F. *J. Geophys. Res.* **1997**, *102*, 1251.

(236) Sumathi, R.; Peyerimhoff, S. D. *Phys. Chem. Chem. Phys.* **1999**, *1*, 5429.

(237) Lee, T. J.; Rendell, A. P. *J. Phys. Chem.* **1993**, *97*, 6999.

(238) Zhu, R.; Xu, Z. F.; Lin, M. C. *J. Chem. Phys.* **2002**, *116*, 7452.

(239) Weissman, L. G.; Shum, L. G. S.; Heneghan, S. P.; Benson, S. W. *J. Phys. Chem.* **1981**, *85*, 2863.

(240) Riffault, V.; Clark, J.; Hansen, J. C.; Ravishankara, A. R.; Burkholder, J. B. *ChemPhysChem* **2010**, *11*, 4060.